Technische Universität München

TECHNISCHE UNIVERSITÄT MÜNCHEN
Max-Planck Institut für Extraterrestrische Physik

Probing the Connection between Supernovae and Gamma-Ray Bursts

Felipe A. Olivares Estay

Vollständiger Abdruck der von der Fakultät für Physik der Technischen Universität München zur Erlangung des akademischen Grades eines

Doktors der Naturwissenschaften (Dr. rer. nat.)

genehmigten Dissertation.

Vorsitzender:		Univ.-Prof. Dr. Martin Beneke
Prüfer der Dissertation:	1.	Priv.-Doz. Dr. Jochen Greiner
	2.	Univ.-Prof. Dr. Lothar Oberauer

Die Dissertation wurde am 08.03.2013 bei der Technischen Universität München eingereicht und durch die Fakultät für Physik am 23.04.2013 angenommen.

Abstract

Gamma-ray bursts (GRBs) are the most compact and luminous electromagnetic explosions in the Universe. They emit a large amount of energy, of the order of $\sim 10^{51}$ erg in γ-rays, on very short time scales between 10^{-3} and 10^{3} seconds. Supernovae (SNe) are very optically luminous transient events, which often outshine their entire host galaxy before fading over several weeks or months. They release kinetic and radiative energy of the order of the GRB energy budget and both are thought to originate from the core collapse of massive stars. The first observational evidence of a connection between this two transient phenomena was found about a decade ago. Since then, only half a dozen spectroscopically confirmed associations have been discovered.

In this thesis I analysed the four recent GRB-SN associations. Physical parameters such as the progenitor radius, the host-galaxy extinction, and the ejected mass of the explosion are derived. I study the brightness and colours of the four GRB-SNe candidates, of which one was rejected as a synchrotron rebrightening. For a complete GRB-SN sample 23 objects were added from the literature along with two additional objects observed by GROND. With a total of 28 events, a statistical analysis was approached. Promoted by the fact that ^{56}Ni mass synthesised in the explosion powers the SN light, a correlation between nickel mass and maximum bolometric luminosity was found. Based also on the ejecta mass, two populations with different mass-loss histories were discovered. No correlations were evident between the GRB and the SN luminosity, which would suggest that the GRB and SN explosion mechanisms are independent, although they are triggered by a unique core-collapse event. However, a weak trend was found for a comparison between the kinetic SN energy and the total isotropic GRB energy release, which introduces a scenario where the energy of the core collapse is partitioned between the GRB and the SN. A few other GRB-SN events remain to be analysed to be included in the sample statistical analysis. Observations for a sample of SNe not associated to GRBs has been acquired in order to build a comparison sample and tackle several other scientific studies.

From the full GRB sample, late-time rebrightenings are found at a rate of 3 per year. Those with SN nature are 55% of all observed rebrightenings. The additional case of GRB 100902A shed light on the late-time rebrightenings, which are originated by the GRB central engine rather than SN. Episodes of mass accretion after the core collapse would trigger such phenomenon. These events represent one fifth of all detectable rebrightenings in GRB optical light curves and provide insight on how the central engine of GRBs operates.

Zusammenfassung

Gammastrahleblitze (Englisch: Gamma-Ray Burst, GRBs) sind die am kompaktesten und hellsten elektromagnetischen Explosionen des Universums. Sie strahlen große Mengen an Energie ab, in der Größenordnung von $\sim 10^{51}$ erg, auf sehr kurzen Zeitskalen zwischen 10^{-3} und 10^{3} Sekunden. Supernovae (SNe) sind sehr optisch leuchtenden transienten Ereignissen, die oft überstrahlen die gesamte Galaxie vor dem Einblenden ber mehrere Wochen oder Monaten. Sie geben kinetische und Strahlungsenergie der Reihenfolge der GRB Energiehaushalt und beide sind vermutlich aus dem Kern stammen massereicher Sterne. Die erste empirische Nachweis einer Verbindung zwischen diesen beiden vorübergehende Phänomene wurde über ein gefundenes vor zehn Jahren. Seitdem nur ein halbes Dutzend spektroskopisch bestätigt Assoziationen entdeckt worden.

Die Analyse von drei SNe, welche in Verbindung mit einem GRB stehen, erlaubt es uns, physikalische Parameter der Explosionen zu bestimmen, wie den Radius des Vorgngersterns, die Extinktion in der Galaxie der SN, und die in der Explosion ausgestoene Masse. Für eine vollständige GRB-SN Sample, 23 Objekte wurden aus den Literatur angenommen. Zustzlich wurden zwei Objekte aus unverffentlichten Untersuchungen angenommen, die auch GROND Dateien nutzen. Die 28 GRB-SNe vom Gesamt-Sample teilen sich in zwei Populationen auf, die sich durch verschieden verlaufenden Massenverlust des Vorgngersterns voneinander unterscheiden. Es zeigten sich keine Zusammenhnge zwischen der Leuchtkraft von GRB und SN, was ein Hinweis darauf ist, dass die Explosionsmechanismen von GRB und SN voneinander unabhngig sind, obwohl SN und GRB beide vom Kollaps des Sternenkerns verursacht werden. Es wurde jedoch ein schwacher Trend zwischen der kinetischen Energie der SN und der beim GRB isotrop freigesetzten Gesamtenergie gefunden, was auf ein Szenario hindeutet, in dem die Energie des Kernkollapses sich auf GRB und SN aufteilt. Einige andere GRB-SN Ereignisse bleiben analysiert werden, um in den aufgelegten Probe statistische Analyse. Beobachtungen bei einer Stichprobe von SNe nicht zugeordnet GRBs erworben wurde, um einen Vergleich zu bauen probieren und zu bekämpfen mehrere andere wissenschaftliche Studien.

Aus dem vollen GRB Probe werden späten Zeit rebrightenings mit einer Rate gefunden von 3 pro Jahr. Diejenigen mit SN Natur sind 55% aller beobachteten rebrightenings. Die zusätzlichen Fall von GRB 100902A Licht auf die spten Zeitpunkt rebrightenings, die von der zentralen GRB, zuzuschreiben sind, Motor anstatt SN. Episoden von Massenakkretionsrate nachdem der Kern Zusammenbruch auslösen würde ein solches Phänomen. Diese Ereignisse stellen ein Fünftel aller nachweisbaren rebrightenings in GRB optischen Lichtkurven und Einblick, wie die zentralen Motor der GRBs arbeitet.

Contents

1 Introduction **1**
1.1 Bursts of Gamma-Rays . . . 1
1.2 Supernovae . . . 3
1.3 The Association between GRBs and SNe . . . 8

2 Data and Instrumentation **13**
2.1 The Swift Satellite . . . 13
2.1.1 The XRT Data . . . 15
2.1.2 The UVOT Data . . . 15
2.2 The GROND . . . 15
2.2.1 Observing . . . 19
2.2.2 Reduction of the Images . . . 20
2.2.3 Astrometric and Photometric Calibrations . . . 21
2.2.4 Image Subtraction . . . 22
2.3 Final Data Analysis . . . 23
2.3.1 Galactic Foreground Extinction . . . 23
2.3.2 Light Curve Fitting . . . 23
2.3.3 SN 1998bw Template Fitting . . . 24
2.3.4 Broad-Band Spectral Energy Distribution . . . 24
2.3.5 Additional Extinction in the Host . . . 27
2.3.6 Quasi-Bolometric Light Curves . . . 30
2.4 The case of GRB 110420A . . . 33

3 The Fast Evolution of SN 2010bh/XRF 100316D **35**
3.1 Introduction . . . 35
3.2 Observations . . . 36
3.2.1 GROND . . . 37
3.2.2 *Swift*/XRT and UVOT . . . 37
3.3 Early Broad-Band SED . . . 38
3.3.1 Modelling Scheme . . . 38
3.3.2 Host-Galaxy Extinction . . . 42
3.3.3 Evolution of the Thermal Component . . . 44
3.4 Multicolour Light Curves . . . 46
3.4.1 Optical and Near-Infrared Light Curves . . . 46
3.4.2 Colour Evolution . . . 46
3.4.3 Comparison with SN 1998bw . . . 46
3.4.4 Comparison with SN 2006aj . . . 50

3.5 Bolometric Light Curve . . . 51
3.5.1 Physical Parameters of the Explosion . . . 51
3.6 Conclusions . . . 55

4 SN Constraints for GRB 090424 57
4.1 Introduction . . . 57
4.2 Observations . . . 58
4.2.1 Prompt Emission . . . 58
4.2.2 The Afterglow . . . 58
4.3 Results . . . 60
4.3.1 The Nature of the Host Galaxy . . . 60
4.3.2 The Broad-band Spectral Energy Distribution . . . 60
4.3.3 Modelling the Light Curves . . . 62
4.3.4 Spectral Energy Distributions . . . 65
4.4 Discussion . . . 66
4.5 Conclusions . . . 69

5 Four Late-Time Rebrightenings 71
5.1 Multicolour Light-Curve Fitting . . . 73
5.2 Spectral Energy Distributions . . . 77
5.3 Quasi-Bolometric Light Curves . . . 83
5.3.1 Physical Parameters of the Explosion . . . 86

6 The Updated GRB-SN Sample 89
6.1 Luminosity, Stretch, and Redshift . . . 89
6.2 Correlations with Explosion Parameters . . . 92
6.3 GRB vs. SN Properties . . . 98
6.4 Rate of GRB-SN Events . . . 102

7 GROND Statistics of Light-Curve Bumps 105

8 The Stripped-Envelope SN Sample 107
8.1 The SN follow-up . . . 107
8.1.1 Logistics . . . 107
8.1.2 Observations . . . 107
8.2 Science Prospects . . . 109
8.2.1 Physical Parameters of the Explosion . . . 109
8.2.2 A Standard NIR Light Curve . . . 110
8.2.3 Classification tool using NIR colours . . . 111
8.2.4 Dereddening Techniques . . . 111
8.2.5 Rise Times . . . 112

9 Summary and prospects 115

Bibliography 117

Acknowledgments 131

Chapter 1

Introduction

1.1 Bursts of Gamma-Rays

As many other findings by humanity, gamma-ray bursts (GRBs) were discovered serendipitously by the Vela satellites, which consisted of USA military instrumentation monitoring γ-ray signals for compliance with the treaty that prohibited test detonations of nuclear weapons. In the late '60s, the Vela 4 and Vela 3 satellites detected a flash of γ radiation unlike any known nuclear weapon signature. The first scientific results were published by Klebesadel et al. (1973), who claimed that these were extraterrestrial events of cosmic origin. The true origin and also the nature of GRBs remained a mystery for two decades until the launch of the Compton Gamma-Ray Observatory (CGRO) in 1991 equipped with the Burst and Transient Experiment (BATSE). The most important BATSE discovery was that GRBs are isotropically distributed in the sky, strongly suggesting their cosmological origin (Meegan et al., 1992). This result was confirmed in 1997 with the launch of the Italian-Dutch satellite BeppoSAX (Boella et al., 1997), which detected and localised GRBs at X-ray energies. Immediately followed the discovery of the first X-ray "afterglow" (AG) of GRB 970228 (Costa et al., 1997b). The BeppoSAX AG localisation of $\sim 1'$ accuracy allowed ground-based follow-up observations, which facilitated the discovery of the first optical AG also connected to GRB 970228 (van Paradijs et al., 1997; Sahu et al., 1997). The redshift measurements from optical spectroscopy confirmed the cosmological distances of these events (Metzger et al., 1997; Kulkarni et al., 1998).

The cosmological origin of GRBs implies an extreme luminosity of these γ-ray sources. They release $E_\gamma \sim 10^{51} - 10^{53}$ erg or even more over a time of just a few seconds (Piran, 1999), making them the most concentrated and brightest electromagnetic explosions in the Universe. The BATSE satellite recorded over 2700 GRBs over the 9-year CGRO mission at an average rate of 1 burst per day (see catalogue by Kaneko et al., 2006). The bursts exhibited a non-thermal spectrum composed by a smoothly-joined broken power law with the break at $E_{\rm peak} \sim 0.1 - 1$ MeV (Kouveliotou et al., 1993). The duration [1] of GRBs range from 10^{-3} to 10^{3} s following a bimodal distribution of (1) *short* GRBs with a duration $T_{90} \lesssim 2$ s and (2) *long* GRBs lasting $T_{90} \gtrsim 2$ s (Kouveliotou et al., 1993). These classes are also dubbed type I and II, respectively, and shown in Fig. 1.1. Figure 1.2 illustrates that the γ-ray spectrum of type I's has a significantly larger high-to-low energy flux ratio (the so-called hardness ratio). In consequence, short and long GRBs are also distinguished as hard and soft, respectively (Qin et al., 2000). The AGs of short GRBs were only detected after the launch of the *Swift* satellite in 2004 (Gehrels et al.,

[1] The duration of γ-ray emission is estimated by means of T_{90}. This is the period of time in which 90% of the flux is measured.

2004), which started a third era of GRB discoveries after BATSE and BeppoSAX. Thanks to its precise localisation of GRBs in γ-ray, X-ray, and ultraviolet (UV) wavelengths, ground-based follow-ups were possible starting minutes after the burst trigger. These revealed the early X-ray behaviour, covering the transition from the prompt emission to the later long-lasting AG, as well as the diverse properties of the optical light curves. Based on the duration distribution, a third class of GRBs with intermediate duration has been proposed (e.g., Mukherjee et al., 1998; Horváth, 1998; Horváth et al., 2006), however, this claim is still inconclusive.

In principle, GRBs are a rather simple observational phenomenon: an explosion in a remote galaxy originally signalled by the γ-rays and followed by an AG emission at lower energies. Nevertheless, the nature of GRBs remained unknown for a long time due to their brief duration and difficult localisation. Nowadays the observational evidence for long GRBs points towards a catastrophic energy release of a dying star (see van Paradijs et al., 2000, for a review). This is supported by a rising number of observed supernovae events associated with GRBs (e.g., Galama et al., 1998b; Stanek et al., 2003; Hjorth et al., 2003; Campana et al., 2006; Malesani et al., 2004, see §1.3 for a detailed review on the connection). Short GRBs on the other hand are believed to originate from mergers of neutron-star (NS) binaries or neutron-star black-hole (BH) binaries (Paczyński, 1986; Goodman, 1986; Eichler et al., 1989; Mészáros and Rees, 1992, 1997). These binaries would lose angular momentum by emitting gravitational waves and would undergo a merger (Mészáros, 2006). In both the collapsar and merger scenarios, the result of the explosion is a BH. The gravitational energy released in the first few milliseconds is then further increased on timescales of seconds to hundreds of seconds by the accretion of the surrounding gas onto this BH (Mészáros, 2006). The γ-ray emission itself is generated within the outflow which reaches ultra-relativistic ($\Gamma > 100$) velocities and is collimated into a jet (see Zhang et al., 2009, for a review), which drills its way out of the star for the core-collapse case (see Fig. 1.3). The interactions between fireball shells with different speeds, the so-called "internal shocks", are

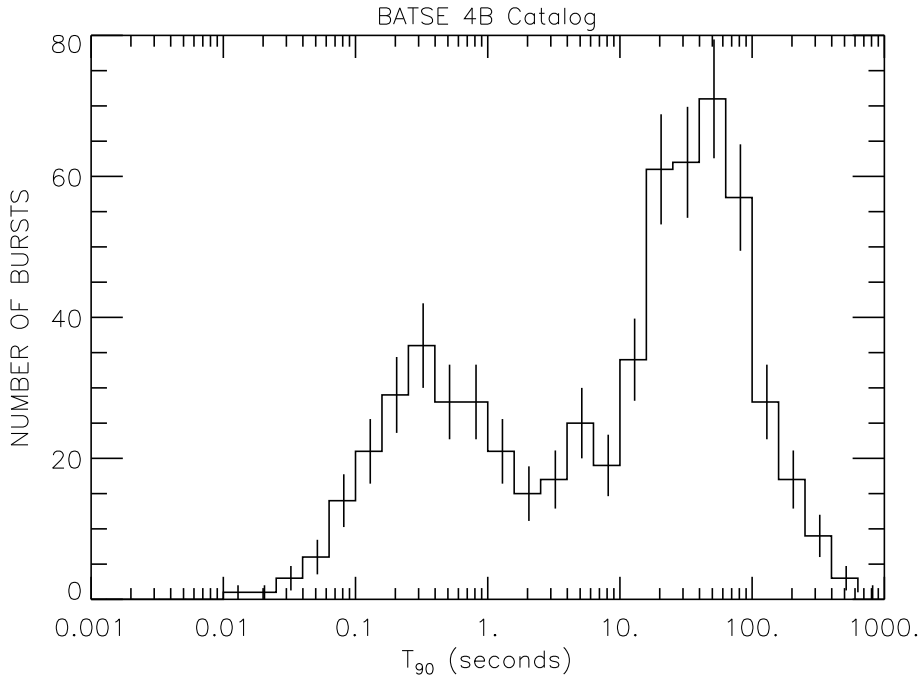

Figure 1.1. Bimodal distribution of BATSE bursts showing two types of GRBs based on their duration, short bursts with $T_{90} < 2$ s and long bursts with $T_{90} > 2$ s. Credit: Paciesas et al. (1999).

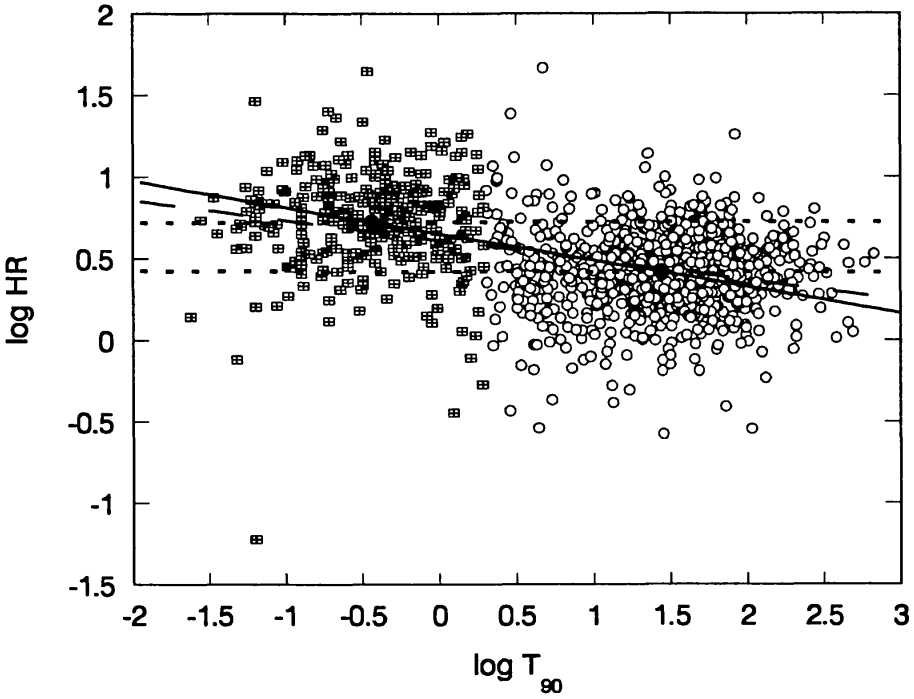

Figure 1.2. The hardness ratio (HR) against the duration T_{90} of BATSE GRBs. Separated at $T_{90} = 2$ s, the squares represent short bursts and the empty circles are long bursts. The filled circles and the dotted lines show the mean values for each class, which are connected by the dashed line. The solid line is a linear regression for the whole sample. Credit: Qin et al. (2000).

responsible for the prompt γ-ray emission, while the collisions of fireball shells with the external medium, the so-called "external shocks", produce the AG emission, which can be detected in all wavelength ranges from radio, optical to X-rays, up to days or months after the explosion. In the standard model, the multi-wavelength AG is explained by the synchrotron emission produced in the interaction between the circumburst medium and the relativistic jet that powers the γ-rays (for a review, see Zhang and Mészáros, 2004).

1.2 Supernovae

Supernovae (hereafter SNe) correspond to the explosive, high-energy final stages of some stars. The mechanical energy released in these powerful events can reach as much as 10^{51} erg (or 1 foe), and their peak luminosities can be comparable to the total light of their host-galaxies. SNe can be classified in two types, either "Core Collapse" or "Thermonuclear", depending on their explosion mechanisms.

Thermonuclear SNe, observationally referred as type-Ia SNe, are characterised by the lack of hydrogen and helium in their spectra. Their early-time spectra show strong lines due to intermediate mass elements (e.g., Si II, Ca II, Mg II; Filippenko, 1997, see also Fig. 1.4). They are found both in elliptical, spiral, or irregular galaxies. These objects are thought to originate in low-mass stars that end their lifes as white dwarfs and explode after a period of mass accretion from a companion star, leaving no compact remnants behind them (Hillebrandt and Niemeyer, 2000).

Core-collapse SNe (CCSNe) are closely associated to star forming regions in late-type galaxies

(Anderson and James, 2008). Therefore, they have been attributed to massive stars born with $\gtrsim 8\,\mathrm{M}_\odot$ that undergo the collapse of their iron cores after a few million years of evolution and the subsequent ejection of their envelopes (Burrows, 2000; Heger et al., 2003). These SNe leave a compact object as a remnant, either a NS or a BH (Baade and Zwicky, 1934; Arnett, 1996). The core-collapse model received considerable support with the first detection of neutrinos from the type-II SN 1987A (Svoboda et al., 1987), although no compact remnant has been found so far in the explosion site. Among CCSNe we can observationally distinguish those with prominent hydrogen lines in their spectra (dubbed type II), those with no H but strong He lines (type Ib), and those lacking H or He lines (type Ic) (Minkowski, 1941; Filippenko, 1997). The spectral differences among these SN types are shown in Fig. 1.4. There is also a class that is an intermediate case between type-II and Ib SNe. Type-IIb SNe show weak H lines in early spectra, however, they vanish with time and He signatures appear (Ensman and Woosley, 1987; Chevalier and Soderberg, 2010). Moreover, at later times they resemble spectroscopically

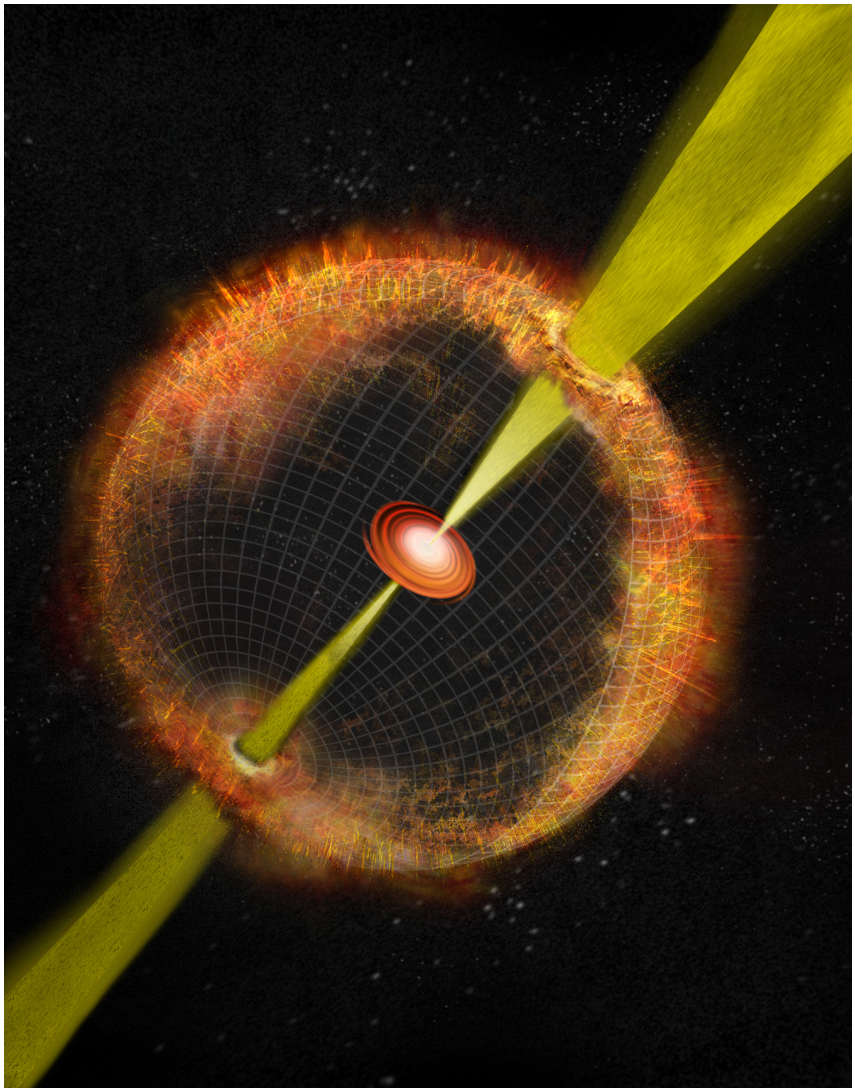

Figure 1.3. A schematic diagram of a long GRB with a single-star progenitor. Credit: Bill Saxton (NRAO/AUI/NSF).

and photometrically a type-Ib SN (e.g., SN 1993J; Nomoto et al., 1993; Filippenko et al., 1994; Utrobin, 1996).

Although all CCSNe are thought to share the same explosion mechanism, their different observational properties are explained in terms of how much of their H-rich and He-rich envelopes were retained prior to explosion. When the star explodes with a significant fraction of its initial H-rich envelope, in theory it should display a H-rich spectrum and a light curve characterised by a phase of ~ 100 days of nearly constant luminosity followed by a sudden drop of $2-3$ mag (Nadyozhin, 2003; Utrobin, 2007; Bersten et al., 2011). Nearly 50% of all CCSNe belong to this class of type-II *plateau* SNe, which are powered by the H recombination and the radioactive decay of the ^{56}Ni synthesised in the explosion. On the other hand, it is generally accepted that type-Ib and type-Ic SNe are formed from evolved high-mass progenitors like Wolf-Rayet (WR) stars, which have liberated their outer shells through a combination between pre-SN stellar winds and mass transfer to a binary companion due to Roche-lobe overflow. If the progenitor has lost its envelope through these mechanisms, the explosion of the star is referred as"stripped-envelope" supernova (SE SN Clocchiatti and Wheeler, 1997). Supernovae Ic, Ib, and IIb are members of

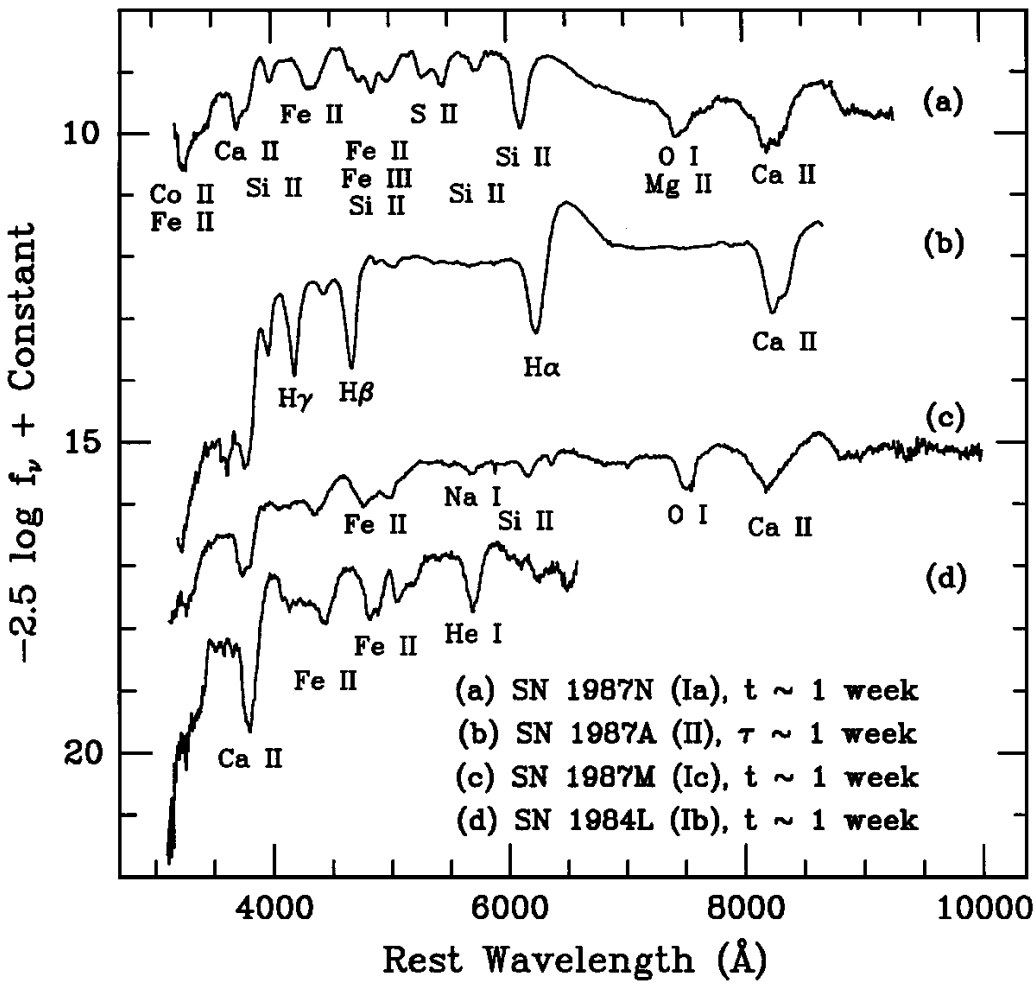

Figure 1.4. Early-time spectra of the four major SN types. The figure and the text that follows were taken from Filippenko (1997). The variables t and τ represent time after observed B-band maximum and time after core collapse, respectively.

this classification. These are exclusively powered by the radioactive decay of ^{56}Ni $\rightarrow^{56}$Co with the post-maximum addition of ^{56}Co $\rightarrow^{56}$Fe. Therefore, the nickel mass is the main tracer of the SE SN luminosity.

A subclass of type-Ic SNe are those called "broad-lined" (BL) SNe, which exhibit unusually broad-line profiles due to their extreme expansion velocities ($v \sim 15,000-30,000$ km s^{-1}). Also given their high luminosities they are dubbed "hypernovae" in the literature (HNe, e.g., Paczyński, 1998b; Hansen, 1999). This SN subtype has been found to be sometimes associated with GRBs (see next section for more details). Cases of BL SNe without a GRB connection are those of SNe 1999as (Umeda and Nomoto, 2008), 2003jd (Valenti et al., 2008), 2005bf (Folatelli et al., 2006), 2007ru (Sahu et al., 2009), 2009bb (Pignata et al., 2011), 2010ah (Corsi et al., 2011), and 2010ay (Sanders et al., 2012) to mention a few. Some of these events have shown indications of asymmetric ejecta in spectro-polarimetry and radio observations, which hints at fast pre-explosion rotation. A few years back, SN 2003bg was discovered as the first type-IIb HN (Hamuy et al., 2009), showing that BL features are not exclusive to the Ic class. Due to their large luminosities, BL HNe produce more than $\sim 0.2\,M_\odot$ of ^{56}Ni, are thought to have very massive progenitors, and are often connected to BH formation (see Fig. 1.5).

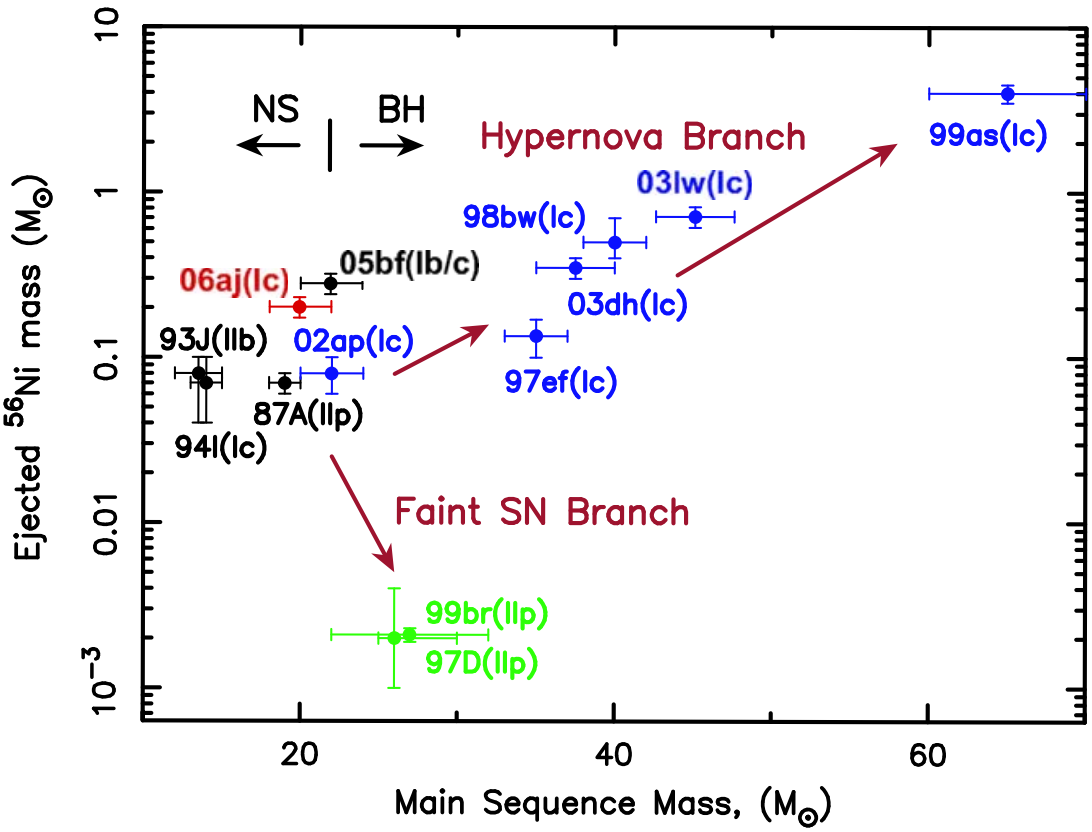

Figure 1.5. The ejected ^{56}Ni mass as a function of the main-sequence mass of the progenitors for several CCSNe. Type-Ic SNe are shown with red and blue symbols, other SE SNe in black, and SNe IIP with green symbols. The main-sequence mass is estimated from the progenitor model that best fits the observations. The theoretical limit between NS and BH formation is placed at a progenitor's (main sequence) mass of $\sim 22\,M_\odot$. Graphics was taken from Nomoto et al. (2010).

Unlike the progenitors of H-rich type-II events, progenitors of type-Ibc SNe are difficult to detect in the pre-SN high-resolution images of the host galaxies. There are only few cases, like SNe 2000ds, 2000ew, 2001B and 2004gt, where upper limits on the brightness of their progenitors were reported (Maund and Smartt, 2005; Maund et al., 2005). After analysing the evolutionary models of massive He stars and comparing the results with Galactic WR stars, it has been found that progenitors of type-Ibc SNe have surface properties resemble those of hot Galactic WR stars of the WO sub-type, which are visually faint (V-band absolute magnitude of $M_V \approx 2$ mag) despite of having a high bolometric luminosity ($L/L_\odot = 5.6-5.7$; Yoon et al., 2012). Detection of type-Ic progenitors is even more challenging than that of type-Ib's. Therefore, thorough monitoring and analysis of these class of SNe is extremely crucial, not only to investigate the post-explosion scenario, but also to understand the pre-explosion properties of the progenitors.

Given their large intrinsic luminosities, SNe have long been considered potential probes for extra-galactic distance determinations and the measurement of the cosmological parameters that drive the Universe dynamics. Among all types of SNe, the type-Ia family is the one displaying the highest degree of homogeneity (Li et al., 2001), both photometrically and spectroscopically. However, these objects are not perfect standard candles (Olivares E. and Hamuy, 2011). Empirical calibrations have allowed us to standardise their luminosities to levels of $\sim 0.15-0.22$ mag and determine distances to their host-galaxies with an unrivalled precision of $\sim 7\%-10\%$ (Phillips, 1993; Hamuy et al., 1996; Phillips et al., 1999). This powerful technique led a decade ago to the construction of Hubble diagrams between $z = 0-0.5$ and measure very precisely the history of the expansion of the Universe over 5 Gyr of look-back time. Contrary to our intuition these observations revealed that the Universe dynamics is described by an accelerated expansion (Riess et al., 1998; Perlmutter et al., 1999; Astier et al., 2006; Wood-Vasey et al., 2007). The discovery of the accelerating Universe is profoundly connected with theoretical cosmology as it implies the possible existence of a cosmological constant, a concept initially introduced by Albert Einstein at the beginning of the 20th century, whose origin still is a mystery. Although not as bright and uniform as the type Ia's, it was shown that the luminosities of SNe IIP can be standardised to levels of $\sim 30\%$ (e.g., Hamuy and Pinto, 2002; Olivares E. et al., 2010; Eastman et al., 1996; Dessart and Hillier, 2005; Jones et al., 2009), thus converting these objects into potentially useful tools to measure cosmological parameters. Although there have been attempts at standardising the luminosity of type-Ibc SNe (Ferrero et al., 2006; Drout et al., 2011), no conclusive results have been obtained.

1.3 The Association between GRBs and SNe

Massive stars are thought to give birth to both GRBs and SNe after the collapse of their cores into a BH (Woosley, 1993; Paczyński, 1998a; Fryer et al., 1999; MacFadyen and Woosley, 1999). This is known as the collapsar model (Bromberg et al., 2012) and is presented in Fig. 1.6. In theory, the collapsing core of a very massive star, whose envelope has been blown away by its own stellar winds, i.e., a WR star, can lead to the formation of a relativistic jet that will produce high-energy emission (Woosley, 1993; Woosley and MacFadyen, 1999) in the form of a GRB or an X-ray flash (XRF, softer events thought to be mainly produced by the same mechanism as GRBs; Heise et al., 2001; Kippen et al., 2004; Sakamoto et al., 2005; Heise and in 't Zand, 2001). When the jet collides with the circumstellar material, it produces a multi-wavelength AG (see Zhang and Mészáros, 2004, for a review). Theoretically, the energy of the core collapse should also be capable of expanding the remaining envelope. However, it is unclear how this can happen, or even if there is always enough energy for a SN explosion (the so-called "fall-back" events, e.g., Fryer et al., 2007, and references therein). Moreover, it is unknown exactly how, when, and to what extent the progenitors has to lose their envelope to produce or not a GRB. Whether the SN is triggered by the accretion disk that powers relativistic jet is still unclear. Based on energy conservation, it can be speculated that the energy budget of the core collapse should be partitioned between the GRB and the SN, however, no evidence has been found in this direction yet. To date, long GRBs have been associated only with type-Ic SNe (for a review, see Woosley and Bloom, 2006).

The first and most representative case of the GRB-SN connection was that of SN 1998bw, which was found to be associated with the soft GRB 980425 (e.g., Galama et al., 1998b; Kippen, 1998). A couple of days after the trigger, SN 1998bw was discovered (Galama et al., 1998a; Sadler et al., 1998) inside the $8'$ error circle of GRB 980425 (Soffitta et al., 1998) in the underluminous late-type galaxy ESO184–G82 ($z = 0.0085$; Tinney et al., 1998). Although initially controversial (Galama et al., 1998b; Pian et al., 1998), the physical association between these objects was supported on temporal and spatial grounds by the slowly variable X-ray source at the position of the SN (Pian et al., 2000; Kouveliotou et al., 2004). As a result of this connection, both the GRB and SN research fields, which until then had both evolved more or less independently, were revolutionised by a single event.

Five years after the SN 1998bw, the association between GRB 030329 and SN 2003dh came to light through a clear spectroscopic identification (Hjorth et al., 2003; Kawabata et al., 2003; Stanek et al., 2003; Matheson et al., 2003) and became the first truly solid piece of evidence in favour of the GRB-SN connection. Moreover, after 1998 there have been many other spectroscopic associations, such as the cases of GRBs 021211 (SN 2002lt; Della Valle et al., 2003), 020903 (Soderberg et al., 2005; Bersier et al., 2006), 031203 (SN 2003lw; Malesani et al., 2004), 050525A (SN 2005nc; Della Valle et al., 2006b), 060218 (SN 2006aj; Pian et al., 2006), 081007 (SN 2008hw; Della Valle et al., 2008), 091127 (SN 2009nz; Berger et al., 2011; Cobb et al., 2010c; Filgas et al., 2011), and 101219B (SN 2010ma; Sparre et al., 2011) based on HN features in their spectra.

Furthermore, late-time bumps in the light curves of GRB AGs have been interpreted as SN signals, e.g., GRBs 970228 (Reichart, 1999; Galama et al., 2000; Reichart et al., 2000), 980326 (Castro-Tirado and Gorosabel, 1999; Bloom et al., 1999), 011121 (Bloom et al., 2002b; Greiner et al., 2003), 020405 (Price et al., 2003; Masetti et al., 2003), 040924 (Soderberg et al., 2006; Wiersema et al., 2008), 041006 (Stanek et al., 2005; Soderberg et al., 2006), 050824 (Sollerman et al., 2007), 060729, and 090618 (both in Cano et al., 2011a) to mention a few. These bumps

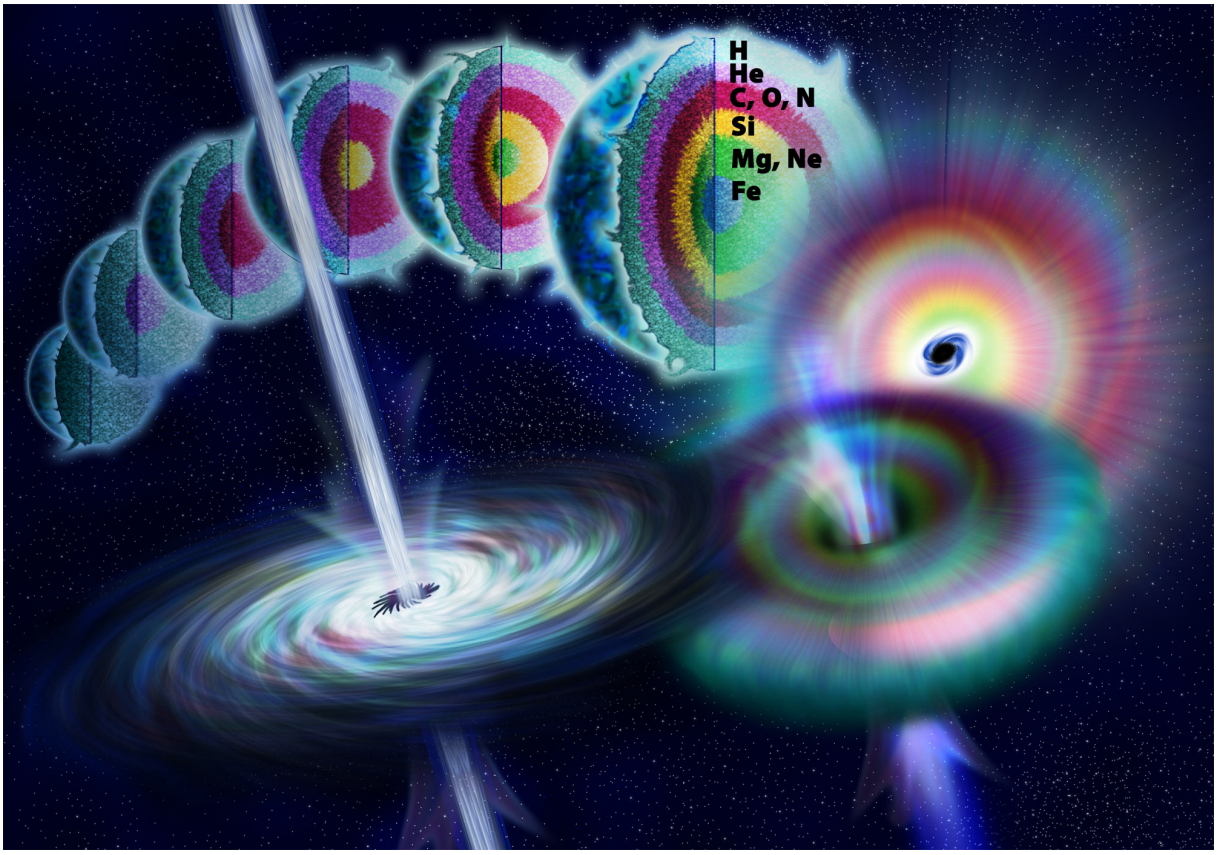

Figure 1.6. The collapsar model: a massive star burns its core until it is made of iron. Nuclear reactions cease causing the star to collapse, a BH to form with a surrounding disc, and magnetically collimated jets to blast out along the polar axis and produce γ-rays. Credit: Nicolle Rager Fuller (NSF).

show consistency in terms of colour, timing, and brightness with those expected for the GRB-SN population, but they are usually faint, which hampers the spectroscopic identification. These re-brightenings have been detected in GRB light curves out to redshifts of ~ 1 (Masetti et al., 2005; Della Valle et al., 2003; Bloom et al., 2009; Tanvir et al., 2010) owing to the sensitivity of current ground-based telescopes dedicated to follow-up observations. Sample studies of GRB-SNe (including bumps not spectroscopically identified) have been carried out to determine the luminosity distribution, the morphology of the light curves, and the physical parameters of the explosion such as kinetic energy, ejected mass, and ^{56}Ni mass (Zeh et al., 2004; Ferrero et al., 2006; Richardson, 2009; Thöne et al., 2011). They concluded that GRB-SNe are in general brighter than the local sample of SE SNe, except for cases such as the super-luminous type-Ic SN 2010ay (Sanders et al., 2012). Regarding the morphology of the GRB-SN light curves, no correlation has been found between the brightness at maximum with the shape of the light curve (Ferrero et al., 2006) contrary to the claims of Stanek et al. (2005). While more than 20 photometric bumps in AG light curves have been claimed to be SN rebrightenings (e.g., Richardson, 2009, see §6 for the complete sample), so far only six have been spectroscopically confirmed as solid connections (see Table 1.1). The SN counterpart can be as bright as $M_V = -19.8$ mag (SN 2003lw associated with GRB 031203 at $z = 0.105$; Malesani et al., 2004).

Additional information about the explosion can be obtained from its early emission. One particular case is that of the soft XRF 060218 associated with SN 2006aj (Campana et al.,

2006; Pian et al., 2006; Ferrero et al., 2006; Cobb et al., 2006; Modjaz et al., 2006; Sollerman et al., 2006; Mirabal et al., 2006). This displayed an early X-ray and UV emission, which was interpreted as thermal radiation produced by the shock breakout from the surface of the progenitor (Colgate, 1974; Falk, 1978; Klein and Chevalier, 1978; Matzner and McKee, 1999; Waxman et al., 2007; Nakar and Sari, 2010). The envelope is heated up and owing to expansion it starts to adiabatically cool, which then shifts the emission to UV and optical wavelengths. From the analysis of this a signal, it is possible to constrain the AG component, derive both the temperature and luminosity of the thermal component, and compute the apparent radius of emission (e.g., Thöne et al., 2011). Other examples include SNe without detectable γ-ray emission that nevertheless exhibit adiabatic cooling in the UV/optical and/or X-ray observations: SN 2008D (Soderberg et al., 2008b; Malesani et al., 2009; Modjaz et al., 2009; Mazzali et al., 2008), SN 2008ax (Roming et al., 2009), SNLS-04D2dc (Schawinski et al., 2008), and SN 2010aq (Gezari et al., 2010), to mention a few. As additional information, it has been claimed that high-energy emission in GRB-SNe comes from accelerated shock-breakout photons rather than highly relativistic jets (Wang et al., 2007).

Whilst no SN signature is expected for short GRBs, which are thought to be produced by the mergers of compact objects (see the cases of short GRBs 050509B in Hjorth et al. 2005a and Bloom et al. 2006, and 050709 in Fox et al. 2005 and Hjorth et al. 2005b for deep non-detections), there are a few supposedly long events where an expected SN appearance was never detected. In the cases of GRBs 060505 (Fynbo et al., 2006; Ofek et al., 2007) and 060614 (Fynbo et al., 2006; Gal-Yam et al., 2006; Della Valle et al., 2006a), there are very tight constraints on the SN signature, which go down to 1% as bright as SN 1998bw. Although GRBs 060614 (Zhang et al., 2007) and 071227 (Sato et al., 2007; D'Avanzo et al., 2009) were thought to be disguised short bursts, i.e. expected not to produce the SN counterpart, evidence has been found showing that these GRBs have properties consistent with those of normal long GRBs (Amati et al., 2007; McBreen et al., 2008). Nevertheless, GRB 060614 is dominated by a soft extended emission component and this type of emission is in agreement with the $E_{\rm peak}$-$E_{\gamma,\rm iso}$ correlation also for GRBs like 050724 (Amati, 2008; Zhang et al., 2007), which has been proposed to belong to the short class due to its location in an elliptical galaxy with no star formation down to deep limits (Berger et al., 2005; Malesani et al., 2007; Gorosabel et al., 2006; Fong et al., 2011). Furthermore, the short spike in GRB 060614 is not consistent with long-GRB properties (Amati, 2008). Neither GRB 060505 agrees with the $E_{\rm peak}$-$E_{\gamma,\rm iso}$ relation for long

Table 1.1. Spectroscopically-confirmed SNe associated to GRBs.

GRB	SN	z	$\upsilon_{\rm ph}$ [a] [km s^{-1}]	References
980425	1998bw	0.0085	14,000	Galama et al. 1998b; Patat et al. 2001
030329	2003dh	0.1685	17,000	Stanek et al. 2003; Deng et al. 2005
031203	2003lw	0.1055	24,000	Malesani et al. 2004; Mazzali et al. 2006b
060218	2006aj	0.0334	18,000	Pian et al. 2006; Mazzali et al. 2006a
100316D	2010bh	0.0591	28,000	Chornock et al. 2010a; Bufano et al. 2012
120422A	2012bz	0.2831	19,000	S. Schulze et al.,in preparation

Note.— The table lists the events with spectroscopic observations only where the P-Cygni profiles allow for the determination of expansion velocities.

[a] Estimation of the photospheric expansion velocity at maximum luminosity.

GRBs (Krimm et al., 2009), however, there is evidence that it likely belongs to the long-duration class of GRBs (McBreen et al., 2008). The validity of the non-detections of SNe counterparts as a classification tool is a point of controversy (e.g., Zhang et al., 2009). No definite answer has been found yet (see Kann et al. 2011 for an exhaustive discussion on GRBs 060505 and 060614 in the light of the optical luminosity of their AGs).

Chapter 2

Data and Instrumentation

2.1 The *Swift* Satellite[1]

The *Swift* satellite (Gehrels et al., 2004) was launched in 2004 with the main mission to quickly locate and observe GRBs and their AGs at different wavelengths. It is part of the NASA's medium explorer (MIDEX) program and the project was developed by an international team, which members are from the United States, the United Kingdom, and Italy. X-ray instrument calibrations have been done in the PANTER facility in Germany. France, Japan, Denmark, Spain, and South Africa are scientifically involved as well. The main scientific goals of the *Swift* GRB mission are to determine the origin of GRBs, classify them, study the environment around them and their interaction, use GRBs as the probes of the early universe, and carry out an all-sky hard X-ray survey. *Swift* discovers about 90 GRBs per year using its γ-ray instrumentation, the Burst Alert Telescope (BAT, sensitive at $15-150$ keV; Barthelmy et al., 2005), and monitoring the sky with its 1.4 steradian field of view. Thanks to its very rapid slewing capability (50 degrees in less than 75 seconds), the satellite detects the AG using the X-Ray Telescope (XRT; Burrows et al., 2005) and the Ultra-Violet Optical Telescope (UVOT; Roming et al., 2005) after slewing to the BAT position ($\sim$ 3 arcmin accuracy). With the consecutive use of this three telescopes, *Swift* localises the GRB and the AG precisely (few arcsec positions for almost every event). When the GRB or AG are detected, the information about the burst brightness and position are immediately transferred to ground and communicated to the community using the Gamma-Ray Burst Coordinates Network (GCN; Barthelmy et al., 2000).

The focusing X-ray CCD imaging spectrometer at the XRT is designed to obtain fluxes and spectra over time of GRB AGs at energies of $0.2-10$ keV. It has a 110 cm^2 effective area and 23.6×23.6 arcmin field of view. The XRT is capable to start observing just $20-70$ s after the BAT discovery of a GRB and localise it within 5 arcsec, which is precise enough for the fields of view at ground-based telescopes. The XRT supports several science modes to enable an efficient coverage of the strong temporal variability expected for GRB AGs. Based on the source brightness, it autonomously determines which readout mode to use. When observing a new GRB, the XRT first executes an integration in Image mode to calculate the on-board source position. Afterwards it runs the following modes in sequence: Photodiode, Windowed Timing, and Photon Counting, switching automatically between modes according to the source intensity. The Photodiode mode is designed for very bright GRBs, it does not provide spatial information, but produces a high resolution light curve and a spectrum. The Windowed Timing

[1]This section uses information from the *Swift* user manuals and from `http://heasarc.nasa.gov/docs/swift/` and `http://www.nasa.gov/mission_pages/swift/main/index.html`.

mode is obtained by compressing 10 rows into a single row and then reading out only the central 200 columns of the CCD. It thus provides a one-dimensional image and a time resolution of 1.7 ms. Most of the AG observation time is spent in the Photon Counting mode, which retains full imaging and spectroscopic resolution, but the time resolution is limited to 2.5 s.

The UVOT is a UV/optical diffraction-limited 30-cm Ritchey-Chrétien reflector sensitive in the wavelength range 170 – 650 nm. It has a field of view of 17×17 arcmin and locates the AG down to 0.5 arcsec accuracy. When a new GRB triggers the BAT and the *Swift* has slewed to the position, the UVOT acquires a 150 s white exposure of the target field and then continues through a predetermined program of exposure times and filter combinations. Thanks to its seven filters, low-resolution spectral energy distributions can be obtained for the brightest UV/optical AGs, which can then be used to determine the redshift via the Lyman-α cut-off (e.g., Krühler et al., 2011). The UVOT is well suited for any astrophysical study, because of its UV capability, which is impossible from the ground, and the absence of atmospheric extinction, diffraction, and background. On the other hand, the main constraints for the observation with the UVOT and other instruments on board *Swift* are the Moon (e.g., D'Elia et al., 2011) and Earth limb (e.g., Perri et al., 2007), plus its $\sim$ 96 min orbital period around the Earth.

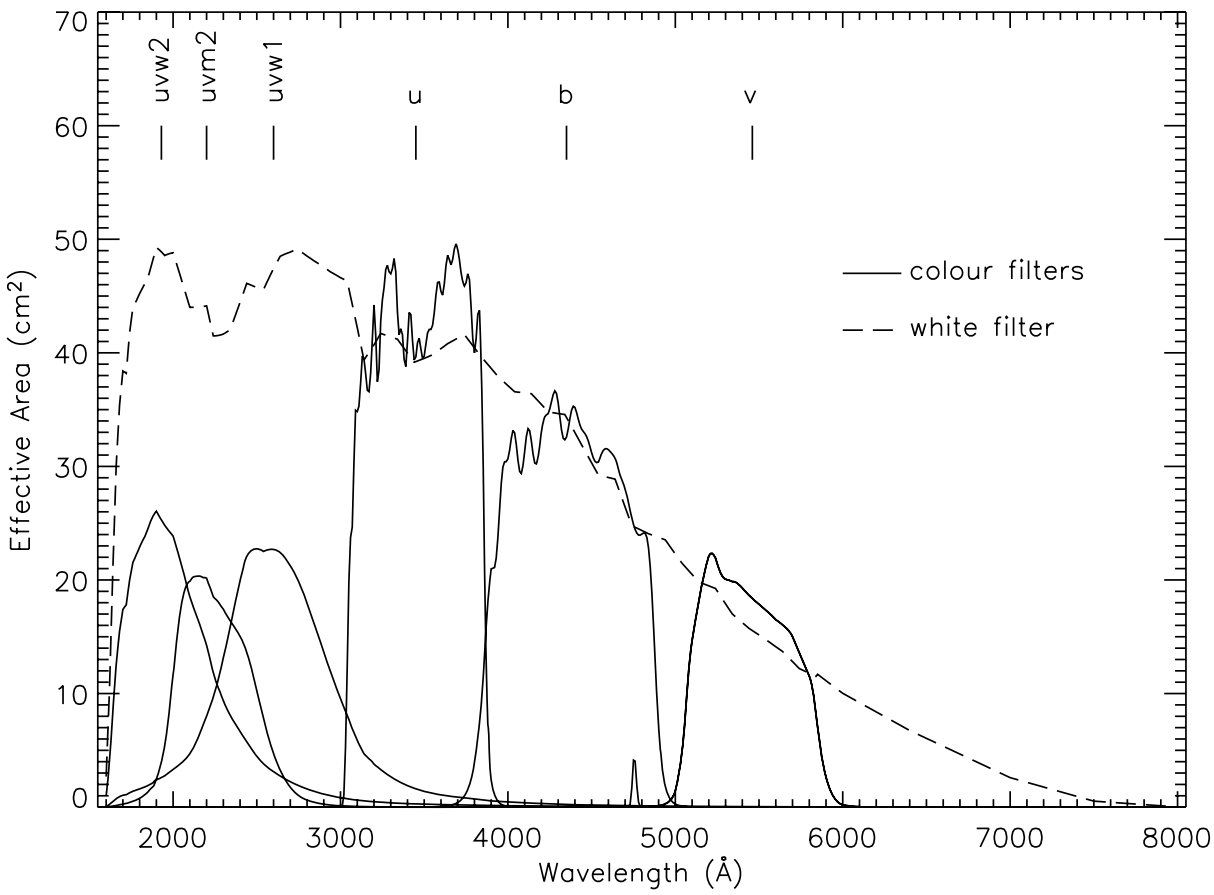

Figure 2.1. Effective-area curves for the seven UVOT filters. Graphics taken from Poole et al. (2008).

2.1.1 The XRT Data

All XRT light curves and spectra in this thesis were obtained from the *Swift*/XRT GRB light curve repository (Evans et al., 2007, 2009) at `http://www.swift.ac.uk/xrt_curves/`. Light-curve data obtained in the Windowed Timing (WT) mode and the Photon Counting (PC) mode were downloaded as ASCII tables containing each row the exposure mid-time, the time span, the source count rate and its corresponding error. These tables were then used in light-curve fitting procedure described in the next sections. Regarding the spectra, the repository automatically creates a time-average spectrum of any observed GRB, although it also allows the user to create custom time-sliced spectra for any given time interval. Such a spectrum is retrieved by defining a time interval during which the XRT has observed and the repository provides a download link to the spectral data. The download includes files with the unbinned source spectrum and a background spectrum for the requested time interval and observing mode, and an ancillary response file. The response matrices were obtained from the most recent CALDB (*Swift* calibration database) release. The spectral data are then grouped using the `grppha` task and modelled as explained in detail in §2.3.4.

2.1.2 The UVOT Data

All UVOT data were retrieved and reduced by Patricia Schady, post-doc of the GROND team at the MPE. She followed the procedure described in Poole et al. (2008). To minimise the contamination from the underlying host galaxies, the source flux was measured within a circular source-extraction region. Then, an aperture correction was applied in order to remain compatible with the UVOT effective area calibrations, which are based on $5''$ aperture photometry (Poole et al., 2008). The background was taken from a source-free region close to our source.

2.2 The *G*amma-*R*ay burst *O*ptical and *N*ear-infrared *D*etector

The seven-channel imager GROND (Gamma-Ray burst Optical and Near-infrared Detector; Greiner et al., 2007, 2008) at La Silla Observatory, Chile, served as the main astronomical instrument in this work. It is mounted on the ESO/MPI 2.2-m telescope with the primary mission of executing target-of-opportunity (ToO) observations of every gamma-ray burst (GRB) visible in the Chilean nighttime. Built at the *Max-Planck-Institut für Extraterrestrische Physik* (MPE Garching) in April 2007, its observing capabilities encompasses four optical and three near-infrared (NIR) detectors, being sensitive in a wavelength range from approximately 380 to 2400 nm. Each optical CCD of 2046×2046 pixels (pixel size 13.5 μm) receives the light beam from a filter of the Sloan system, $g'r'i'z'$ respectively (Fukugita et al., 1996). The NIR Rockwell HAWAII-1 detectors of 1024×1024 pixels each (pixel size 18.5 μm) are coupled to $JHK_{\rm s}$ filters of the extended Johnson system (Johnson and Morgan, 1953). The optical and NIR fields of view are 5.4×5.4 arcmin and 10×10 arcmin, respectively.

Thanks to a set of dichroics (or *splitters* as called in Figs. 2.2 and 2.3; see Fig. 2.4 for the transmission curves in the light path), GROND is able to observe in all seven bands simultaneously, which turns this instrument in a very powerful astronomical tool not only for GRB science, but also for observations of other fast optical transients such as cataclysmic variables, X-ray binaries, active-galaxy nuclei, novae, tidal disruptions, stellar eruptions, etc.

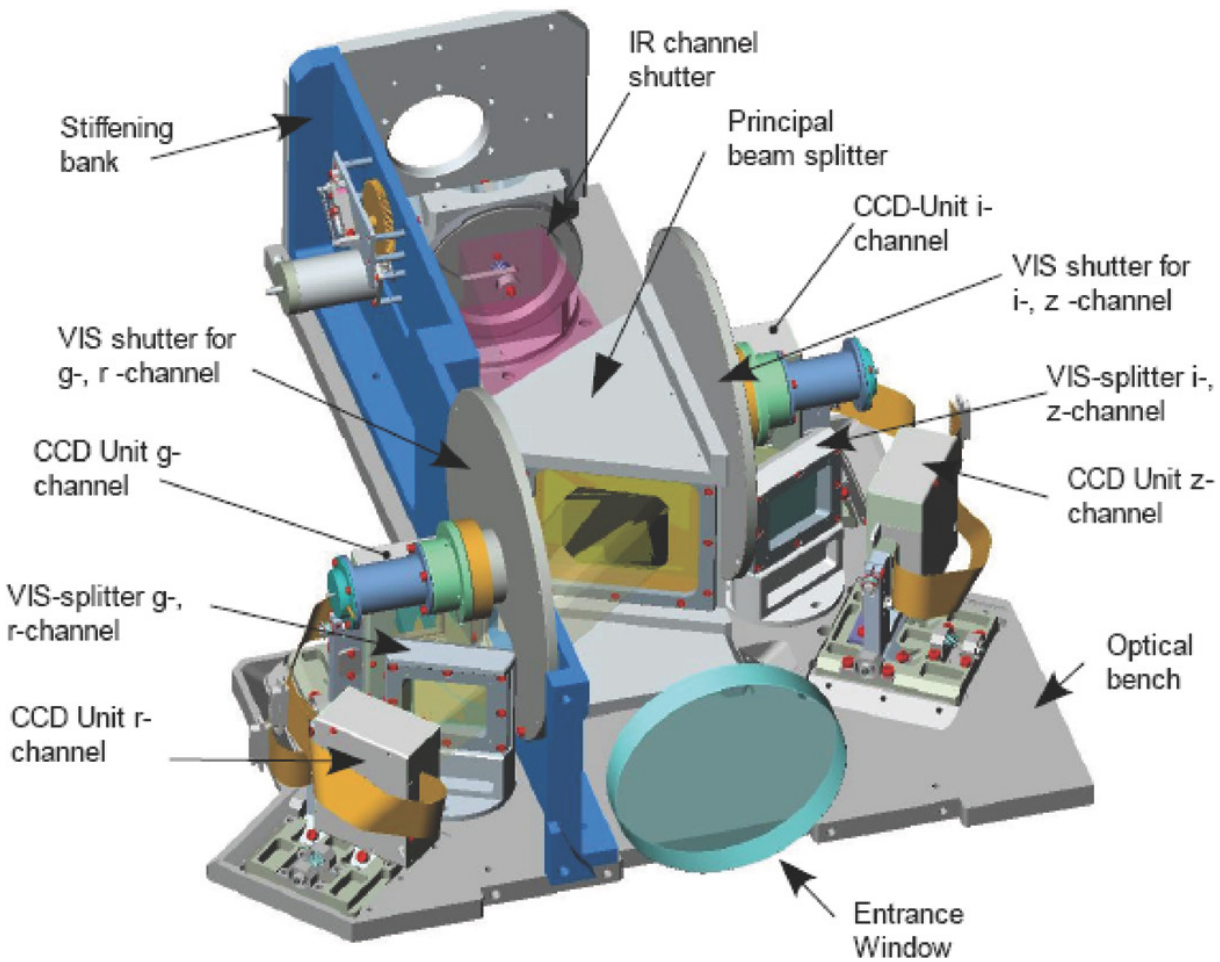

Figure 2.2. Visual base plate with nearly all optical and mechanical components marked. The splitters (or *dichroics* as in the main text) are defined by a certain wavelength value; radiation with longer wavelength goes through and the remainder with shorter wavelength is reflected. This figure was taken from Greiner et al. (2008).

Simultaneous multi-band observation is required for a very quick photometric redshift determination based on the Lyman-alpha break (Lamb and Reichart, 2000), in which GROND excels with high accuracy (Krühler et al., 2011). Given that GRB AGs fade rapidly, high redshift value determined by GROND is then used as a trigger for more detailed follow-up observation with larger telescopes, while the AG is still bright enough for a high resolution spectroscopy for example, required to measure the physical conditions of the burst environment (Molinari et al., 2007). While the UVOT (the Ultraviolet and Optical Telescope; Roming et al., 2005) on board the *Swift* satellite measures redshift using the same principle, its range is limited to $z \approx 1.3 - 5$. Compared to that, GROND has a range of $z \approx 3.5 - 13$ and can therefore detect AGs of the most distant GRBs, including the current record holder GRB 090429B with the redshift of ≈ 9.4 (Cucchiara et al., 2011). While the GROND instrument was designed to be fully autonomous, the needed promptness in the GRB localisation, redshift determination and solving of potential HW and SW problems, together with the slow Internet connection to La Silla, requires that at least one member of the GROND observers team, composed mainly of PhD students and Post-docs, is present at La Silla observatory.

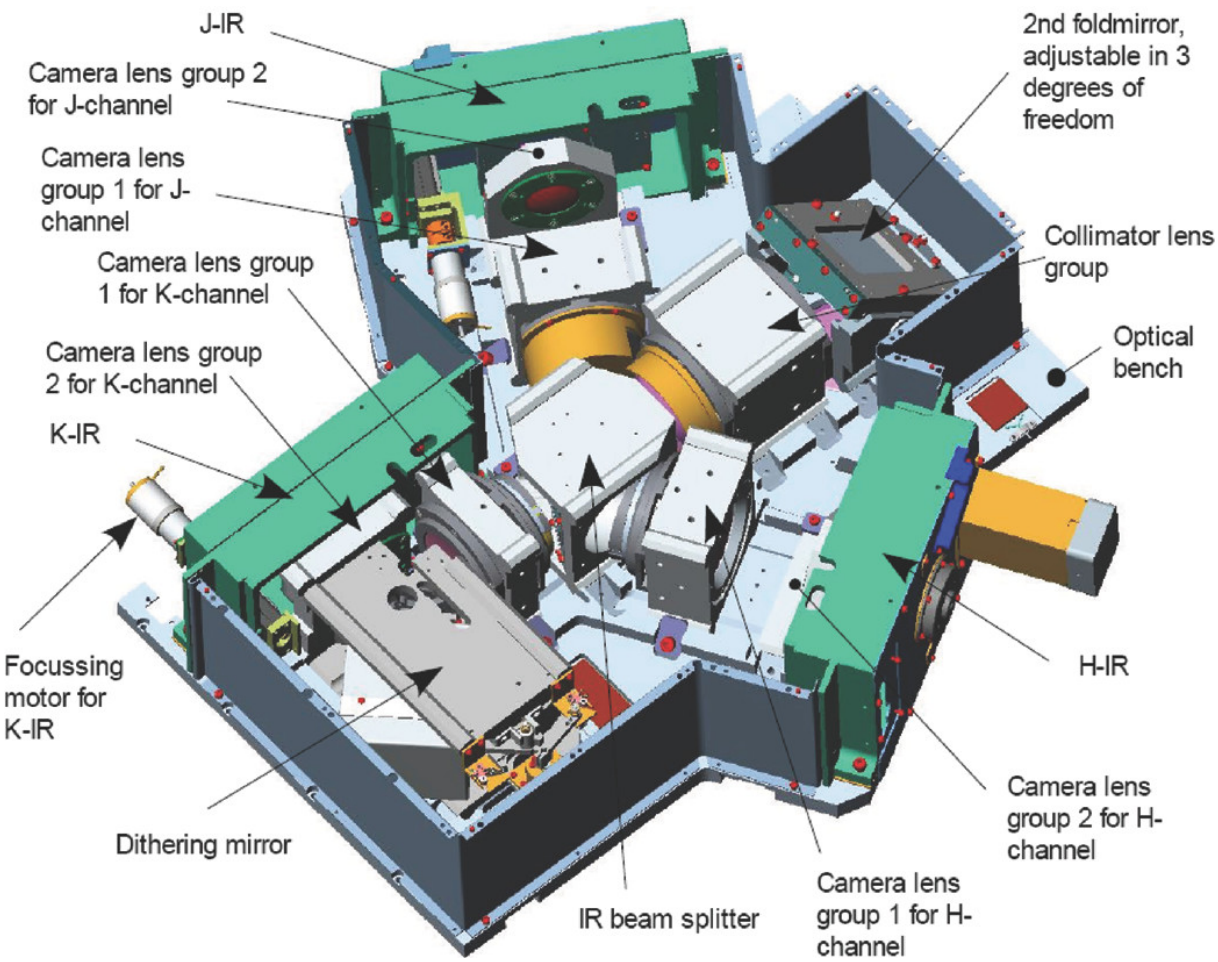

Figure 2.3. Infrared base plate with all optical and mechanical components. Apart from the splitters (see Fig. 2.2), the NIR arm is equipped with a focal reducer system, which consists of five collimator lenses and one camera lens for each NIR channel. This figure was taken from Greiner et al. (2008).

The GROND instrument can observe any object in the sky and is often used for a study of quasars (Morganson et al., 2012), supernovae (Olivares E. et al., 2012), blazars (Rau et al., 2012), transiting exoplanets (Nikolov et al., 2012), and others. However, it was mainly designed for a prompt automatic GRB follow-up observation. To be able to do this, GROND is running in the Rapid Response Mode (RRM), which ensures that it automatically stops all other ongoing observations and moves the telescope to the latest trigger position. The override rule of the RRM applies not only for the ongoing observations with GROND but also for the other two instruments mounted on the 2.2 m telescope; the Wide Field Imager (WFI; Wisotzki et al., 2001) and the fiber-fed Echelle spectrograph FEROS (Kaufer et al., 1999). In order to produce the smallest possible impact on these two instruments, a movable M3 mirror was designed for the 2.2 m telescope. In the case of a GRB trigger, the M3 mirror is folded in 20 seconds and reflects the light from the source towards the side of the telescope (Coudé-like focus), where GROND is permanently mounted. In case GROND is not used, the M3 mirror moves away and the light goes directly in the Cassegrain focus of the telescope to the WFI or FEROS.

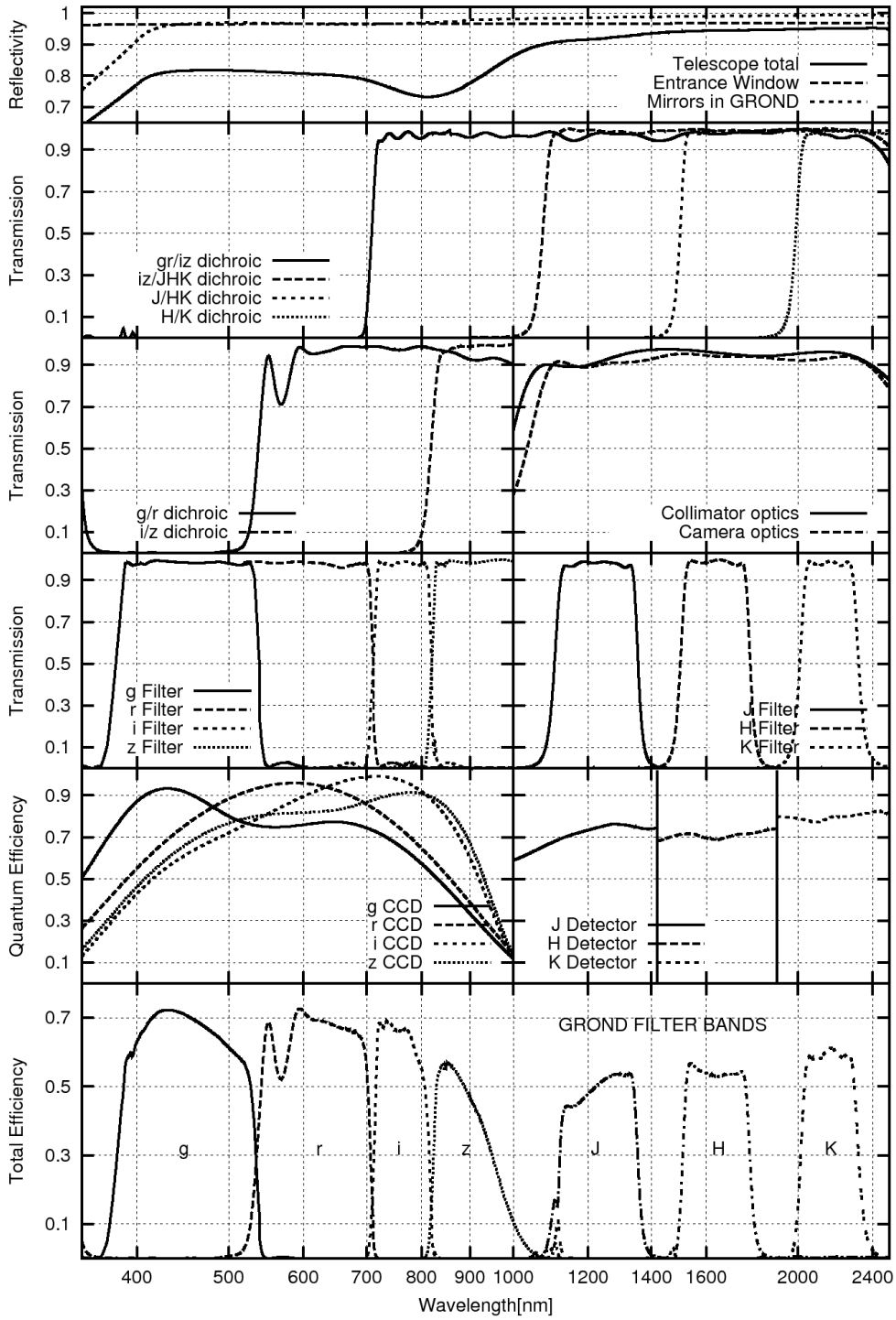

Figure 2.4. Efficiencies of the 2.2-m telescope and GROND along the light path. From the top, panels are: (1) reflectivity of the telescope and GROND-internal mirrors, (2) and (3) transmission of the dichroics and the NIR lens systems, (4) transmission of the filters, (5) detector quantum efficiency, and (6) the total efficiency in each of the seven GROND bands. This figure was taken from Greiner et al. (2008).

2.2.1 Observing

The GROND observations themselves are performed using the observation blocks (OBs; Chavan et al., 2000), which are combinations of different number and time of exposures in the seven detectors. Each OB contains set of parameters, the most important ones are the number of telescope dither positions (TDPs, used to determine the sky variations in the NIR channels), the number of exposures per TDP in the optical bands and their duration, the number of K_s-band mirror dither positions (MDPs, used due to a higher sky brightness), and the number of exposures per MDP in the NIR bands and their duration. Different default OB types are defined for GROND observations to comply with the science objectives and to sort and organise exposure, readout, and transfer times in all channels efficiently. These OBs are named after the total integration time of a single NIR channel and the total number of the TDPs of the OB. The OBs most commonly used for GRB AG observations are the 4min4TD, the 8min4TD, and the 20min4TD. In the case of highly crowded fields in the Galactic plane, OBs with higher number of TDPs are used for better background subtraction, e.g., the 12min6TD, the 30min6TD, the 10min8TD, etc. The number of K_s-band MDPs is always six per TDP.

Given the relatively long exposures (the 4min4TD OB is the shortest), GROND OBs are designed for observations of faint objects like GRB AGs, which moreover fade rapidly. The layout of the 4min4TD OB consists of six K_s-band MDPs and a 10-s exposure per MDP in the NIR channels. The exposure time in the optical channels is ≈ 35 s in the slow readout mode or 66 s in the fast readout mode, for which the noise is higher, but reduces the readout time from 46 s to 4.4 s. The readout in the NIR channels takes only 2 s and allows GROND to integrate in the NIR channels even while optical channels are reading out. This configuration is repeated four times at four different TDPs. The output data of the 4min4TD OB are four images for each optical band ($g'r'i'z'$) in the form of `FITS` data cubes and 24 images for each NIR band (JHK_s) in the form of `FITS` files. The longer OBs simply increase the exposure time in the optical channels and number of exposures per K_s-band MDP, while the exposure time in the NIR channels stays in 10 s to avoid saturation due to the bright NIR sky background. The difference in exposure mid-times between the optical and the NIR channels is discussed in the next section.

Non-RRM OBs can either be created and executed via the ESO `p2pp` software, used for all ESO instruments, or via the GROND Pipeline (GP; Küpcü-Yoldaş et al., 2008), a custom-designed software for GROND. The GP is used for automatic scheduling of OBs in the RRM mode and is operated through a web interface (`http://wgrpipe.ls.eso.org:9222/gp/app/`) with administrator access for any member of the GROND team from any place in the world. The prime objective of the GP is to schedule immediate observations of GRB AGs and determine their brightnesses and redshifts as quickly as possible. When a GRB alert comes in via the GCN socket connection, the GP extracts all information from the packet, decides whether it is a valid trigger for a new GRB, and calculates the visibility of the target. If the target is observable and complies with other checks (e.g., Moon distance), the GP schedules a sequence of OBs with an increasing exposure time. In case of incoming new or additional information on the target, this sequence can be modified or deleted anytime by the user via the web interface. If the RRM is on line at the start time of the scheduled observation, the GP sends and executes an RRM OB, which ends any ongoing observation (even if performed by other instruments), presets the telescope to the new position, rotates the M3 mirror if needed, and sets up GROND for observations. The predefined sequence of OBs is executed after the telescope has slewed. To not lose precious time, the guiding has to be quickly started before the exposures begin. When the sequence ends, the M3 is rotated back and the observation of the previous program can be

resumed. Apart from choosing a guiding star, all the steps above are done autonomously without the need of any intervention by the GROND observer, who mainly takes care of adjusting the OB sequence according to new target information, real-time brightness measurements, and weather conditions. For purposes of instrument calibration, bias and dark frames are taken daily and sky-flats at least weekly (see §2.2.2 for details on the corrections).

The second independent block of the GP software system conducts the processing of the observed data immediately after the OB finishes. The processing includes an time-optimised reduction of the images, the astrometric correction, and the photometric calibration. Details on the data handling are described in the next section. Unless a precise AG position had been reported in the GCN publicly, the main goal of the GROND observer is to identify the AG in the GROND images. This is done by looking for uncatalogued sources inside the area given by the error circle of the γ-ray or X-ray position distributed by the GCN packets. The GRB candidate is then confirmed by its brightness variability and colours that resemble optical/NIR AGs (Rhoads, 2001). If no suitable candidate is found in any GROND band, the observer increases the OB exposure time or stacks several OBs together (see §2.2.2). After finding the AG and obtaining all seven magnitudes, the photometric redshift is determined using a customised version of the publicly available `hyperZ` code (Bolzonella et al., 2000). The script fits the seven magnitudes with a power law possibly attenuated by dust extinction in the host galaxy and by the Lyman-α break if covered by the data. This method determines redshifts in the range of $z \approx 3.5-13$ with an accuracy of $\sigma_z \approx 0.3-0.5$ using data from 380 to 2400 nm.

In case of a high redshift is measured, usually $z > 6$, and if an ESO proposal was accepted for the current period, a spectrograph at a larger-aperture telescope can be immediately triggered and the spectroscopic confirmation of the redshift follows. In any case, the observer and another GROND-team member, who is currently on "home shift", write a GCN circular reporting either the AG position and magnitudes if detected (e.g., Olivares E. et al., 2009a) or upper limits if not (e.g., my first GCN circular, Olivares E. et al., 2009c).

To obtain an AG light curve with a dense temporal sampling during the whole visibility period of the GRB, follow-up observations are scheduled in the course of following days, weeks and even months. If the source field does not coincide with the fields covered by the Sloan Digital Sky Survey (SDSS) catalogue, an observation of the closest photometric Sloan standard star (Smith et al., 2002) or the closest SDSS field is scheduled for execution during photometric conditions. To perform relative photometry, a short observation of the GRB field follows the calibration observation (see §2.2.3 for more details).

At the end of the observing shift, the GROND-team member copies the data to a USB disk and brings them along to Garching for further and detailed analysis.

2.2.2 Reduction of the Images

Once the GROND data are transferred to Garching, they are reduced and analysed, similarly to the procedure described in detail by Krühler et al. (2008). All the reduction and analysis processes utilise `pyraf/IRAF` [2] tasks (Tody, 1993) and are conducted using the GROND analysis pipeline (see PhD thesis of Thomas Krühler, TUM, for details), similar to the one used by the GP on La Silla. The main difference is that the GP is configured in fast mode, skipping some

[2]IRAF, the Image Reduction and Analysis Facility, is distributed by the National Optical Astronomy Observatory (NOAO), which is operated by the Association of Universities for Research in Astronomy (AURA), Inc., under cooperative agreement with the National Science Foundation (NSF); see `http://iraf.noao.edu`. Pyraf is a Python wrapper for IRAF, provided by the Space Telescope Science Institute (STSI); see `http://www.stsci.edu/resources/softwarehardware/pyraf`.

steps in the image pre-processing. The GROND analysis pipeline is slower, but configured for maximum precision of the final photometry.

The first step in the reduction procedure is the processing of the raw images. All images are corrected for the effects introduced by the detector and electronics. The bias level (or over-scan) and bias noise are subtracted from all images. Next, the sky-flats are employed to correct for the pixel-to-pixel sensitivity and the illumination variations across the image. The NIR images are sky-subtracted and corrected for the geometrical distortion introduced by the focal-reducer lenses in the light path before of the infrared detectors. The TDP images are then shifted and added to create a single image per OB for each band. However, if the source is bright enough, the astrometry and photometry can be performed (see §2.2.3) not only on the final OB image, but also on each TDP image. Thus, for example, four TDP magnitudes and a single OB magnitude are possible to be obtained for each object in each band in case of a 4min4TD OB. For exceptionally bright GRBs ($J < 16$ mag), even the 10-s NIR exposures can be reduced and analysed individually. In case of a very faint source, the images can be stacked together to produce an image with longer exposure time, which is equal to the sum of exposure times of the stacked images. Whatever the combination of TDPs and OBs, astrometry and photometry is conducted on the resulting images as described in the next section.

2.2.3 Astrometric and Photometric Calibrations

Astrometry is performed by matching the objects detected in the images to those in the optical or infrared catalogues, namely USNO A-2, USNO B1, SDSS, DENIS, 2MASS, NOMAD and GSC22, which are downloaded from `http://vizier.u-strasbg.fr/viz-bin/VizieR`. The pixel coordinates of the images is then transformed to sky coordinates. The resulting astrometric uncertainty is as good as ~ 0.3 arcsec.

Photometry is performed by constructing a general model for the point-spread function (PSF) of each image using bright field stars, from which the full width at half maximum (FWHM) was also derived for each image. The PSF photometry is then obtained by fitting the PSF model to the source count profile. In addition, aperture photometry is also carried out using an aperture size equal to the FWHM. Both techniques show comparable results for point sources.

Photometric calibration is performed relative to several secondary standards in the GRB field. In case of NIR bands, the secondary standards have $JHK_{\rm s}$ measurements in the Two Micron All Sky Survey (2MASS; Skrutskie et al., 2006), against which the apparent magnitudes are compared and calibrated. The same method is applied for the optical bands when the field is covered by the SDSS catalogue. Otherwise, the magnitudes of the nearest Sloan standard star or the stars of the nearest SDSS field are transformed to the GROND filter system using their spectra and the GROND filter curves (Greiner et al., 2008). The obtained zero points are then corrected for atmospheric extinction differences and used to calibrate the secondary standards in the GRB field, which has to be observed shortly before or after the standard field. Then, the apparent magnitudes of the source of interest are calibrated using the magnitudes of the secondary stars. The NIR data are converted from the Vega to the AB photometric system to be consistent with optical data. The transformation factors for the GROND filter system are $\Delta J = 0.91$ mag, $\Delta H = 1.38$ mag, $\Delta K_{\rm s} = 1.80$ mag. The systematic uncertainties of the respective catalogues are 0.03 mag for the $g'r'i'z'$ bands and 0.07 for the $JHK_{\rm s}$ bands.

2.2.4 Image Subtraction

When the position of the object of interest is highly contaminated by host-galaxy light, I had to perform image subtraction. A deep late-time host-galaxy observation is carried out after the transient has faded and it is used as a reference image —or template image— for the subtraction procedure. The input images —or science images— are those from which the light curve will be obtained, i.e., those that show detections of the transient.

To align the input and reference images, we use the `WCSREMAP` package[3]. To leave science images untouched, I created for each input image the corresponding template image, *remap*ped to match the science image pixel by pixel using sky coordinates. Then both images were *trim*med using IRAF routines to a common area leaving no blank regions.

For the main purpose of subtracting template from science images, the `HOTPANTS` package[4] was employed. The routine consists of three steps:

1. The routine fits the PSF. It uses Gaussian functions to model the PSF of point sources in sub-regions of the input image. Since reduced GROND images are essentially the combination of at least four $g'r'i'z'$ and 24 $JHK_{\rm s}$ dithered individual exposures, three and five Gaussian functions of different widths and degrees of freedom are employed for $g'r'i'z'$ and $JHK_{\rm s}$, respectively. Then, the PSF model or kernel is used to *convolve* the template image to match the sharpness of the input image.

2. Next step is flux scaling, which matches the count flux of both images. Point sources define the transformation that is used to *scale* the template image to the flux of the science image.

3. Finally, the template is *subtract*ed from the science image. This leaves only the transient flux in the difference image. That is, only our object of interest remains in the final image.

To summarise the procedure, the following equation describes it briefly:

$$\textsc{diff} = trim(\textsc{input};A) - scale(trim(remap(\textsc{templ};\textsc{input});A) \times K) \tag{2.1}$$

where images are highlighted with small caps, subroutines in italic style, and after the semicolon the parameters are the common area for trimming A and the input image for remapping. Convolution is represented by the multiplication of the kernel K. An example of the image sequence of the subtraction procedure can be found in Fig. 3.1 of §3.2 for the case of SN 2010bh.

The `HOTPANTS` routine outputs a noise map of the resulting difference image, which is employed to derive the uncertainties in the measured fluxes. The package `DAOPHOT/IRAF` was used to compute the aperture magnitudes and their corresponding errors.

It is intuitive that, since convolution degrades the reference image, it has to be acquired under better seeing conditions than the science images. When this is not the case and the template has similar PSF to that of the science image, the kernel computation fails. Given the similarity in sharpness of both images, flux scaling and direct subtraction are performed manually. For a few exceptional cases, the seeing conditions of the science image is unbeatable and flux subtraction of the host galaxy is performed numerically. This has larger uncertainties but it is the only possibility when the PSF of the input image is exceptionally narrow.

[3] `http://www.astro.washington.edu/users/becker/wcsremap.html`
[4] `http://www.astro.washington.edu/users/becker/hotpants.html`

2.3 Final Data Analysis

In what follows, I describe in detail the last sequence of steps to finalise the data analysis and deliver scientific end results.

2.3.1 Galactic Foreground Extinction

Before starting the analysis, all data are corrected for the Galactic foreground reddening $E(B-V)_{\rm Gal}$ in the direction of the burst. This selective absorption is produced by the interstellar medium in the Milky Way (MW). Its value is obtained from the NASA/IPAC web interface at `http://irsa.ipac.caltech.edu/applications/DUST/`. The reddening is derived using the data and technique that Schlegel et al. (1998) pioneered using all-sky infrared dust maps. The uncertainty is estimated to be the standard deviation of $E(B-V)_{\rm Gal}$ in a given field, which can be chosen down to 2 degrees in size. This uncertainty varies considerably from field to field. For instance, this source of error takes values of about 5% for the sample of GRB-SNe discussed here, which is added quadratically to the total error of our photometry. I notice also that the error in $E(B-V)_{\rm Gal}$ is considerably lower than the uncertainty of the host-galaxy reddening $E(B-V)_{\rm host}$ of 10% approximately (see §2.3.5). To correct our photometry, the reddening is finally transformed to the extinction $A_{V,\rm Gal}$ by assuming a ratio of total to selective absorption of $R_{V,\rm Gal} = A_{V,\rm Gal}/E(B-V)_{\rm Gal} = 3.1$ (Schlegel et al., 1998) from the MW reddening law (red solid line in Fig. 2.8).

2.3.2 Light Curve Fitting

For fitting the light curves of GRB AGs observed with GROND and *Swift*/XRT, a Python script was designed and coded (PhD thesis of Thomas Krühler, TUM), which allows the user to fit the observed data with various models using χ^2 statistics. The models are combinations of straight power laws, power laws with one or two smooth breaks, host contributions, etc. While working with the code, I included the option to fit templates of SN 1998bw in addition to the AG power-law contribution (see next 2.3.3).

The light curves are parametrised as a sum of the different components j and fitted using all available multicolour data simultaneously. The global χ^2 of $F_{\nu,i}(t)$, where F_ν is the flux density and i denotes the individual filters, was minimised by assuming an achromatic functional form of $F_{\nu,i,j}(t) = F_{\nu,i}\sum_j F_{\nu,j}(t)$, where only the overall flux normalisation $F_{\nu,i}$ depends on the filter. The simplest model fits a straight power law to the data with the temporal slope α. The broken power-law model connects two power laws smoothly using the formula from Beuermann et al. (1999)

$$F_{\nu,i}(t) = N_{\nu,i}\left[((t/t_{\rm break})^{-\eta\alpha_1} + (t/t_{\rm break})^{-\eta\alpha_2})\right]^{-1/\eta}, \tag{2.2}$$

where $F_{\nu,i}(t)$ is the flux density as a function of time, $N_{\nu,i}$ is the normalisation for each band, $t_{\rm break}$ is the time of the break or slope change in seconds, and η is the smoothness of the transition between both power-law slopes α_1 and α_2. The smaller the value of η, the smoother the break connecting the two power laws and conversely.

The resulting fit to the light curve is then a superposition of all the components used. The fitting can be done to seven GROND bands and XRT simultaneously (e.g., Fig. 5.1) or on any smaller combination of the eight bands down to a single band. When fitting several bands simultaneously, to output is the best fit to all filters at once, the only parameter differing between bands is the normalisation. The script also computes χ^2 statistics of the fit and 1σ errors of all free parameters.

2.3.3 SN 1998bw Template Fitting

To study the luminosity evolution ^{56}Ni-powered SNe, SN 1998bw templates were derived from the publicly available $UVBRI$ photometry of Galama et al. (1998b) to each of our GROND filters. The process of compiling these templates from the observed light curve of SN 1998bw is based on Zeh et al. (2004) and consist of: (a) correcting for the Galactic extinction through the line of sight of SN 1998bw and for its redshift, (b) constructing a smooth SED from the $UVBRI$ data, (c) correcting the SED to the redshift of the source of interest and applying the Galactic extinction along the line of sight through its host galaxy, (d) obtaining the flux for the GROND filters from the corrected SED, and (e) interpolating to a equally spaced time grid. The host-galaxy extinction for SN 1998bw was assumed to be zero (Clocchiatti et al., 2011, and references therein). Given this modus operandi, the NIR templates are inaccurate because they rely on an extrapolation of the $UVBRI$ data. Therefore, the three epochs of $JHK_{\rm s}$ data in Patat et al. (2001) were used to define the zero points of the flux scale. For all filters, it is assumed that the host-galaxy extinction of SN 1998bw is equal to zero (Patat et al., 2001; Clocchiatti et al., 2011).

To parametrise the SN 1998bw templates, an analytic function was then employed. Thus, the SN density flux was expressed as

$$F_i^{\rm SN}(t) = k_i \left[a_1\, \xi(t)^{p_1}\, e^{-(\xi(t)-d)^2/w} + a_2\, \xi(t)^{p_2}\, e^{-c\,\xi(t)} \right] \tag{2.3}$$

where a_1, a_2, p_1, p_2, d, w, and c are the seven parameters fitted to the template data. The luminosity ratio, i.e., the luminosity fraction with respect to SN 1998bw, is k_i, where i represents for different filters. The function $\xi(t) = (t - t_{\rm delay})/s$ depends on $t_{\rm delay}$, which is a simple time offset, and s, which is the stretch factor with respect to SN 1998bw. To obtain the seven parameters from the template data, $k_i = 1$, $s = 1$, and $t_{\rm delay} = 0$ are fixed to model SN 1998bw at a certain redshift (Zeh et al., 2004). An example of the fitting is shown in Fig. 2.5 for the specific case of SN 2008hw. After determining the seven parameters, the luminosity ratio k_i, the stretch factor s, and when needed $t_{\rm delay}$ will model the observed data of the object of interest. The stretch factor s is usually fixed to have a single value for all filters, however, it can be left free for single bands when data quality allows (e.g., §3.4). The delay parameter $t_{\rm delay}$ is fixed to zero unless it is necessary. Note that $t_{\rm delay} \neq 0$ does not necessarily imply that the onset of the SN is out of phase with respect to the core collapse. This is because the functional form of the templates and its parameters are totally and exclusively empirical and do not aim at a physical understanding of the explosion.

2.3.4 Broad-Band Spectral Energy Distribution

The spectral energy distributions (SED) are of special interest to study global spectral properties of astronomical sources. Using a narrow filter set, SEDs can allow to determine cosmological redshifts and host-galaxy extinctions when compared to a library of template spectra. For the specific case of GRB AGs, the spectral slope can be accurately determined. In this thesis I use SEDs from the GROND filter set alone and also complemented with X-ray data, after which inclusion the broad wavelength coverage allows for better determination of extinction and absorption.

Construction of the SED

From the seven flux measurements of GROND at different wavelength, we have immediately a spectral energy distribution with seven bins. The advantage in using a Sloan filter set is that

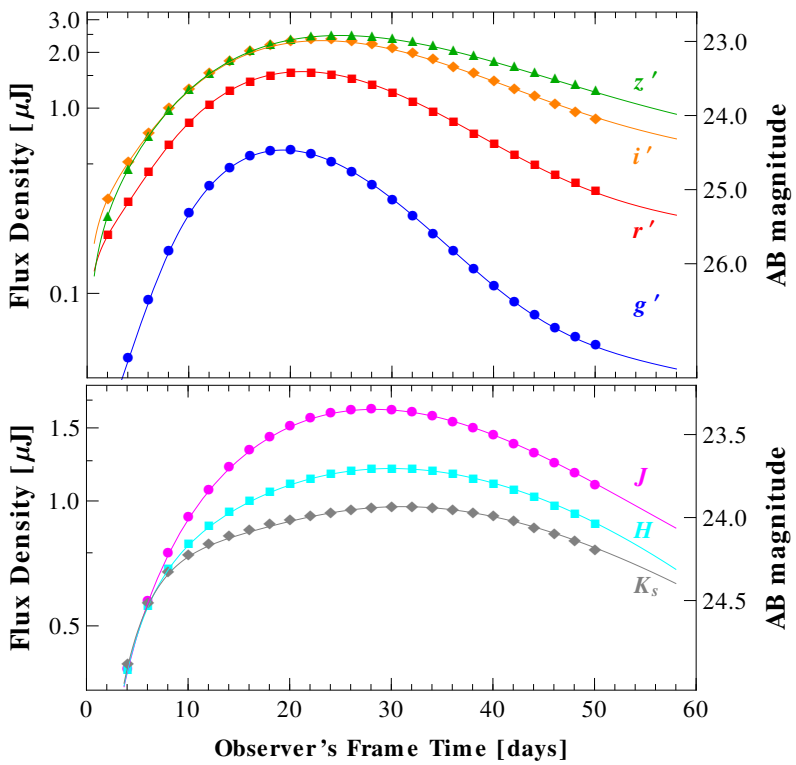

Figure 2.5. Templates of SN 1998bw used for SN 2008hw at $z = 0.53$. The $g'r'i'z'$ bands are shown in the top panel using blue circles, red squares, orange diamonds, and green triangles, respectively. The JHK_s bands are shown in the bottom panel using magenta circles, cyan squares, and grey diamonds, respectively.

count fluxes can be converted easily in physical fluxes after calibration with SDSS reference stars. The following expressions allow us to convert the AB magnitude to a flux with physical units along with the corresponding uncertainty:

$$m = 23.9 - 2.5 \log F_{\mu\mathrm{Jy}} \quad \text{and} \quad \sigma_{F_{\mu\mathrm{Jy}}} = \frac{2.5\,\sigma_m}{\ln 10}, \tag{2.4}$$

where m is the photometric magnitude in the AB system, $F_{\mu\mathrm{Jy}}$ is the flux in unit of micro Jansky (μJy), and σ_m and $\sigma_{F_{\mu\mathrm{Jy}}}$ are the respective statistical uncertainties. In addition to the statistical magnitude error, the corresponding calibration uncertainty coming from the reference catalogues (USNO, 2MASS, SDSS, APASS; see §2.2.3) and the Galactic-extinction error (Schlegel et al., 1998) are both added in quadrature. Having the SED fluxes and the corresponding errors, the central wavelengths of the filters are retrieved from the GROND specification manual. The wavelength size of the bins are defined by the full width at half maximum for each filter, i.e., by the wavelengths at which the filters transmit 50% of the maximum flux (see Fig. 2.4 for reference). Now we have all the ingredients of the GROND SED, which covers the broad band from 380 to 2400 nm.

Data from GROND and *Swift*/XRT can be used together to create a *broader*-band SED, which allows us to study a large portion of the radiation spectrum. First, a time interval of the light curve is selected, in which the broad-band SEDs will be constructed. After obtaining XRT spectral data from the repository and GROND data from the analysis, both described above, the XRT data are renormalised so that the mean photon arrival time for the XRT spectrum is equal to the mid-time of the GROND observation (TDP, OB, or stacked image). While mid-times

of optical and NIR bands of GROND observations differ due to dissimilar readout times of the detectors, the differences are in order of seconds and are therefore neglected. A modified version of `hyperZ` is used to fit GROND SEDs alone, while `XSPEC`[5], a NASA's HEASARC software, is used to fit combined XRT/GROND SEDs as explained below.

The `XSPEC` Modelling

After renormalising each XRT spectrum to the mid-time of the GROND SED with which it should be combined, the GROND magnitudes are converted into the `XSPEC` format and fitted together with the XRT data. Only two types of models are used in this thesis: the single power law and a broken power law. The modelling with `XSPEC` includes several parameters, which can be either fixed to a known value or left free to vary. Known parameters are usually the redshift of the GRB, the Galactic foreground extinction (see §2.3.1), and the Galactic foreground X-ray absorption by metals estimated based on an equivalent hydrogen column density $N_{\rm H,Gal}$ obtained from Kalberla et al. (2005). The parameters obtained from the single power-law model are the photon index Γ, which is defined as $\Gamma = \beta + 1$ where β is the spectral index or the power-law slope, and the intrinsic equivalent hydrogen column density $N_{\rm H,host}$, which estimates the local X-ray absorption by metals in the GRB host galaxy. In case of the broken power-law model, the value of the break energy $E_{\rm break}$ is obtained in addition to the low- and high-energy spectral indexes. Only a sharply broken power-law model is available by default. Similar to light-curve fitting script, `XSPEC` calculates χ^2 and 1σ errors for all free parameters.

Figure 2.6 shows an example of a broad-band SED using the UVOT, GROND, VLT, and the XRT for GRB 080928 (Rossi et al., 2011), which analysis was lead by the GROND team from Tautenburg, Germany. The absorption by the ISM was small in this case ($A_{V,\rm host} = 0.12$,$N_{\rm H,host} = 3.5 \times 10^{21}$ cm^{-2}), although the Lyman-α break affects the two higher-energy UV band clearly.

The SNID code

This method of spectral fitting uses the available Supernova Identification tool (SNID; `http://marwww.in2p3.fr/~blondin/software/snid/index.html`) by (Blondin and Tonry, 2007). The library used for cross-correlation has more than 1500 spectra of all types of SN at different epochs, AGNs, Galaxies, LBVs, and M-stars. This code is intended to identify spectra only, nevertheless, I found it also useful when entering the photometry as a broad-band SED, which was interpreted by the code as a poor-resolution spectrum. It assesses the goodness of the fit by computing the correlation height-noise ratio r, which quantifies the significance of a peak in the normalised correlation function (see Blondin and Tonry, 2007, for details). In general, correlations with $r > 5$ are worth considering. For SN templates, the output parameters are SN type, redshift, and age with respect to V-band maximum. There are no attempts at computing an intrinsic extinction when using this tool. As reference for age determination, a spectral sequence of SN 1994I are shown in Fig. 2.7.

[5] `http://heasarc.nasa.gov/xanadu/xspec/`

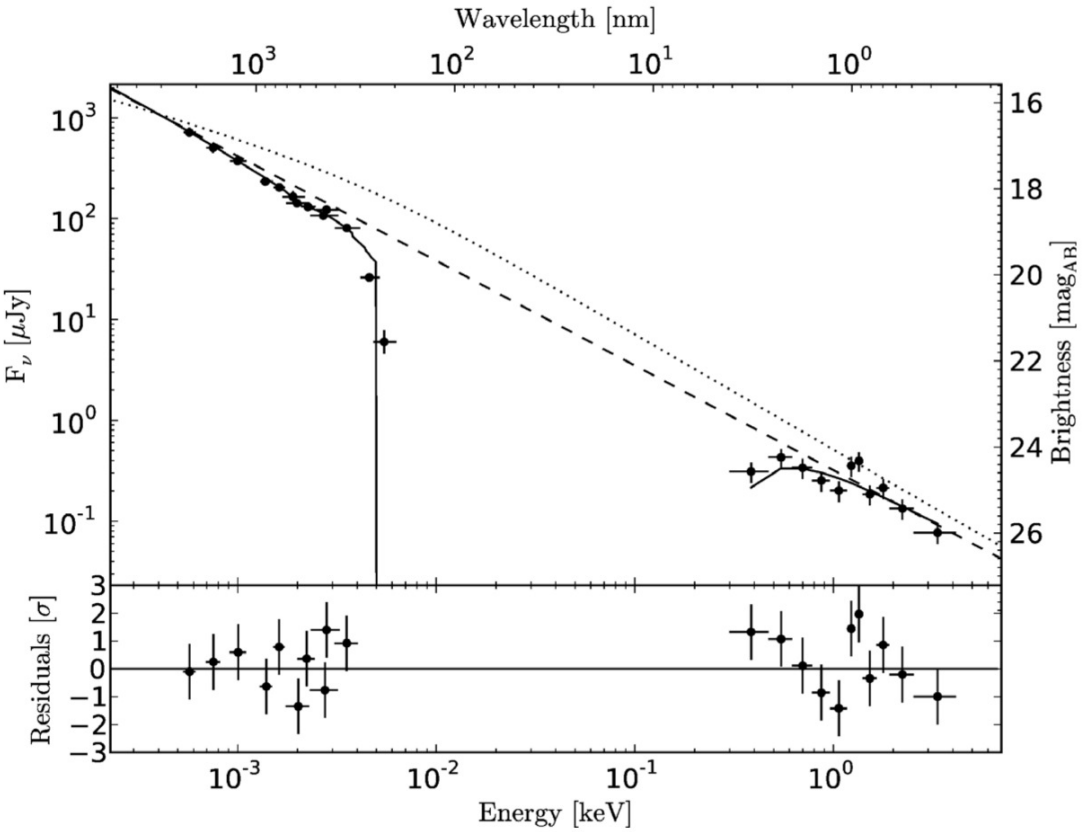

Figure 2.6. SED of GRB 080928 using UVOT, GROND, VLT, and XRT data taken from Rossi et al. (2011). The dashed line shows a single power law; the solid line shows the absorbed power law; the dotted line is a numerical energy-injection model.

2.3.5 Additional Extinction in the Host

Additionally to the Galactic foreground extinction discussed in §2.3.1, a correction for the extinction in the host galaxy has to be determined. From the analysis in §2.3.4 I obtain the V-filter extinction $A_{V,\mathrm{host}}$ and the corresponding reddening law (MW, Large Magellanic Cloud, or Small Magellanic Cloud) that fit best the broad-band SED. Then, to correct our data, I made use of the parametrisation by Pei (1992) to compute the extinction for our GROND filters using their central wavelength blue-shifted to the emission redshift. The parametrisation as follows

$$\frac{A_\lambda}{A_V} = \frac{A_B}{A_V} \sum_{i=1}^{6} \frac{a_i}{(\lambda/\lambda_i)^{n_i} + (\lambda_i/\lambda)^{n_i} + b_i} \tag{2.5}$$

where a_i, λ_i, b_i, and n_i are free parameters (see table 4 of Pei 1992 for numerical values). The six terms represent the background, the far-ultraviolet, the far-infrared, and the 2175 Å, the 9.7 μm, and the 18 μm features. The ratio A_B/A_V is introduced to use A_V instead of A_B as the normalisation. Using the polynomials in eq. 2.5, the different extinction laws are plotted in Fig. 2.8 as a function of wavelength. As an extra comparison, I also included the extinction law for SN-induced dust (Stratta et al., 2007; Maiolino et al., 2004; Todini and Ferrara, 2001).

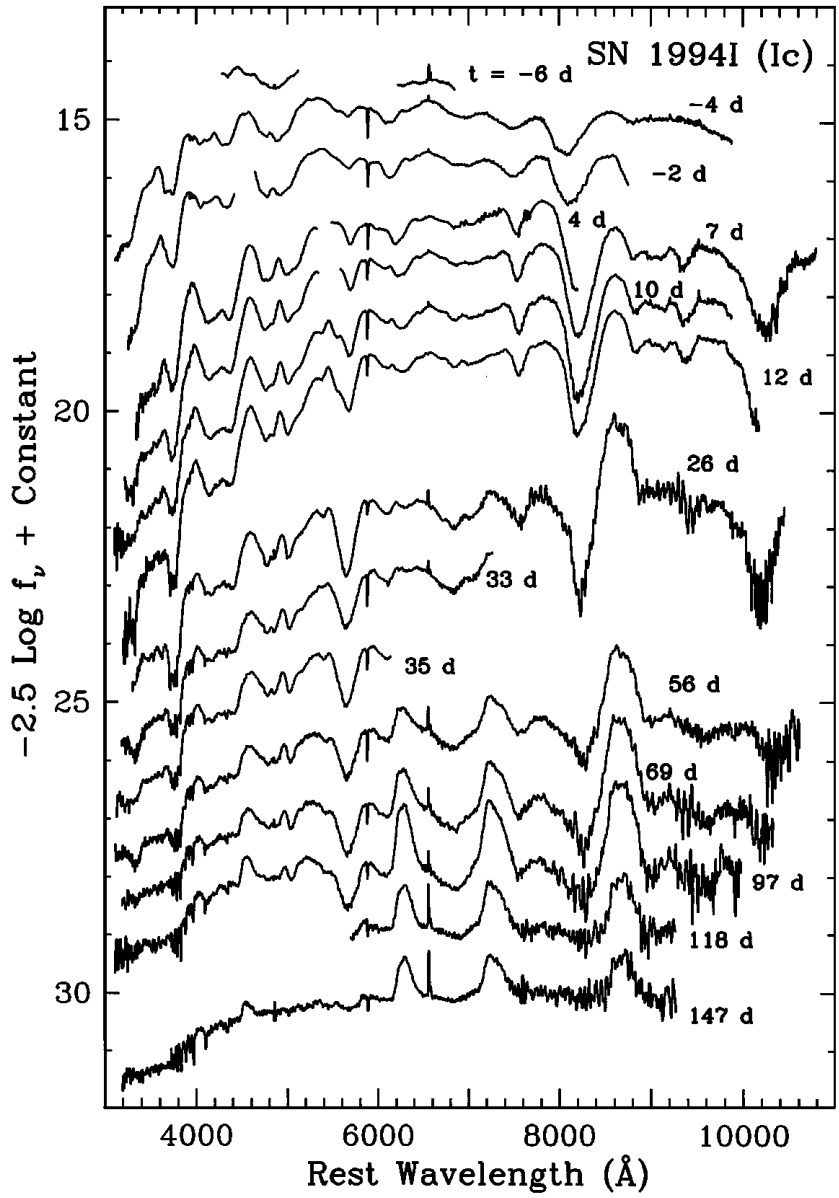

Figure 2.7. Spectral sequence of SN 1994I, one of the best-observed type-Ic SNe. The figure and the text that follows were taken from Filippenko (1997). Epochs in days are given relative to maximum B brightness. The late-time spectra are significantly contaminated by gas and early-type stars in the host galaxy; note the blue continuum, as well as the Balmer absorption and emission lines. Blueshifted He I λ10,830 is prominent at early times, and the transition to the nebular phase is rapid.

As an quantitative example of how the extinction affects SEDs, Figure 2.9 shows a typical AG SED ($\beta = 1.2$) redden by an SMC extinction with different A_V values. While UV wavelengths are already affected strongly at the smallest extinction value ($A_V = 0.3$ mag), the K_s band at ~ 200 nm barely shows any flux decrease with $A_V = 3$ mag. This proves the necessity of having NIR channels to accurately determine extinction values.

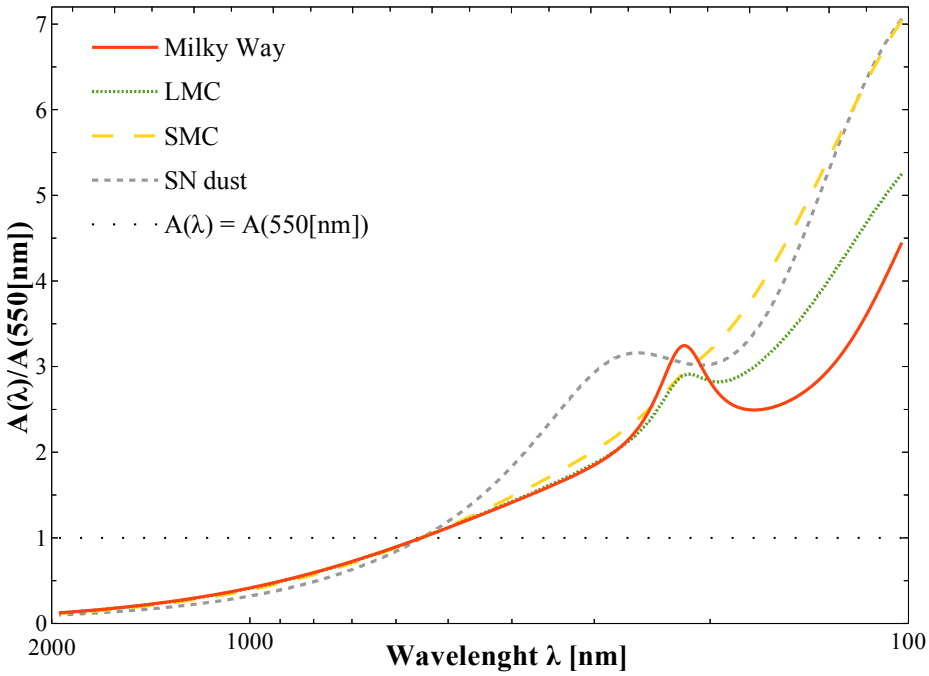

Figure 2.8. Parametrisation of the extinction laws in different host-galaxy environments. The extinction is described as a function of wavelength $A(\lambda)$ and normalised by $A_V = A(550\,\mathrm{nm})$. The MW extinction is shown with a red solid line; for the Large Magellanic Cloud (LMC) with a green dotted line; the yellow long-dashed line for the Small Magellanic Cloud (SMC); and the short-dashed line for the SN-induced dust. The spaced-dotted black line indicates the normalisation used.

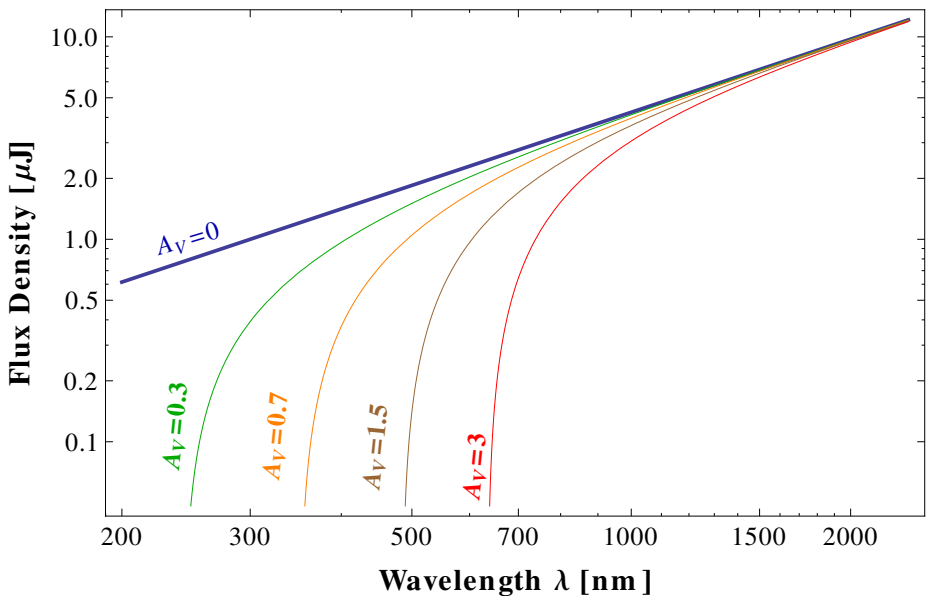

Figure 2.9. Typical AG SED ($\beta = 1.2$, dark-blue thick line) extinguished by an SMC reddening law with values of $A_V = 0.3$ (green), 0.7 (orange), 1.5 (brown), and 3.0 mag (red line).

2.3.6 Quasi-Bolometric Light Curves

The ideal bolometric light curve would describe the temporal evolution of the luminosity integrated from $\lambda = 0$ to infinity. The determination total luminosity would allow us to compare with other SNe and theoretical models. In practice, this is impossible to achieve. The detectors have wavelength-limited sensitivity and the best bolometers are far from the full wavelength coverage. Therefore we refer to *quasi*-bolometric light curves. The sensitivity range in which GROND operates goes from 380 to 2400 nm, which by coincidence covers spectral maximum of SNe. Their SED is approximately described by blackbody radiation at 4,000 – 5,000 K, therefore in principle it also extends beyond the observed wavelength range. However, the UV contributions are generally treated as second-order corrections only. Although UV radiation is highly energetic, it is handled in this manner, because line absorption by metals and line blanketing are dominant below 400 nm (Filippenko, 1997). In fact, flux below 250 nm is hardly detected and not considered in the bolometric estimates. On the other hand, the low-energy tail or NIR emission contributes more significantly at late stages after the SN has cooled due to expansion. For type-Ic SNe, the fraction of NIR flux (JHK bands) is about 20% around blue maximum (Valenti et al., 2008), which is 10 – 20 days after the explosion. Ten days later the NIR flux has increased to about 40%. Thus, there is the need to compute this corrections when NIR observations are not available. Low-redshift events ($z < 0.1$) will have more chances to be detected at these wavelength, however, at larger redshifts the NIR capabilities of GROND are insufficient.

To construct a quasi-bolometric light curve using monochromatic fluxes of each bandpass, I define sets of three filters to interpolate fluxes using the Simpson's rule. The resulting second-degree polynomial is then integrated over frequency for each set of filters. Finally, I add up the integrated fluxes of all sets and compute the total flux in the full wavelength range. The flux is transformed to a luminosity using the distance to the galaxy hosting the transient as computed from the redshift by the NED database[6] following the standard ΛCDM model using a Hubble constant of $H_0 = 74.2$ km s^{-1} Mpc^{-1} (Riess et al., 2009) and the model of the local velocity field by Mould et al. (2000). The latter redshift correction consist in taking into account the relative motions of the MW inside the Local Group, cluster of galaxies to which the MW belongs, and of the Local Group itself towards the Virgo super-cluster of galaxies.

The time-dependent analytical model for SE SNe

Having the quasi-bolometric light curve, i.e., luminosity over time, it is possible now to compare against theoretical model to derive the physical parameters of the explosion, such as the synthesised nickel mass $M_{\rm Ni}$, the total ejecta mass $M_{\rm ej}$, and the kinetic energy of the ejecta $E_{\rm k}$. For this purpose, I made use of the Arnett's analytical model (Arnett, 1982), initially aimed for type-Ia SNe and adapted to SE SNe (e.g., Maeda et al., 2003; Taubenberger et al., 2006; Valenti et al., 2008; Pignata et al., 2011; Benetti et al., 2011). This model is well suited for SNe lacking a hydrogen recombination phase and assumes that

→ the ejecta expansion is homologous,

→ radiation pressure is dominant,

→ symmetry is spherical,

→ opacity is constant,

[6] `http://nedwww.ipac.caltech.edu/`

→ diffusion approximation for photons holds,

→ radioactive nickel and cobalt are centrally located,

→ no nickel and cobalt mixing occurs, and

→ the initial radius is much smaller that 10^{14} cm.

The latter condition actually hold for SE SNe, which are thought to have progenitors with $R_0 \approx 10^{11}$ cm (see §1.3). This analytical model is meant to describe the photospheric phase, i.e., the period in which the expanding SN envelope remains optically thick and the diffusion approximation for photons is applicable. This regime is thought to end at around 30 days past the explosion, therefore, this modelling is valid until then. The approach by Valenti et al. (2008) is based on the Arnett's model and includes, in addition to the ^{56}Ni terms, the ^{56}Co contribution as energy source. The luminosity evolution in the photospheric phase is described as a function of $M_{\rm Ni}$, $M_{\rm ej}$, and $E_{\rm k}$ by the following equation

$$L_{ph} = M_{\rm Ni}\, e^{-x} \left((\epsilon_{\rm Ni} - \epsilon_{\rm Co}) \int_0^x A(z)dz + \epsilon_{\rm Co} \int_0^x B(z)dz \right)$$
$$\text{with} \qquad A(z) = 2z\, e^{-2zy+z^2} \qquad \text{and} \qquad B(z) = 2z\, e^{-2zy+2zs+z^2}, \tag{2.6}$$

where $x = t/\tau_m$, $y = \tau_m/(2\,\tau_{\rm Ni})$, $s = \tau_m(\tau_{\rm Co} - \tau_{\rm Ni})/(2\,\tau_{Co}\,\tau_{Ni})$ help simplify the expression for L_{ph}. The ^{56}Ni and the ^{56}Co decay times $\tau_{\rm Ni}$ and $\tau_{\rm Co}$ are 8.8 and 111 days[7], respectively. The energy inputs by ^{56}Ni and ^{56}Co, $\epsilon_{\rm Ni}$ and $\epsilon_{\rm Co}$, are 3.90×10^{10} and 6.78×10^9 erg s^{-1} g^{-1}, respectively (Sutherland and Wheeler, 1984; Cappellaro et al., 1997). Assuming an homogeneous density, the light-curve time scale τ_m is

$$\tau_m = \left(\frac{\kappa_{\rm opt}}{\beta c} \right)^{1/2} \left(\frac{10 M_{\rm ej}^3}{3E_k} \right)^{1/4} \tag{2.7}$$

where $\beta \simeq 13.8$ is an integration constant (Arnett, 1982), c is the speed of light, and $k_{\rm opt}$ is the optical opacity. Following the grey approximation, I used a constant optical opacity value of $\kappa_{opt} = 0.06$ cm^2 g^{-1}, which was proposed by Maeda et al. (2003) for HNe. In reality, the opacity changes with time and across the ejecta and depends on temperature and composition. Although attempts at variable $\kappa_{\rm opt}$ has also been made (Nakamura et al., 2001), it has been found that a reasonable choice of κ_{opt} is able to reproduce most SE SNe (Mazzali et al., 2000; Maeda et al., 2003).

As for later stages, when the diffusion approximation does not hold anymore and the SN envelope becomes optically thin or *nebular*, I followed the prescription by Sutherland and Wheeler (1984) and Cappellaro et al. (1997), explained in detail by Valenti et al. (2008) in the appendix. The nebular phase should start after 60 days past the explosion, therefore a transition from

[7]Equivalent to half lives of 6.1 and 77.2 days, respectively, both fetched from the Nuclear Data Center web interface at `http://www.nndc.bnl.gov/nudat2/`.

optically thick to thin takes place at $30 \lesssim t \lesssim 60$ days, when none of the two regimes should be valid by themselves. The luminosity evolution at late times is described by

$$L_{\rm neb} = \overbrace{S_\gamma^{\rm Ni}}^{\text{Nickel decay}} + \overbrace{S_\gamma^{\rm Co}}^{\text{Cobalt decay}} + \overbrace{S_{\gamma,{\rm e}^+}^{\rm Co}}^{\text{positron annihilation}} + \overbrace{S_{E_{\rm k},{\rm e}^+}^{\rm Co}}^{\text{positron kinetic energy}} \tag{2.8}$$

$$= M_{\rm Ni}\left\{\epsilon_{\rm Ni}\, e^{-t/\tau_{\rm Ni}} + \epsilon_{\rm Co}\left(e^{-t/\tau_{\rm Co}} - e^{-t/\tau_{\rm Ni}}\right)(0.81\, m + 0.164\, m\, w + 0.036\, w)\right\},$$

where the definitions $m = 1 - e^{-(T_\gamma/t)^2}$ and $w = 1 - e^{-(T_{\rm e^+}/t)^2}$ correspond to approximate probabilities of absorption of γ-ray photons and positron annihilation, respectively (Clocchiatti and Wheeler, 1997). The characteristic times T_γ and $T_{\rm e^+}$ depend on the ejecta mass, kinetic energy, and opacity as follows:

$$T_\gamma = \sqrt{C(\rho)\,\kappa_\gamma\, M_{\rm ej}^2/E_{\rm k}} \qquad \text{and} \qquad T_{\rm e^+} = \sqrt{C(\rho)\,\kappa_{\rm e^+}\, M_{\rm ej}^2/E_{\rm k}}, \tag{2.9}$$

where $C(\rho)$ is a function of the density ρ. Assuming an homogeneous density and opacity values of $\kappa_\gamma = 0.027$ cm^2 g^{-1}, and $\kappa_{\rm e^+} = 7$ cm^2 g^{-1} (Clocchiatti and Wheeler, 1997), the characteristic times turn out to be $T_\gamma \simeq 32\, M_{\rm ej,\odot}/\sqrt{E_{\rm k,51}}$ and $T_{\rm e^+} \simeq 515\, M_{\rm ej,\odot}/\sqrt{E_{\rm k,51}}$ in units of seconds, where $M_{\rm ej,\odot}$ is the ejecta mass in units of solar masses and $E_{\rm k,51}$ is the kinetic energy in units of 10^{51} erg.

Figure 2.10 shows the four different components of $L_{\rm neb}$ as presented by eq. 2.8 for physical parameters of $M_{\rm Ni} = 0.2\,{\rm M}_\odot$, $M_{\rm ej} = 1\,{\rm M}_\odot$, and $E_{\rm k,51} = 3$. The resulting nickel luminosity decays at the standard pace of about 0.05 dex per day. Given that the ^{56}Co is a product of

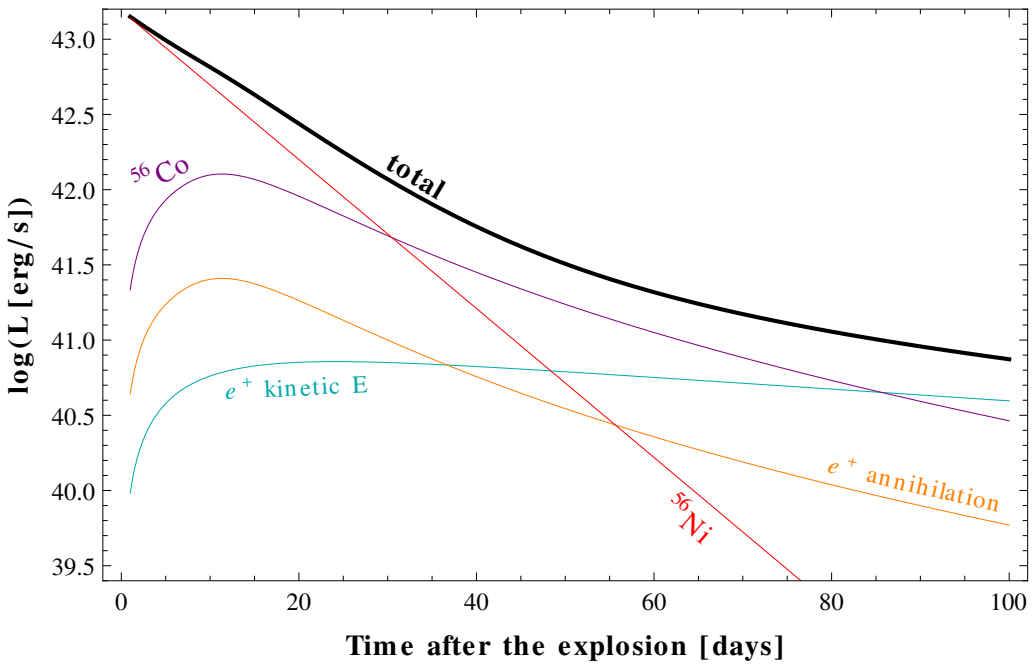

Figure 2.10. Decomposed model in eq. 2.8 for the nebular regime.

the radioactive ^{56}Ni, the dominant contributions in the total luminosity are as expected those of nickel at early times ($t \lesssim 30$ days) and cobalt at later times. At $t \approx 35$ days the e$^+$ kinetic luminosity takes over the production by e$^+$ annihilation, because the latter becomes less likely as the envelope expands. Since the ^{56}Co luminosity decays as there is less radioactive ^{56}Ni, the e$^+$ kinetic luminosity takes over the former too at around 85 days after the explosion. Note that $L_{\rm neb}$ is valid only after $t \gtrsim 30-60$, which will be assumed for modelling of observed data.

Having the luminosity for the two different regimes, I implemented the model of the two ejecta components by Maeda et al. (2003), which consist of an inner central component acting as a dense core plus an outer component as the envelope with lower density. The motivation for the development of this two-component model lies on the inconsistencies found between the parameters derived from fitting the early and late light curves of SNe Ic, caused mainly by a constant γ-ray trapping over time.

In the first part of the modelling procedure, I fit the optically thick regime under the reasonable assumption that the inner component remains hidden and only the outer component contributes to the luminosity. This step yields the physical parameters $M_{\rm Ni}$, $M_{\rm ej}$, and $E_{\rm k}$ for the envelope. In the second part of the modelling, I fit both components to the data fixing the parameters found in the first step. Therefore, only the fractions of mass f_M and kinetic energy f_E in the inner component are free to vary. This way we are able to compute the usual physical parameters from the quasi-bolometric light curve and additionally the latter two, which give insights on the structure of the SN explosion.

2.4 The case of GRB 110420A: importance of host subtraction

The *Swift*/BAT was triggered by GRB 110420A at 11:02 UT (Mangano et al., 2011) and promptly XRT and UVOT detections were reported. The γ-ray prompt emission was long and relatively soft ($T_{90} \approx 18$ s, $E_{\rm peak} \approx 43$ keV; Golenetskii et al., 2011a), which would be compatible with the bulk of SN-related GRBs. The UVOT detected the AG in all filters (Oates and Mangano, 2011), which constrains the redshift to $z \lesssim 1.6$ and proves more likely to detect a SN bump. Ground-based observations were publicly reported only by Afonso et al. (2011) with preliminary results of the GROND r'-band first epoch. No redshift measurement was reported for this event. Deep imaging observations were performed with the purpose of image subtraction of the host galaxy on November 22 and 24, 2011, i.e., seven months after the GRB. While $g'r'i'z'$ detections were possible, no NIR counterpart was detected.

The GROND, UVOT, and XRT data was reduced and analysed as described above. The broad-band SED was constructed using $g'r'i'z'JH$ from GROND, $u/uvw2/uvm2$ from UVOT, and XRT data. For a redshift range from $z = 0.1$ to 0.9, the data are best described by a single power law of index $\beta = 0.97 \pm 0.02$, $N_{\rm H,host} = (8-17) \times 10^{20}$ cm^{-2}, $A_{V,\rm host} = 0.14^{+0.20}_{-0.08}$ mag, and with ${\chi_\mu}^2 \approx 1.1$. The multicolour light curve is shown in Fig. 2.11. Until about 10 days after the burst, the data including X-rays is best described by a broken power law. Before image subtraction of the host galaxy (filled circles in Fig. 2.11), the optical light curves show a flattening followed by a flux decay resembling a SN bump. These data were fitted with a broken power law plus templates of SN 1998bw (see §2.3.3) plus the host contribution (dotted lines). The difference with the model without the SN contribution (dashed lines) is quite clear in Fig. 2.11. The host contribution —as well as the images for image subtraction— were obtained $t > 200$ d after the burst to avoid contamination by the transient.

After image subtraction of the host galaxy, the resulting photometry looks puzzling (open circles in Fig. 2.11). No residual flux is detected at $t > 10$ d and the data is now well fitted

with a broken power law alone (solid lines for $g'r'i'z'$). Many reasons were attributed to the defective initial $r'i'z'$ photometry and are sorted by importance as follows:

1. A time-dependant noise pattern produced by defective electronics in charge of the images readout acted on the photometry of the $r'i'z'$ bands.
2. An object inside the aperture ($r \sim 1.8''$) contaminated the photometry in the r' band. The contamination varied with the FWHM at different epochs.
3. Coincidental zero-point variations due to atmospheric disturbances (seeing and transparency) could have been present with a much lower intensity.

These three effects combined contributed to the "fake" SN bump observed in the preliminary photometry of GRB 110420A. Even the best analysis pipeline can be affected by these issues, therefore, it probes always necessary to perform the proper image subtraction of the host before doing any scientific analysis of the transient object of interest.

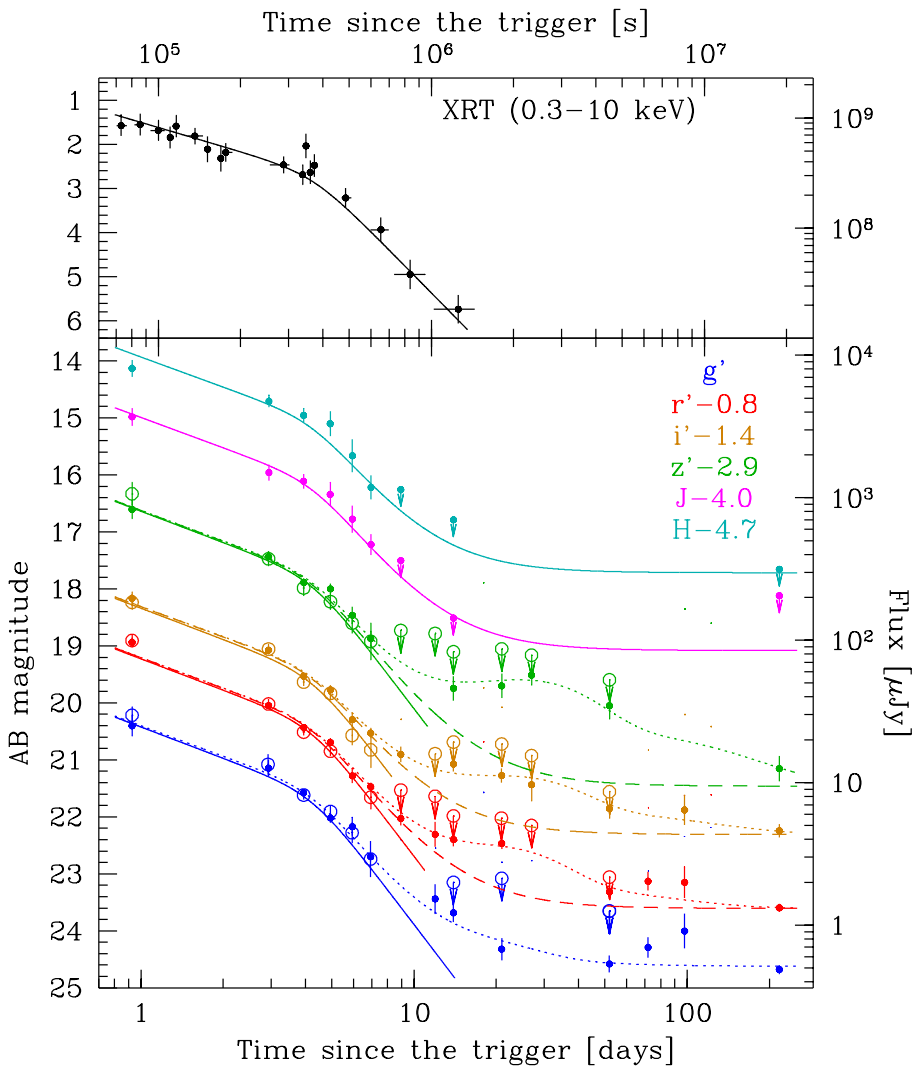

Figure 2.11. GROND multicolour light curve of GRB 110420A. The solid line includes a speculative host component in the JH bands. Upper limits are depicted by arrows.

Chapter 3

The Fast Evolution of SN 2010bh associated with XRF 100316D[1]

3.1 Introduction

The core collapse of massive stars is thought to give rise to both SNe and long GRBs ($T_{90} > 2$ s; Kouveliotou et al., 1993). The first clue to the connection between these events is the similarity in their kinetic-energy scale (see Woosley and Bloom, 2006, for a review). Even before the discoveries of the late 90's, a few authors discussed the possible association between high-energy outbursts and SNe (Colgate, 1968; Paczyński, 1986). The kind of SN thought to be associated with GRBs are those labelled SE SNe, whose hydrogen envelope have mostly been removed (see §1.2 for more details).

So far, only a few type-Ic SNe observed to be related to GRBs. The association between SN 1998bw and GRB 980425 (e.g., Galama et al., 1998b; Kippen, 1998) was the first and still is the foundation stone for the following events (see §1.3 for more cases and references). Late-time bumps in the light curves of GRB AGs stands as the most popular SN signature (see, e.g., Zeh et al., 2004; Richardson, 2009). These re-brightenings have been usually faint for spectroscopy and have been detected in GRB light curves out to redshifts of ~ 1 (Masetti et al., 2005; Della Valle et al., 2003; Bloom et al., 2009; Tanvir et al., 2010). Sample studies of GRB-SNe have included bumps not spectroscopically identified and have aimed at determining the luminosity distribution, the morphology of the light curves, and the physical parameters of the explosion such as kinetic energy, ejected mass, and ^{56}Ni mass (Zeh et al., 2004; Ferrero et al., 2006; Richardson, 2009; Thöne et al., 2011). It has been asserted that GRB-SNe are generally brighter than the local sample of SE SNe.

Yet, there are a few supposedly long GRB events where an expected SN appearance was never detected. Very tight constraints have been placed on the SN signature for GRBs 060505 (Fynbo et al., 2006; Ofek et al., 2007) and 060614 (Fynbo et al., 2006; Gal-Yam et al., 2006; Della Valle et al., 2006a). The non-detections of SNe components for these two GRBs (down to 1% as bright as SN 1998bw) could serve as a GRB classification tool. This is however still a point of controversy (e.g., Zhang et al., 2009, more information in §1.3).

Another additional line of research in the study of GRB-SNe is their early emission, which can reveal information about the explosion. This X-ray and UV emission was usually interpreted

[1]Based on the article by F. Olivares E., J. Greiner, P. Schady, A. Rau, S. Klose, T. Krühler, P. M. J. Afonso, A. C. Updike, M. Nardini, R. Filgas, A. Nicuesa Guelbenzu, C. Clemens, J. Elliott, D. A. Kann, A. Rossi, and V. Sudilovsky (2011, A&A, 539, A76)

as thermal radiation produced by the shock breakout from the surface of the progenitor (Colgate, 1974; Falk, 1978; Klein and Chevalier, 1978; Matzner and McKee, 1999; Waxman et al., 2007; Nakar and Sari, 2010, refer to §1.3 for examples and detailed explanation). From the analysis of this a signal, it is possible to constrain the AG component, derive both the temperature and luminosity of the thermal component, and compute the apparent radius of emission (e.g., Thöne et al., 2011).

We analysed the optical and near-infrared (NIR) data of XRF 100316D and its associated SN 2010bh. The paper is organised by summarising the observations, data acquisition, reduction, and analysis in §3.2. The main results are treated separately as three different sections. The modelling of the early broad-band spectral energy distribution (SED) provides the progenitor radius and the host-galaxy extinction and is presented in §3.3. The multi-wavelength light and colour curves are analysed in §3.4 along with comparisons with previous GRB-SN events. In §3.5, the quasi-bolometric light curve is analysed and the physical parameters of the explosion are derived. Finally we gather our conclusions in §3.6.

3.2 Observations

Gamma-ray emission from XRF 100316D triggered the Burst Alert Telescope (BAT; Barthelmy et al., 2005)) on board the *Swift* satellite (Gehrels et al., 2004) on March 16, 2010, at t_0 = 12:44:50 UT (Stamatikos et al., 2010a). It turned out to show a soft γ-ray spectrum (Sakamoto et al., 2010a) and a duration of at least 1300 s, one of the longest ever measured (Fan et al., 2011; Starling et al., 2011). About 15 h thereafter, a spectroscopic redshift of 0.059 was published for the host galaxy (Vergani et al., 2010a,b). Observations of the Gamma-Ray burst Optical and Near-infrared Detector (GROND; Greiner et al., 2007, 2008) confirmed that the new source became evident about 16 h after the burst (Afonso et al., 2010). The rising of the supernova was verified photometrically by Wiersema et al. (2010) only three days after the trigger. The spectroscopic confirmation of Chornock et al. (2010b) came approximately six days after the burst, which was confirmed two days later by Bufano et al. (2010a). The SN was officially named SN

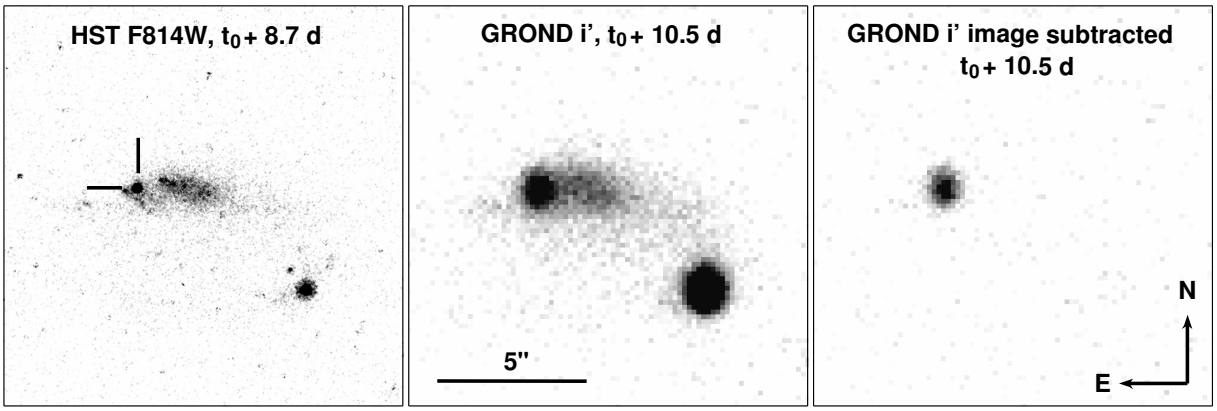

Figure 3.1. HST/WFC3 $F814W$, GROND i'-band, and GROND host-subtracted i'-band images of the GRB-SN field, respectively, from left to right. Images were taken at around maximum brightness. Each panel is approximately $13'' \times 13''$ in size. The HST image shows significant galaxy structure near the explosion site (marked with two lines), which is blended with the object of interest in the GROND image shown in the middle panel. GROND images in the middle and right panels are shown using the same flux scale.

2010dh eight days after the trigger (Bufano et al., 2010b; Chornock et al., 2010c). On March 26, 2010, additional GROND observations of SN 2010bh were reported along with results at the first attempts of host-galaxy subtraction (Rau et al., 2010).

3.2.1 GROND

Observations of XRF 100316D performed simultaneously in $g'r'i'z'JHK_{\rm s}$ by GROND (refer to §2.2 for instrument information) started 11.7 h after the trigger, with an average seeing of $1\farcs1$, as soon as the astronomical night began.

The GROND data were reduced in a standard manner (see §2.2.2 for details). Aperture photometry was selected for science and calibration objects. The SDSS field at coordinates R.A.(J2000) = $06^{\rm h}59^{\rm m}33^{\rm s}.6$, Dec.(J2000) = $-17°27'00''$ was observed during photometric conditions to calibrate our images by performing relative photometry. A total of six stars in the field of XRF 100316D were employed for this purpose (see appendix of Olivares E. et al. (2012)). The same set of stars was used to calibrate $JHK_{\rm s}$ against the 2MASS catalogue. Calibration uncertainties vary in the range $0.002-0.020$ mag for $g'r'i'z'$ and $0.02-0.12$ mag for $JHK_{\rm s}$, which together with catalogue systematics are added in quadrature to the statistical error.

A deep host-galaxy observation was carried out on November 5, 2010. This observation resulted in images with mean seeing of $0\farcs74$ and was used as a reference image for the subtraction of the host contribution from the early epochs. To develop a notion of the host contamination, we refer to Fig. 3.1, where the position of the transient relative to the host galaxy is shown along with an $F814W$ image of the Wield Field Camera 3 (WFC3) on board the Hubble Space Telescope (HST) as reference. In addition, the coordinates of the centre of the host galaxy, catalogue name Anon J071031–5615, were obtained from the last GROND observation: R.A.(J2000) = $7^{\rm h}10^{\rm m}30^{\rm s}.37(\pm0^{\rm s}.07)$, Dec.(J2000) = $-56°15'20\farcs2(\pm0\farcs3)$. Following the procedure described in detail in §2.2.4, the images were aligned, convolved to a unique PSF, scaled in flux, and subtracted. This procedure was executed for a total of 140 individual images in a total of 20 epochs (see Fig. 3.1 for an example of image subtraction in the i' band). The position of the transient is R.A.(J2000) = $7^{\rm h}10^{\rm m}30^{\rm s}.55(\pm0^{\rm s}.05)$, Dec.(J2000) = $-56°15'20\farcs0(\pm0\farcs2)$ in host-subtracted optical images. The resulting photometry is tabulated in the appendix of Olivares E. et al. (2012).

3.2.2 *Swift*/XRT and UVOT

On board the *Swift* satellite, the X-Ray Telescope (XRT; Burrows et al., 2005) and the UVOT (Roming et al., 2005) started observations of XRF 100316D at $t_0 + 2.4$ min (Stamatikos et al., 2010a). Whilst a bright X-ray source was detected inside the BAT error circle, initially no AG candidate was found by UVOT (Oates et al., 2010).

However, in deeper images taken at $t_0 + 33$ ks in the $uvw1$ filter and at $t_0 + 63$ ks in the u band, we found evidence of emission in excess of the host-galaxy contribution. To remove the contribution from the host galaxy, we requested ToO observations in the $uvw1$ and u filters, which were taken at $t_0 + 3 \times 10^7$ s (347 d after the burst), and amounted to a total exposure time of 1525 and 1369 s, respectively. We measured a host galaxy contribution within the source aperture of 25 ± 2 and 39 ± 3 μJy in the $uvw1$ and u bands, respectively. Subtracting this contribution from our earlier-time data gave us a 3σ detection in 1894 s of $uvw1$- and in 4901 s of u-band data taken at mid-times of $t_0 + 33$ ks and $t_0 + 63$ ks respectively. In our analysis, we include only the $uvw1$ detection at t_0+33 ks, since there were no GROND data contemporaneous with the epoch of our u-band detection. All UVOT data were handled as detailed in §2.1.2.

To minimise the contamination from the underlying host galaxy, the source flux was measured within a circular source-extraction region of a $3\farcs5$ radius. An aperture correction was then applied in order to remain compatible with the UVOT effective area calibrations, which are based on $5''$ aperture photometry (Poole et al., 2008).

The relatively bright X-ray AG (30 – 40 cnt s^{-1} between 144 and 737 s after the trigger) faded considerably at the beginning of the second XRT epoch ($t_0 + 33$ ks; see Starling et al., 2011, for a detailed analysis). In the subsequent analysis, we employed XRT data at stages contemporaneous to GROND observations, specifically in the interval from 33 to 508 ks after the burst. These data were obtained from the public Swift archive and reduced in the standard manner using the `xrtpipeline` task from the HEAsoft package, with response matrices from the most recent `CALDB` release. All data were obtained in photon counting mode and downloaded from the XRT light curve repository (Evans et al., 2007, 2009). Spectra were grouped using the `grppha` task.

All the data discussed throughout the paper were corrected for the Galactic foreground extinction of $E(B-V)_{\rm Gal} = 0.117$ mag with $R_V = 3.08$ (Schlegel et al., 1998). All uncertainties in the following analysis are quoted at the 1σ confidence level.

3.3 Early Broad-Band SED

Using data between 33 and 54 ks (roughly from 11 to 15 h) after the burst, we compiled two early broad-band SEDs of XRF 100316D. GROND provides detections in $g'r'i'z'J$ and upper limits in $HK_{\rm s}$, whilst the count rate of contemporaneous *Swift*/XRT observations is already 0.01 cnt s^{-1} at $t_0 + 33$ ks and decaying. After combining data from 33 to 508 ks after the trigger, XRT provides only three bins in the X-ray energy range. In the following, XRT data are scaled to the GROND first two epochs by using a decay index of $\alpha = -1.3 \pm 0.2$, which is derived from the same XRT data over time. *Swift*/UVOT observed only in the $uvw1$ filter at these stages.

3.3.1 Modelling Scheme

Early blue emission coming from the XRF position was detected by GROND. For data acquired 42.5 ks after the burst, we measured a colour $g' - r' = -0.30 \pm 0.06$ mag, in contrast to the red AGs that usually follow a GRB (photon index Γ in the range 1.2 – 2.5). Similar observations were made by Cano et al. (2011b), who found that this emission is incompatible with synchrotron radiation. The adiabatic cooling of the expanding atmosphere following the shock breakout gives us a reasonable explanation of the observed blue colours (e.g., Cano et al., 2011b). In this scenario, the emission from the shock breakout lasts only a few hours after the core collapse and its SED resembles a blackbody at a high temperature of the order of 10^6 K (or 0.1 keV equivalently; e.g., Campana et al., 2006). Thus, we interpret the blue colours in our observations as the thermal component associated with the cooling of the shock breakout, which is similar to what has been claimed for XRF 060218/SN 2006aj (Campana et al., 2006; Waxman et al., 2007) and other early-caught SNe (e.g., Soderberg et al. 2008b; Modjaz et al. 2009 on SN 2008D; Roming et al. 2009 on SN 2008ax). In contrast to the idea of a thermal component producing the observed emission, there are no significant contemporaneous detections of UVOT in the $uvw1$ bandpass, which alludes to high reddening. On the other hand, $i' - J = 0.06 \pm 0.15$ mag measured at the same epoch appears to have an underlying additive red component, which is represented in this case by the GRB AG synchrotron emission (see Fig. 3.2).

To test this hypothesis, we modelled the SEDs at 42.5 and 50.0 ks (the latter shown in Fig.

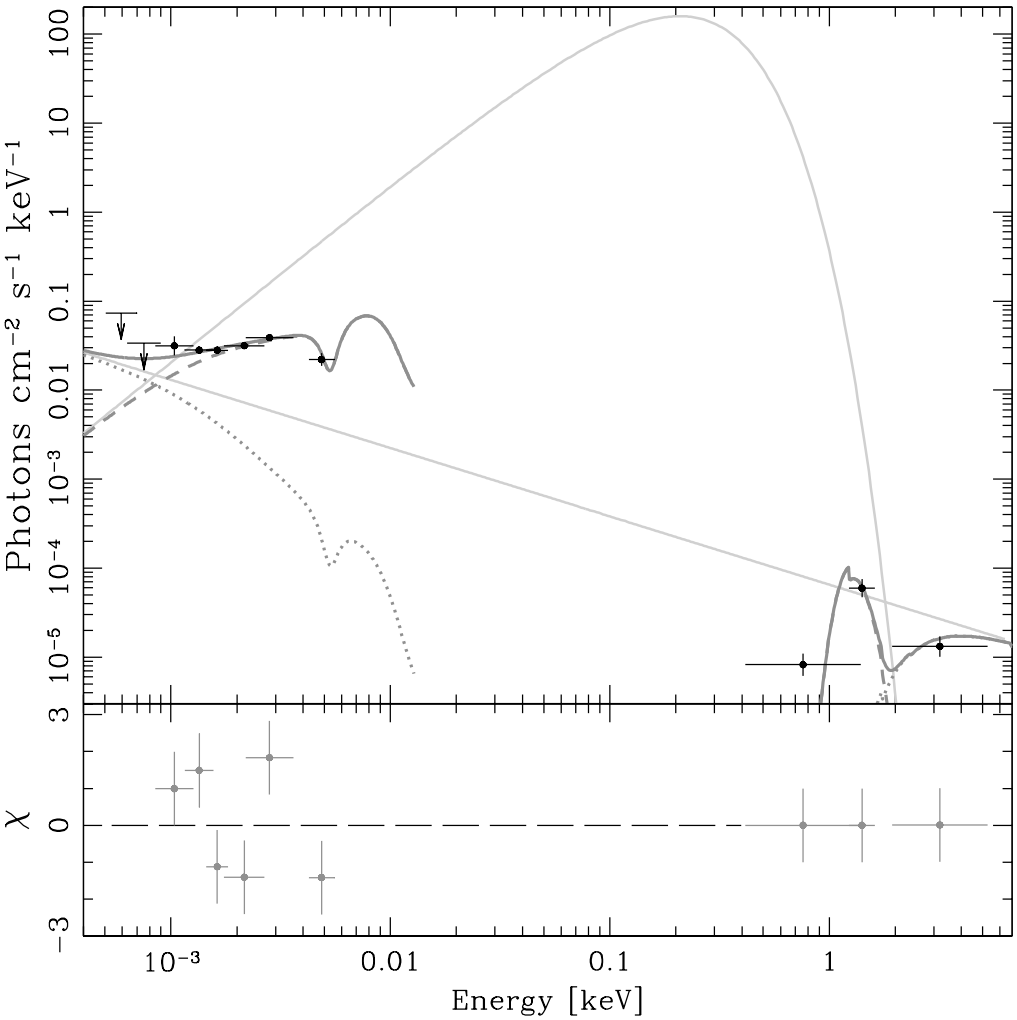

Figure 3.2. Broad-band SED at 50 ks after trigger. The observed data are represented by black filled circles. The HK_s bands provide only 3σ upper limits shown as arrows. The thick grey line shows the best-fit model able to reproduce the data: extinguished power law plus blackbody components, which are shown individually with dotted and dashed grey lines, respectively. The thin continuous grey lines show the unextinguished versions of the power law corresponding to the AG and the thermal component. In the lower panel, the residuals of the best fit are plotted.

3.2) using two additive components: (1) a power law for the AG, and (2) an ideal blackbody for the thermal component, respectively, of the forms

$$P_E(\Gamma) = C_1\, E^{-\Gamma} \qquad \text{and} \tag{3.1}$$

$$B_E(T_{\rm BB}) = \frac{C_2\, E^2\, dE}{(kT_{\rm BB})^4 (e^{E(1+z)/kT_{\rm BB}} - 1)}, \tag{3.2}$$

where C_1 and C_2 are normalisations, E is the spectral energy in units of keV, Γ is the photon index, k is the Boltzmann constant, $T_{\rm BB}$ the intrinsic blackbody temperature, and $z = 0.059$ is the redshift (Chornock et al., 2010c). The model also accounts for host-galaxy extinction based on either MW ($R_V = 3.08$), LMC ($R_V = 3.16$), or SMC ($R_V = 2.98$) extinction laws and soft X-ray metal absorption. The Galactic metal absorption is fixed to be $N_{\rm H,Gal} = 7.05 \times 10^{20}$ cm^{-2}

(Kalberla et al., 2005). The model has a total of six free parameters: C_1, C_2, Γ, $T_{\rm BB}$, $E(B-V)_{\rm host}$, and $N_{\rm H,host}$. The luminosity of the blackbody is computed as $L_{\rm BB} = 8.0525\, C_2\, (1+z)\, D_{10}^2$ erg s^{-1}, where D_{10} is the luminosity distance to the transient in units of 10 kpc. A luminosity distance of 240 ± 17 Mpc to the host galaxy of XRF 100316D is employed as computed by the NED database[2] following the standard ΛCDM model, using the redshift measured by Chornock et al. (2010c), a Hubble constant of 74.2 km s^{-1} Mpc^{-1} (Riess et al., 2009), and the model of the local velocity field by Mould et al. (2000).

The different set of parameters are summarised in Table 3.1. All best-fit parameters are consistent between the two epochs within their statistical uncertainties between both epochs. The temperature $T_{\rm BB}$ and luminosity $L_{\rm BB}$ of the thermal component are in the range $78-81$ eV and $4-7 \times 10^{47}$ erg s^{-1} from Cols. 4 and 5 of Table 3.1, respectively. The AG power-law photon index $\Gamma \approx 1.8$ is shown in Col. 7. The reduced χ^2 (or ${\chi_\mu}^2 \equiv \chi^2/\mu$, where μ is the number of degrees of freedom) improves from 16.6 for the model without extinction to 2.7 for the model extinguished by MW-like dust. The best fit to the second SED epoch is shown in Fig. 3.2 with a thick grey line. The UV dust feature characteristic of the MW extinction law gives the more precise results, although it is poorly constrained at the bluer end. The X-ray tail of the blackbody fits the two data bins at around 1 keV, whilst the power law fits the only data point at ≈ 3 keV; both components contain significant absorption. We note that the fitting of the X-ray data has practically no residuals, i.e., the model over-predicts the data in this energy range.

In addition to the luminosity and temperature, it is possible to compute an apparent emission radius of the thermal component ($R_{\rm BB}$) from these two measured quantities by assuming isotropic radiation from an ideal blackbody. For all our trial models, the corresponding radii were calculated as $R_{\rm BB} = (4\pi\sigma L_{\rm BB}^{-1} T_{\rm BB}^4)^{-1/2}$, where σ is the Stefan-Boltzmann constant (Col. 6 of Table 3.1). Our best-fit parameters yield a radius of $3-4 \times 10^{13}$ cm, which is two orders of magnitude larger than the typical sizes of the most likely GRB progenitors (WR stars; Cappa et al., 2004).

The amount of metal absorption (estimated based on an equivalent hydrogen column density at solar metallicity) and dust extinction required for a good fit are $N_{\rm H,host} \approx 4 \times 10^{22}$ cm^{-2} and $E(B-V)_{\rm host} = 0.2-0.4$ mag, respectively. These two parameters are fitted independently and with no assumption being made about the environment gas-to-dust ratio. However, the available data is not enough to allow us to distinguish among the different extinction laws employed in the modelling procedure. Whilst the reddening is consistent with values found in previous studies (Starling et al., 2011; Cano et al., 2011b), the hydrogen column density differs significantly from the results of Starling et al. (2011). The discrepancy is due to the additional constraints provided by the optical/NIR data, which were included to derive the parameters of the blackbody contribution. With our data set it is possible to tie the thermal component at both low and high energies, which provides a more accurate value for the absorption by heavy elements because of the greater constraint on the X-ray flux.

[2]http://nedwww.ipac.caltech.edu/

Table 3.1. Fits to broad-band spectra constructed using GROND and *Swift*/XRT data.

Time Interval [s] after the trigger	Reddening Law	$E(B-V)_{\rm host}$ [mag]	$kT_{\rm BB}$ [eV]	$L_{\rm BB}$ [10^{47} erg s^{-1}]	$R_{\rm BB}$ [10^{12} cm]	Γ	$N_{\rm H,host}$ [10^{22} cm^{-2}]	χ^2/μ
42182 – 42879	MW	$0.21^{+0.11}_{-0.21}$	81^{+6}_{-4}	$4.1^{+2.0}_{-2.5}$	27±8	1.82±0.05	4.2±0.5	4.9/4
42182 – 42879	LMC	$0.19^{+0.10}_{-0.19}$	81^{+6}_{-4}	$4.0^{+1.9}_{-2.3}$	26±8	1.82±0.05	4.2±0.5	4.9/4
42182 – 42879	SMC	$0.16^{+0.11}_{-0.16}$	82^{+5}_{-4}	3.4 ± 1.7	24^{+7}_{-6}	1.82±0.05	4.1±0.5	4.9/4
42182 – 42879	MW	0.39 fixed	79 ± 3	7.4 ± 0.9	39 ± 4	1.73 ± 0.06	$4.4^{+0.5}_{-0.4}$	8.7/5
46630 – 53807	MW	0.39 ± 0.03	78 ± 2	7.2 ± 1.1	38 ± 3	1.77 ± 0.05	4.4 ± 0.4	13/5
46630 – 53807	LMC	0.38 ± 0.03	78 ± 2	7.0 ± 1.0	38 ± 3	1.76 ± 0.06	4.4 ± 0.4	16/5
46630 – 53807	SMC	0.37 ± 0.04	79 ± 2	6.2 ± 0.9	35 ± 3	1.77 ± 0.05	4.4 ± 0.4	18/5

Note.— The model consists of a blackbody plus a power law, both attenuated by optical/NIR reddening and X-ray metal absorption.

3.3.2 Host-Galaxy Extinction

We then attempted to evaluate the constraint on the extinction value derived in the previous section. Contour plots of reddening against blackbody temperature, luminosity, and spectral index from the best fit to the data are shown in Fig. 3.3, respectively. The 1σ and 2σ contours show that the solution to our best-fit relation is well-defined in all three panels. In the first panel there is a second solution to our best-fit relation at the 3σ level, which is at lower temperatures and similar reddening, although its significance is rather low. In the middle panel, the contours show a slight trend of proportionality between luminosity and extinction, which is expected. At luminosities higher than 1.1×10^{48} erg s^{-1}, there is no possible solution, because the model becomes much brighter than the X-ray data and $N_{\rm H,host}$ cannot be allowed to vary and compensate for the X-ray luminosity of the model. Contours of the variations in the reddening and spectral index are shown in the lower panel, where the extinction is again restricted to high values.

Analyses of optical spectroscopy of the host galaxy have found that the line-flux ratio of Hα to Hβ in the H II region coincident with the SN position is consistent with zero extinction (Starling et al., 2011; Levesque et al., 2011). Nevertheless, the $A_{V,\rm host} \sim 0$ estimate from the spatially resolved spectroscopy of Levesque et al. (2011) probes a much larger region (≈ 1.3 kpc^2) than the one probed by our line of sight to the GRB-SNe. A sufficiently high dust clumpiness could explain our high extinction values along the line of sight and $A_{V,\rm host} \sim 0$ when integrated over a larger patch. The position at which the hydrogen lines are formed, i.e., the H II region, might be located in front of the explosion site and not probe the same line of sight through the host galaxy.

Alternatively a broken power-law model was fitted to the data in Fig. 3.2 for which ${\chi_\mu}^2 = 3.0$, which is slightly larger than that of the model that consists of a blackbody plus power law. The broken power law provided a closer fit when we assume that there is no host-galaxy extinction, significantly different from our results for the blackbody plus power-law model. However, the low-energy spectral slope of $\beta = +0.5$ is incompatible with synchrotron radiation ($\beta_{\rm max} = +1/3$; e.g., Sari et al., 1998). Furthermore, the spectral break lies between the g' and the $uvw1$ bands at $\nu_{\rm break} = (8 \pm 3) \times 10^5$ GHz, which is inconsistent with the self-absorption feature usually observed at radio frequencies ($\nu_a \sim 2-13$ GHz; Galama et al., 1998c; Taylor et al., 1998; Granot et al., 1999; Galama et al., 2000). Given also that $A_{V,\rm host} > 0.2$ mag is derived in §3.3.1 and preferred by other authors (see next paragraph), the broken power-law model can be discarded with confidence.

Additional evidence of large reddening along the line of sight inside the host galaxy was found by Starling et al. (2011), $E(B-V)_{\rm host} \approx 0.9$ mag. The reddening was derived by fitting *Swift*/BAT+XRT data and a u-band 3σ upper limit provided by *Swift*/UVOT data in the interval from 638 to 737 s after the burst. We employed a model that consists of a blackbody plus power law extinguished by SMC dust. A similar method was used here and by Campana et al. (2006), who determined $E(B-V)_{\rm host} = 0.20$ for SN 2006aj. Another attempt at dereddening SN 2010bh was carried out by Cano et al. (2011b), who found $E(B-V)_{\rm host} = 0.18 \pm 0.08$ mag by assuming that the colours of SE SNe are all the same ten days after the V-band maximum brightness (Drout et al., 2011). Whilst this method is supported for the hydrogen atmospheres of type-IIP SNe by a line of physical arguments (e.g., Olivares E. et al., 2010), it is entirely empirical for SE SNe. Nevertheless, their reddening value is larger than zero with a significance of 2.3σ and consistent with our calculations for our second-epoch SED of $E(B-V)_{\rm host} = 0.39 \pm 0.03$ mag at the 2.5σ confidence level.

After correcting for $E(B-V)_{\rm host} = 0.39 \pm 0.03$ mag, we obtained $uvw1 = 18.15 \pm 0.27$ and

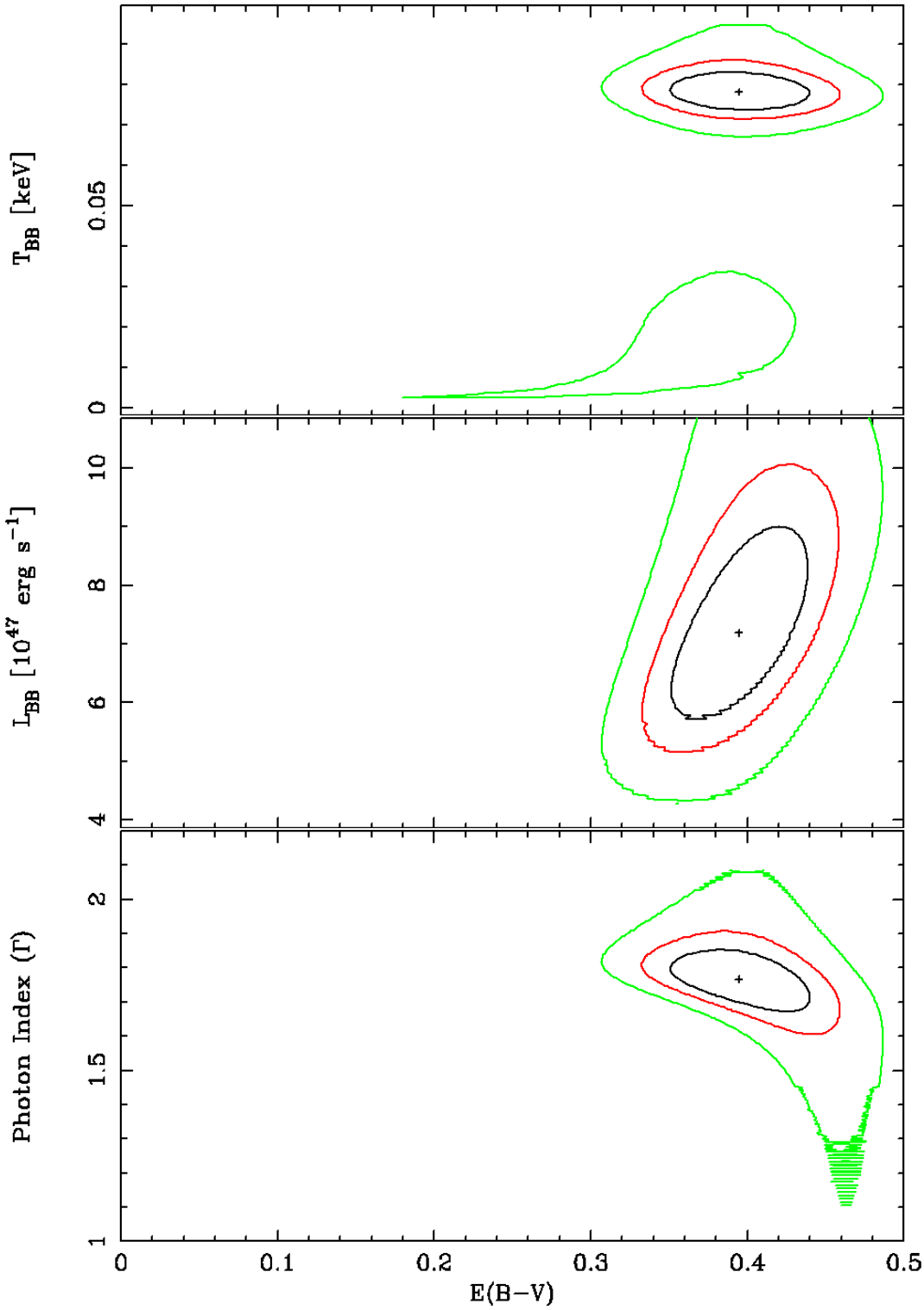

Figure 3.3. Contour plots for the best-fit parameters from the modelling of the second epoch. From the outer- to the innermost contours, the green, red, and black lines are 3, 2, and 1σ, respectively. In the bottom panel, the tail at low Γ values is caused by numerical inaccuracies.

$u = 19.70 \pm 0.45$ mag in the AB system at 33 and 63 ks after the burst, respectively. For SN 2006aj (Campana et al., 2006), these values were $uvw1 = 17.73 \pm 0.21$ and $u = 17.77 \pm 0.15$ mag at the same phase and redshift of SN 2010bh. If we had assumed that we should have seen a cooling envelope for SN 2010bh of comparable brightness and evolution as that shown by SN 2006aj, the host-galaxy extinction should have been higher than that estimated by our method. Nevertheless, the uncertainties are large and the comparison of the *uvw1* measurements is consistent at the 1.2σ confidence level. Although in the u band the uncertainty is even larger, there is no consistency with the brightness of SN 2006aj at the 4σ confidence level and a higher host-galaxy extinction ($A_{V,\mathrm{host}} \approx 2.1$ mag) would be required to reach the 1σ level of consistency.

In conclusion, we use the extinction value from the fit to the second-epoch broad-band SED throughout the paper, $E(B-V)_{\mathrm{host}} = 0.39 \pm 0.03$ mag for MW-like dust with $R_V = 3.08$, given that compared to the first epoch the statistical errors in the $g'r'i'z'J$ photometry are smaller and additional $uvw1$ photometry is available. Moreover, when fixing the host-galaxy reddening to $E(B-V)_{\mathrm{host}} = 0.39$ mag, the quality of the fit to the first epoch is still acceptable ($\chi_\mu{}^2 = 1.6$), whilst the fit to the second epoch using $E(B-V)_{\mathrm{host}} = 0.21$ mag from the first-epoch modelling results in $\chi_\mu{}^2 = 3.7$ and unphysical parameters. Hence, values of host-galaxy extinction including the correction for redshift (K-correction based on the spectral model) for the GROND filters and their corresponding statistical uncertainty are $A_{g',\mathrm{host}} = 1.50 \pm 0.12$, $A_{r',\mathrm{host}} = 1.10 \pm 0.09$, $A_{i',\mathrm{host}} = 0.80 \pm 0.08$, $A_{z',\mathrm{host}} = 0.60 \pm 0.06$, $A_{J,\mathrm{host}} = 0.39 \pm 0.04$, $A_{H,\mathrm{host}} = 0.22 \pm 0.02$, and $A_{K_\mathrm{s},\mathrm{host}} = 0.14 \pm 0.01$, all in units of magnitude.

3.3.3 Evolution of the Thermal Component

Having determined temperature, luminosity, and radius for the thermal component, it was then possible to study their evolution. Starling et al. (2011) analysed combined BAT+XRT data until 737 s after the trigger and derived blackbody temperatures, data that we used in the following analysis. Temperature and radius over time are shown in Fig. 3.4. The decrease in temperature and the increase in radius are both trends that are consistent with the cooling of the envelope due to expansion and, thus, with the explosive scenario.

The temperature and radius of an expanding envelope that is cooling adiabatically have been theoretically shown to evolve as power laws (Waxman et al., 2007; Nakar and Sari, 2010). We therefore fit power laws to the decay and rise of temperature and radius to the combined data presented here and in Starling et al. (2011). The expression $T_{\mathrm{BB}}(t) = T_i - \kappa t^\delta$ was fitted to the evolving temperature (solid line in the upper panel of Fig. 3.4), which gave a decay index of $\delta = 0.3 \pm 0.2$ for an initial temperature of $T_i = 0.17 \pm 0.04$ keV with $\chi_\mu{}^2 = 0.8$, where κ is the normalisation of the power law.

A model of the form $R_{\mathrm{BB}}(t) = R_0 + \upsilon t^\gamma$ was employed to fit the radius measurements. In the case of linear expansion, i.e., $\gamma = 1$, the radius grows at a mean velocity of $\upsilon \approx 8,000$ km s^{-1} between BAT+XRT (until 737 s) and GROND observations (at $42-54$ ks after the burst). When γ was allowed to vary, we obtained a growth index of $\gamma = 1.4 \pm 0.3$ and an initial radius of $R_0 = (7.0 \pm 0.9) \times 10^{11}$ cm with $\chi_\mu{}^2 = 1.1$ (solid line in the lower panel of Fig. 3.4). The resulting radius is slightly larger than the size of WR stars ($\sim 10^{11}$ cm; Cappa et al., 2004), which are thought to be the progenitors of long-duration gamma-ray bursts and type-Ic SNe (Woosley et al., 2002). Because of this, the initial emission radius of the thermal component might indicate the position at which a preexisting dense wind surrounding the progenitor becomes optically thin (e.g., Campana et al., 2006; Soderberg et al., 2008b; Balberg and Loeb, 2011). From the theoretical point of view, it is $\gamma = 0.8$ (Waxman et al., 2007), although, the data do not favour this solution delivering $\chi_\mu{}^2 = 8$ (dotted line in the lower panel of Fig. 3.4).

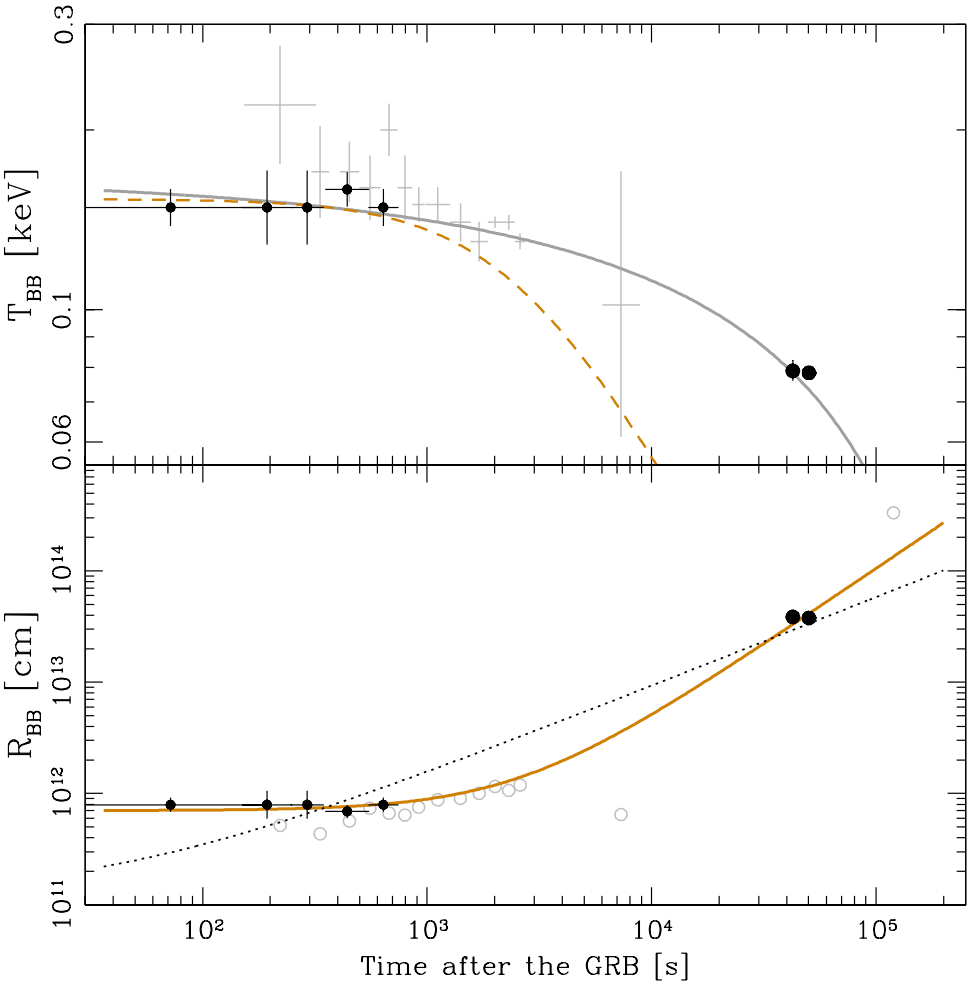

Figure 3.4. Temperature and radius evolution of the blackbody component. Black data points are those derived using combined BAT+XRT data (Starling et al., 2011) plus the temperature determinations using GROND data ($\approx$ 46 ks). The first data bin from Starling et al. (2011) represents the interval from -175 to 144 s, however, due to fitting and plotting purposes, here it corresponds to $0-144$ s. Solid, dashed and dotted lines are different power-law models (see main text). Best fits to temperature and radius are shown in grey and brown solid lines, respectively. Grey crosses (upper panel) and open circles (lower panel)) are measurements of XRF 060218/SN 2006aj taken from Kaneko et al. (2007) and Campana et al. (2006), respectively.

For an assumption of adiabatic cooling, the luminosity must be constant and was fixed to $L_{\rm BB} = 3.5 \times 10^{45}$ erg s^{-1}, value derived from early-time X-ray measurements (Starling et al., 2011). Assuming the best-fit model for the radius evolution from the previous paragraph, we computed the evolution of the adiabatic temperature as $T_{\rm BB} = (4\pi\sigma\, L_{\rm BB}^{-1}\, R_{\rm BB}^{2}\,)^{-1/4}$, which is shown by the dashed line in the upper panel of Fig. 3.4. This model is clearly inconsistent with our data set; however, it indeed shows consistency with the XRF 060218/SN 2006aj data set (grey crosses in the upper panel of Fig. 3.4; from Kaneko et al. 2007). Since the blackbody luminosity changes to $4-6 \times 10^{47}$ erg s^{-1} in our late-time measurements, the assumption of a constant luminosity is invalid and inconsistent with the late-time temperature determination. This result implies that either the cooling is not strictly adiabatic for which energy injection from the inner core is needed, or $T_{\rm BB}$ and $L_{\rm BB}$ are overestimated by our modelling procedure,

or underestimated by Starling et al. (2011).

3.4 Multicolour Evolution of SN 2010bh

We now present the entire GROND data set, which includes data in seven different bands covering the wavelength range from 380 to 2300 nm. Photometry was corrected for host-galaxy extinction computed at the end of §3.3.2. In addition, the AG component derived in §3.3.1 was subtracted from the data. Assuming a power-law decay for the optical AG with $\alpha = -1.3 \pm 0.2$ computed from the contemporaneous X-ray data, a flux and its corresponding uncertainty were derived from the power-law model fitted to the early SEDs for each epoch. We note however that typically $\alpha_X \neq \alpha_{\rm opt}$. The correction for the AG contribution is more significant at earlier times and in redder bands and it has a lower significance at around maximum brightness for all bands.

3.4.1 Optical and Near-Infrared Light Curves

Figure 3.5 shows the light curves in the optical $g'r'i'z'$ and the NIR JH bandpasses. The $g'r'i'z'J$ light curves show the usual pattern of SE SNe: the redder the filter, the later and broader the peak. The H band peaks a few days earlier than J, although given the large uncertainties, the time difference is insignificant. The $K_{\rm s}$ band shows no credible detections in any of our observations down to limits in the range of 18.4 – 18.9 mag (AB system) despite our observations covering the expected peak of the SN (10.5 – 25.5 d after the burst). In the following section, we analyse our data of SN 2010bh, one of the best-observed GRB-SNe to date, and compare the light curve with those of other SNe connected to GRBs.

3.4.2 Colour Evolution

Six GROND colour curves are presented in Fig. 3.6 to analyse the colour evolution of SN 2010bh. Most colours show drastic evolution, where the cooling of the SN photosphere is evident as colours become redder. Non-significant variations over time are shown in $r' - i'$ and $J - H$ colours.

3.4.3 Comparison with SN 1998bw

To study the luminosity evolution of SN 2010bh to other SNe, we fit SN 1998bw templates as described in §2.3.3. Given that the early blue emission is inconsistent with the templates even after subtraction of the AG component derived in §3.3.1, an empirical power-law component was required (dashed in Fig. 3.5). The power-law slope was fixed to $\alpha = -1.3$. Leaving α free did not improve the fit and different values of α only negligibly affected the stretch and luminosity ratios derived for the SN component. Table 3.2 summarises the results of fitting the SN 1998bw templates and the empirical power-law to the GROND data. The overall fits are shown in Fig. 3.5 for each band using solid lines.

Luminosity ratios listed in the first line of Table 3.2, which include the uncertainty in $A_{V,\rm host}$, reflect differences between the colours of SN 2010bh and those of SN 1998bw. The g' band is as bright as SN 1998bw and, as a rough comparison, disagrees with the fainter B-band results from Cano et al. (2011b) at the 5σ confidence level after including the uncertainty in their extinction determination. Our $r'i'$ luminosity ratios are also larger than previously reported from optical photometry of SN 2010bh ($k \approx 0.4 - 0.5$; Cano et al., 2011b) mainly owing to the use of a

Table 3.2. Fits of SN 1998bw templates to SN 2010bh.

	g'	r'	i'	z'	J	H	K_s
SN amplitude (k) [a]	1.10 ± 0.12	0.65 ± 0.05	0.54 ± 0.04	1.25 ± 0.07	0.69 ± 0.07	0.63 ± 0.08	< 1.4
Stretch factor (s)	0.77 ± 0.01	0.78 ± 0.01	0.65 ± 0.02	0.73 ± 0.02	0.84 ± 0.04	0.67 ± 0.07	$\cdots$
Peak delay ($t_{\rm delay}$) [b]	-3.3	-3.2	-2.6	-0.4	-1.0	0	$\cdots$

[a] For AG-subtracted and host-extinction-corrected data ($A_{V,\rm host} = 1.2 \pm 0.1$ mag).
[b] Relative to maximum luminosity of SN 1998bw after applying a time offset due to the stretch factor.

different extinction correction. There is certainly some intrinsic blue excess in the g' band, although the difference from the r' band of 40% has a rather large uncertainty of 13%. Higher luminosities at bluer wavelengths indicate that the photosphere has a higher temperature at its peak luminosity than that of SN 1998bw. Given that the expanding atmospheres of SNe cool down over time and SN 2010bh peaks about a week earlier than SN 1998bw in g', it is a natural conclusion that it must be hotter at maximum brightness. It is also possible that a g'-band peak as early as 8 d after the trigger still contains a non-negligible contribution from the cooling shock breakout. We also note that the z'-band luminosity ratio is much larger than in the other

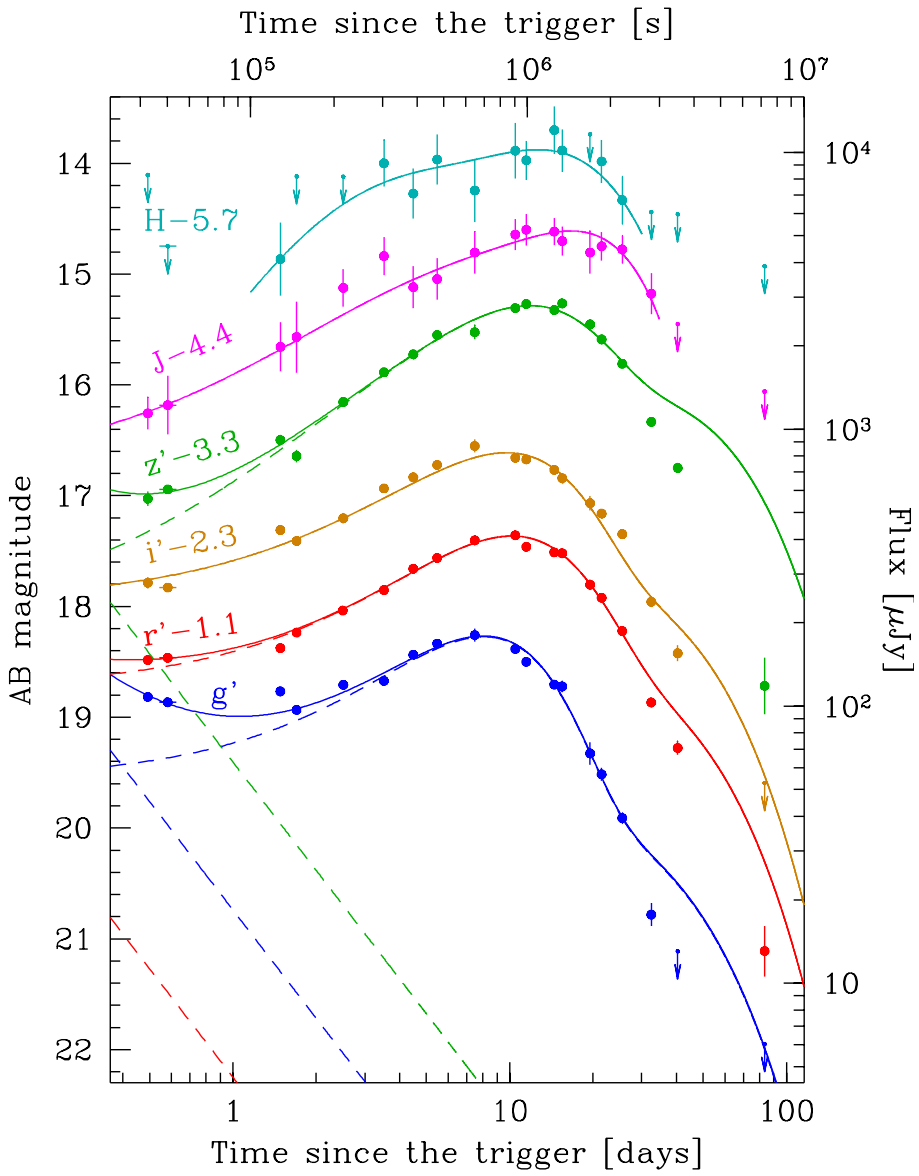

Figure 3.5. Multicolour light curves corrected for host-galaxy extinction and AG-subtracted. Filled circles represent detections and arrows are upper limits. Solid lines represent the overall fits and dashed lines individual components. Fits of SN 1998bw templates are extrapolated from $\approx t_0 + 60$ d. For reasons of clarity, light curves were shifted along the magnitude axis and the systematical error in $A_{V,\mathrm{host}}$ was not added to the error bars.

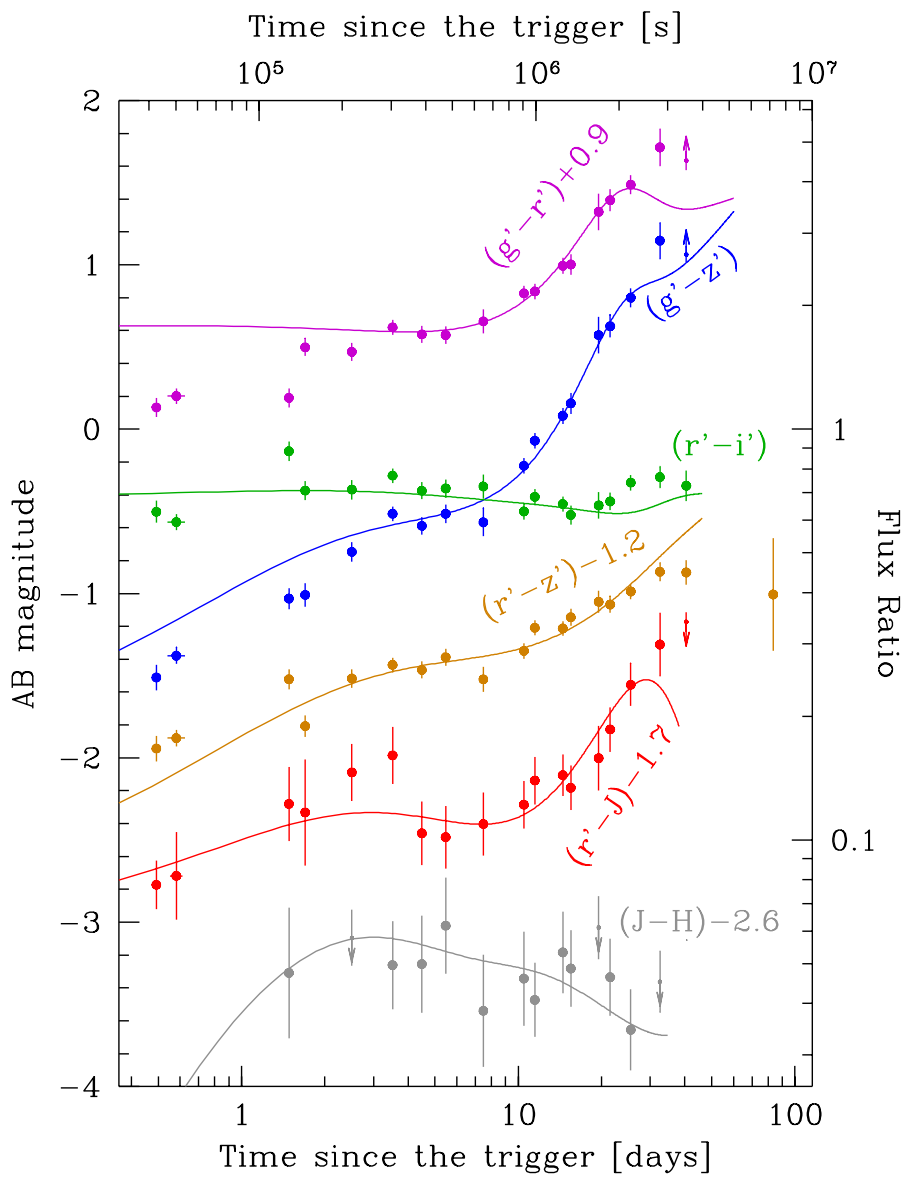

Figure 3.6. Colour curves corrected for host-galaxy extinction and AG-subtracted. Filled circles represent detections in both filters and arrows are upper limits derived from detections in a single band. Solid lines represent the colour evolution of SN 1998bw derived from the light-curve fits in §3.4.3. For clarity, error bars do not include the systematic error in $A_{V,\mathrm{host}}$ and upper limits of the last epoch are not shown.

bands; it is brighter than SN 1998bw at the 3σ confidence level. After inspection of the spectra around maximum light presented by Bufano et al. (2011), the Ca II λ8579 emission line was found to contribute roughly 2 – 4% to the continuum flux integrated in the z'-band sensitivity range (8254 – 9528 Å). The contribution of this spectral feature is not enough to account for the excess of 45% in the z' band relative to the infrared. The discrepancy is therefore attributed to the systematical uncertainties introduced when extrapolating the $UBVRI$ data from Galama et al. (1998b) to construct the templates of SN 1998bw. In summary, the luminosity of SN 2010bh is a factor 0.5 – 0.7 fainter than SN 1998bw in optical $r'i'$ bands and 0.6 – 0.7 in NIR

JH bands. We also note that at late times SN 2010bh fades more rapidly in the optical than SN 1998bw did, although the fluxes if the templates were extrapolated after $\approx t_0 + 60$ d.

The stretch factors listed in the second line of Table 3.2 range from 0.6 to 0.8 and are at the low end of the GRB-SNe distribution (see figure 5 of Ferrero et al., 2006). These are also consistent with the findings by Cano et al. (2011b) for SN 2010bh. The optical light curves are wider than the stretch factor suggests, or in other words, the stretch factor predicts later peak times for the optical light curves. To account for this, $t_{\rm delay}$ shifts the templates to earlier times by about three days in $g'r'i'$, which means that the optical light curves of SN 2010bh peak even earlier than the stretch factor suggests. After the inclusion of the delay parameter $t_{\rm delay}$, the stretch factors now solely represent the width of the light curves and not the time of the maximum brightness compared to SN 1998bw. Moreover, peak times of roughly $8-9$ d in the $g'r'$ bands (equivalent to the V in the Johnson filter system) corresponds to the earliest and fastest light curves of GRB-SNe observed to date (see table 2 of Richardson, 2009).

Offsets in peak time, in our case represented by $t_{\rm delay}$, can be explained as the result of delayed BH formation (Vietri and Stella, 1999). In this scenario, the XRF might be triggered by the core collapse of the progenitor to a NS star, soon after which accretion holds. The supernova would then occur after the further collapse of the NS into a BH. The delay could be of the order of months or years or perhaps as short as hours (see Zeh et al., 2004). Nevertheless, the time delay here is negative and it is much more plausible that the comparison of light-curve morphology to SN 1998bw may need more than two parameters to be accurate.

Fits of SN 1998bw templates were used to study the colour evolution of SN 2010bh in detail as presented in Fig. 3.6, where the curves are shown without the empirical AG component. From the first two data points, it is clear from the $g'-r'$ and $g'-z'$ colours that there is a blue component that cannot be modelled by the templates and is interpreted as the shock breakout in §3.3.1. From these two colours, it is also possible to see that SN 2010bh becomes red faster than SN 1998bw did. The $r'-i'$ and $J-H$ colours remain roughly constant, which shows that the changes occur on a broader wavelength scale. The standard colour evolution from blue to red is shown by $r'-z'$ and $r'-J$, which at late times evolve bluer and redder than SN 1998bw templates, respectively.

3.4.4 Comparison with SN 2006aj

We now compare results from optical data by Ferrero et al. (2006), who used the same technique and templates to get the luminosity and stretch factors for SN 2006aj. They computed luminosity ratios in the range $0.62-0.76$, which are approximately in the same range as SN 2010bh without considering the measurements in $g'z'$. Their stretch factors ranged from about 0.62 to 0.69, which makes the SN 2010bh optical light curves wider than those of SN 2006aj. In contrast to the definition of the stretch factor, namely that earlier peak times tend to correspond to a narrower light curve, peak times are earlier in the case of SN 2010bh. Whilst the BV photometry for SN 2006aj peaked roughly 9 and 11 d after the burst, respectively, the $g'r'$ photometry for SN 2010bh peaks approximately 8 and 9 d after trigger, respectively. This supports the statement that SN 2010bh has evolved more rapidly than any other GRB-SNe, given that SN 2006aj had the fastest evolution until the discovery of SN 2010bh. The JH light curves of SN 2006aj (Cobb et al., 2006; Kocevski et al., 2007) are scaled to the luminosity distance of SN 2010bh for comparison. After the host-extinction correction, SN 2010bh turns out to be as bright as SN 2006aj in the NIR as well. Hence, SN 2010bh is similar to SN 2006aj in terms of light-curve shape and luminosity.

3.5 Bolometric Light Curve

The bolometric light curves of SNe are an essential tool for examining global luminosity features and enable us to compare with other SNe and theoretical models. However, it is difficult to obtain such a light curve because of the limited information at UV and infrared wavelengths. Only a *quasi*-bolometric light curve can be constructed by using a broad spectral coverage to derive a total flux that is then used as a proxy of the bolometric flux. To accomplish this task, we employed the wavelength range covered by our $g'r'i'z'JH$ filters, i.e., from 380 to 1800 nm.

In the case of SN 2010bh, there are no UV constraints. In the following description, no attempts at correcting for the UV flux were made. By using the AG-subtracted $g'r'i'z'JH$ photometry corrected for host-galaxy extinction, monochromatic fluxes for each bandpass were derived. Sets of three bandpasses were defined to interpolate their corresponding monochromatic fluxes using the Simpson's rule. The second-degree polynomial result of the interpolation was then integrated over frequency in the range of each set of bandpasses. Finally, the total flux in the range from 380 to 1800 nm was determined by adding up the integrated fluxes of all sets of bandpasses. The total flux is transformed to a quasi-bolometric luminosity using a distance of 240 ± 17 Mpc to the host galaxy of SN 2010bh (see §3.3.1 for more details). No attempts of extrapolation beyond the limits of the g' and the H bandpasses were made. Corrections for the NIR flux at late times were found to be the most significant. The data at $t_0 + 30.7$ d (rest frame) were corrected for the H-band non-detection by assuming that the fraction of H-band flux compared to the total bolometric flux remains constant at 8% starting from $t_0 + 24.1$ d. Similar corrections were performed for JH non-detections at 38.6 and 78.8 d after the burst under the assumption of a constant JH flux fraction of 27% at $t_0 + 30.7$ d. Results are shown in Fig. 3.7 along with quasi-bolometric light curves from SE and other GRB-SNe.

The analysis of the quasi-bolometric light-curve morphology yields a peak luminosity of 4.3×10^{42} erg s^{-1} at about 8 d after the trigger (equivalent to $M_{bol} \approx -17.87$), i.e., approximately two times fainter and six days sooner than for SN 1998bw. Our luminosity is 16% higher than that computed by Cano et al. (2011b), although consistent to within our 11% of uncertainty. Whilst the early peak of SN 2010bh correlates with its narrowness and low luminosity, this is the case for neither the entire GRB-SNe sample nor the local sample of SE SNe (Zeh et al., 2004; Richardson et al., 2006; Richardson, 2009). The morphology of the light curve is similar to that of SN 2006aj (Pian et al., 2006), although 21% fainter. The peak time also resembles that of the type-Ic SN 1994I (Richmond et al., 1996), although SN 2010bh has a much wider light curve, which is 77% brighter at maximum. In terms of peak luminosity, SN 2010bh is similar to the BL Ic SN 2009bb (Pignata et al., 2011). It also underwent the most dramatic late-time decay in the sample, which implies that its envelope became rapidly optically thin to γ-rays. The last statement is supported by the extremely high expansion velocities measured for SN 2010bh of the order of 30,000 km s^{-1} (Chornock et al., 2010a). Another clear feature is the sudden decrease in luminosity at around $t_0 + 30$ d, which contrasts with the smooth decay in the comparison SNe at similar stages. This indicates either that the atmosphere becomes rapidly optically thin or that the assumption of a constant NIR contribution after $\approx t_0 + 31$ d underestimates the flux in the JH bands.

3.5.1 Physical Parameters of the Explosion

We followed the approach described in Valenti et al. (2008) to derive the physical quantities that characterise the explosion, i.e., we modelled the early and late light curves separately. The early-time phase corresponds to the photospheric regime for which the analytical model

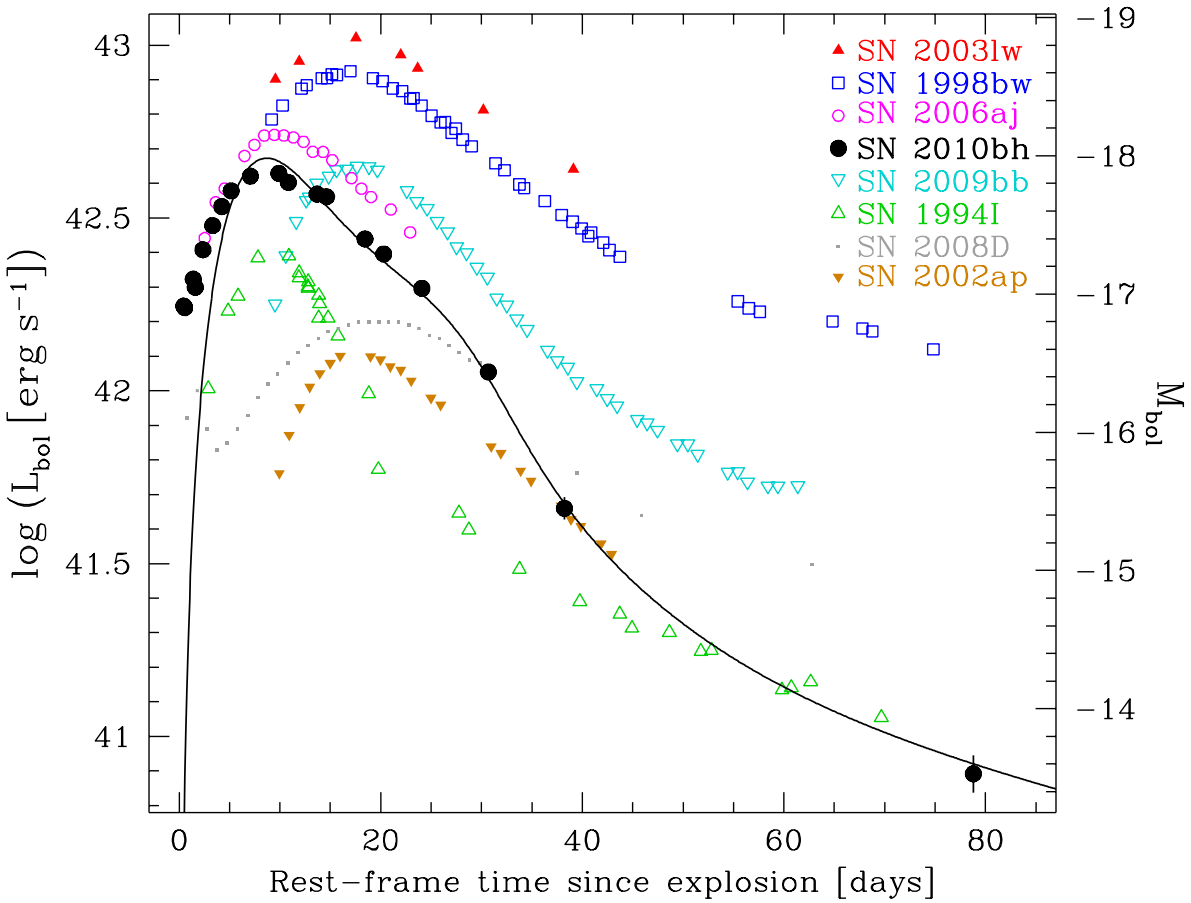

Figure 3.7. Quasi-bolometric light curve of SN 2010bh produced by using GROND $g'r'i'z'JH$ filters (black open circles) in the rest frame. A single black continuous line represents the best-fit model. Early and late components of the model are smoothly joined at $t_0 + 30$ d. SE and other GRB-SNe quasi-bolometric light curves have been plotted as a comparison sample: SN 2003lw (GRB 031203; Malesani et al., 2004), SN 1998bw (GRB 980425; Galama et al., 1998b), SN 2006aj (GRB 060218; Pian et al., 2006), the BL Ic SN 2009bb (Pignata et al., 2011), the type-Ic SN 1994I (Richmond et al., 1996), the type-Ibc SN 2008D (XRO 080109; Modjaz et al., 2009; Soderberg et al., 2008b), and the type-Ic SN 2002ap (Gal-Yam et al., 2002; Foley et al., 2003; Yoshii et al., 2003).

developed by Arnett (1982) has been adopted, initially used for SNe Ia and adapted to SE SNe (e.g., Taubenberger et al., 2006; Valenti et al., 2008; Pignata et al., 2011; Benetti et al., 2011). At late stages, the atmosphere becomes nebular, i.e., optically thin, and the emitted luminosity is powered by the energy deposition of: (1) γ-rays from ^{56}Co decay, (2) γ-rays from electron-positron annihilation, and (3) the kinetic energy of the positrons (see appendix A in Valenti et al., 2008). However, Maeda et al. (2003) noted that the two-component configuration leads to inconsistencies between the parameters derived from fitting the early and late light curves of SNe Ic, caused mainly by the model limitations in varying the γ-ray trapping over time. To enable low and high γ-ray trapping at early and late times, respectively, Maeda et al. (2003) divided the ejecta into a high-density inner region and a low-density outer region. The emission from the outer region dominates the total emission in the optically thick regime at early times, and that from the inner region, which has a higher γ-ray opacity, dominates in the nebular phase at late times. Here, we use the same procedure to model the $g'r'i'z'JH$ quasi-bolometric light

curve of SN 2010bh.

Given the model explained above, a total of four free parameters were used to fit the quasi-bolometric light curve of SN 2010bh: the total mass of ^{56}Ni produced in the envelope $M_{\rm Ni}$, the total ejecta mass $M_{\rm ej}$, the fraction of mass in the inner component f_M, and the fraction of kinetic energy in the inner component f_E. The kinetic-energy-to-ejected-mass ratio of the outer region was fixed by using its correlation with photospheric velocity at peak luminosity (Arnett, 1982)

$$\upsilon_{\rm ph}^2 \approx \frac{3}{5}\,\frac{2E_{\rm k,out}}{M_{\rm ej,out}}. \tag{3.3}$$

This expression assumes that the density of the ejecta is homogeneous and that the inner component does not contribute to the emitted luminosity in the optically-thick regime. Since the photospheric velocity was not available directly from observations, the velocity measured by fitting P-Cygni line profiles was used as a proxy of $\upsilon_{\rm ph}$. However, the envelope layer where the blue-shifted absorption line forms does not necessarily coincide with the position of the photosphere, as found when measuring different expansion velocities from absorption lines of different species. The spread can amount to several hundreds km s^{-1} (see Jones et al. 2009 for an example of type-II SNe). For the spectra of SN 2010bh, Chornock et al. (2010a) obtained velocities of about 35,000 and 26,000 km s^{-1} from the Si II λ6355 feature roughly 21 and 6 d after the burst, respectively. Since there is no measurement at the time of maximum light, which is about 8 – 9 d after the trigger, a range of expansion velocities was used in the modelling. Assuming that the photosphere lies at deeper layers than those where lines are formed and recedes in mass exposing deeper and slower layers, in the modelling we employed photospheric expansion velocities of 2.5, 2.8, and 3.1 $\times 10^4$ km s^{-1}. Other physical and mathematical quantities such as opacity and integration constants were chosen to be the same as in Cano et al. (2011b).

Our fitting procedure consisted of two steps. First of all, we modelled the data around maximum luminosity ($5 < t - t_0 \leq 30$ d) using the Arnett's model, assuming that only the outer component contributes to the total luminosity at this stage. We then obtained $M_{\rm Ni,out}$ and $M_{\rm ej,out}$. Secondly, we modelled the late-time data ($t - t_0 > 30$) using the nebular-phase components of Valenti et al. (2008) assuming that both the inner and outer regions contribute to the total emitted luminosity. Here, we fixed $M_{\rm Ni,out}$ and $M_{\rm ej,out}$ to the values obtained in the first step of the fitting procedure and only f_M and f_E were allowed to vary.

From the above modelling scheme, our best-fit parameters were $M_{\rm Ni,out} = (0.135 \pm 0.001)\,{\rm M}_\odot$, $M_{\rm ej,out} = 2.37 - 2.90\,{\rm M}_\odot$, $f_M = 0.36 \pm 0.04$, and $f_E = 0.11 - 0.15$ for the three selected expansion velocities at the photosphere. All of these results combined together provided the total masses and energy of the explosion listed in Table 3.3 (statistical errors only). The ^{56}Ni mass is independent of the chosen expansion velocity at the photosphere, $M_{\rm Ni} = (0.21 \pm 0.03)\,{\rm M}_\odot$, given that it is proportional to the luminosity. In contrast, since the ejected mass changes significantly, the weighted mean and the RMS of the results of the three models in Table 3.3 were employed to compute a final value of $M_{\rm ej} = (2.60 \pm 0.23)\,{\rm M}_\odot$. The total kinetic energy and energy fraction were derived in the same way, implying that $E_{\rm k} = (2.4 \pm 0.7) \times 10^{52}$ erg and $f_E = 0.12 \pm 0.02$.

Using comparable independent data, Cano et al. (2011b) followed a similar procedure to derive physical quantities from quasi-bolometric data. Whilst our values for $M_{\rm ej}$ are consistent with those in Cano et al. (2011b) to within 1.5σ, they found that $M_{\rm Ni} = (0.10 \pm 0.01)\,{\rm M}_\odot$ for SN 2010bh, which is two times lower than our value. The discrepancy affects the determination of the kinetic energy as well, which is connected in Eq. 3.3 to $\upsilon_{\rm ph}$ and $M_{\rm ej}$. The causes of these inconsistencies are: (1) the host-galaxy extinction employed, which is $E(B-V)_{\rm host} = 0.39 \pm 0.03$

Table 3.3. Physical parameters of the explosion with a varying expansion velocity.

$v_{\rm ph}$ [km s^{-1}]	$M_{\rm Ni,out}$ [M$_\odot$]	$M_{\rm ej,out}$ [M$_\odot$]	f_M	f_E	$M_{\rm Ni}$ [M$_\odot$]	$M_{\rm ej}$ [M$_\odot$]	$E_{\rm k}$ [10^{52} erg]
25,000	0.135 ± 0.001	1.52 ± 0.05	0.36 ± 0.02	0.15 ± 0.03	0.21 ± 0.02	2.37 ± 0.10	1.85 ± 0.09
28,000	0.135 ± 0.001	1.70 ± 0.05	0.36 ± 0.04	0.13 ± 0.07	0.21 ± 0.03	2.64 ± 0.14	2.52 ± 0.22
31,000	0.135 ± 0.001	1.87 ± 0.06	0.36 ± 0.02	0.11 ± 0.02	0.21 ± 0.02	2.90 ± 0.12	3.37 ± 0.13

mag in our case and 0.18 ± 0.08 mag in Cano et al. (2011b); (2) the inclusion of an inner component hidden at optically thick stages, which increases the ^{56}Ni mass by a factor of f_M; and (3) the choice of different expansion velocities of the photosphere. Furthermore, even when including the uncertainties in the host-extinction determination, which are $\sigma_{M_{\rm Ni}} \sim 0.02$ both here and for Cano et al. (2011b), the discrepancy persisted. Nevertheless, evidence for the existence of a dense inner layer of $0.94 \pm 0.15\,{\rm M}_\odot$ is provided and supported by the sub-luminous post-maximum phase of SN 2010bh, which is indicative of a high trapping of γ-rays.

The large amount of ^{56}Ni produced is consistent with the class of SN associated with GRBs, but also matches the value derived for the highly energetic type-Ic SN 2004aw (Valenti et al., 2008), which in contrast had a much broader light curve that varied more slowly with time. Most interestingly, SN 2010bh resembles SN 2006aj in terms of light-curve shape. The ^{56}Ni mass produced in the explosion is practically the same (Mazzali et al., 2006a), whilst the ejected mass is 20% higher for SN 2010bh and the total kinetic energy is significantly different ($\sim 2\times10^{51}$ erg in the case of SN 2006aj). This ensures that SN 2010bh is remarkable in terms of expansion velocity, which has been one of the greatest ever measured (Chornock et al., 2010a).

We note that the end of the optically-thick regime and the beginning of the nebular phase cannot be accurately defined. The rule of thumb is that the photospheric phase ends 30 d after explosion at the earliest and that the nebular phase starts 60 d after the explosion at the latest. Since Arnett's model fits our data relatively well until day 30, it is defined as the end of the optically-thick era. Nevertheless, we are unable to clearly establish whether the period between 30 and 60 d after the burst corresponds to the nebular phase already, as the ejecta are most probably neither completely thick nor sufficiently thin.

The model reproduces the luminosity at maximum brightness and thereafter, despite under-predicting the luminosity during the rising phase. This is because the light curve is dominated by shock-breakout emission at early stages. The same is obtained in §3.4, when trying to fit templates of SN 1998bw to our multicolour light curve, where an extra component for the shock breakout is required. The light curves of SN 2010bh peak so early that an even more rapid evolution than observed is expected after maximum luminosity. This early-wide peak dichotomy could be explained by the ^{56}Ni distribution in the envelope. If there were more ^{56}Ni produced near the surface, the peak would be early and wide, i.e., the SN would rise more slowly but much earlier. In contrast, if the ^{56}Ni were concentrated towards the centre, it would lead to a much later peak, although sharper rise, producing a narrower shape of the maximum (M. Bersten, 2010, private communication; Nomoto et al. 2010).

3.6 Conclusions

Spanning a time range from 12 hours to 83 days after the trigger and covering from 190 to 2300 nm in wavelength (see Sect. 3.2), we have presented UV/optical/NIR photometric data of XRF 100316D/SN 2010bh. Given the results introduced and discussed in Sect. 3.3, 3.4, and 3.5, we have drawn the following conclusions:

- Broad-band SEDs at early times demonstrate the existence of red and blue components identified as synchrotron emission from the XRF AG and the cooling envelope after shock breakout, respectively.
- A significant amount of dust along the line of sight through the host galaxy ($A_{V,\rm host} = 1.2 \pm 0.1$ mag) is consistent with the two-component SED model and agrees with the faint detections at UV wavelengths.

- By comparing with earlier X-ray results from Starling et al. (2011), we have demonstrated that the temperature of the blackbody component decreases with time, which is consistent with a scenario of a cooling expanding atmosphere.

- By performing an additional analysis of the thermal component and the earlier X-ray measurements we have measured expansion velocities that are consistent with SN expansion and an initial apparent emission radius of 7×10^{11} cm. This radius is slightly larger than the size of WR stars, which are the most likely GRB-SNe progenitors. If a WR star were the progenitor of XRF 100316D/SN 2010bh, then the initial radius could indicate that there was a massive dense stellar wind surrounding the progenitor.

- Our multicolour light curves after host-galaxy correction and subtraction of the AG component, have peak $r'i'$ luminosities of about $0.5-0.7$ times that of SN 1998bw and consistent with those of SN 2006aj. Similarly the NIR luminosity at maximum is as bright as SN 2006aj and $0.6-0.7$ times that of SN 1998bw. The excess in the g' band indicates that SN 2010bh has a hotter photosphere than that of SN 1998bw at the time of maximum brightness.

- We have found that SN 2010bh is the most rapidly evolving GRB-SNe to date, reaching maximum luminosity $8-9$ days after the burst in the $g'r'$ bands. At late times, it also fades more rapidly than SN 1998bw showing redder colours as well. This behaviour is also evident in the bolometric light curve, which decays faster than for any SN in the comparison sample.

- The physical parameters of the explosion are derived by means of the quasi-bolometric light curve constructed from our $g'r'i'z'JH$ photometry. The modelling is performed using Arnett's model (Arnett, 1982) for data around peak and standard γ-ray deposition at later times. A high-density inner component with roughly 26% of the total mass is required to reproduce the flux ratio between maximum luminosity and tail. The total mass of ^{56}Ni produced in the envelope is $M_{\rm Ni} = 0.21 \pm 0.03\,{\rm M}_\odot$, which precisely matches the value derived for SN 2006aj, whilst the total ejecta mass of $M_{\rm ej} = 2.6 \pm 0.2\,{\rm M}_\odot$ exceeds the value for SN 2006aj by 20%. However, the kinetic energy turns out to be higher at $E_k = (2.4 \pm 0.7) \times 10^{52}$ erg, making SN 2010bh the second most energetic GRB-SN after SN 1998bw.

The association between XRF 100316D and SN 2010bh is particularly interesting, since for the second time the cooling of the shock breakout has been detected in a GRB-SN. It is also unique in revealing a hot component that possibly contributes even at blue maximum brightness, one of the largest host-galaxy extinctions measured for this kind of transient, and the fastest rise among GRB-connected SNe.

Chapter 4

SN Constraints for GRB 090424

4.1 Introduction

The connection between GRBs and SNe has been extensively studied by both observers and theoreticians (see Woosley and Bloom, 2006, for a review). The collapsing core of a very massive star, whose envelope has been blown by its own stellar winds, induces the formation of a relativistic jet that will produce a gamma rays. When it collides with the circumstellar material, the jet will produce a multi-wavelength AG. In theory, the energy of the core collapse should be also capable of making the remaining envelope expand. However, it is not clear how this happen, or even if there is enough energy for a SN explosion.

During the late 1990s we witnessed the first conclusive proof supporting the GRB/SN connection. The soft GRB 980425 was detected by both BeppoSAX and BATSE with a precision of $8'$ (Galama et al., 1998a; Kippen, 1998). A couple of days later SN 1998bw was discovered as a young supernova (Galama et al., 1998b; Sadler et al., 1998), that exploded inside the error circle of GRB 980425 in the under-luminous late-type galaxy ESO184–G82 ($z = 0.0085$; Tinney et al., 1998). Initially controversial (Galama et al., 1998b; Pian et al., 1998), the physical association between these objects was based on temporal and spatial grounds, supported by the slowly variable X-ray source at the position of the SN (Pian et al., 2000). Nowadays the coincidence between GRB 980425 and SN 1998bw is widely accepted (Kouveliotou et al., 2004), mostly due to the spectroscopic evidence for SN 2003dh (Hjorth et al., 2003; Kawabata et al., 2003; Stanek et al., 2003) associated to GRB 030329, the brightest burst HETE-2 had ever detected. Since then attempts of finding the SN signal at the position of nearby ($z < 1$) GRBs have become usual.

Using data from GROND, the Very Large Telescope (VLT), the *Swift*/UVOT, and the *Swift*/XRT, I carried out a multi-wavelength analysis of the nearby GRB 090424 in search of a SN signature. Observations, data reduction and calibration are summarised in §4.2, while in §4.3 the main results are gathered. In §4.4 I discuss the results by comparing GRB 090424 and its host galaxy with other long GRBs and GRB/SN associations. Finally, I summarise the conclusions in §4.5.

4.2 Observations

4.2.1 Prompt Emission

On the 24th of April 2009 at t_0 = 14:12:09 UT the BATe on board the *Swift* satellite was triggered (Cannizzo et al., 2009). GRB 090424 started off showing several bright peaks between $t_0 - 2$ and $t_0 + 5$ s, and then several weaker and broader peaks at $t_0 + 7$, $t_0 + 15$, and $t_0 + 50$ s (Sakamoto et al., 2009). The total duration was about 150 s with a T_{90} (in the energy range 15 – 350 keV) of 48 ± 3 s (estimated error including systematics; Sakamoto et al., 2009). The peak count rate was $\sim 50,000$ counts per second (15 – 350 keV), at ~ 3 s after the trigger.

The Gamma-ray Burst Monitor (GBM) on board of the *Fermi* satellite (Meegan et al., 2009) detected the burst as well, triggering 236 s before *Swift*/BAT (Connaughton, 2009). The duration (T_{90}) was about 52 s in the energy range from 8 keV to 1 MeV. A Band function (Band et al., 1993) with $E_{\rm peak} = 177 \pm 3$ keV, $\alpha = 0.90 \pm 0.02$, and $\beta = -2.9 \pm 0.1$ fits best the time-averaged spectrum of the main spike from $t_0 - 0.3$ to $t_0 + 5.5$ s. The event fluence (8 – 1000 keV) over the entire event is $(5.2 \pm 0.1) \times 10^{-5}$ erg cm^{-2}.

4.2.2 The Afterglow

The *Swift*/XRT (Burrows et al., 2005) and the *Swift*/UVOT (Roming et al., 2005) started observing about 1.5 min after the trigger, and immediately found both an AG candidate (Cannizzo et al., 2009). The final XRT position enhanced by UVOT placed the AG at coordinates R.A.(J2000) = $12^h38^m5^s.09$, Dec.(J2000) = $+16°50'15''.7$, with an uncertainty of 1.4 arcsec (Goad et al., 2009). The X-ray AG was pretty bright ($\sim$ 100 counts per second at maximum luminosity), and detectable by XRT until 15 days after the burst. XRT data were obtained from the public *Swift* archive and reduced in the standard manner using the `xrtpipeline` task from the HEAsoft package, with response matrices from the most recent `CALDB` release. XRT data was used in photon counting mode and obtained from the XRT light curve repository (Evans et al., 2007, 2009). Spectra were grouped using the `grppha` task. UVOT photometry has been acquired following Poole et al. (2008). As UVOT operates through filter cycles, the measurements had to be interpolated to a common epoch, procedure detailed in Schady et al. (2010).

Shortly after the trigger the optical counterpart was confirmed by ROTSE-IIIa (Yuan, 2009). As noticed by Evans and Holland (2009), there is an extended SDSS source inside the XRT position, $\sim$ 1 arcsec away from its centre, and with a photo-z of 0.26. Soon an absorption redshift of $z = 0.544$ was reported by Chornock et al. (2009) and later confirmed by Wiersema et al. (2009). In the standard ΛCDM model of the universe ($\Omega_M = 0.27$, $\Omega_\Lambda = 0.73$) with $H_0 = 74.2$ km s^{-1} Mpc^{-1} (Riess et al., 2009) a luminosity distance of 2992 Mpc is computed for this redshift.

The multichannel imager GROND (Greiner et al., 2007, 2008), mounted at the MPG/ESO 2.2m telescope on La Silla, Chile, started observations of GRB 090424 in $g'r'i'z'JHK_{\rm s}$ filters simultaneously $\approx$ 12.5 hours after the GRB trigger at a average seeing of $\approx$ 1 arcsec. A variable source was detected in all seven bands (Olivares E. et al., 2009b) using the automated GROND pipeline (Küpcü-Yoldaş et al., 2008), with a 0.75-arcsec offset from the XRT/UVOT position and 0.31 arcsec away from the SDSS source.

The Focal Reducer/low dispersion Spectrograph (FORS2; Appenzeller et al., 1998), mounted on the Cassegrain focus at the VLT/Antu (Unit Telescope 1), started observations of the GRB field on the 1st of May 2010 at 01:54 UT, approximately 6.5 days after the burst. A total of seven epochs of imaging in the R and I bands were obtained until July 5, 2010. The photometric

data was used in order to complement GROND observations.

GROND and VLT data for this burst were reduced using standard pyraf/IRAF tasks (Tody, 1993). The PSF and aperture photometry were performed as described in §2.2.3. Although poorly spatially resolved, the extended host galaxy is blended with the AG, therefore, an aperture of size 1.5 × FWHM was employed for the photometry. Absolute photometry for $g'r'i'z'$ has been tied to the SDSS standard star network (Smith et al., 2002), and calibrated relative to five field stars of the SDSS catalog DR7 (Abazajian et al., 2009), which are shown in Fig. 4.1.The FORS2 $R_{\rm C}\,I_{\rm C}$ photometry has been transformed to $r'i'$ by employing colour terms computed from field stars. The photometry for $JHK_{\rm s}$ has been derived against 2MASS field stars in all cases (Skrutskie et al., 2006). For all filters and epochs, the obtained zero-points were corrected for atmospheric extinction. All data were corrected for a Galactic reddening of $E(B-V) = 0.025$ (Schlegel et al., 1998), assuming the interstellar extinction law by Cardelli et al. (1989) and a ratio of total-to-selective extinction of $R_V = 3.1$. Finally, the $JHK_{\rm s}$ data were transformed from the Vega to the AB system as described in §2.2.3. A total of 18 epochs of observation were obtained, the last on the 3rd of February 2010, all of them summing up 124 data points in all seven bands.

Weather conditions during the 9th and 10th epochs of observation were not good, with seeing of $\approx 1.6''$ and low transparency due to cirrus. Therefore, the two epochs taken three days apart were combined to obtain detections in $g'r'i'z'$. The last three observations were performed between 271 and 285 nights after the burst and aimed to detect the host galaxy without any GRB or SN contamination. After selecting the best images, I derived the average brightness of

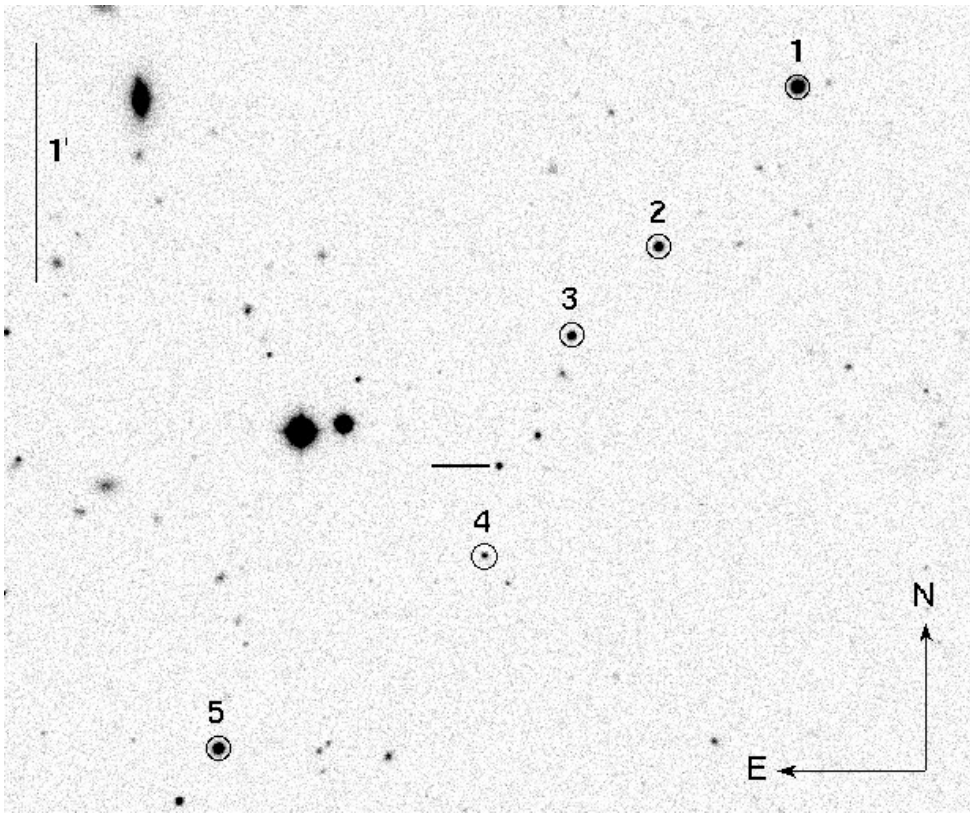

Figure 4.1. GROND r-band image of at about 12.5 hours after the burst. The red circle shows the XRT position enhanced by UVOT with an uncertainty of 1.4 arcsec.

those measurements, which will be used as a single latest epoch.

4.3 Results

4.3.1 The Nature of the Host Galaxy

The coordinates of the host galaxy, obtained from the latest r'-band images, are R.A.(J2000) = $12^{\rm h}38^{\rm m}5^{\rm s}.11$, Dec.(J2000) = $+16°50'14''.8$, with an uncertainty of $0.15''$. Comparing with the AG position in the first epoch —same precision— implies that the burst site was only $0.03'' \pm 0.20''$, i.e. negligible against our spatial resolution. Therefore, we can assume that the offset between the explosion site and the center of the galaxy is less than $0.2''$ at the 1σ level. Based on an angular scale of 6.36 kpc/$''$ at the redshift of GRB 090424 computed from a standard cosmology, this offset translates into 1.3 kpc, which is identical to the mean projected distance found by Bloom et al. (2002a) for a sample of 20 hosts of long GRBs.

The $g'r'i'z'JHK_{\rm s}$ photometry of the host galaxy corrected by Galactic extinction is listed in Table 4.1. By using `hyperZ` (Bolzonella et al., 2000), these data were compared to a library of galaxy spectral templates extinguished by different reddening laws. Results are shown Fig. 4.2, where the best fit is the SED of a type-a spiral galaxy of 64.1 Myr old with an absolute V magnitude of $M_V = -19.56$, and reddened by SN-induced dust (Maiolino et al., 2004). To derive wavelength-dependant extinction values, the parametrisation in Greiner et al. (2009) was used for the SN-induced reddening model. The dust-free upper limit in the $K_{\rm s}$ band translates into an upper limit on the absolute brightness of $M_{K_{\rm s}} > -21.92$, which places our object on the less luminous half of the GRB host sample compiled by Savaglio et al. (2009). Furthermore, the upper limit on the galaxy stellar mass is $M_\star < 1.2 \times 10^{10}\,{\rm M}_\odot$ by using the relation of Savaglio et al. (2009) for $z \leq 1.6$ GRB host galaxies. After dereddening the best-fit $K_{\rm s}$ band from an Sa-type galaxy, I obtain $M_{K_{\rm s}} = -21.79$, which translates into $M_\star = 1.0 \times 10^{10}\,{\rm M}_\odot$ for the stellar mass of the galaxy. Thus, despite the large photometric uncertainties, this galaxy in particular can be excluded from the category of dwarf galaxies, very common among GRB hosts. In comparison, Savaglio et al. (2009) found a smaller mean stellar mass of about $2 \times 10^9\,{\rm M}_\odot$ for host galaxies of long GRBs, which faces the host galaxy of GRB 090424 against the brightest half.

4.3.2 The Broad-band Spectral Energy Distribution

By combining XRT, UVOT, and GROND data, the broad-band SED of GRB 090424 at 47,138 s after the burst was built as shown in Fig. 4.3. The XRT data has been shifted to the GROND mid-time. In addition, UVOT measurements from 1000 s after the trigger were shifted to the GROND time using the synthetic colour terms (see Krühler et al., 2011, for details). The host-galaxy contribution has been subtracted from the complete photometric data set before modelling. The SED has been fitted similarly to some GRBs in Greiner et al. (2011). The spectral break at 0.42 keV is necessary to model X-ray and UV/optical/NIR data simultaneously and has been allow to vary. The ratio between the high-energy and the low-energy spectral indexes has been fixed to 0.5 and all other parameters were left free. The reduced χ squared was ${\chi_\mu}^2 = 1.31$ for the LMC dust model ($R_V = 3.16$; Fitzpatrick, 1986). The low-energy spectral index is $\beta_{\rm opt} = 0.61^{+0.07}_{-0.06}$, the dust extinction is $A_{V,{\rm host}} = 0.86^{+0.05}_{-0.06}$ mag, and the hydrogen column density is $N_{\rm H,host} = (7.8 \pm 0.7) \times 10^{22}$ cm^{-2}.

Table 4.1. Brightness of the host galaxy and constraints on the SN contribution.

	g'	r'	i'	z'	J	H	K_s
Host obs. mag	23.15 ± 0.06	22.21 ± 0.07	21.74 ± 0.05	21.68 ± 0.17	21.38 ± 0.17	20.75 ± 0.39	> 20.73
Host fit mag [a]	23.20 ± 0.04	22.40 ± 0.03	21.88 ± 0.03	21.74 ± 0.03	21.33 ± 0.06	21.04 ± 0.12	20.46 ± 0.10
SN amplitude (k) [b]	< 2.30	< 1.83	< 2.34	< 0.07	< 1.94	< 2.69	$\cdots$

[a] Magnitudes derived from the light-curve modelling using a power-law and a host-galaxy component.
[b] Luminosity ratio compared to SN 1998bw.

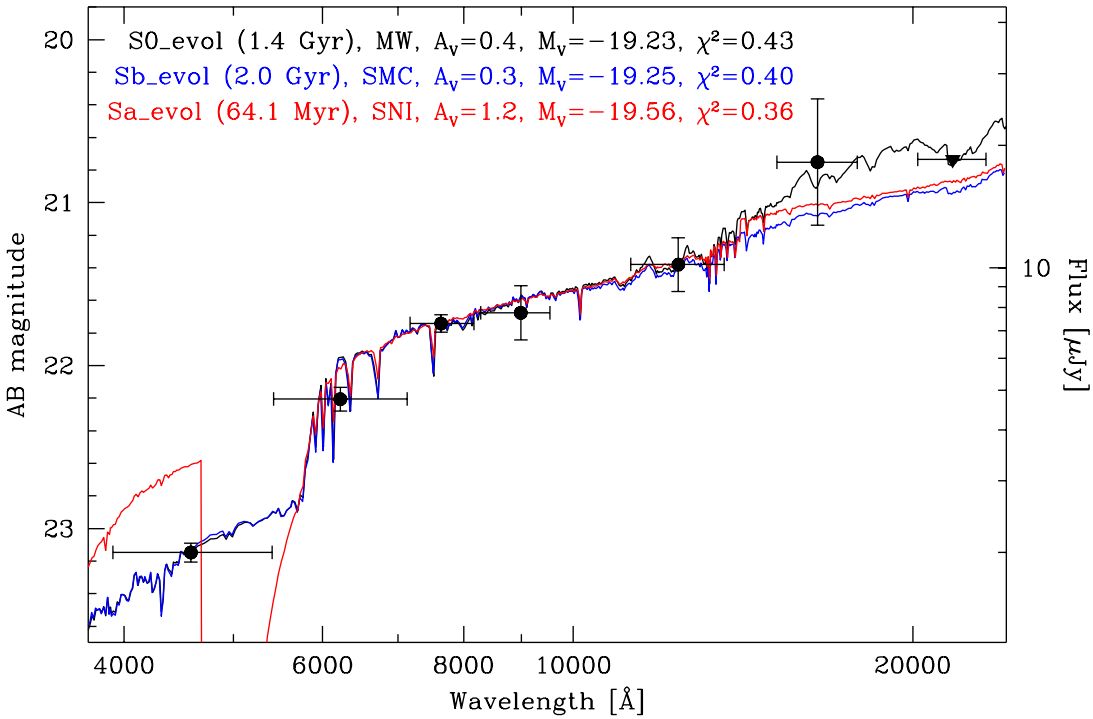

Figure 4.2. Spectral energy distribution of GRB 090424's host galaxy using GROND filters (black filled circles). The black line represents a lenticular galaxy of 1.4 Gyr old, reddened by a MW extinction law (Allen, 1976). The blue line shows the SED of a type-*b* spiral galaxy of 2 Gyr old, reddened by a Small-Magallenic-Cloud extinction law (Prevot et al., 1984; Bouchet et al., 1985). The best fit (red line) is a type-*a* spiral galaxy of 64.1 Myr old, reddened by SN-induced dust (Maiolino et al., 2004).

4.3.3 Modelling the Light Curves

X-Rays

The light curve as seen by *Swift*/XRT in the energy range 0.3 − 10 keV is shown in Fig. 4.4. The complete data set was modelled with a very smooth Beuermann-like broken power law with the break at $t_{\rm break} \approx 4$ ks and the early and late slopes of $\alpha_{X1} = -0.88 \pm 0.01$ and $\alpha_{X2} = -1.20 \pm 0.01$, respectively. The initial discrepancy between data points and model might be caused by the prompt emission extended to the X-ray regime. According to the BAT, the γ-ray emission stops actually 150 s after the GRB.

Optical and Near Infrared

The combined model of a power-law decay plus a constant host-galaxy contribution was fitted to the optical/NIR data. All bands were modelled simultaneously, leading to a common AG decay slope of 1.05 and a ${\chi_\mu}^2$ of 2.5. The host magnitudes inferred from this first fit are listed in Table 4.1. Moreover, Fig. 4.5 shows the resulting fit to the data, where the two components of the model are additionally shown for the g' band in dotted lines.

Using the deep GROND imaging of the host galaxy of GRB 090424, the image-subtracted light curve of the AG was constructed as described in §2.2.4. The results are plotted in Fig. 4.6, where an achromatic break, invisible in the observed light curves, appears clearly. A Beuermann-like broken power law was fitted to the data. The early and late decay slopes are $\alpha_{\rm opt1} =$

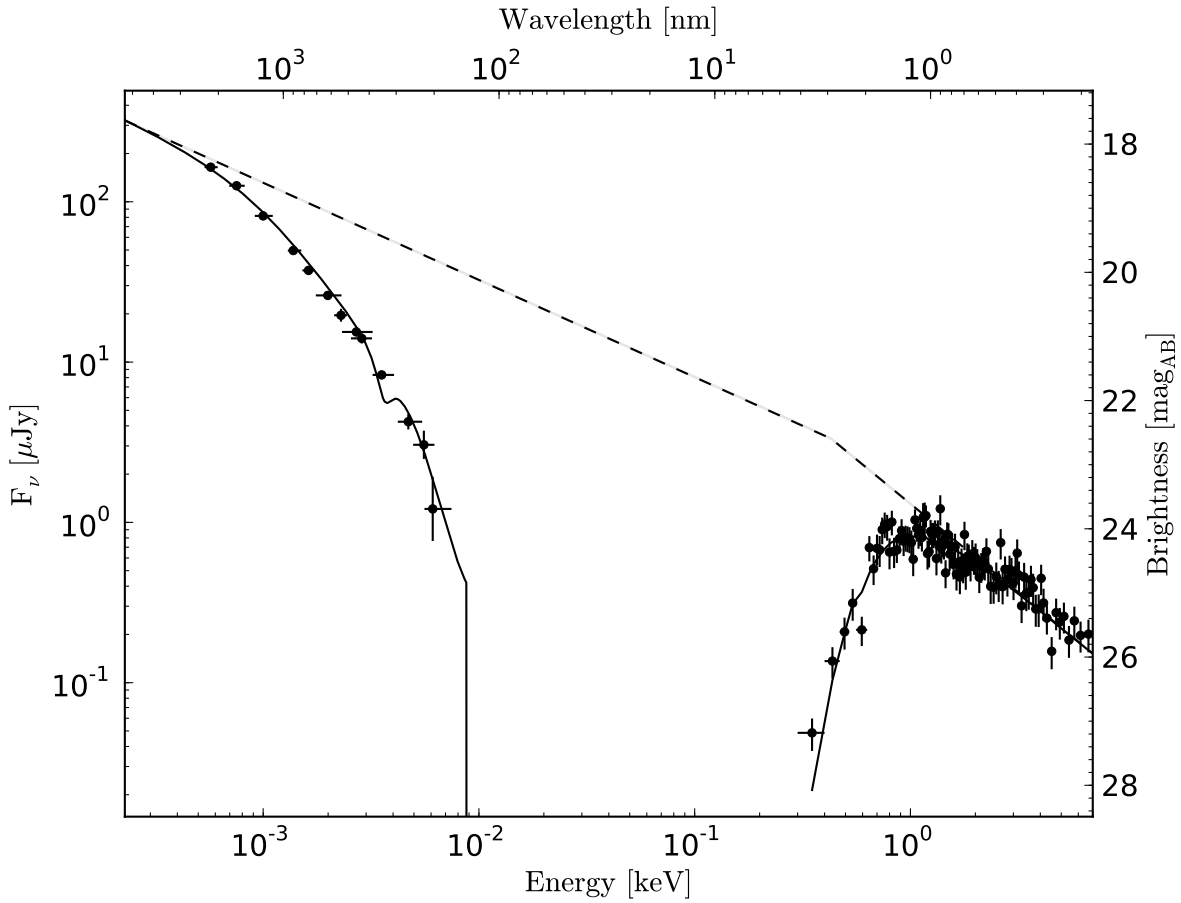

Figure 4.3. The SED of GRB 090424 using XRT, UVOT, and GROND filters.

-1.02 ± 0.02 and $\alpha_{\rm opt2} = -1.99 \pm 0.05$, respectively. While the smoothness parameter was $n = 3.3 \pm 0.3$, the time of the break was 3.06 ± 0.15 days after the burst. These parameters are very different from what is derived above for the X-ray data, therefore, it is probable that X-rays and optical/NIR light have dissimilar origin. This evidence supports the inclusion of a spectral break in the broad-band SED, and give us confidence in using derived value for $A_{V,\rm host}$ §4.3.2.

To describe temporally the SN contribution, I made used of SN 1998bw templates for each of our GROND filters derived from its $UVBRI$ photometry (Galama et al., 1998a) as described in §2.3.3. After discarding unusual peak times, I have arrived to the conservative range of $10-30$ days after the GRB to constrain the peak time in the r' band. I used 2-days steps inside these range, obtaining a total of 11 different models. When fitting these templates to the image-subtracted light curve as an extra component, the SN amplitude and its corresponding error are obtained, which were modelled independently for each band. Given that no obvious bump appears in the light curves, 1σ upper limits were derived by adding up the fitted SN amplitude to its 1σ uncertainty for each of the 11 different models in each band. The results of such approach are shown in Fig. 4.7. The abscissa corresponds to the peak time of the SN and the ordinate is in units of SN 1998bw luminosities (k). Table 4.1 shows the most constraining limits in the selected peak-time interval for each band. Due to the non-detection of the host in the $K_{\rm s}$ band, it is not possible to constrain the SN contribution for this filter. The z'' band proves to constrain better,

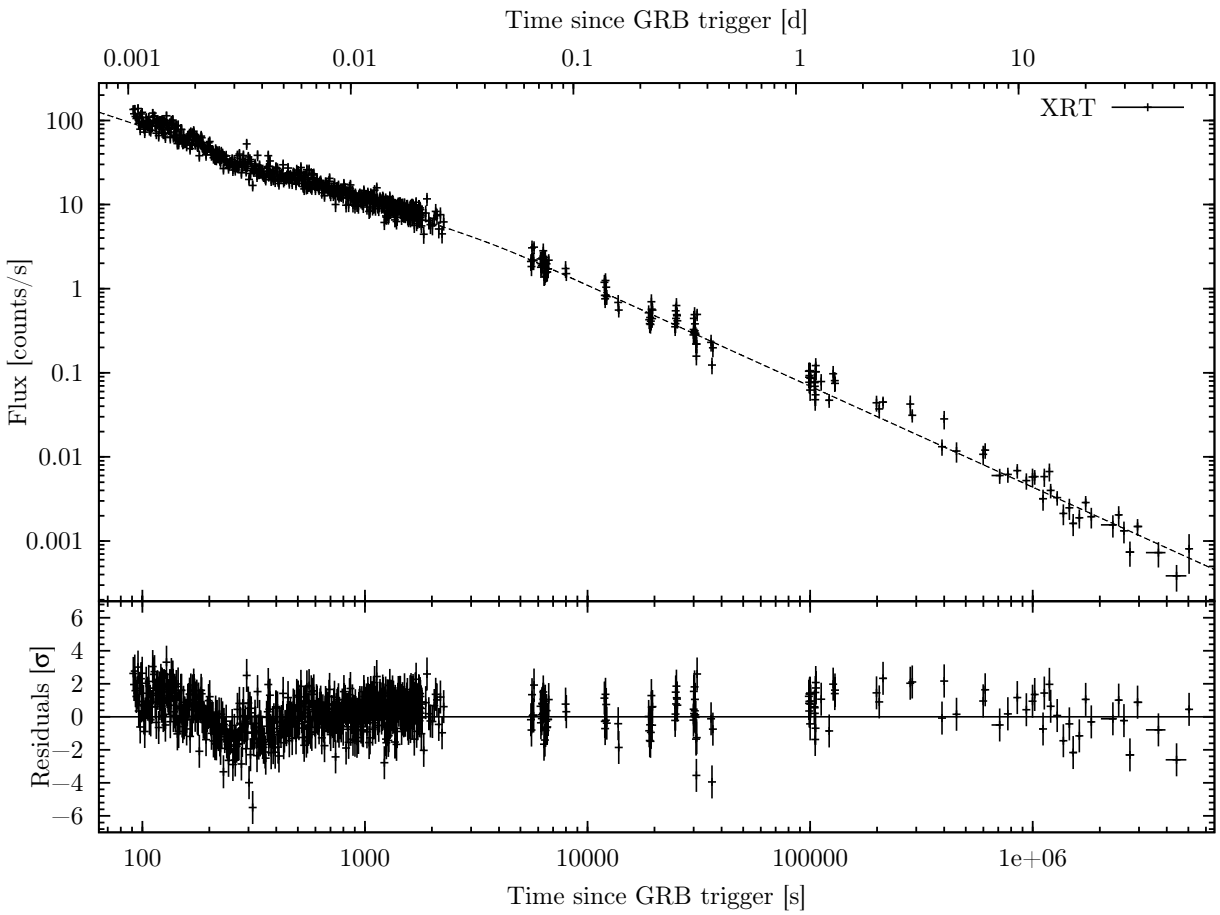

Figure 4.4. *Swift*/XRT light curve of GRB 090424.

in which case the SN amplitude was fitted to 0.00 ± 0.065 in the most conservative case. This fitted value is translated into a 3σ upper limit of 19.5% of the peak luminosity of SN 1998bw. In the following, a 3σ upper limit of $A_{V,\mathrm{host}} < 1.01$ measured from the broad-band SED in §4.3.2 is considered. I utilise the parametrisation of Pei (1992) for the LMC extinction law in order to compute the extinction for the z' band, considering that the light detected was bluer when extinguished by the host-galaxy ISM. Assuming that there was a SN explosion in GRB 090424 with the same colours of SN 1998bw, the SN peak luminosity has to be less than 49% that of SN 1998bw at the 3σ confidence level.

Colour Curves

The analysis of the colours may offer insights on different spectral light that might be rising. The SN is expected to be bluer than the AG, which is normally red. In Fig. 4.8 I plotted four different optical colour curves derived by using the GROND host-subtracted photometry from the previous section. Due to the achromacity of the fitted broken power law, no evolution in color is expected. Since the errors are large at late stages, no significant change in colour are found that might reveal a SN. However, a deviation slightly larger than 2σ is seen in $r' - i'$, where at day ~ 7.5 after the burst this colour index becomes redder than expected.

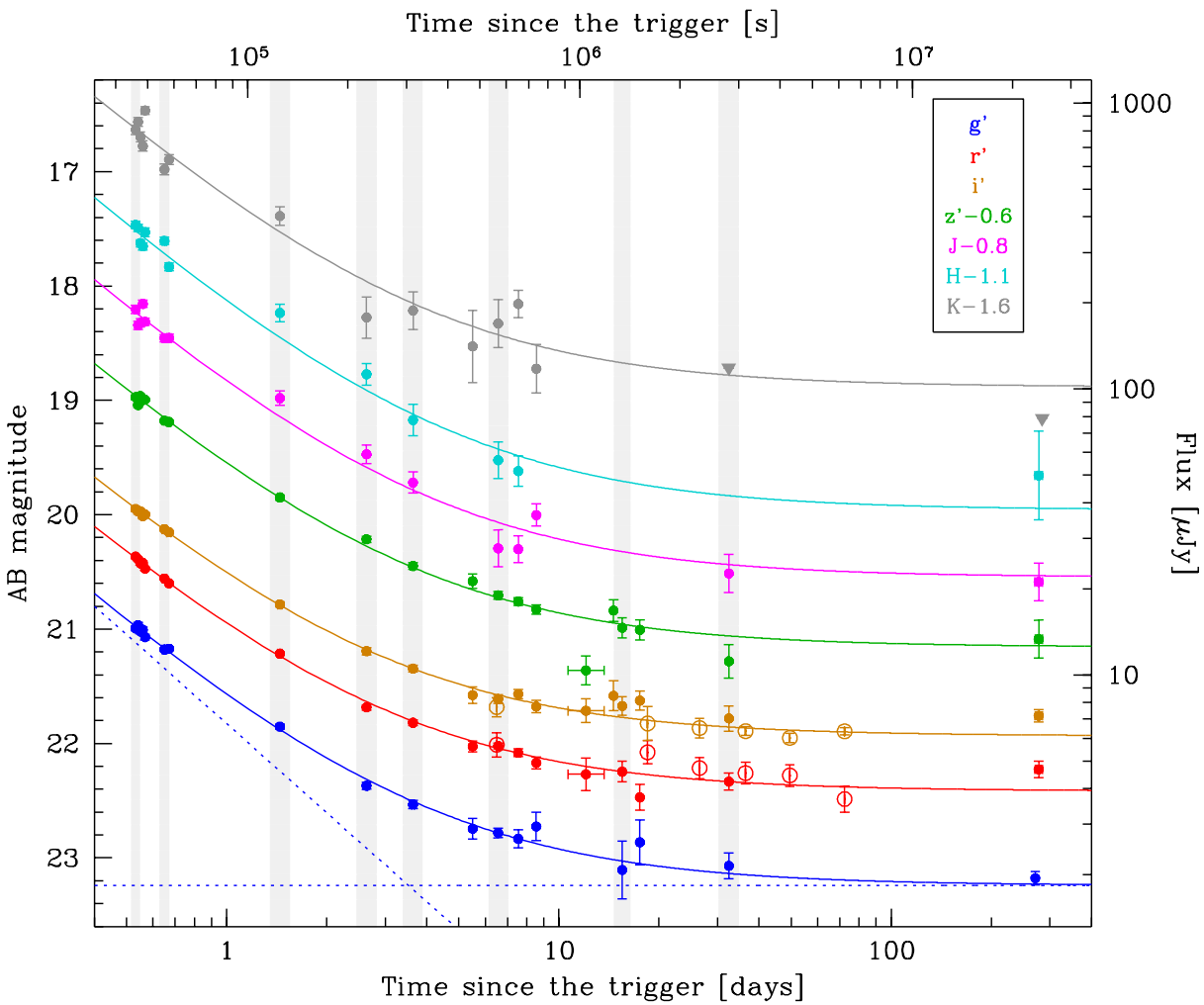

Figure 4.5. Optical/NIR light curves of GRB 090424 for $g'r'i'z'JHK_s$ respectively in blue, red, brown, green, magenta, cyan, and grey dots. The VLT/FORS2 data is plotted with open circles. The continuous line corresponds to the fits, which include a common power-law decay and a constant host-galaxy component different for each band. The two components are drawn separate with dotted lines for the g' band. For clarity, the $z'JHK_s$ data points have been shifted. The triangle at the end of the K_s-band light curve is an upper limit. The shaded areas are the selected intervals for SED construction (see §4.3.4).

4.3.4 Spectral Energy Distributions

Fig. 4.9 shows the SED of six different epochs of GROND observations, marked using shaded areas in Fig. 4.5 and 4.6. All SEDs are corrected by Galactic extinction and fitted using the `hyperZ` code (Bolzonella et al., 2000) with power laws extinguished at the redshift of the GRB. The same parameters derived in §4.3.2 were employed for the host-galaxy extinction and the spectral slope was left free to vary. If we had detected the SN contribution, we would expect significant blackbody-like curvature, however, this is not the case.

4.4 Discussion

Even though there was no reliable constraints on the extinction law from the host-galaxy SED, the broad-band SED fitting in §4.3.2 gives us a hint on the properties of the ISM along the line of sight of GRB 090424. The LMC dust model with $R_V = 3.16$ is the best-fit reddening law, in accordance with the low-metallicity environment in which GRBs prefer to explode. In comparison with the $A_{V,\mathrm{host}}$ distribution of Greiner et al. (2011), the value of $A_{V,\mathrm{host}} = 0.86^{+0.05}_{-0.06}$ mag places GRB 090424 among the 10% most extinguished bursts. Nevertheless this extinction value could be argued to be low, since a spectral break between the UV and the X-rays was inserted in the calculation. In the case of no spectral break, grey dust would have to be invoked and $A_{V,\mathrm{host}} \simeq 2.2$ mag would fit the single spectral slope to the optical. Assuming that $A_{\lambda,\mathrm{host}} = A_{V,\mathrm{host}}$ due to grey dust, the new z'-band constraint will be $k \lesssim 1.48$. Anyhow, I have argued the need of a spectral break by showing the difference between the X-ray and the optical evolution. The optical decays differently than the X-rays at all times, starting at 46 ks with $\alpha_{\mathrm{opt1}} = -1.02 \pm 0.02$ and then becoming even steeper with $\alpha_{\mathrm{opt2}} = -1.99 \pm 0.05$ at 350 ks after

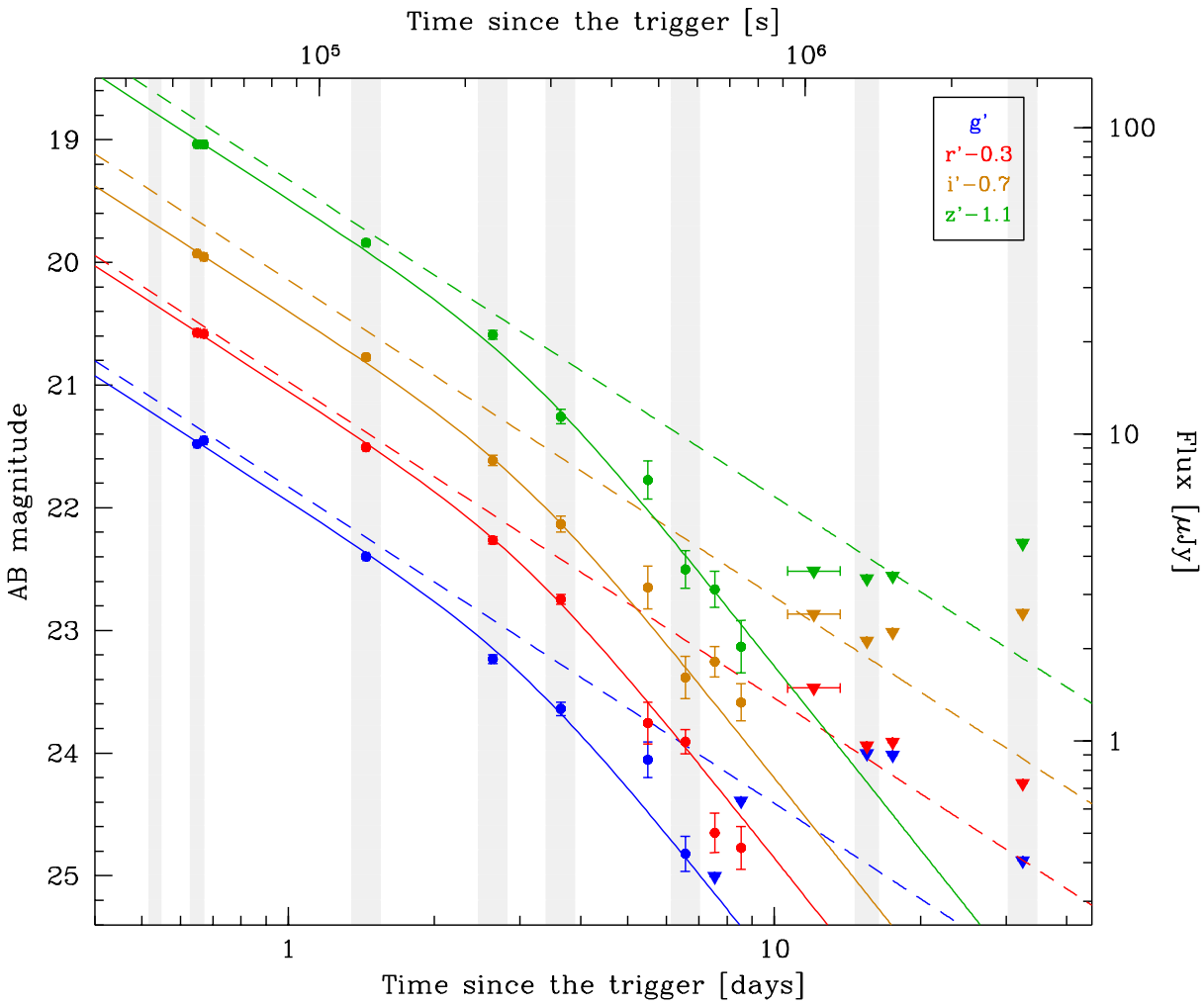

Figure 4.6. Light curve of GRB 090424 after host-galaxy subtraction. The dashed lines correspond to the single power law derived from the observed light curves as shown in Fig. 4.5.

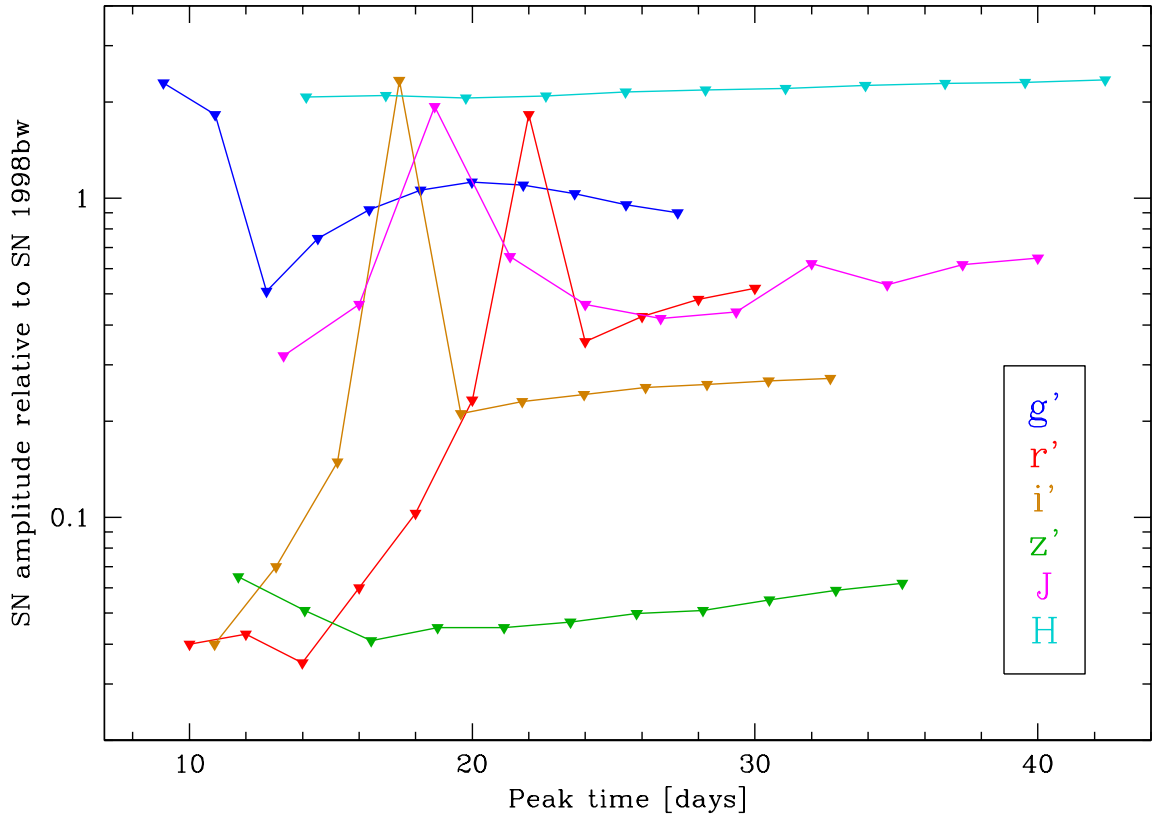

Figure 4.7. Upper limits on the SN contribution as a function of peak time. The zero point of the abscissa is the time of the burst, and the ordinate has units of SN 1998bw luminosities (k). The colour coding is the same as in Fig. 4.5.

the burst. Meanwhile the X-rays decay with a much shallower slope of $\alpha_{\rm X2} = -1.20 \pm 0.01$ in the same interval, thus showing us that X-rays and optical radiation must have a different origin. This evidence strongly supports the existence of a spectral break, which gives us confidence in using $A_{V,\rm host} = 0.86^{+0.05}_{-0.06}$ mag with the LCM extinction law throughout the paper.

Richardson (2009) collected and modelled recently optical light curves of 14 GRB AGs showing SN bumps, with and without spectroscopic confirmation. His analysis is important to characterise the nature of the detected SNe, however, it lacks the less luminous end of the distribution, i.e., the non-detections. From his results, the V-band absolute magnitudes M_V of detected SN associated to GRBs ranges approximately from -19.6 to -17.3 for the $H_0 = 74.2$ km s^{-1} Mpc^{-1} from the latest SN Ia data set (Riess et al., 2009). Using the data presented by Clocchiatti et al. (2011), M_V is -19.35 for SN 1998bw at peak. The 3σ upper limit for GRB 090424 of $k < 0.49$ (§4.3.3) is transformed then into $M_V > -18.58$, which lies in the less luminous half of the distribution and is slightly brighter than the peak of the SE SN distribution (Richardson et al., 2006; Woosley and Bloom, 2006). Now we wonder whether there is a smooth transition between local stripped-envelope SNe and GRB/SN associations or they are just different populations of SNe. Unfortunately incompleteness of the faint end of the GRB/SN sample hampers currently a statistical analysis (see §6).

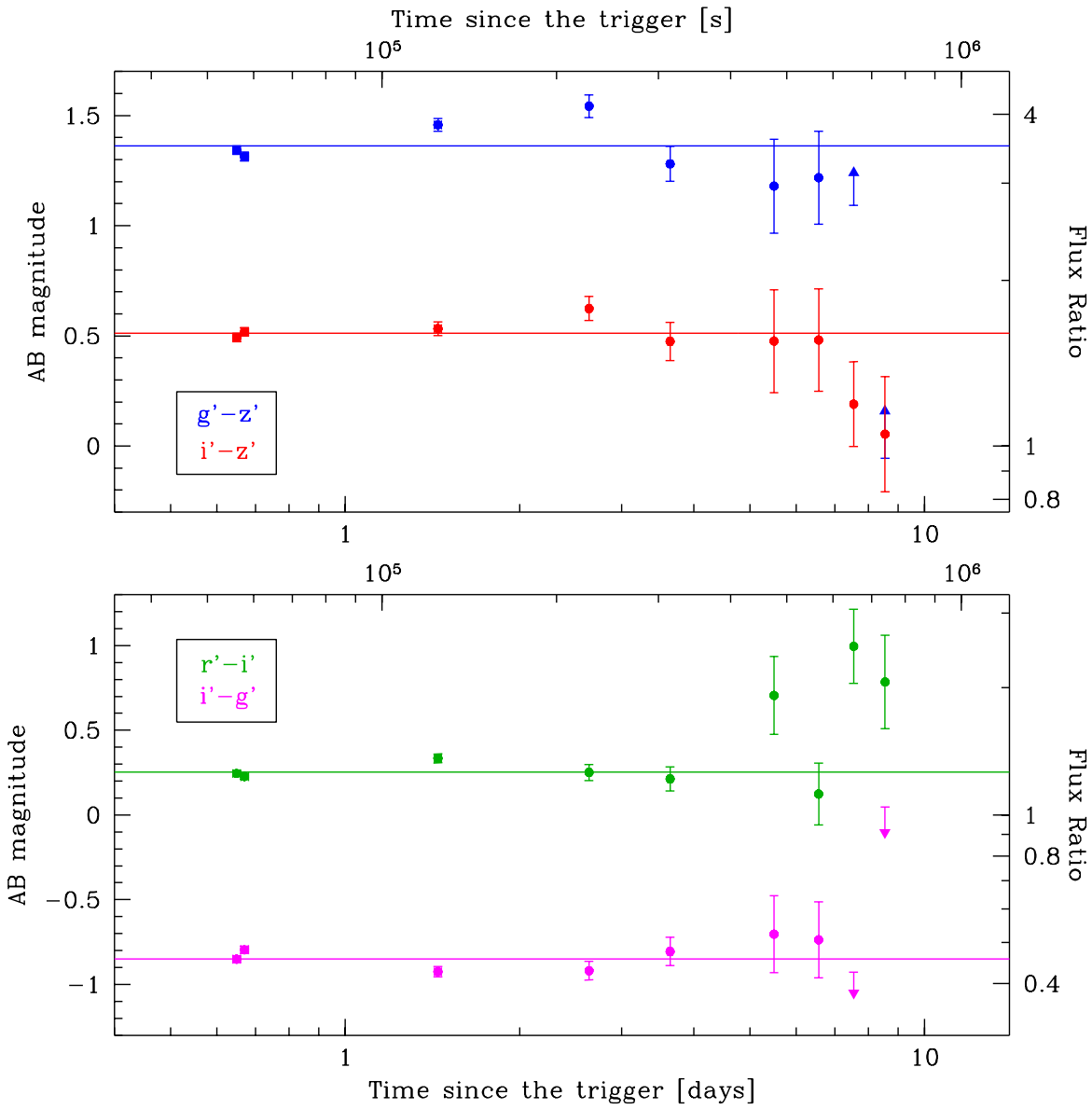

Figure 4.8. Colour curves of GRB 090424 using GROND filters. The upper panel shows $g' - z'$ and $i' - z'$ in blue and red, respectively. The lower panel shows $r' - i'$ and $i' - g'$ in green and magenta, respectively. The continuous lines represent the achromatic AG evolution and are derived using the same parameters of the light-curve model showed in Fig. 4.5.

4.5 Conclusions

For the purpose of characterising the SN contribution of GRB 090424 and its host galaxy I utilised multi-wavelength data from diverse telescopes and instruments: (i) GROND $g'r'i'z'JHK_{\rm s}$, (ii) VLT/FORS2 $R_{\rm C}\,I_{\rm C}$, (iii) *Swift*/UVOT, and (iv) *Swift*/XRT. Below I summarise and enumerate the main conclusions coming out from our analysis.

1. Supported by the fact that the fitting of the host-galaxy SED hints at a spiral morphology, the stellar mass of $M_\star = 1.0 \times 10^{10}\,{\rm M}_\odot$ places the host of GRB 090424 on the massive half of GRB hosts.

2. The broad-band AG SED shows us that there has to be a spectral break between the

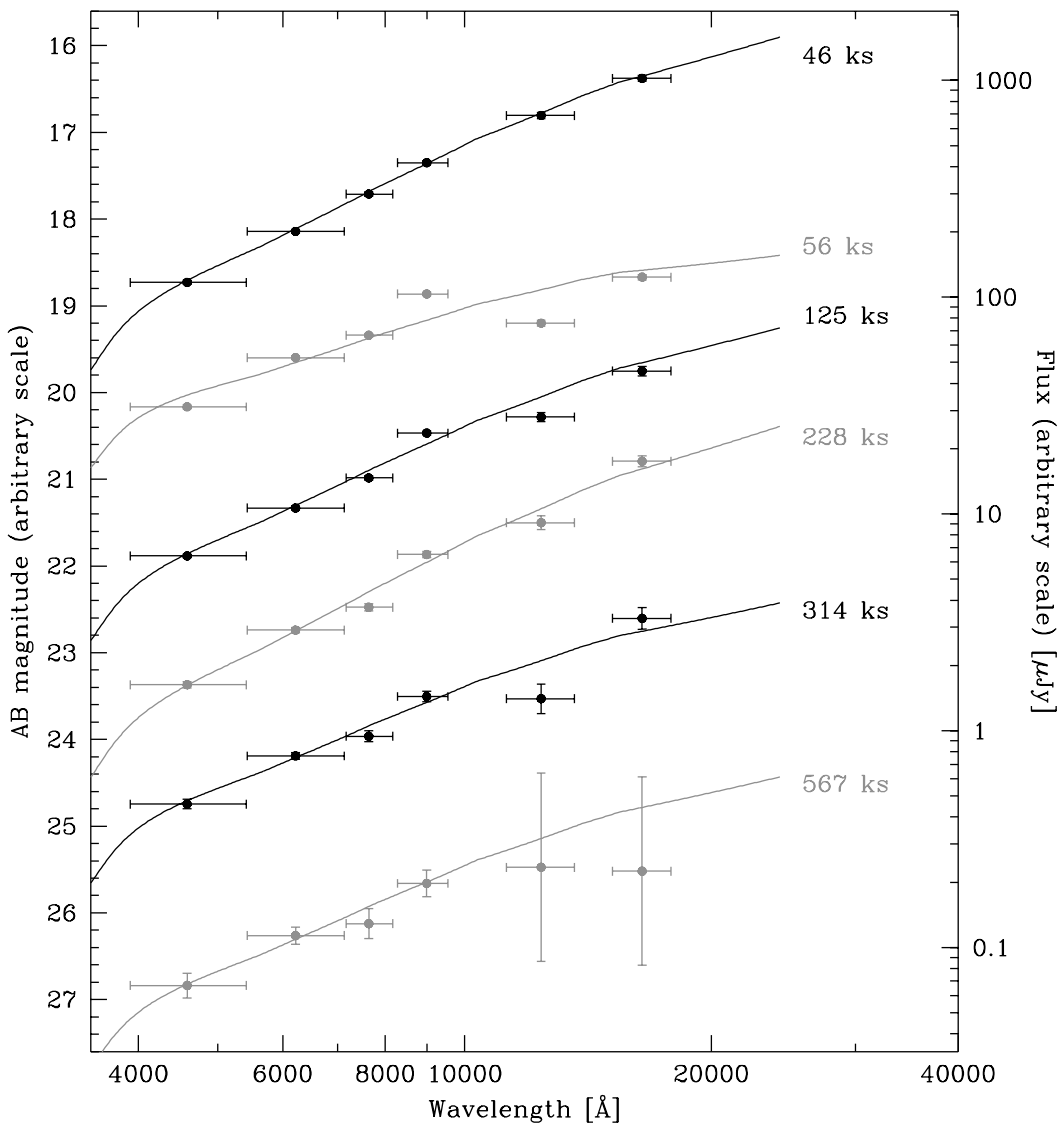

Figure 4.9. Spectral energy distributions of GRB 090424 at different epochs. Each SED is labelled on the right with the mid-time of the observation. All SEDs are fitted with a power law plus a LMC-like extinction of $A_{V,\rm host} = 0.86$. The triangular dot is an upper limit.

UV/optical/NIR and X-rays to make them consistent. Further evidence of this break is provided by the different decay slopes between the X-rays and the optical/NIR, which make us believe that both types of radiation have a different origin.

3. Given the conclusion above, the UV/optical/NIR extinction derived from the broad-band SED fitting ($A_{V,\mathrm{host}} = 0.86^{+0.05}_{-0.06}$ with LMC reddening law) was used throughout the paper.

4. The SN contribution in GRB 090424 derived from the host-subtracted light curve is less than 49% of SN 1998bw peak luminosity after correcting by host dust extinction. In conclusion, this object is among the less luminous half of the GRB-SN associations.

Chapter 5

Four Late-Time Rebrightenings

Table 5.1 presents a sub-sample of GRBs with late-time optical rebrightenings in their AG light curves. All of them were observed by GROND (see §2.2) mounted at the 2.2-m ESO/MPI telescope at La Silla Observatory. Deep late-time observations were carried out for each of them to constrain the contribution from their host galaxies and performed image subtraction when detected. Table 5.2 presents the resulting photometry for the host galaxies. In the following, observational facts and general properties of each event are summarised from the literature. When possible, mass estimates are derived for the host galaxies following a similar approach to that presented in §4.3.1.

Table 5.1. GROND sample of late-time AG rebrightenings.

GRB	SN	RA(J2000) [h : m : s]	Dec.(J2000) [° : ′ : ″]	z	$A_{V,\mathrm{Gal}}$ [a] [mag]	$N_{\mathrm{H,Gal}}$ [b] [10^{20} cm^{-2}]
081007	2008hw	22:39:50.40	−40:08:48.8	0.530	0.05	1.4
091127	2009nz	02:26:19.87	−18:57:08.6	0.490	0.12	2.8
100902A	···	03:14:30.97	+30:58:45.2	···	1.00	11.3
101219B	2010ma	00:48:55.35	−34:33:59.3	0.552	0.06	3.1

Note.— The coordinates are derived by comparing field stars in GROND images to USNO-B reference stars (Monet et al., 2003). The astrometric solution is accurate down to ≈ 0.3 arcsec. The references for the redshifts are Berger et al. (2008) for GRB 081007/SN 2008hw, Vergani et al. (2011) for GRB 091127/SN 2009nz, and Sparre et al. (011b) for GRB 101219B/SN 2010ma.

[a] The values for Galactic foreground extinction are taken from the dust maps of Schlegel et al. (1998).
[b] The absorption column densities are taken from the Galactic H I maps of Kalberla et al. (2005).

Table 5.2. GROND photometry of the host galaxies.

GRB	g'	r'	i'	z'	J	H	K_{s}
081007	24.66 ± 0.11	24.49 ± 0.11	24.08 ± 0.19	23.96 ± 0.24	> 21.98	> 21.05	> 20.07
091127	24.08 ± 0.09	23.45 ± 0.06	22.85 ± 0.07	23.57 ± 0.14	> 21.69	> 21.37	> 19.92
100902A	> 24.29	> 24.72	> 24.04	> 23.90	> 21.66	> 20.83	20.07
101219B	> 25.40	> 25.18	> 24.52	> 24.45	> 22.21	> 22.03	> 20.21

Note.— The host-galaxy magnitudes are all in the AB system and corrected for the corresponding Galactic foreground extinction. The upper limits were derived from the deepest observation available showing no detection and are quoted at the 3σ confidence level.

GRB 081007/SN 2008hw The *Swift*/BAT discovered GRB 081007 at 05:23:52 UT on 2008 October 7 (Baumgartner et al., 2008). The prompt emission had a duration of $T_{90} \approx 10$ s and a soft spectrum with $E_{\rm peak} \lesssim 30$ keV (Markwardt et al., 2008), therefore, the burst was classified as an XRF. The redshift of $z = 0.5295$ was found by Berger et al. (2008) through optical spectroscopy. A subsequent optical spectrum taken 17 days after the burst shows broad features indicative of an emerging SN, which was thereafter classified as type I (no Hydrogen lines) and named SN 2008hw (Della Valle et al., 2008). The SN bump was also reported as a flux excess with respect to the AG (Soderberg et al., 2008a). From the optical photometry of the host galaxy and the upper limits in the NIR (Table 5.2), a stellar-mass range of $M_\star \sim 10^{8-9}\,{\rm M}_\odot$ is derived, which is compatible with the population of GRB hosts (Savaglio et al., 2009).

GRB 091127/SN 2009nz The *Swift*/BAT was triggered by GRB 091127 at 23:25:45 UT on 2009 November 27 (Troja et al., 2009). The γ-ray emission lasted for $T_{90} = 7.1$ s and showed a soft spectrum Stamatikos et al. (2009). A redshift of $z = 0.490$ was obtained from optical spectroscopy (Cucchiara et al., 2009; Thöne et al., 2009). Observations by Konus-Wind confirmed the results from the *Swift*/BAT (Golenetskii et al., 2009) and additionally yielded an energy release typical for cosmological GRBs ($E_{\gamma,\rm iso} \sim 10^{52}$ erg). The optical AG was confirmed with GROND observations (Updike et al., 2009) adding NIR detections. The SN classification became official based on the photometric SN bump only Cobb et al. (2010a,b) and low-quality spectroscopy was published much later (Berger et al., 2011). Photometry depicting the SN rebrightening was published in Cobb et al. (2010c) and Vergani et al. (2011). Using the GROND optical detections and the NIR detections from Vergani et al. (2011) for the host galaxy, a stellar mass of $M_\star = 10^{7.8\pm0.2}\,{\rm M}_\odot$ is obtained. This value falls in the low-mass end of the distribution of GRB host masses Savaglio et al. (2009).

GRB 100902A At 19:31:54 UT on 2010 September 2, the *Swift*/BAT was triggered by GRB 100902A and the *Swift*/XRT started observations 316.2 s thereafter (Sakamoto et al., 2010b). The gamma-ray emission is characterised by several strong peaks and has a long duration of $T_{90} = 429 \pm 43$ s (15 − 350 keV; Stamatikos et al., 2010b). The time-averaged spectrum is best fit by a single power law with an index of -1.98 ± 0.13 (Stamatikos et al., 2010b), which reveals a soft GRB event. The duration and the softness of the high-energy emission show similarities with GRB events at redshifts of $z < 0.2$, which have been associated with SNe. The XRT light curve shows flaring activity at around 400 s after the trigger, which is consistent with the late gamma-ray emission. At later times the evolution of the X-ray counterpart shows a shallow decay followed by a steeper decay (Starling and Sakamoto, 2010), normal behaviour for average GRB AGs. The UV/optical counterpart was initially not detected down to deep limits (Krushinski et al., 2010; Guidorzi et al., 2010; Gorbovskoy et al., 2010; Andreev et al., 2010; Landsman and Sakamoto, 2010; Tello et al., 2010; Kuroda et al., 2010; Strobl et al., 2010), which might hint at a high redshift event. According to Gorbovskoy et al. (2012), the ratio between the optical and the X-ray prompt fluxes might indicate that GRB 100902A is actually a dark burst, although the foreground Galactic extinction is particularly high ($A_{V,\rm Gal} = 1.00 \pm 0.04$; Schlegel et al., 1998). Nevertheless, an AG candidate was firstly reported by GROND (Updike et al., 2010). At about 1.5 days after the burst, a source at $r' \simeq 24$ mag was found inside the enhanced XRT error circle (Beardmore et al., 2010). Observations in the NIR were also reported for a similar epoch by Im et al. (2010), which are consistent with our upper limits. Moreover, a rebrightening was discovered thereafter by Huang et al. (2010), which was also detected by GROND (see Fig. 5.3). Unfortunately no spectra were taken and neither the nature of the rebrightening nor the

redshift were constrained. To determine redshift limits for the event, Gorbovskoy et al. (2012) used the technique develop by Grupe et al. (2007), which anti-correlates the excess absorption column density and the redshift. This is an observational effect as the SED is shifted to lower energies, i.e., out of the XRT observable energy range, and less absorbed radiation is detected as the redshift increases. Using a late-time XRT spectrum, Gorbovskoy et al. (2012) set an upper limit for the redshift of $z \lesssim 3.2$. Another attempt at constraining the redshift was performed by Campana et al. (2010). They fitted a cutoff power law to the early and late time-average XRT spectra, where the redshift and intrinsic absorption are allowed to vary. They computed a redshift of $z = 4.5^{+0.3}_{-0.2}$, which is incompatible with the upper limit found by Gorbovskoy et al. (2012). One reason for the inconsistency could be that the X-ray emission consists actually of more than just a single power law. This is the case of a thermal component, which has been already detected in a few *Swift* bursts (e.g., Campana et al., 2006; Waxman et al., 2007; Starling et al., 2011; Olivares E. et al., 2012). In consequence, these redshift estimates might be affected by large systematic uncertainties.

GRB 101219B/SN 2010ma At 16:27:53 UT on 2010 December 19, the *Swift*/BAT discovered GRB 101219B (Gelbord et al., 2010). The BAT burst lasted $T_{90} \simeq 34$ s (Cummings et al., 2010) and consisted of a spectrum with $E_{\rm peak} \simeq 70$ as observed by *Fermi*/GBM (van der Horst, 2010). The SN discovery was first reported photometrically by Olivares E. et al. (2011) along with a redshift estimation assuming the brightness of SN 1998bw for the rebrightening ($z = 0.4-0.7$). The spectroscopic confirmation of SN 2010ma came in later by Sparre et al. (2011) along with the redshift determination of $z = 0.55185$ from weak Mg absorption lines. The spectroscopy lead to further analysis by Sparre et al. (011b) that shows broad-line features characteristic of GRB-SNe. Late-time GROND observations show no signal of a host-galaxy down to deep limits (Table 5.2), therefore no image-subtraction procedure was performed. These upper limits imply a stellar mass for the host galaxy of $M_\star \lesssim 10^{9.2}\,{\rm M}_\odot$, which makes the host of GRB 101219B belong to the low-mass half of GRB host galaxies and marginally compatible with the SMC.

5.1 Multicolour Light-Curve Fitting

After image subtraction of the host galaxy (§2.2.4) in the cases where it was detected (Table 5.2), the light curves were fitted according to §2.3.2 using one or two power-law components and the SN 1998bw templates (§2.3.3). The luminosity ratio with respect to SN 1998bw k was fitted to the light curve corrected for Galactic extinction only, therefore we need to correct the luminosity ratios for the host-galaxy extinction A_V determined by the SED modelling next in §5.2. The following expression was used:

$$k_\lambda = k_{\lambda,\rm obs} \times 10^{A_\lambda/2.5}, \tag{5.1}$$

where the λ subscript represents each different bandpass. The results of the modelling are summarise in Tables 5.3 and 5.4. In the following, detailed description of the fitting for each event.

GRB 081007/SN 2008hw The light curves in all seven bands are well modelled using a broken power law of the form shown by eq. 2.2. Models and data are shown in Fig. 5.1. Additionally I included the X-ray light curve from the *Swift*/XRT in order to constrain the decay

Table 5.3. Parameters of the AG component and goodness of the light-curve modelling.

GRB	α_1	$t_{\rm break}$ [days]	η	α_2	χ^2/μ [a]
081007	-0.66 ± 0.01	0.91 ± 0.05	15 fixed	-1.40 ± 0.05	167/109
091127 [b]	-0.38 ± 0.01	0.34 ± 0.01	1.3 ± 0.1	-1.63 ± 0.02	52/38
101219B	-1.01 ± 0.01	...	...	...	118/67

Note.— Due to the rather sparse temporal sampling of GRB 100902A light curve, no AG evolution parameters were determined.

[a] The ratio χ^2/μ is computed in the multiple-component fitting procedure, which includes AG plus SN modelling. See Table 5.4 for the SN parameters.

[b] The values of α_1, $t_{\rm break}$, and η were taken from the complete GROND r'-band light-curve fitting in Filgas et al. (2011) and α_2 was fitted by a single power law using the data presented in Fig. 5.2 only.

Table 5.4. Parameters of the SN component with respect to SN 1998bw templates.

SN	Stretch factor (s)	Luminosity ratio (k) [a] g'	r'	i'	z'
2008hw	0.85 ± 0.11	< 0.90	0.80 ± 0.10	0.65 ± 0.08	0.69 ± 0.10
2009nz	1.03 ± 0.04	< 1.21	1.15 ± 0.09	0.96 ± 0.14	0.73 ± 0.12
2010ma	0.76 ± 0.10	0.85 ± 0.17	$1.78^{+0.08}_{-0.17}$	1.36 ± 0.08	0.63 ± 0.09

[a] Luminosity ratios are all corrected for Galactic and host-galaxy extinction (see §5.2).

after the break, where there is only a single optical epoch. For the $r'i'z'$ bands was necessary to add a supernova component. The brightest host galaxy allowed by the data was included in the model for $JHK_{\rm s}$ at late times. With luminosities of about 30% that of SN 1998bw (see Table 5.4), this SN turned out to be one of the faintest GRB-SNe ever detected. The g' upper limit is strongly affected by absorption of metal lines and template extrapolation (see case of SN 2009nz in the next paragraph).

GRB 091127/SN 2009nz No $K_{\rm s}$-band detections were obtained for this event. The rest six bands are all well fitted by a single power law, which needed the SN component for the $g'r'i'z'$ bands (Fig. 5.2). The brightest host galaxy allowed by the data was included in the model for JH at late times. Luminosity ratios and the common stretch factor reflect strong similarities to SN 1998bw in the $r'i'$ bands. The g' band is probing wavelengths centred at $\sim$ 3000Å for the redshift of SN 2009nz ($z = 0.490$). The flux at this wavelengths is strongly affected by absorption-line blanketing of metals, which intensity can differ from SN to SN. Moreover, since the U band, the bluest band from which the SN 1998bw templates are constructed, is only sensitive down to just above 3000Å, extrapolations dominate in computing the g'-band template. Given also the poor detections, the low value of $k_g{}'$ in Table 5.4 is untrustworthy.

GRB 100902A Figure 5.3 shows the GROND light curves of GRB 100902A. Additionally, the JH observations reported by Im et al. (2010) and the r'-band magnitude reported by Huang et al. (2010) are plotted using open circles, however, not included in the modelling. Due to the sparse sampling and to assess the SN origin, no power-law component was fitted to the light curves of GRB 100902A. All seven bands were fitted by SN templates only, which turn out to have very unusual parameters. No uncertainties were allowed to be computed due to

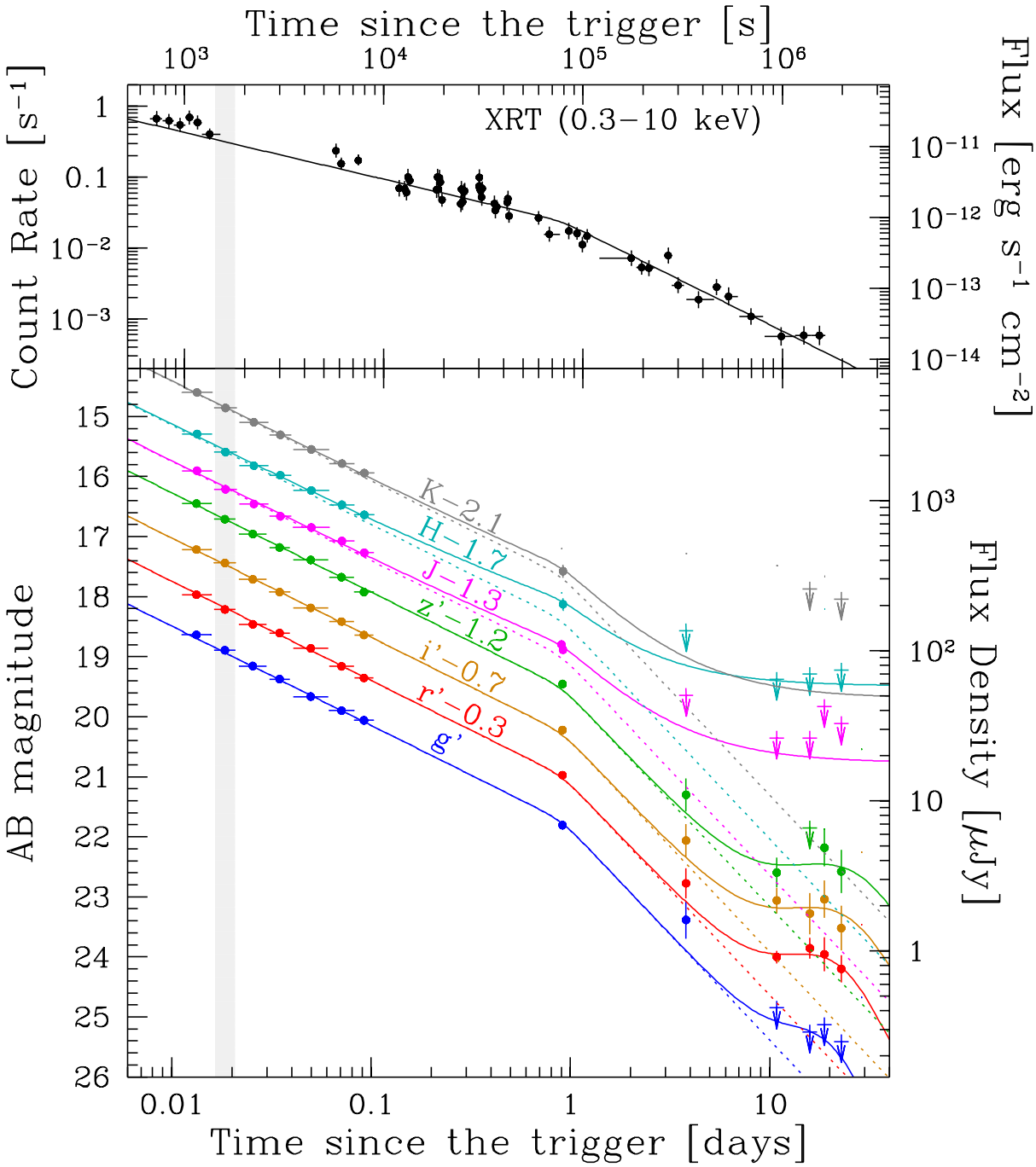

Figure 5.1. Multicolour light curve of GRB 081007/SN 2008hw corrected for Galactic extinction as observed by the *Swift*/XRT (upper panel) and GROND (lower panel). Filled circles represent detections and arrows are upper limits. Solid lines represent the overall fits and dotted lines the AG component. For reasons of clarity, light curves were shifted along the magnitude axis. The grey-shaded area marks the epoch at which the SED was analysed (Fig. 5.5).

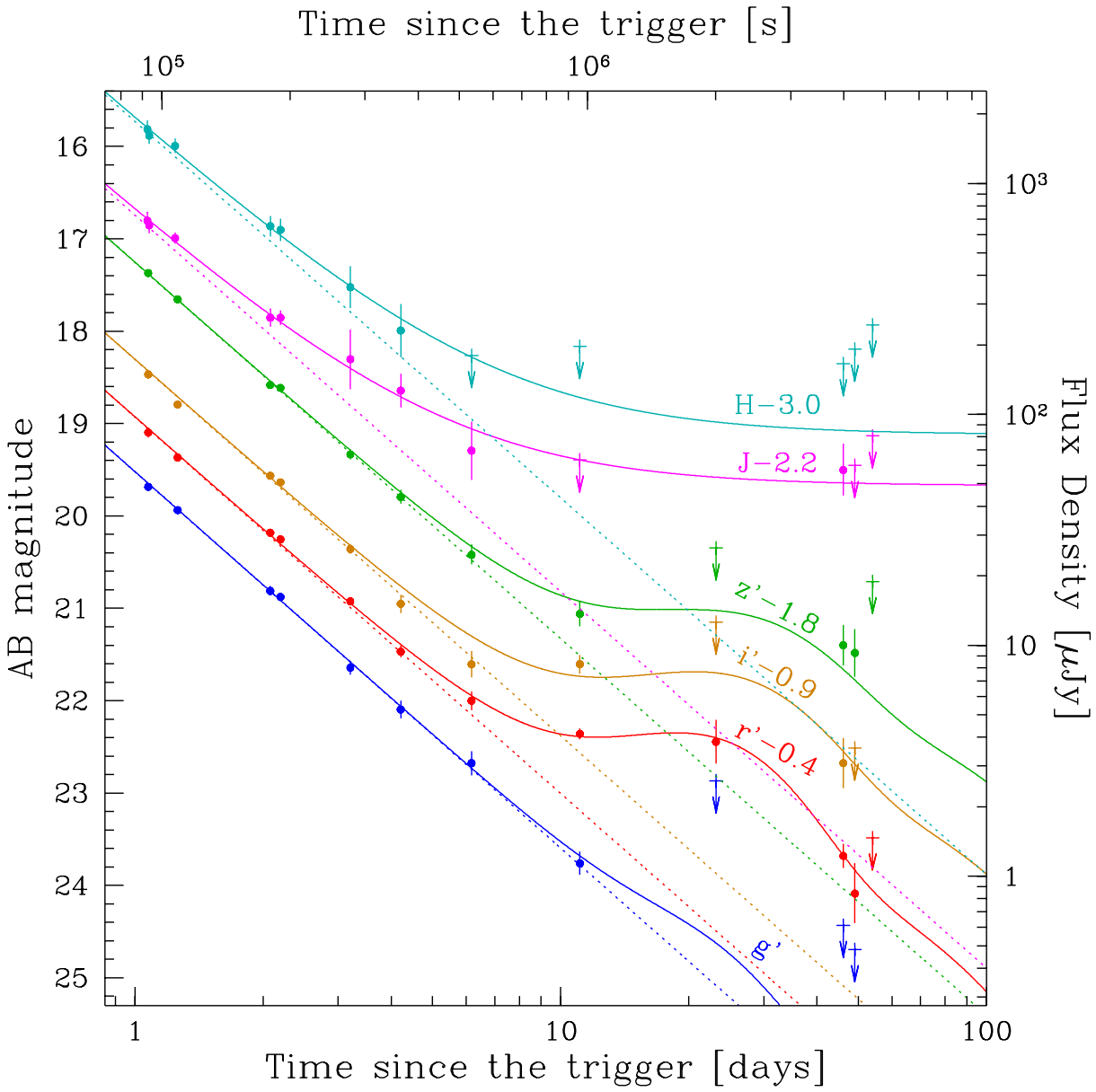

Figure 5.2. Multicolour light curve of GRB 091127/SN 2009nz corrected for Galactic extinction as observed by GROND. Only data after day one is used. Filled circles represent detections and arrows are upper limits. Solid lines represent the overall fits and dotted lines the AG component. For reasons of clarity, light curves were shifted along the magnitude axis.

the small number of data points. For the redshift of $z = 0.37$ that assumes the SN origin (see 5.2), the optical luminosity is somewhat brighter than SN 1998bw. The $JHK_{\rm s}$ luminosity is extreme and the difference with the optical would suggest a very infrared-rich SN. Moreover, the stretch factor is extremely small ($s = 0.27$) compared to the smallest ever measured for GRB-SNe ($s = 0.52$ for the SN bump of GRB 050824; Sollerman et al., 2007), which makes the SN origin doubtful. As a consequence, the peak time at ~ 5 days is much earlier than any other SN observed. Moreover, the r'-band measurement by Huang et al. (2010) would suggest an even faster rise, which would be incompatible with the SN templates.

GRB 101219B/SN 2010ma Figure 5.4 shows the GROND light curves of GRB 101219B's optical transient. The SN bump is clear in the $r'i'z'$ bands, however, less significant in the g' band. At the redshift of the event, the g' band actually probes the UV regime, therefore, the lower g'-band SN luminosity is explained by a combination of both the extrapolation of the templates and the UV line blanketing by metals, which is very common among SE SNe. Given the flux decrement in the $i'z'$ bands at around 2.5 days after the GRB, there could be an AG break hidden by early SN emission in the bluer bands. The host galaxy remained undetected, however, it may explain the flux excess 35 days after the burst in the r' band (dashed line in Fig. 5.4). The luminosity ratio would decrease $\sim 14\%$ in this case for the host at $r' = 25.35 \pm 0.25$. Therefore, the lower error in $k_{r'}$ was increased to match the 3σ lower limit when assuming the brightest host component possible (see Table 5.4).

5.2 Spectral Energy Distributions

Using the available X-ray data from the *Swift*/XRT and the optical/NIR data from GROND, I constructed a single AG SED per event with the purpose of determining the extinction in the line of sight through the host galaxy. Details on the construction and modelling of the SED can be reviewed in §2.3.4. The results of the SED modelling are presented in Table 5.5.

There is to note that the AG may probe a slightly different line of sight than the SN photosphere. If anything, the extinction for the SN should be larger than for the AG, because the AG forms further out, where the material ejected by the GRB hits the circumstellar medium. In the standard fireball shock model, this radius is in the range of $10^{14} - 10^{16}$ cm. Therefore, it is hard to believe that in less than 0.003 parsecs there is enough ISM to contribute significantly to the intrinsic extinction.

GRB 081007/SN 2008hw To include contemporaneous *Swift*/UVOT data, the second GROND epoch was chosen to study the broad-band SED of GRB 081007 (see grey-shaded region in Fig. 5.1). From the UVOT, useful upper limits in the UV bands are included, which help constraining the host-galaxy extinction. The time-integrated *Swift*/XRT spectrum was renormalised to the epoch of the UV/optical observations as explained in detail by §2.3.4. The resulting values of host-galaxy extinction including the correction for redshift (K-correction) and their corresponding statistical uncertainty are for the GROND filters $A_{g',\rm host} = 1.39 \pm 0.16$, $A_{r',\rm host} = 0.99 \pm 0.12$, $A_{i',\rm host} = 0.77 \pm 0.09$, $A_{z',\rm host} = 0.63 \pm 0.07$, $A_{J,\rm host} = 0.38 \pm 0.04$, $A_{H,\rm host} = 0.24 \pm 0.03$, and $A_{K_{\rm s},\rm host} = 0.14 \pm 0.02$; all in units of magnitude. These values were used to correct the SN luminosity ratios in Table 5.4.

GRB 091127/SN 2009nz The SEDs of the early AG of GRB 091127 were presented by Filgas et al. (2011). A detailed analysis by Schady et al. (2012) includes *Swift*/UVOT data and

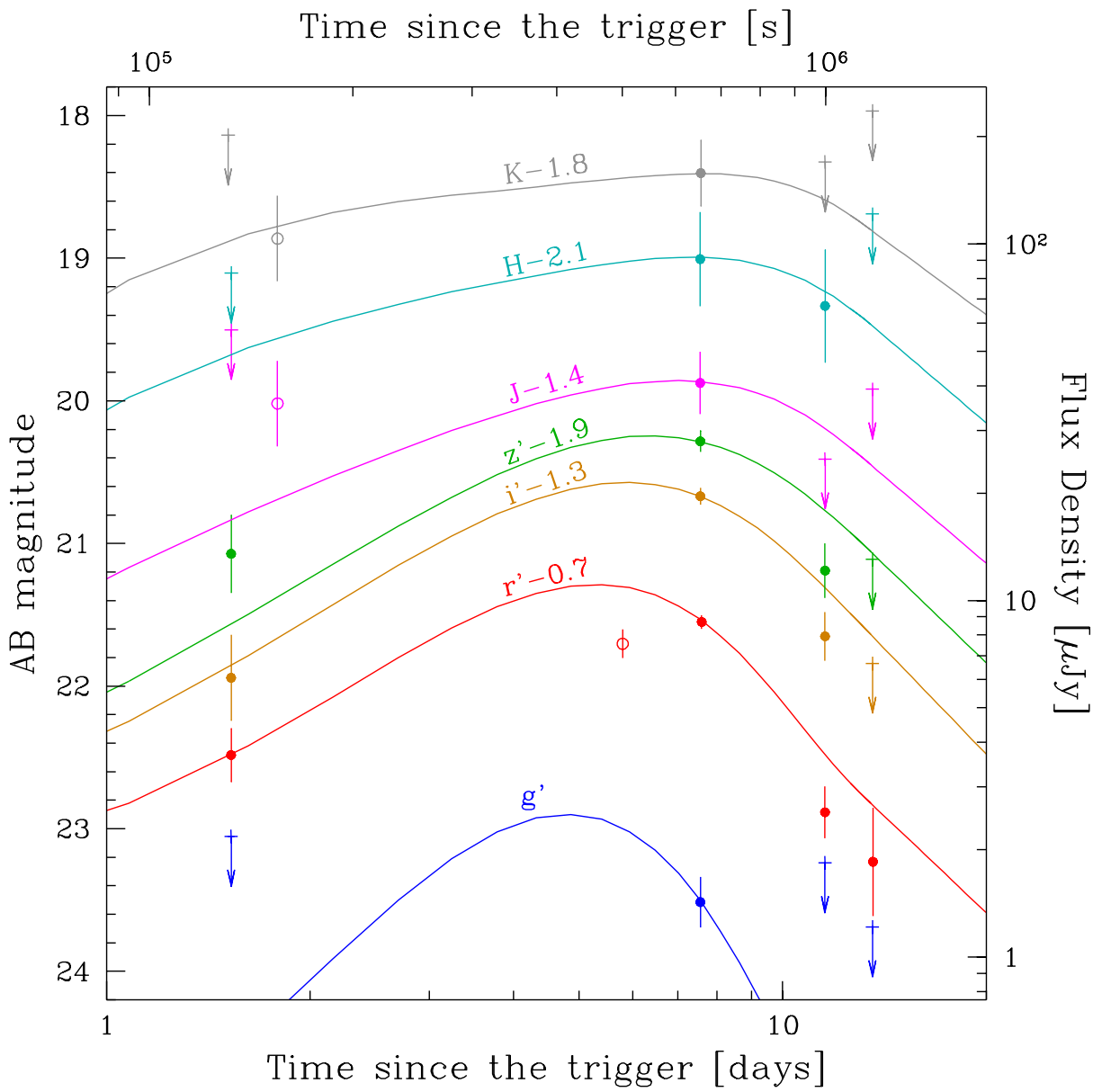

Figure 5.3. Multicolour light curve of GRB 100902A corrected for Galactic extinction as observed by GROND. Filled circles represent detections and arrows are upper limits. The solid lines are stretched and scaled templates of SN 1998bw at $z = 0.37$. For reasons of clarity, light curves were shifted along the magnitude axis.

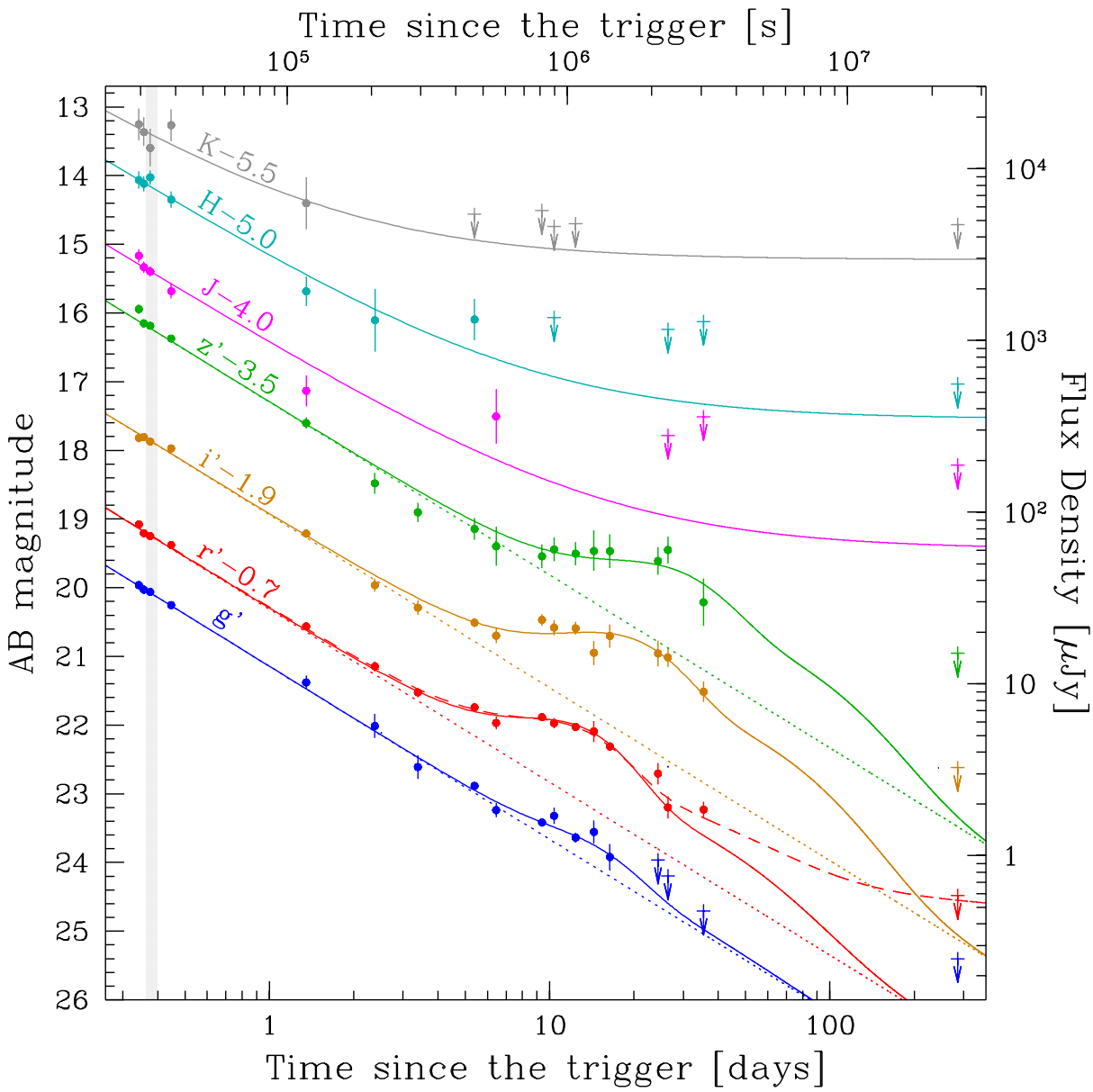

Figure 5.4. Multicolour light curve of GRB 101219B/SN 2010ma corrected for Galactic extinction as observed GROND. Filled circles represent detections and arrows are upper limits. Solid lines represent the overall fits and dotted lines the AG component. The red dashed line represents a model with an extra host-galaxy component needed to explain the flux excess in the r' band 35 days after the burst. For reasons of clarity, light curves were shifted along the magnitude axis. The grey-shaded area marks the epoch at which the SED was analysed (Fig. 5.8).

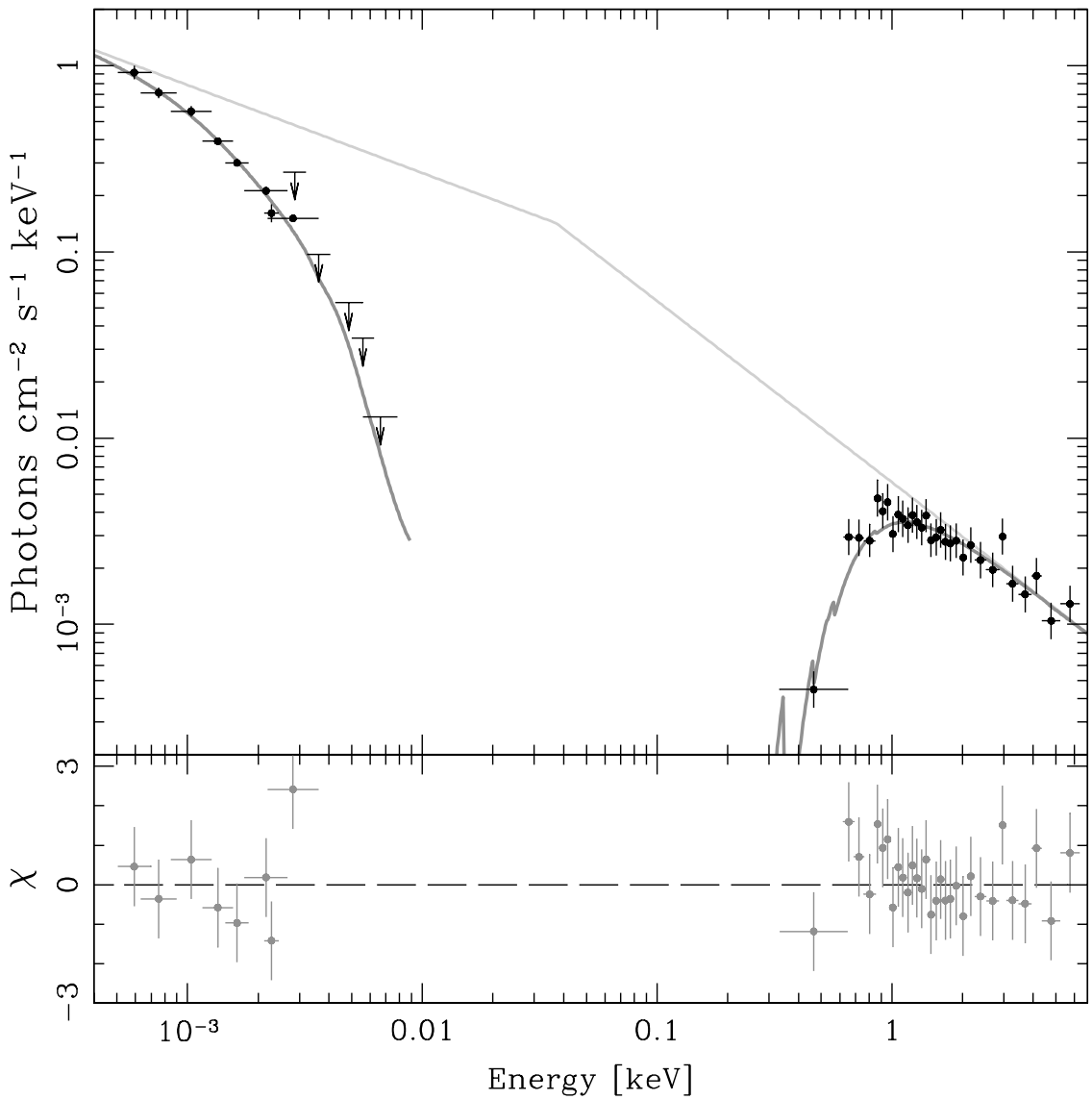

Figure 5.5. Broad-band SED of GRB 081007 at 1.6 ks after trigger. The observed data are represented by black filled circles. The UV bands provide 3σ upper limits shown as arrows. The thick grey line shows the best-fit model able to reproduce the data, the broken power law. The thin continuous grey line shows the unextinguished versions of the model. In the lower panel, the residuals of the best fit are plotted.

Table 5.5. Parameters of the SED modelling of the AG.

GRB	β_X	$A_{\rm V,host}$ [mag]	$E_{\rm break}$ [eV]	$N_{\rm H,host}$ [10^{21} cm^{-2}]	χ^2/μ
081007	1.97 ± 0.09	0.68 ± 0.08 (SMC)	37 ± 54	5.6 ± 0.7	41/39
091127 [a]	0.748 ± 0.004	< 0.03 (LMC)	$2.6-29.9$	0.32 ± 0.06	1.1
100902A	1.43 ± 0.05 [b]	0.7 ± 0.2 (MW) [c]	$\cdots$	3.1 ± 0.2 [b]	$\cdots$
101219B	2.12 ± 0.01	0.12 ± 0.01 (SMC)	9.0 fixed	0.6 ± 0.3	27/32

Note.— Obeying the fireball model for GRB AGs, the high-energy (β_X) and the low-energy (β_O) spectral indexes are correlated by $\beta_X = \beta_{\rm opt} + 0.5$, except in the case of GRB 091127 were $\beta_{\rm opt}$ varies in the range $0.25-0.62$.

[a] In the case of GRB 091127, the quoted values of β_X, $N_{\rm H,host}$, and reduced χ^2 are computed from the simultaneous best fit to all eight GROND/XRT SEDs by Filgas et al. (2011). The $E_{\rm break}$ range comes from an observed evolution of $\beta_{\rm opt}$. The $A_{V,\rm host}$ upper limit was taken from Schady et al. (2012).

[b] These values were taken from the modelling of the WT-mode XRT spectrum alone at `http://www.swift.ac.uk/xrt_spectra/00433160/`, where $z = 0$ is assumed.

[c] This extinction is from the modelling of the optical/NIR SED only (see Fig. 5.6 and Table 5.6).

aims to constrain the host-galaxy extinction, which results in $A_{\rm V,host} = 0.00 \pm 0.02$ mag. The SED parameters are shown in Table 5.5.

GRB 100902A The optical/NIR SED of GRB 100902A was modelled using two different strategies: (1) SN-template fitting via a correlation function and (2) power-law fitting plus extinction via χ^2 statistics. The first approach consist in using the SNID tool from Blondin and Tonry (2007) to compare our photometry to a library of SN spectra (see §2.3.4 for more details). The second approach uses a power-law model extinguished by three different extinction laws: MW, LMC, and SMC (see §2.3.5 for details). To perform the χ^2 minimisation, I used of the `XSPEC` analysis tool (see §2.3.4 for details). Figure 5.6 shows the SED of 100902A at maximum brightness and the results of the modelling. To evaluate the NIR detections, Fig. 5.7 shows the $JHK_{\rm s}$ images for this particular epoch. Given that the redshift is unknown, for both methods it was left free to vary. The SNID code works reliably in the range $z = 0-1.2$ and for higher redshifts the overlap between input and template becomes restrictive. The purpose is to find out the nature of the rebrightening of GRB 100902A, for which the observations of our second epoch, 7.6 days after the burst, are available. The first detections of the transient were 1.5 days after the burst, which give the baseline to claim the rebrightening (see Fig. 5.3). At 11.6 days after the burst, the third epoch shows a fading transient, therefore, maximum light can be conservatively estimated to have been occurred before day 12. Thus, the age of the possible SN at the time of our observation of the rebrightening should lie between -4 and $+6$ days with respect to optical maximum. In the first fitting attempt, all SN spectra (1474 in total; types Ia, Ib, Ic, and II) were used in the SNID analysis. Only the normal type-Ic SN 2004aw [1] (Taubenberger et al., 2006) yields a correlation ratio $r \geq 5$, however, with an age of 31.9 days and given that the modelled observation should be around maximum, the correlation is unreliable. In a second trial, the template library was restricted to 20 BL type-Ic SN spectra only, i.e., fast-expanding SNe which are sometimes accompanied by a GRB. It resulted in SN 2002ap [1] (Gal-Yam et al., 2002; Foley et al., 2003) having the best correlation, but not good

[1] Previously unpublished spectra from the CfA Supernova Program, `http://www.cfa.harvard.edu/supernova/index.html`

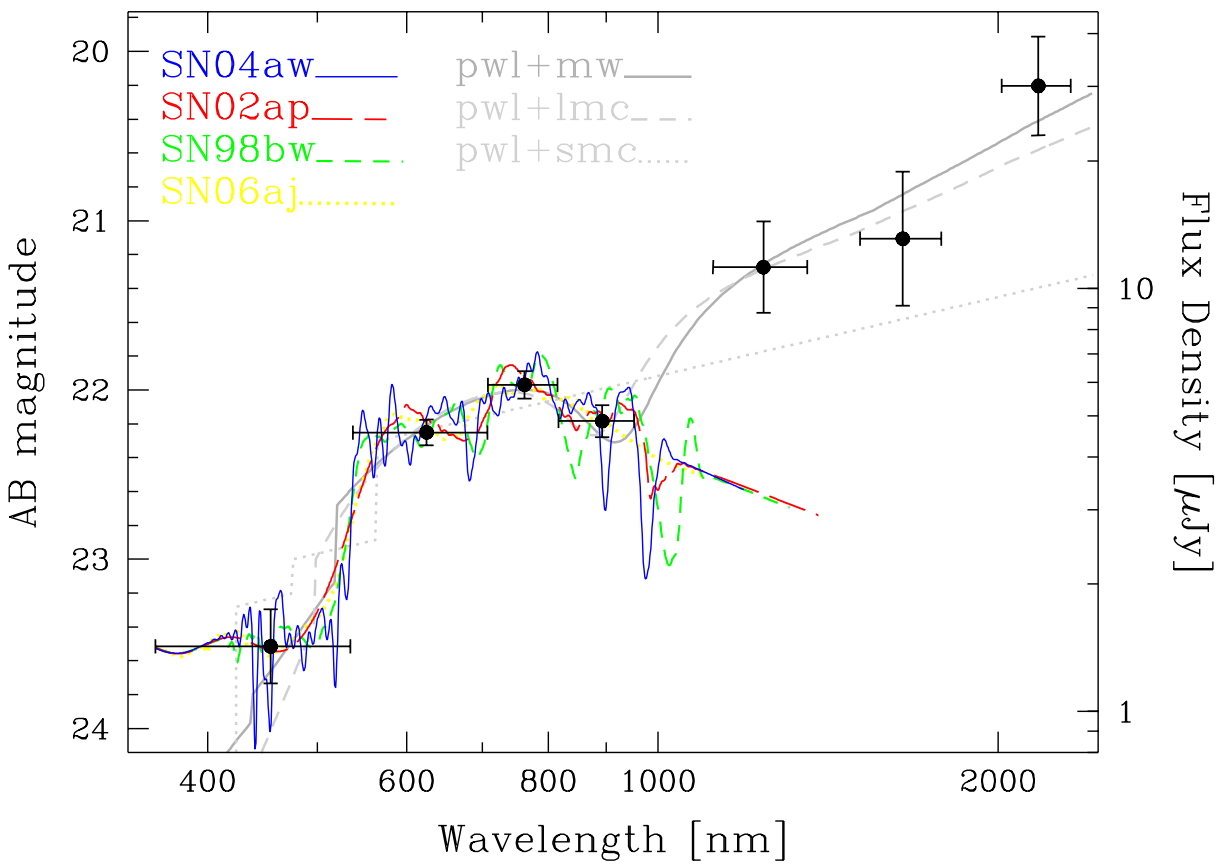

Figure 5.6. Broad-band SED of GRB 100902A at 7.6 days after trigger. The observed data are presented in black filled circles. The grey lines show the power-law models extinguished by MW (solid line), LMC (dashed line), and SMC (dotted line) reddening laws at different redshifts. The coloured lines show the SN spectral templates fitted to the data: SN 2004aw (blue continuous line), SN 2002ap (red long-dashed line, SN 1998bw (green short-dashed line), and SN 2006aj (yellow dotted line).

enough ($r = 4.3$). The third and fourth tests consisted in restricting the template library to spectra of SN 1998bw (Patat et al., 2001) and SN 2006aj (Modjaz et al., 2006), respectively, which have been both related to GRBs. The best correlation for SN 2006aj templates turned out to have a bad correlation and a late age, which is incompatible with the light curve (see Fig. 5.3). Table 5.6 summarises the parameters of the SN template fitting. In conclusion, none of the correlations have parameters are satisfactory, basically because the NIR magnitudes are much brighter than the reddest end of any SN template and only the optical bands are appropriately modelled. On the other hand, only the correlations of SN 2002ap and SN 1998bw have ages near maximum. These two have redshifts estimations that are quite different from those of SN 2004aw and SN 2006aj correlations. The average redshift from the correlations with the best ages is $z = 0.37 \pm 0.06$, which we will use when assessing the SN scenario. When evaluating the power law scenario, much more reliable results are obtained (see Table 5.6).

GRB 101219B/SN 2010ma Using GROND, XRT, and UVOT data combined, the SED of 101219B was constructed at 9 h after the GRB (see §2.3.4 for details). Figure 5.8 shows the results of the modelling. A broken power law was required to fit the spectral behaviour. The values of host-galaxy extinction including the correction for redshift (K-correction) for

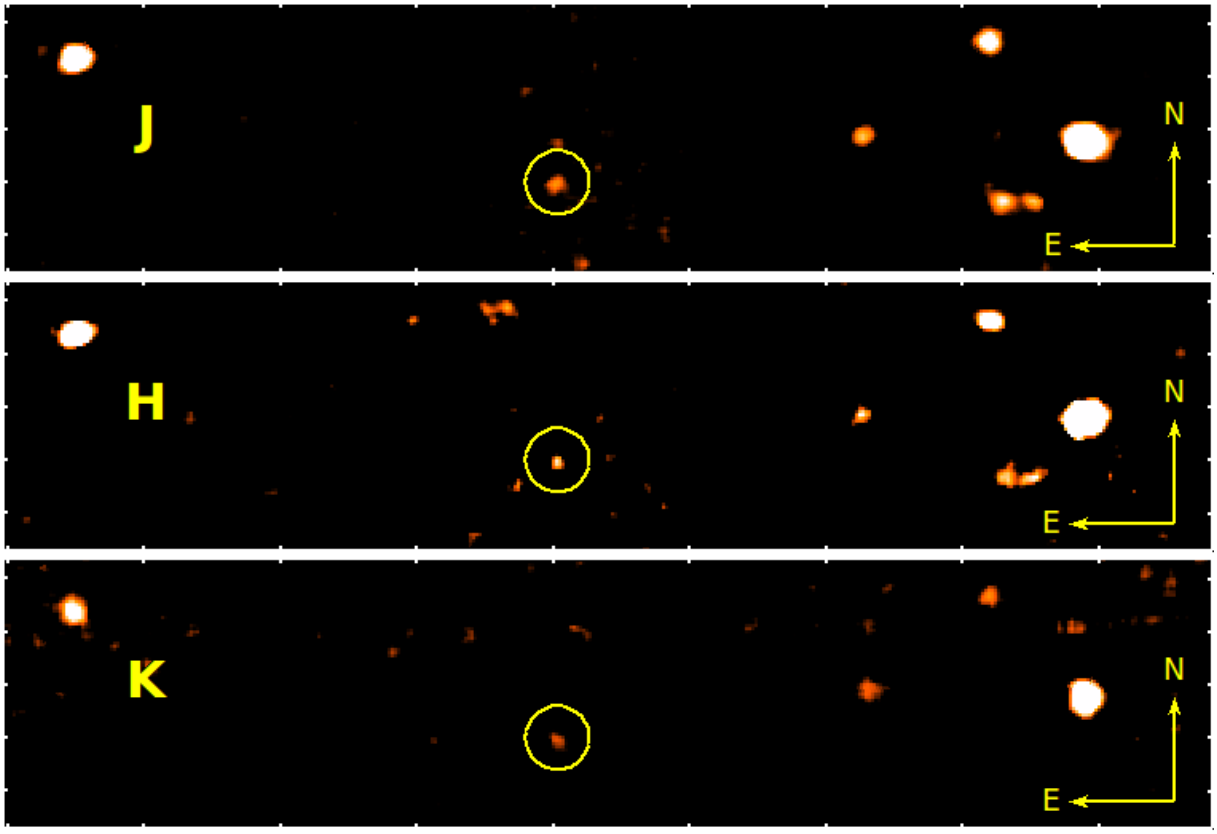

Figure 5.7. GROND JHK_s images at 7.6 days after the trigger. The circle around the AG position has a 3-arcsec radius.

the GROND filters and their corresponding statistical uncertainty are $A_{g',\mathrm{host}} = 0.25 \pm 0.03$, $A_{r',\mathrm{host}} = 0.18 \pm 0.02$, $A_{i',\mathrm{host}} = 0.14 \pm 0.02$, $A_{z',\mathrm{host}} = 0.11 \pm 0.01$, $A_{J,\mathrm{host}} = 0.07 \pm 0.01$, $A_{H,\mathrm{host}} = 0.04 \pm 0.01$, and $A_{K_s,\mathrm{host}} = 0.026 \pm 0.003$, all in units of magnitude.

5.3 Quasi-Bolometric Light Curves

To isolate the SN from the AG evolution, the light-curve models computed in §5.1 were employed. The AG contribution was calculated from the model for the stages were the SN bump was observed and it was subtracted from the light curves for each filter. The uncertainties in the model were appropriately propagated to the final magnitude errors. After the AG subtraction, quasi-bolometric light curves were computed as described in §2.3.6 for each of the four events. Used to transform fluxes to luminosities, the luminosity distances to the host galaxies of the transients in the sample have been computed following the standard ΛCDM model, using the redshift measurements in Table 5.1, a Hubble constant of 74.2 km s^{-1} Mpc^{-1} (Riess et al., 2009), and the model of the local velocity field by Mould et al. (2000), whose corrections have been implemented at the NED website[2]. The distances employed are 2885 Mpc for GRB 081007/SN 2008hw, 2628 Mpc for GRB 091127/SN 2009nz, 1879 Mpc for GRB 100902A (under the assumption $z = 0.37$ from the SN scenario in §5.2), and 3022 Mpc for GRB 101219B/SN 2010ma. The uncertainties in the luminosity distance are of estimated at $\sim 10\%$ and have not

[2] `http://nedwww.ipac.caltech.edu/`

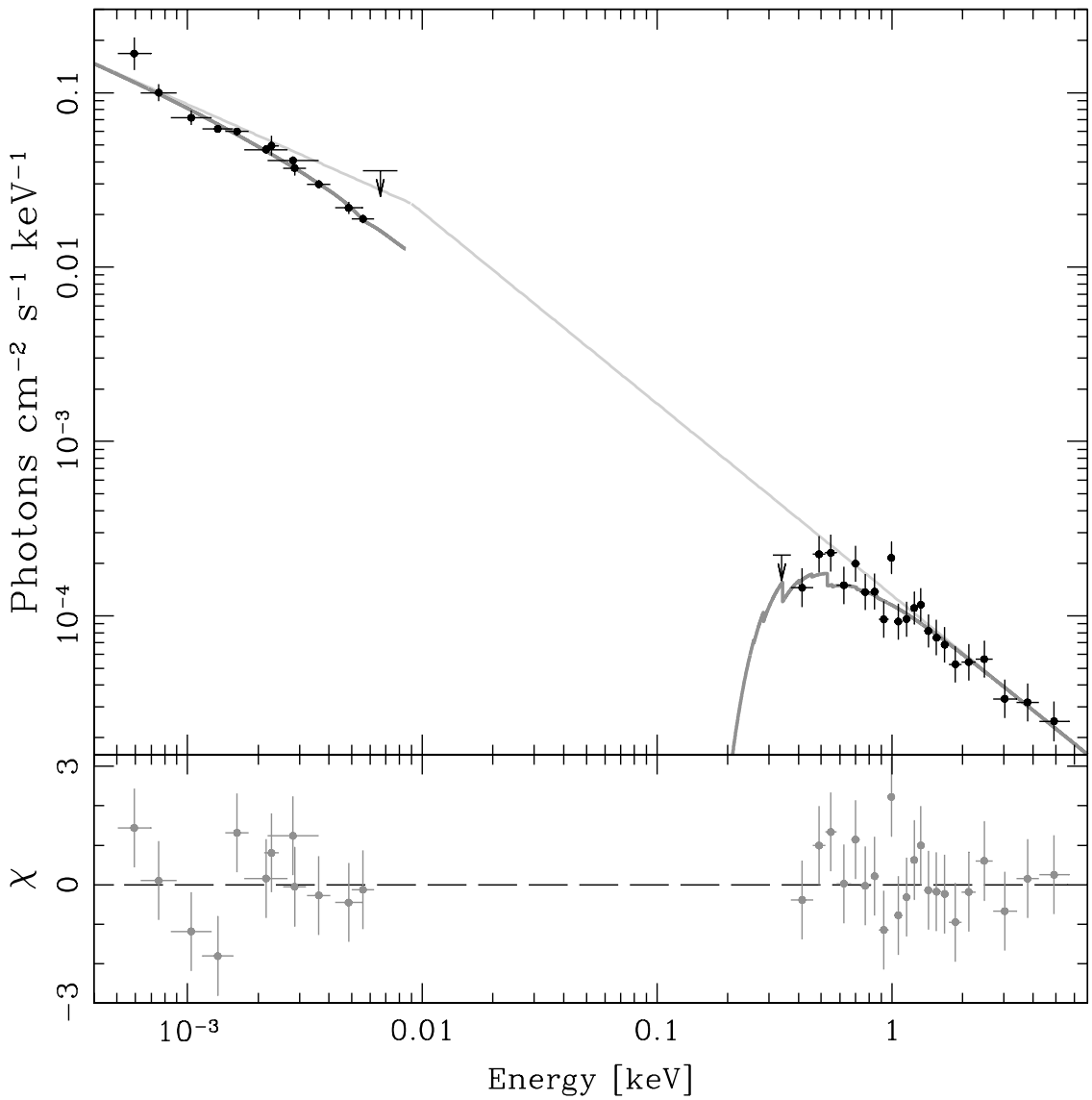

Figure 5.8. Broad-band SED of GRB 101219B at 9.0 h after trigger. The observed data are represented by black filled circles. The UV bands provide 3σ upper limits shown as arrows. The thick grey line shows the best-fit model able to reproduce the data: the broken power law. The thin continuous grey line shows the unextinguished versions of the model. In the lower panel, the residuals of the best fit are plotted.

Table 5.6. SED modelling of the optical/NIR rebrightening of GRB 100902A.

Template/Model	z	Age/$\beta_{\rm opt}$ [a]	$A_{V,\rm host}$ [mag]	Goodness [b]
SN04aw (Ic)	0.19 ± 0.01	31.9	···	5.0
SN02ap (Ic-BL)	0.43 ± 0.02	-5.5	···	4.3
SN98bw (Ic-BL)	0.31 ± 0.02	-5.0	···	3.7
SN06aj (Ic-BL)	0.10 ± 0.03	66.1	···	2.1
Power Law (MW)	3.3 ± 0.1	$0.6^{+0.2}_{-0.3}$	0.7 ± 0.2	0.5
Power Law (LMC)	3.1 ± 0.1	$0.2^{+0.3}_{-0.2}$	0.8 ± 0.2	1.1
Power Law (SMC)	3.6 ± 0.2	0.6 ± 0.4	0.0 ± 0.1	5.8

[a] Age since V-band maximum for SN templates and optical spectral slope $\beta_{\rm opt}$ for power-law models.
[b] Quality parameter r of the SNID fitting (Blondin and Tonry, 2007) for SN templates and classical reduced χ^2 for power-law models.

been included in the quasi-bolometric light curves. The resulting luminosity measurements are presented in Fig. 5.9.

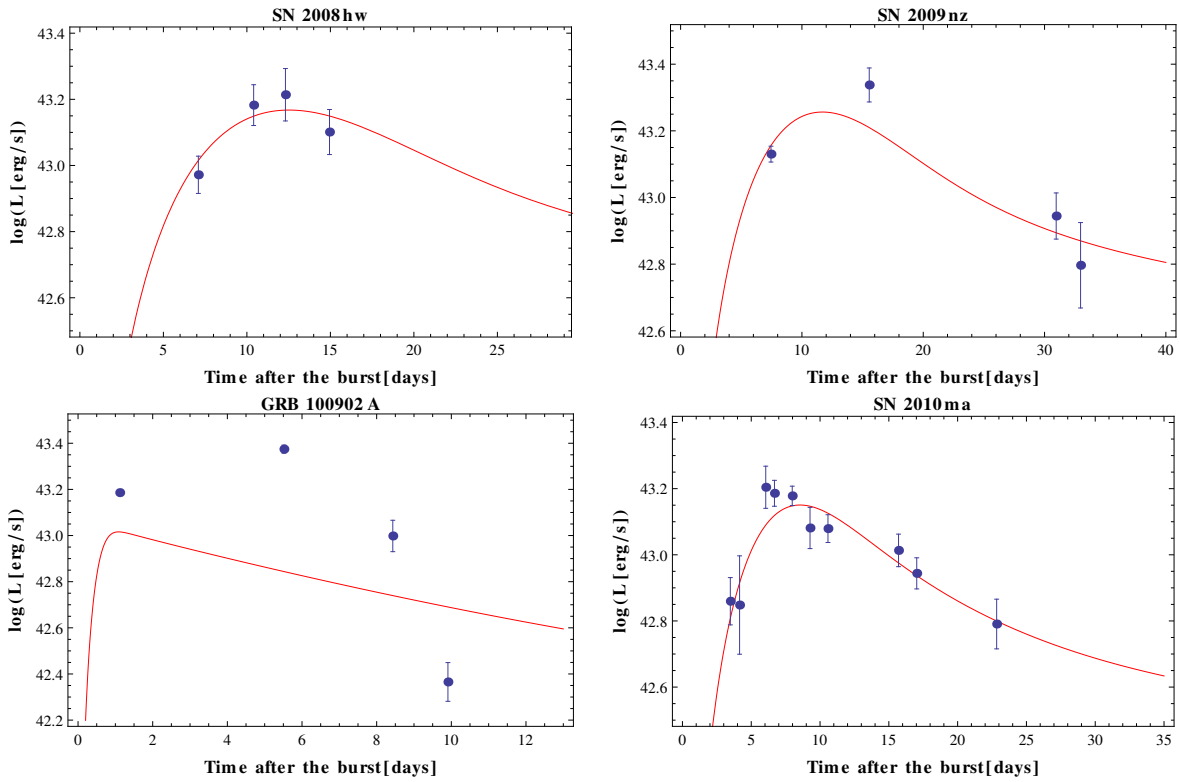

Figure 5.9. Quasi-bolometric light curves. The Arnett's model described by eq. 2.6 is shown in red (see §5.3.1).

5.3.1 Physical Parameters of the Explosion

From the quasi-bolometric light curves, the physical parameters of the explosion were calculated by using Arnett's approach for ^{56}Ni-powered SNe (eq. 2.6) to fit the luminosity. The resulting parameters are compiled in Table 5.7 and the models are plotted along with the measurements in Fig. 5.9.

Table 5.7. Physical parameters of the modelling of the quasi-bolometric light curve.

SN	$M_{\rm Ni}$ [$M_\odot$]	$M_{\rm ej}$ [$M_\odot$]	$E_{\rm k}$ [10^{51} erg]
2008hw	0.54 ± 0.08	2.0 ± 0.7	7.5 ± 2.5
2009nz	0.62 ± 0.08	1.9 ± 1.2	9.1 ± 5.7
100902A	0.15 ± 0.08	0.005 ± 0.666	0.02 ± 2.50
2010ma	0.39 ± 0.03	0.75 ± 0.10	2.8 ± 0.4

Note.— The photospheric velocity at maximum was assumed to be 15,000 km s^{-1}, except in the case of SN 2009nz, for which a velocity of 17,000 km s^{-1} was estimated (Berger et al., 2011). The values for the kinetic energy $E_{\rm k}$ were computed using eq. 3.3.

The NIR component of the bolometric flux, which remained undetected for SNe 2008hw, 2009nz, and 2010ma, was estimated from the NIR data of SNe 1998bw, 2002ap, and 2006aj compiled by Valenti et al. (2008). The NIR fraction of the UV/optical/NIR (UVOIR) bolometric luminosity as a function of time in days after the GRB $f_{\rm NIR}$ and the corresponding uncertainty $\sigma_{f_{\rm NIR}}$ are approximated by

$$\begin{aligned} f_{\rm NIR}(t) &= \begin{cases} 0.0075\,t + 0.22 & \text{if } t \leq 20 \text{ d} \\ 0.0020\,t + 0.33 & \text{if } t > 20 \text{ d} \end{cases} \\ \sigma_{f_{\rm NIR}}(t) &= \begin{cases} 0.002\,t + 0.02 & \text{if } t \leq 20 \text{ d} \\ 0.001\,t + 0.06 & \text{if } t > 20 \text{ d.} \end{cases} \end{aligned} \tag{5.2}$$

This set of linear estimates are only valid for $t < 40$ d. The slope change relies on the fact that after $t = 20$ d the NIR light starts reaching its maximum and the bolometric fraction grows more slowly. The growth of the uncertainty at $t < 20$ d reflects the fact that the NIR bolometric fraction of the reference sample (SNe 1998bw, 2002ap, and 2006aj) evolves from a tight uniformity toward a larger dispersion. The uncertainty is higher after $t > 20$ d due to the lack of reference data at these stages.

The UV contribution is estimated to be negligible below 2500 Å due to blanketing/absorption of numerous metal lines, therefore, when needed, the UV correction was computed by integrating a linear function from the bluest detection available backwards to zero density flux at 2500 Å. This practice is very common when working out quasi-bolometric light curves (e.g., Folatelli et al., 2006).

Given the lack of detections at late times, no nebular component was fitted and therefore only one envelope component was considered, unlike the case of SN 2010bh in §3.5.1 (see §2.3.6 for details on the modelling). For simplicity, the expression for the photospheric expansion velocity from Arnett (1982) was used as described in the case of SN 2010bh by eq. 3.3. When no spectroscopic measurement of the expansion velocity was available in the literature, the standard

$v = 15,000$ km s^{-1} was used. This value represent most GRB-SNe at maximum luminosity as shown by Bufano et al. (2012).

To compute the uncertainties in $M_{\rm Ni}$, $M_{\rm ej}$, and $E_{\rm k}$ shown in Table 5.7, I performed 1000 Monte-Carlo simulations for each event. The resulting histograms for $M_{\rm Ni}$ and $M_{\rm ej}$ were modelled with normal distributions. These fits were used to obtain the final mean values and their corresponding uncertainties from the width of the Gaussian functions.

As shown in Fig. 5.9 with red solid lines, the quasi-bolometric light curves are reasonably well modelled with exception of GRB 100902A, for which the model employed evolves too slowly after maximum. Along with the SED analysis presented in the previous section, this is yet another reason to believe that the rebrightening in the AG of GRB 100902A is inconsistent with the SN nature.

For the case of SN 2009nz, Berger et al. (2011) obtained a value for $M_{\rm Ni}$ almost twice smaller (~ 0.35 M$_\odot$) than the result presented here. This is explained, because they used the photometric results from Cobb et al. (2010c), which consist of I-band observations only. Given that the results in this section were computed from SN detections in three GROND bands ($r'i'z'$) and included UV/NIR corrections, the value $M_{\rm Ni} = 0.62 \pm 0.08$ M$_\odot$ obtained previously proves much more reliable. The value of $M_{\rm ej}$ is consisted with that presented by Berger et al. (2011). The shape of the bolometric light curve, which resembles the optical evolution of the luminosity, depends strongly on $M_{\rm ej}$, therefore it is logical that this parameter matches single-band photometric studies. Regarding SNe 2008hw and 2009nz, no detailed photometric studies have been published for these yet. The comparison of SNe 2008hw, 2009nz, and 2010ma against the complete GRB-SN sample is presented in the next chapter.

Chapter 6

The Updated Sample of GRB-connected SNe

Until the end of the year 2010 the sample of SNe associated to GRBs counts with 28 events in total: 6 solid spectroscopic SN confirmations (Table 1.1), other 6 events classified as SNe due to their spectral broad-line features (SNe 2001ke, 2002lt, 2005nc, 2008hw, 2009nz, and 2010ma), and 16 late-time photometric rebrightenings consistent with the SN nature but had no IAU SN classification and therefore no name (see column 2 of Table 6.1). Data was retrieved from the published work of several authors in literature and is shown in Table 6.1. The more recent events of GRB 111209A and GRB 120422A/SN 2012bz were also observed by GROND and will be soon published (D. A. Kann et al.; S. Schulze et al., respectively, both in preparation). The total number of events becomes now appropriate for sample studies, such as distribution and correlation analyses as detailed in the next sections.

6.1 Luminosity, Stretch, and Redshift

The parameter for the optical brightness will be the optical luminosity ratio $k_{\rm opt}$ (column 4, Table 6.1) defined in §2.3.3 with respect to the luminosity of the emblematic SN 1998bw. In a few cases, this parameter is unavailable from literature directly and instead the absolute V-band magnitude M_V is published. The transformation

$$k_{\rm opt} = 10^{-0.4(M_V - M_{V,98\rm bw})} \tag{6.1}$$

is used to obtain the $k_{\rm opt}$ values from M_V, where $M_{V,98\rm bw}$ is the absolute magnitude of SN 1998bw. Both magnitude quantities should be come from the same cosmological model and are corrected otherwise. Given their proximity in the energy spectrum and because is in the optical range where most SNe show their maxima (i.e., a more or less constant flux density), the r' band ($\lambda_{\rm eff} = 625$ nm) and the V band ($\lambda_{\rm eff} \simeq 550$ nm) are considered to be equivalent for the purposes of optical analysis. The extinction correction in the line of sight through the host galaxy was computed using diverse methods (see references in Table 6.1). Using the curvature in the optical AG SED to calculate $A_{V,\rm host}$ (e.g., §5.2) and obtaining the extinction from the Na I-D interstellar absorption line after assuming a universal gas-to-dust ratio are among the most employed approaches to correct $k_{\rm opt}$. For all 26 events in Table 2.3.3, an $k_{\rm opt}$ estimate corrected for $A_{V,\rm host}$ was obtained from the literature. If no uncertainty is available, a conservative 15% is utilised.

Table 6.1. The complete sample of GRB-SNe.

GRB	SN	z	$k_{\rm opt}$	$s_{\rm opt}$	$M_{\rm Ni}$ [$M_\odot$]	$M_{\rm ej}$ [$M_\odot$]	$E_{\rm k}$ [10^{51} erg]	T_{90}(obs) [s]	$E_{\rm peak}$(obs) [keV]	$E_{\gamma,\rm iso}$ [10^{51} erg]	Refs.
970228	···	0.695	0.40 ± 0.29	···	~ 0.36	~ 6.11	~ 23.2	$\sim 80^{a}$	$\sim 60^{b}$	$4.74 \pm 0.28^{\rm Band}$	1,2,3
980425	1998bw	0.0085	1	1	~ 0.39	~ 10	~ 50	23.3 ± 1.4^{c}	148 ± 33^{c}	$0.001 \pm 0.0001^{\rm Band}$	4,5
990712	···	0.433	0.35 ± 0.09	0.83 ± 0.13	~ 0.13	~ 1.4	~ 5.32	$\sim 40^{a}$	···	$7.11 \pm 0.33^{\rm PWL}$	1,2,6
991208	···	0.706	$2.62^{+1.10}_{-0.65}$	1.12 ± 0.20	···	···	···	$\sim 68^{d}$	···	$581 \pm 56^{\rm PWL}$	1,7,8
000911	···	1.058	$0.85^{+0.44}_{-0.26}$	1.40 ± 0.32	···	···	···	$\sim 306^{e}$	$\sim 714^{e}$	$\sim 533^{\rm Band}$	1,9,10
010921	···	0.450	$1.85^{+2.82}_{-0.79}$	0.69 ± 0.25	···	···	···	$\sim 22^{f}$	$89^{+22}_{-14}{}^{f}$	$11.21 \pm 0.7^{\rm CPL}$	1,11,12
011121	2001ke	0.362	$0.88^{+0.08}_{-0.07}$	0.80 ± 0.02	~ 0.49	~ 3.73	~ 14.2	$\sim 30^{g}$	···	$23.4 \pm 4.7^{\rm PWL}$	1,2,13
020405	···	0.691	$0.90^{+0.15}_{-0.11}$	0.97 ± 0.07	~ 0.48	~ 2.92	~ 11.1	$\sim 40^{d}$	···	···	1,2,14
020903	···	0.251	0.62 ± 0.09	0.92 ± 0.08	···	···	···	10.0 ± 0.7^{f}	$2.6^{+1.4}_{-0.8}{}^{f}$	$0.018^{+0.011}_{-0.005}{}^{\rm Band}$	1,11
021211	2002lt	1.006	0.40 ± 0.19	0.98 ± 0.26	···	···	···	13.3 ± 0.3^{f}	$46^{+8}_{-6}{}^{f}$	$12.5 \pm 0.8^{\rm Band}$	1,11
030329	2003dh	0.1685	$1.50^{+0.19}_{-0.16}$	0.85 ± 0.10	~ 0.35	~ 8	~ 40	33.1 ± 0.5^{f}	68 ± 2^{f}	$5.34 \pm 0.05^{\rm Band}$	1,15,11
031203	2003lw	0.1055	$1.28^{+0.18}_{-0.16}$	1.09 ± 0.07	~ 0.53	~ 13	~ 60	37.0 ± 1.3^{h}	···	$0.15 \pm 0.03^{\rm PWL}$	1,16,17,18
040924	···	0.859	~ 0.25	···	···	···	···	$\sim 1.2^{f}$	$\sim 73.2^{f}$	$\sim 18.4^{\rm CPL}$	19,20,21,12
041006	···	0.716	$1.03^{+0.22}_{-0.09}$	1.38 ± 0.06	~ 0.63	~ 3.81	~ 14.5	27.3 ± 1.44^{f}	22.5 ± 1.7^{f}	$20.0^{+3.6}_{-2.8}{}^{\rm BPL}$	1,2,2
050416A	···	0.654	~ 1.0	···	···	···	···	2.9 ± 0.3^{i}	15 ± 5^{i}	$0.92^{+0.46}_{-0.18}{}^{\rm CPL}$	23,24
050525A	2005nc	0.606	$0.66^{+0.10}_{-0.08}$	0.77 ± 0.04	~ 0.27	~ 4.14	~ 15.7	9.10 ± 0.07^{i}	84.1 ± 1.7^{e}	$85.6 \pm 0.7^{\rm CPL}$	1,2,24,25
050824	···	0.828	1.05 ± 0.42	0.52 ± 0.14	···	···	···	38 ± 5^{i}	$13^{+2}_{-12}{}^{i}$	$1.29^{+7.42}_{-0.35}{}^{\rm CPL}$	26,24
060218	2006aj	0.0334	0.67 ± 0.05	0.67 ± 0.01	~ 0.21	~ 2	~ 2	128 ± 4^{i}	$41^{+30}_{-17}{}^{i}$	$(3.0^{+0.6}_{-0.2})\mathrm{E}+04^{\rm CPL}$	1,27,24
060729	···	0.543	1.01 ± 0.06	···	···	···	···	120 ± 2^{i}	$67^{+229}_{-25}{}^{i}$	$6.54^{+5.75}_{-0.12}{}^{\rm CPL}$	28,24
070419A	···	0.971	1.00 ± 0.05	···	···	···	···	160 ± 14^{i}	$27^{+16}_{-19}{}^{i}$	$3.49^{+3.35}_{-0.07}{}^{\rm CPL}$	29,24
080319B	···	0.937	~ 0.76	···	···	···	···	$\sim 57^{i}$	$651.^{+13}_{-14}{}^{e}$	$1230^{+31}_{-28}{}^{\rm Band}$	30,31,32
081007	2008hw	0.5295	0.80 ± 0.10	0.85 ± 0.11	0.54 ± 0.08	2.0 ± 0.7	7.5 ± 2.5	10 ± 4.5^{i}	40 ± 10^{j}	$1.28 \pm 0.11^{\rm CPL}$	33,34
090618	···	0.54	1.36 ± 0.17	···	···	···	···	133.2 ± 0.6^{i}	$155.5^{+11.1}_{-10.5}{}^{j}$	$233.1 \pm 5.2^{\rm Band}$	35,28,36
091127	2009nz	0.490	1.15 ± 0.09	1.03 ± 0.04	0.62 ± 0.08	1.9 ± 1.2	9.1 ± 5.7	7.1 ± 0.2^{i}	36 ± 2^{j}	$14.93 \pm 0.16^{\rm Band}$	37,38
100316D	2010bh	0.0591	0.65 ± 0.05	0.78 ± 0.01	0.21 ± 0.03	2.6 ± 0.2	24 ± 7	$\sim 1300^{i}$	$19.6^{+3.3}_{-2.8}{}^{i}$	$0.142 \pm 0.038^{\rm CPL}$	39,40,41,42
101219B	2010ma	0.5519	$1.78^{+0.08}_{-0.17}$	0.76 ± 0.10	0.39 ± 0.03	0.75 ± 0.10	2.8 ± 0.4	34 ± 5^{i}	70 ± 8^{j}	$5.60 \pm 0.41^{\rm Band}$	43,44
111209A	···	0.677	2.12 ± 0.17	1.29 ± 0.05	···	···	···	$\sim 1500^{i}$	310 ± 53^{e}	$606 \pm 76^{\rm CPL}$	45,46,47
120422A	2012bz	0.2831	2.53 ± 0.04	0.90 ± 0.01	0.53 ± 0.01	5.87 ± 0.03	41.0 ± 0.03	5.35 ± 1.4^{i}	···	$0.123 \pm 0.02^{\rm PWL}$	48,49

Note.— Along with the $E_{\gamma,\rm iso}$ values, the spectral model is shown. The references are (1) Ferrero et al. (2006), (2) Richardson (2009), (3) Costa et al. (1997a), (4) Galama et al. (1998b), (5) Nakamura et al. (2001), (6) Frontera et al. (2001), (7) Hurley and Cline (1999), (8) Hurley et al. (2000a), (9) Hurley et al. (2000b), (10) Price et al. (2002), (11) Sakamoto et al. (2005), (12) `http://space.mit.edu/HETE/Bursts/`, (13) Greiner et al. (2003), (14) Hurley et al. (2002), (15) Mazzali et al. (2003), (16) Mazzali et al. (2006b), (17) Watson et al. (2004), (18) Sazonov et al. (2004), (19) Soderberg et al. (2006), (20) Fenimore et al. (2004), (21) Golenetskii et al. (2004), (23) Soderberg et al. (2007), (24) Butler et al. (2007), (25) Golenetskii et al. (2005), (26) Sollerman et al. (2007), (27) Nomoto et al. (2010), (28) Cano et al. (2011b), (29) Hill et al. (2007), (30) Vreeswijk et al. (2008), (31) Golenetskii et al. (2008), (32) Tanvir et al. (2010), (33) Markwardt et al. (2008), (34) Bissaldi et al. (2008), (35) Baumgartner et al. (2009), (36) McBreen (2009), (37) Stamatikos et al. (2009), (38) Wilson-Hodge and Preece (2009), (39) Olivares E. et al. (2012), (40) Starling et al. (2011), (41) Sakamoto et al. (2010a), (42) Fan et al. (2011), (43) Cummings et al. (2010), (44) van der Horst (2010), (45) Palmer et al. (2011), (46) Golenetskii et al. (2011b), (47) A. Kann (2013, in preparation), (48) Barthelmy et al. (2012), (49) S. Schulze (2013, in preparation).

[a] BeppoSAX/GRBM, [b] TGRS/Wind, [c] CGRO/BATSE, [d] Ulysses/GRB, [e] Konus-Wind, [f] HETE-2/FREGATE, [g] Mars-Odyssey/HEND, [h] INTEGRAL/IBIS, [i] Swift/BAT, [j] Fermi/GBM.

To quantify the evolution of the optical light, the stretch factor $s_{\rm opt}$ will be employed, which is defined with respect to SN 1998bw (see §2.3.3). Five objects do not have such a parameter published in the literature due to insufficient data quality.

Most $k_{\rm opt}$ and $s_{\rm opt}$ values have been taken from the work by Ferrero et al. (2006). Redshift values in column 2 of Table 6.1 have been extracted from spectroscopic analyses (see last column for references), mostly from the host-galaxy absorption lines of different species. In the following, the observational properties of these SNe are analysed statistically. The redshift z, the luminosity ratio $k_{\rm opt}$, and the stretch factor $s_{\rm opt}$ are presented in distributions and for the latter two their cosmic evolution is assessed.

Figure 6.1 shows the redshift distribution of 26 GRB-SN associations. Within Poisson errors, the distributions is approximately flat. However, it peaks at $z \sim 0.6$ and presents a secondary peak at the low-redshift edge ($z < 0.2$), which represents the 18% of all events and comprises five spectroscopically confirmed SNe. After the primary peak at $z \sim 0.6$, the distribution drops up to redshifts were no detections are possible ($z > 1.2$). No cosmic evolution of the GRB-SN luminosity function can be measured with the current data set.

Next I studied the optical luminosity and stretch distributions of the GRB-SN sample. The distribution of the luminosity ratio $k_{\rm opt}$ with respect to SN 1998bw as defined in §2.3.3 (left panel of Fig. 6.2) grows smoothly from zero to unity. It peaks at around $k_{\rm opt} = 1$, which suggests most GRB-SN events have luminosities similar to that of SN 1998bw. For $k_{\rm opt} > 1$ the the number of events drops more steeply with only five events at $k_{\rm opt} \geq 1.5$. These most luminous GRB-SNe were associated to GRB 991208, GRB 010921 (both taken from Ferrero et al., 2006), GRB 030329/SN 2003dh (Zeh et al., 2006), GRB 111209A (D. A. Kann et al., in preparation), and GRB 120422A/SN 2012bz (S. Schulze et al., in preparation), the latter the most luminous GRB-SN spectroscopically classified to date. The former two cases are not as solid as the latter

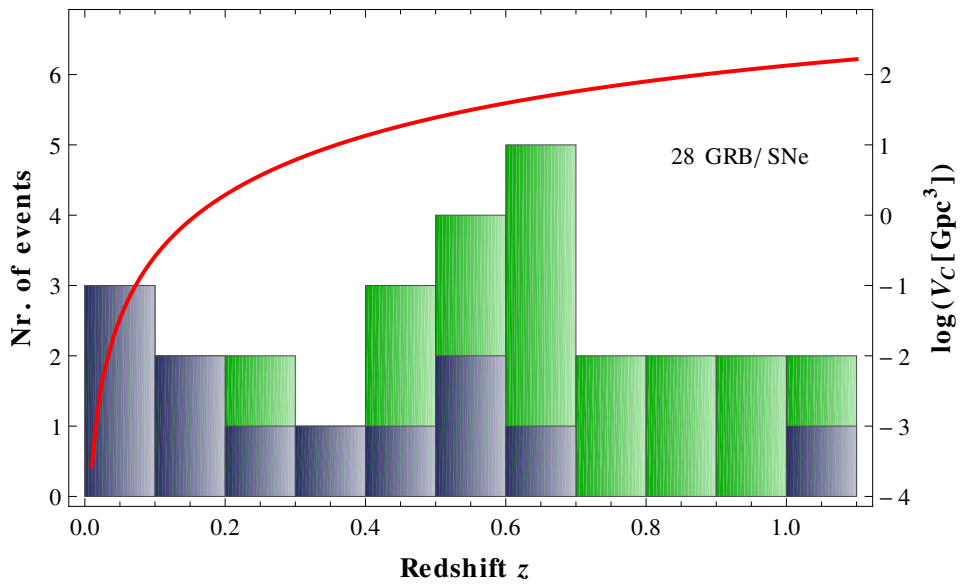

Figure 6.1. The redshift distribution of GRB-associated SNe. The blue histogram represents the 11 GRB-SNe that have shown broad-line features in their spectra. The green histogram shows the GRBs, for which a photometric SN bump has been detected. Additionally, the red line depicts the logarithm of the co-moving volume V_C as a function of redshift (right vertical axis).

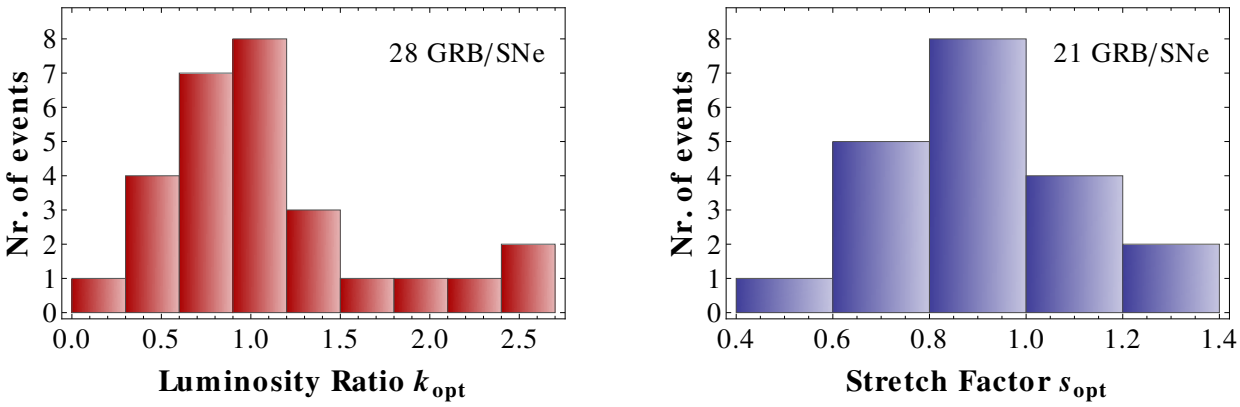

Figure 6.2. Distributions of luminosity ratios $k_{\rm opt}$ (dark red histogram, left panel) and stretch factors $s_{\rm opt}$ (dark blue histogram, right panel) both with respect to SN 1998bw (see §2.3.3 for detailed definitions) for the GRB-SN sample. Availability of $s_{\rm opt}$ depends mainly on the data quality.

three; the 3σ lower limits for the SN luminosity of GRBs 991208 and 010921 are $k_{\rm opt} > 0.67$ and $k_{\rm opt} > 0$, respectively, showing the low significance of the SN bump of GRB 010921. In an attempt to find the most luminous GRB-SN, the brightest 3σ $k_{\rm opt}$ lower limits are those of SN 2010ma at $k_{\rm opt} > 1.3$ (see Sect. 5.1), SN 2003dh at $k_{\rm opt} > 1.0$, that of GRB 111209A at $k_{\rm opt} > 1.6$, and that of SN 2012bz at $k_{\rm opt} > 2.4$. In conclusion, GRB-SNe more luminous than SN 1998bw are rare with only four statistically significant cases (about 14% of events in the whole sample). On the low luminosity end, the SN bump of GRB 040924 stands alone in the $0 < k_{\rm opt} < 0.3$ bin with $k_{\rm opt} \simeq 0.25$ (Soderberg et al., 2006).

Regarding the stretch-factor distribution in the right panel of Fig. 6.2, it resembles quite well a normal distribution peaking at $s_{\rm opt} \sim 0.9$ (see definition of $s_{\rm opt}$ in §2.3.3). Thus, most GRB-SNe evolved roughly like SN 1998bw in the optical bands. Nevertheless, the mean value of $s_{\rm opt}$ shows also that the evolution of SN 1998bw is slightly slower compared to all GRB-SNe, which tend to evolve more like SN 2003dh or SN 2012bz.

Figure 6.3 shows the optical luminosity ratios $k_{\rm opt}$ against the redshift in an attempt to assess the cosmic evolution of the GRB-SN luminosity. Although no events with $k_{\rm opt} < 0.5$ have been detected at redshifts below $z \approx 0.4$, this can be explained as a selection effect. Since low-luminosity GRB-SNe are less common (as shown in Fig. 6.2) and at low redshifts smaller volumes are being probed, it becomes clear that only the most common SNe will be detected at low redshifts, which are those with $k_{\rm opt} \sim 0.9$. No other trend appears clear to the eye, apart from a low-significance lack of events at $z > 0.8$.

6.2 Correlations with Explosion Parameters

In the following, theoretical values derived from the observed data are statistically analysed. Columns 6, 7, and 8 of Table 6.1 present respectively the synthesised nickel mass $M_{\rm Ni}$, the ejecta mass $M_{\rm ej}$, and the kinetic energy of the explosion $E_{\rm k}$. This values have been obtained from the literature and given the variety of cosmologies employed, the $M_{\rm Ni}$ values have been corrected to the standard ΛCDM model [1] prior tabulation. The values coming from spectral modelling (SNe

[1] A Hubble constant of $H_0 = 74.2$ km s^{-1} Mpc^{-1} (Riess et al., 2009), $\Omega_M = 0.27$, and $\Omega_\Lambda = 0.73$ were utilised.

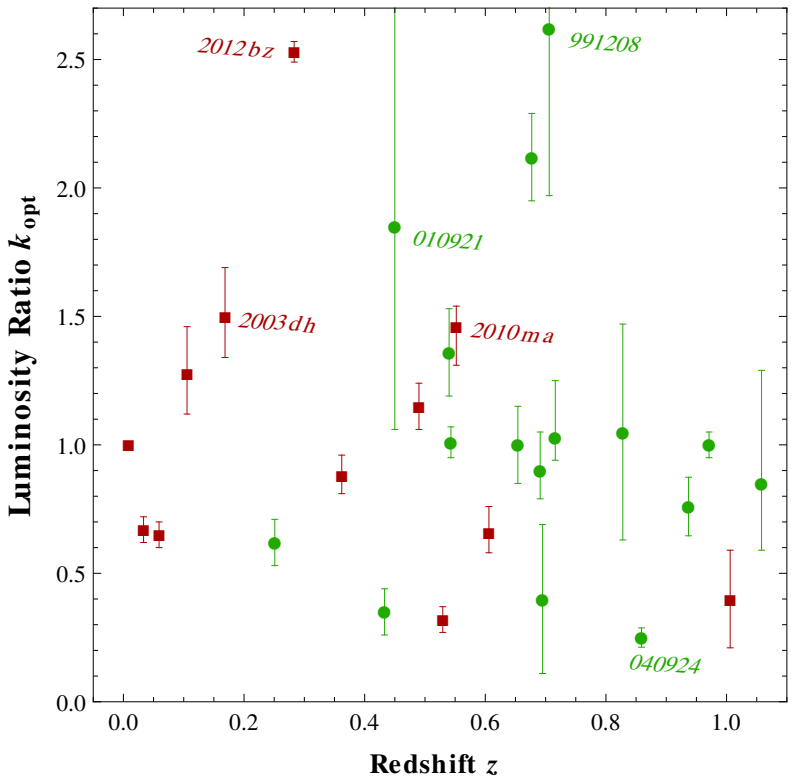

Figure 6.3. Cosmic evolution of the GRB-SN luminosities relative to SN 1998bw. Spectroscopically confirmed GRB-SNe are shown with dark red squares, whereas unclassified SN bumps are depicted by green circles.

2006aj, 2003lw, 2003dh, and 1998bw) and those obtained from the analysis by Richardson (2009) lack a proper uncertainty estimate. For these, a conservative 15% is employed. A comparison sample of 22 "normal" SNe Ibc was obtained from Drout et al. (2011) and the corresponding $M_{\rm Ni}$ values were also corrected to the standard cosmology. Note that the $M_{\rm ej}$ values assume photospheric expansion velocities of 10,000 and 20,000 km s^{-1} for type-Ibc and type-Ic BL SNe, respectively (Drout et al., 2011).

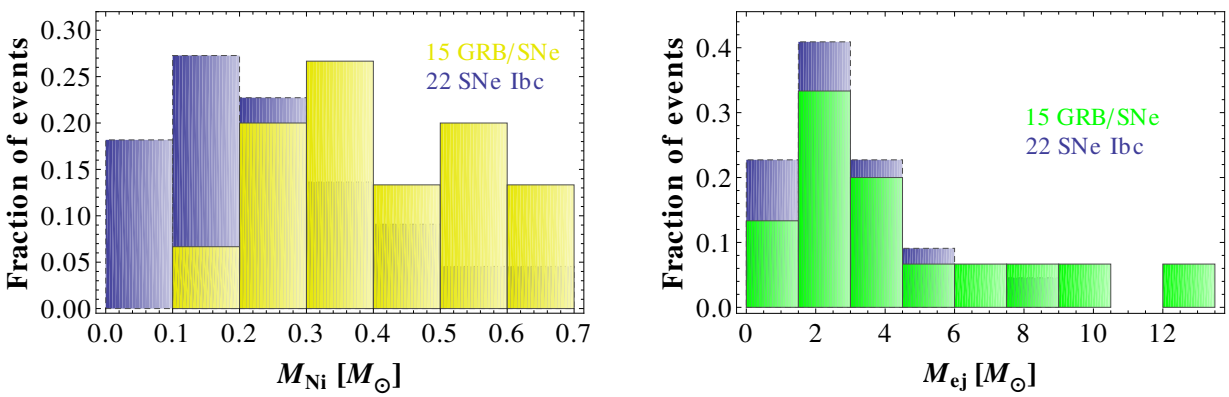

Figure 6.4. Distributions of the ^{56}Ni (yellow) and ejecta masses (cyan) for 15 GRB-SNe in the sample. The dashed blue distributions are from the SNe-Ibc sample.

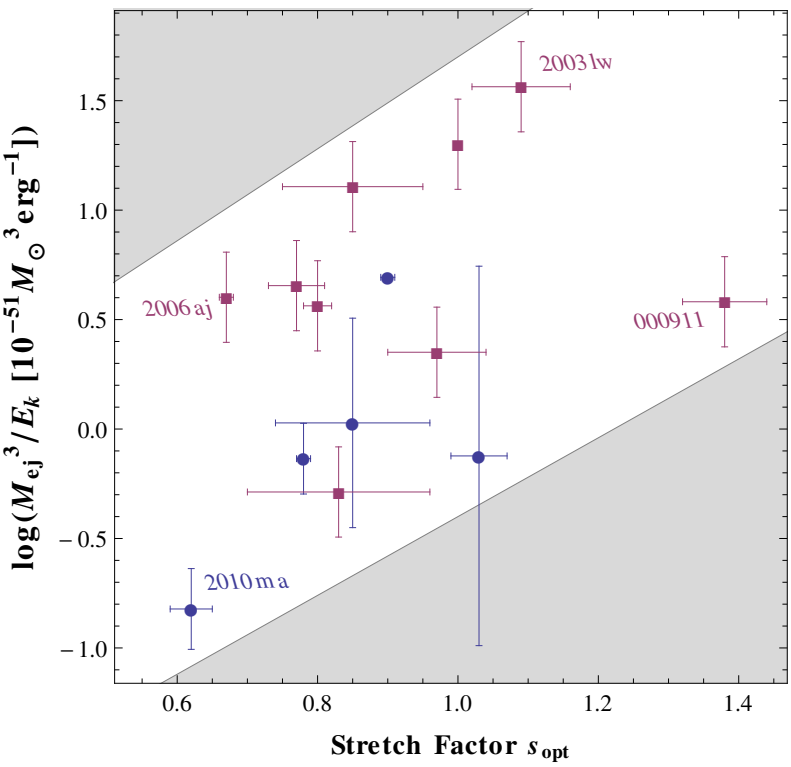

Figure 6.5. The stretch factor $s_{\rm opt}$ against $M_{\rm ej}^3/E_{\rm k}$, proportional to the time scale of the bolometric light-curve model (eq. 2.6). The grey shaded areas highlight the empty regions, which define the trend of the data points.

Figure 6.4 presents the distributions of the ^{56}Ni mass $M_{\rm Ni}$ on the left and that of the ejecta mass $M_{\rm ej}$ on the right for 15 GRB-SN events, for which these parameters could be determined. Additionally, the explosion masses of the SN-Ibc sample were plotted for comparison. The $M_{\rm Ni}$ distribution has a broad peak at $0.4-0.5\,{\rm M}_\odot$ and no event has $M_{\rm Ni} \lesssim 0.1\,{\rm M}_\odot$. The lack of events at $< 0.2\,{\rm M}_\odot$ is interpreted by the fact that the SNe producing little ^{56}Ni are those with less massive progenitors and therefore, less massive cores, which after collapse are unable to trigger the jet that powers the GRB. This fact is supported by the SNe-Ibc sample, which nickel masses are much smaller with $\sim 41\%$ of events having $M_{\rm Ni} < 0.2\,{\rm M}_\odot$. The smallest $M_{\rm Ni}$ for the GRB-SNe is $\sim 0.13\,{\rm M}_\odot$ from GRB 990712 (from Richardson, 2009, after H_0 scaling). If $M_{\rm Ni}$ correlates with luminosity (see Fig. 6.6), the SN bump of GRB 040924 stands as the less luminous GRB-SN ever observed, however, it lacks the proper $M_{\rm Ni}$ determination. Given these observational facts, the lower limit of the nickel mass that can be produced by GRB-SNe is placed at $0.07\,{\rm M}_\odot$ assuming a 15% uncertainty. This would correspond with a progenitor mass of $20\,{\rm M}_\odot$ roughly, more or less where the transition between NS and BH remnant is located (Nomoto et al., 2010).

The $M_{\rm ej}$ distribution in the right panel of Fig. 6.4 peaks strongly at $\sim 2\,{\rm M}_\odot$ similarly to the SN-Ibc sample. However, a high-mass tail, which does not show up in the distribution for SNe Ibc, extends up to $14.2\,{\rm M}_\odot$ for the case of GRB 011121/SN 2001ke (Richardson, 2009). There is an important fraction of events at the low mass end in both distributions, which is consistent with the stripped envelope scenario for this SN type (see §1.3).

The time scale of the bolometric light curve is proportional to $M_{\rm ej}^3/E_{\rm k}$ in the Arnett's model

(eq. 2.6). On the other hand, the stretch factor $s_{\rm opt}$ represents the rate at which the optical light curve evolves. Figure 6.5 shows these quantities plotted against each other for the sample presented in Table 6.1. A trend is evident to the eye, which is expected since $s_{\rm opt}$ and $M_{\rm ej}^3/E_{\rm k}$ trace the evolution of the optical light, however, no correlation can be obtained from such sparse set of data points. The scatter is due to the different choice of envelope opacity, which is also proportional to the light-curve time scale (see §2.3.6).

As mentioned before, from eq. 2.6 it is expected that luminosity would be correlated to the nickel mass. Exploring this with 14 events of Table 6.1 having $M_{\rm Ni}$ determination and using eq. 2.6 to compute the bolometric luminosity at maximum, I found that $L_{\rm max}$ correlates empirically with $M_{\rm Ni}$ through

$$M_{\rm Ni} = (0.39 \pm 0.12)\, \log L_{\rm max} - (16 \pm 5)\, {\rm M}_\odot \tag{6.2}$$

in the approximate range from $10^{42.6}$ to $10^{43.3}$ erg s^{-1} with a coefficient of determination[2] $R^2 = 0.96$. Figure 6.6 shows the data along with the linear regression and the corresponding 3-σ confidence contours. The SN events 2010bh, 2006aj, and 2010ma are outliers of this correlation both at smaller $M_{\rm Ni}$ than the lower confidence contour. The reason would lie in the dependence of eq. 2.6 also on $M_{\rm ej}$ and $E_{\rm k}$. As shown in Fig. 6.5, SN 2010ma has extreme values of light-curve time scale within the sample, which affects the value of $M_{\rm Ni}$. The case of SN 2010bh on the other hand is pretty similar to that of SN 2006aj, which has often been classified as peculiar. It has even been proposed that the multi-wavelength emission of SN 2006aj was produced by the tidal disruption of a white dwarf by a BH rather than by the core collapse of a massive star (Shcherbakov et al., 2012). Moreover, SN 2010bh is one of the fastest-evolving GRB-SNe in the sample (Olivares E. et al., 2012) along with SN 2010ma (see Fig. 5.9), which hints at an under-production of ^{56}Ni with respect to their maximum bolometric luminosity.

The values of $k_{\rm opt}$ serve as a proxy of the optical luminosity in Fig. 6.7, where the available data in Table 6.1 are plotted in the $M_{\rm Ni}$-$k_{\rm opt}$ plane. Two sets of data points were displayed separately. The blue circles represent the $M_{\rm Ni}$ determinations as computed in §3.5 for SN 2010bh and §5.3.1 for SNe 2008hw, 2009nz, and 2010ma. The remaining 10 events, for which the data has been taken from the literature, are shown with purple squares. There is a weak trend overall showing that more luminous objects have higher $M_{\rm Ni}$. A linear regression with slope 0.44 ± 0.07 and a poor $R^2 = 0.74$ has been fitted. The straight-line model is plotted in Fig. 6.7 along with its 3-σ confidence bands. However, SN 2008hw appears to have produce more nickel than expected from its optical luminosity. On the high-luminosity end, SNe 2003dh, 2010ma, and 2012bz appear to have produced less nickel than expected. A tight correlation was unexpected beforehand, because there are intrinsic differences between optical and bolometric light and the latter also depends on the $M_{\rm ej}$ and $E_{\rm k}$ parameters.

Figure 6.8 shows the explosion masses $M_{\rm Ni}$ and $M_{\rm ej}$ from Table 6.1 against each other. Two separate groups are immediately distinguishable: Group 1 that represent SNe with smaller ejecta masses ($M_{\rm ej} \lesssim 4\,{\rm M}_\odot$) but larger $M_{\rm Ni}$ and Group 2 that represent SNe with smaller nickel masses ($M_{\rm Ni} \lesssim 0.5\,{\rm M}_\odot$) but larger $M_{\rm ej}$. The SN 2003lw, which stands near the intersection, has been included in Group 2, which is better constrained. The best-fitting model is for both groups a straight line in the $M_{\rm Ni}$-$\log M_{\rm ej}$ plane. The model function resulted in the following equations

[2] The goodness of the fit is simply assessed through the coefficient of determination defined by $R^2 = 1 - \sum_i (y_i - f_i)^2 / \sum_i (y_i - \bar{y})^2$, where y_i are the data set values, $\bar{y}$ its mean value, and f_i the associated modelled value. The closer to unity is R^2, the better the fitting.

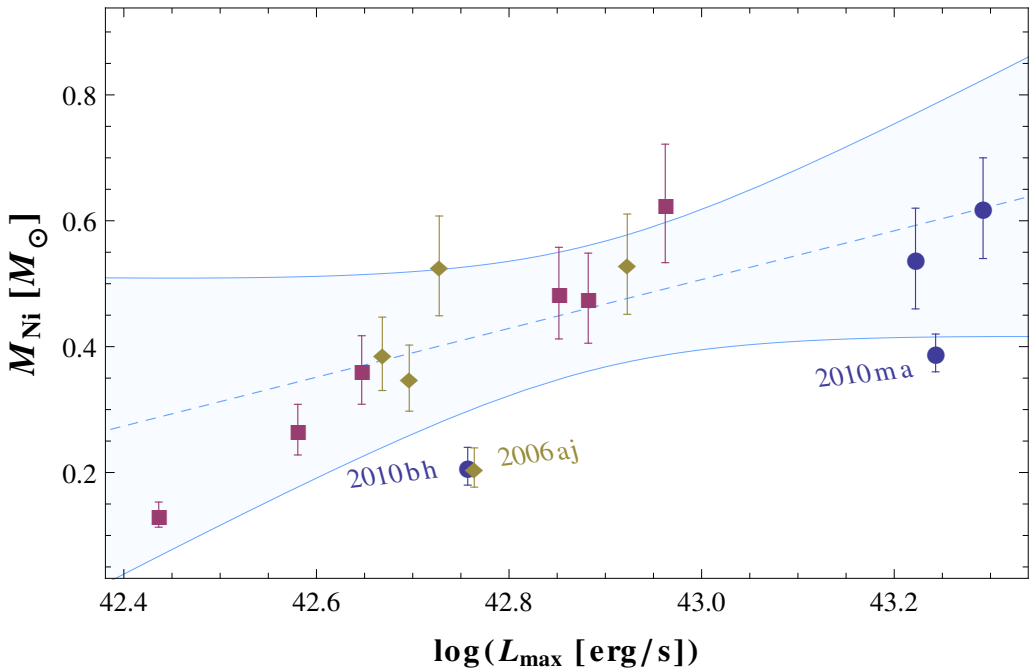

Figure 6.6. The nickel mass $M_{\rm Ni}$ against the maximum quasi-bolometric luminosity Lmax computed from the best-fitting bolometric model.

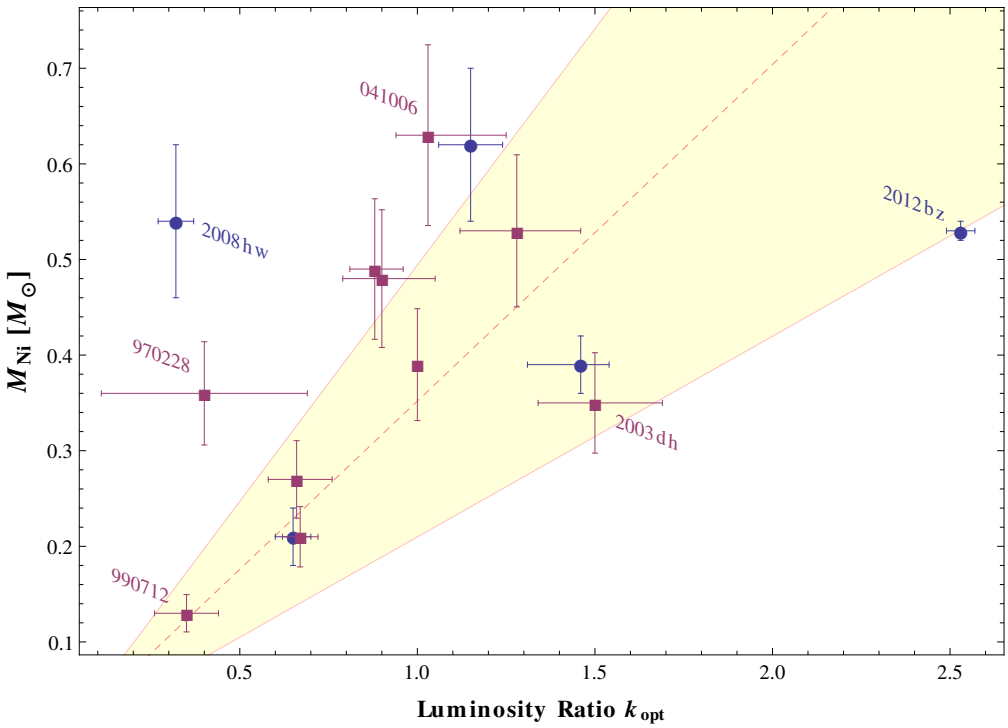

Figure 6.7. The nickel mass $M_{\rm Ni}$ against luminosity ratio $k_{\rm opt}$. While the pink dashed line show the linear regression, the light-yellow-shaded area represents the corresponding 2-σ confidence region. Events observed by GROND are depicted by blue circles, while the rest are shown in purple squares.

$$\text{Group 1:} \quad M_{\rm Ni} = (0.13 \pm 0.11)\, \log M_{\rm ej} + (0.47 \pm 0.05)\, {\rm M}_\odot \text{ and} \tag{6.3}$$

$$\text{Group 2:} \quad M_{\rm Ni} = (0.40 \pm 0.05)\, \log M_{\rm ej} + (0.04 \pm 0.04)\, {\rm M}_\odot, \tag{6.4}$$

which delivered R^2 values of 0.98 and 0.99, respectively. The corresponding 3-σ confidence regions are shown in Fig. 6.8.

In the ideal scenario of a single progenitor star, a correlation between $M_{\rm Ni}$ and $M_{\rm ej}$ is expected, because more massive progenitors have more massive envelopes (hence larger $M_{\rm ej}$) and synthesise more ^{56}Ni in their more massive and denser cores. However, in reality mass loss through pre-explosion winds and interaction with binary companions complicates the theoretical predictions (Nomoto et al., 2010). Here we propose that GRB-SN progenitors of Group 1 suffered mass loss mostly at their final stages, whereas the envelope mass loss occurred at early evolutionary stages for Group 2. This under the assumption that significant mass loss early in the main sequence would produce a smaller iron core just before the explosion. This would produce the higher $M_{\rm Ni}$ for Group 1, while lower $M_{\rm Ni}$ for Group 2. Therefore, we identify Group 1 as having more massive progenitors than Group 2. Moreover, more massive progenitors would have stronger winds and therefore smaller $M_{\rm ej}$ at the time of explosion.

The possible difference in mass-loss history between Groups 1 and 2 gives us insights on the different progenitor systems that gave birth to these explosive events. In this regard, Dessart et al. (2011) points out that SNe Ic, which are those with the most stripped progenitors and found to be associated to GRBs, could stem from both single- and binary-star evolution with an obvious bimodal distribution in $M_{\rm ej}$. Whereas an episodic mass loss applies for single stars, for binary systems a higher mass loss is expected. The similar $M_{\rm ej}$ in the observed bimodality of Fig. 6.8 suggests that the more massive progenitors of Group 1 events have lost more mass linking them to binary-star systems, whereas Group 2 events would be associated with single-star progenitors with lower mass loss.

The green open circles of Fig. 6.8 come from binary evolution models of SNe Ibc (Dessart et al., 2011) and are compared against observations. The masses of the primary star at the end of the main sequence are 3.8, 4.4, and 5.1 $\mathrm{M}_\odot$, which synthesised 0.184, 0.170, and 0.237 $\mathrm{M}_\odot$ of ^{56}Ni and expelled masses of 2.39, 2.91, and 3.61, respectively. For the three progenitors, binary interaction is assumed and taken into account in their mass-loss history. Although these progenitor models are artificially evolved until the iron-core stage and their explosion parameters lie just on top of our Group 2 objects, a little amount of hydrogen is included in the outermost layers (0.002, 0.008, 10^{-6} $\mathrm{M}_\odot$) and therefore these should be only considered as reference values. Contrary to the interpretation presented in the previous paragraph, these theoretical data suggest that the progenitors of Group 2 objects need a companion to end up with such ejected/nickel masses. The higher mass loss of Group 1 progenitors would suggest then that both groups are born from binary systems, where the difference would be dominated by higher mass loss due to strong pre-explosion winds. This is consistent with the interpretation of Group 1 progenitors loosing envelope mass at late evolutionary stages.

Metallicity differences in the progenitor's composition are also employed to explain different mass-loss histories, where Vink and de Koter (2005) found that the mass-loss rate $\dot{M}$ depends on the metallicity Z following a power-law expression of the form $\dot{M} \propto Z^{0.86}$. This is because the more high-mass elements in a stellar atmosphere, the larger photon cross section and thus the higher the radiation pressure. At higher radiation pressure in the progenitor's atmosphere,

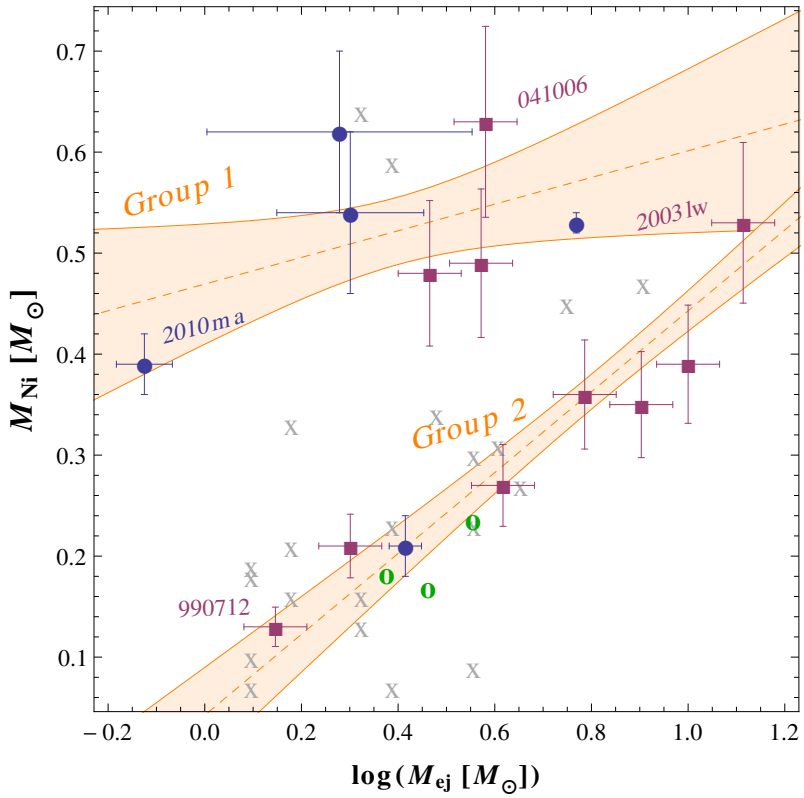

Figure 6.8. The $M_{\rm Ni}$-$M_{\rm ej}$ plane. The blue circles are the events observed by GROND and purple squares are the rest. The dashed lines are the linear regressions for each group. The shaded regions represent 3-σ confidence contours of the fitting. Green open circles correspond to stellar evolution models of SNe Ibc progenitors (Dessart et al., 2011). Since uncertainties for the SN-Ibc sample (grey crosses) are much larger than those for the GRB-SNe ($\sim 14-60\%$), no statistically significant comparison is possible.

stellar winds will be naturally stronger and thus the mass loss higher. In conclusion, mass loss increases with metallicity. However, this effect would generate a continuous set of mass-loss rates and would hardly reproduce the bimodality in the final ejecta masses seen in Fig. 6.8.

If GRBs were found to be associated to both SNe Ib and Ic, a bimodal $M_{\rm ej}$ distribution would be produced only if it was also found for SNe Ib and Ic. However, the local samples of SNe Ib and Ic show negligible difference in $M_{\rm ej}$ (Drout et al., 2011), therefore, the bimodality detected in the $M_{\rm Ni}$-$M_{\rm ej}$ plane could not have been originated from different types of SNe associated to GRBs. Moreover, no SN types other than Ic have been associated to GRBs so far.

6.3 GRB vs. SN Properties

The main γ-ray emission properties of the GRB-SN sample are presented in Table 6.1. The observed duration $T_{90,\rm obs}$ (column 9), the observed spectral peak energy $E_{\rm peak,obs}$ (column 10), and the rest-frame isotropic γ-ray energy release $E_{\gamma,\rm iso}$ (column 11) were taken from the literature. In the analysis below, the former two quantities have been corrected for the expansion of the universe to obtain the rest-frame quantities $T_{90} = T_{90,\rm obs}/(1+z)$ and $E_{\rm peak} = (1+z)E_{\rm peak,obs}$. No attempts at computing upper or lower limits for $E_{\rm peak}$ has been made. The

$E_{\gamma,\mathrm{iso}}$ values are computed from the published spectral modelling as follows. Consider a burst with an observed γ-ray fluence S_γ in the sensitivity energy range of the corresponding instrument $[E_{\mathrm{s1}}, E_{\mathrm{s2}}]$. For a source emitting isotropically at a luminosity distance D, S_γ corresponds to a total energy release of

$$E_{\gamma,\mathrm{iso}} = \frac{4\pi D^2 S_\gamma}{1+z} \left(\int_{E_{\mathrm{rf1}}/(1+z)}^{E_{\mathrm{rf2}}/(1+z)} f(E)\, dE \Big/ \int_{E_{\mathrm{s1}}}^{E_{\mathrm{s2}}} f(E)\, dE \right) \tag{6.5}$$

in the rest-frame energy range from $E_{\mathrm{rf1}} = 1$ keV to $E_{\mathrm{rf2}} = 10$ MeV. The observed spectral model $f(E)$ is integrated numerically.

As follows I explore possible correlations between the GRB prompt-emission properties against parameters determined from the SN light curve. Figure 6.9 shows the distributions of the T_{90} duration and spectral peak energy E_{peak} of the prompt γ-ray emission. The T_{90} distribution (red histogram in the right panel) shows a strong preference in favour of durations of about 25 s. The range of durations spans almost all possible values of a complete long-GRB sample. GRB 040924 has the shortest rest-frame duration of $T_{90} = 0.65$ s (which correlates with low SN luminosity), although it belongs to the long-GRB class due to its γ-ray spectral properties. GRB 100316D/SN 2010bh has the longest duration with $T_{90} \simeq 1300$ s. A sample of 162 *Swift* long GRBs has been gathered and plotted with dashed line blue bins for comparison. The short-GRB population can be distinguished at $\log T_{90} < 0$. The E_{peak} distribution shows what it is expected for the GRBs that have been associated to SNe: a fraction of nearly 70% has peak energies lower than 100 keV, which is at the low-energy end of the cosmological GRB sample (Kaneko et al., 2007).

Regarding the unusual very soft GRBs — XRFs actually — that have been found in asociation with SNe, a good distinction between the prompt GRB pulse and the X-ray tail of the GRB is difficult to determine, therefore the duration parameter T_{90} might be quite off for extremely and intermediately long ($T_{90} > 100$ s) XRFs such as 111209A, 100316D, 070419A, 060729, and 060218.

There is an empirical correlation that the greater the E_{peak} values of a GRB, the larger its total isotropic energy release $E_{\gamma,\mathrm{iso}}$(Amati et al., 2002, 2007). In the top panel of Fig. 6.10, it is assessed whether this is true for E_{peak} in this case against the SN optical luminosity k_{opt}.

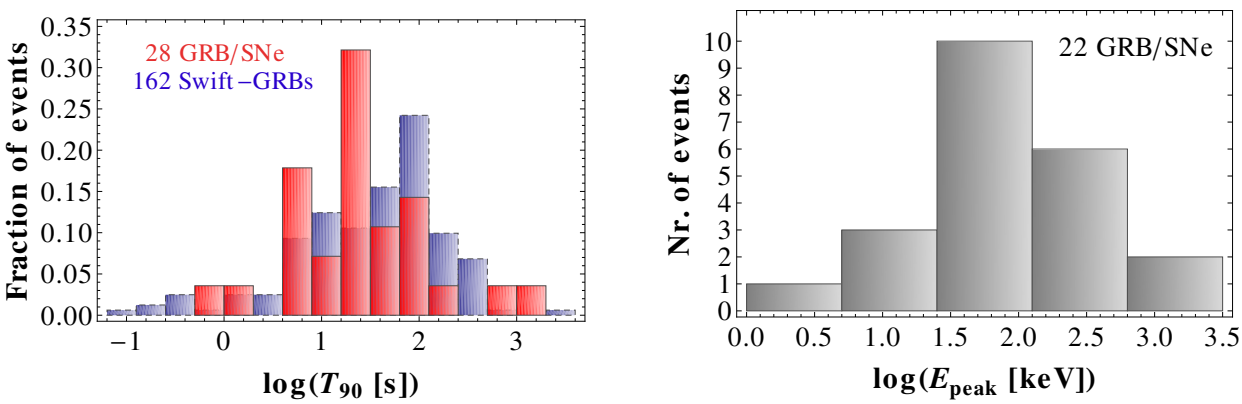

Figure 6.9. Main properties of the GRB prompt emission. *Left Panel:* The GRB duration T_{90} is shown for our GRB-SN sample and for the *Swift* sample (Kaneko et al., 2007). *Right Panel:* The E_{peak} values are shown for a subset of 22 GRBs in our sample, for which E_{peak} determination was possible.

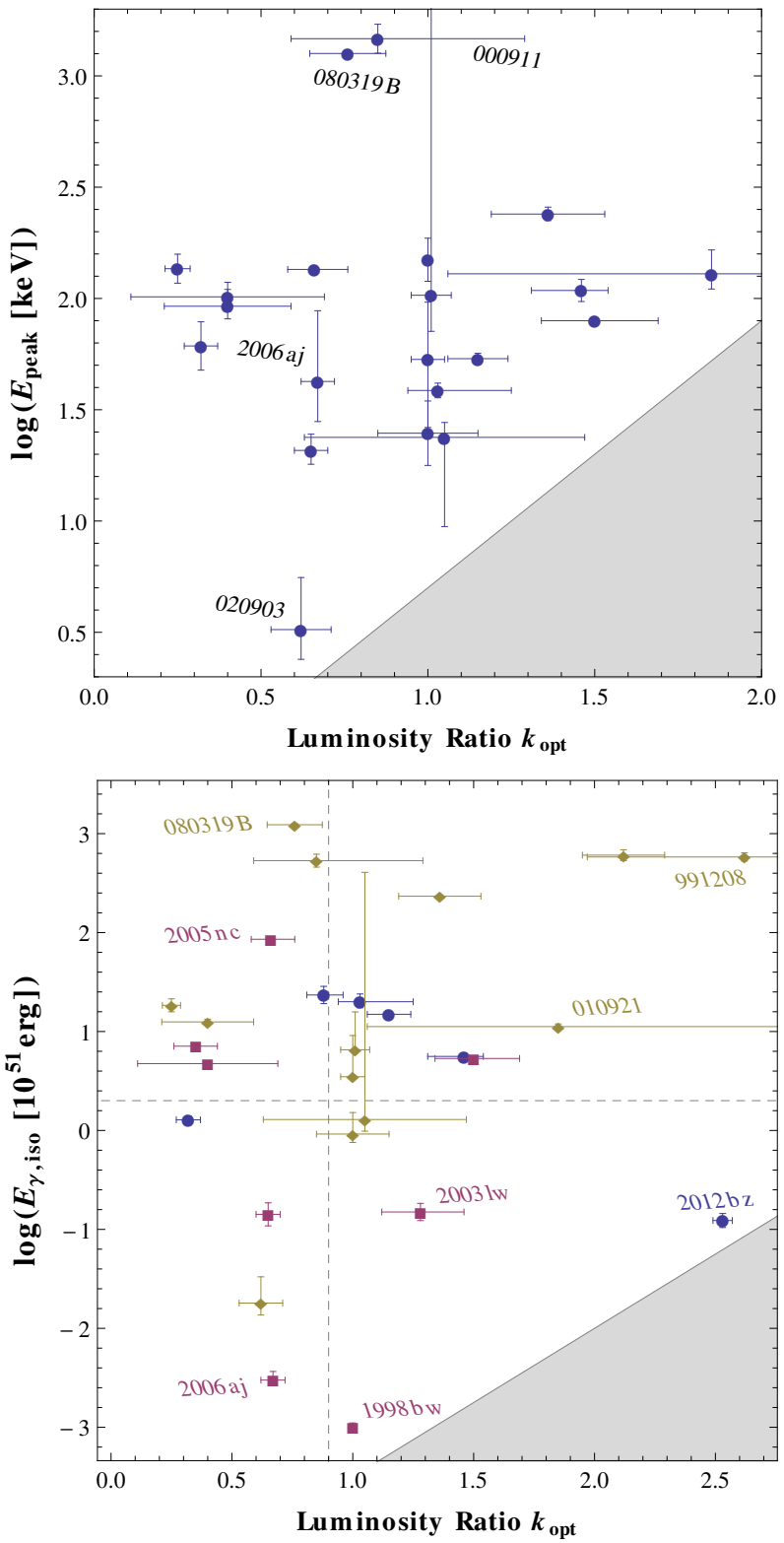

Figure 6.10. GRB and SN energetics. *Top panel:* The SN luminosity ratio $k_{\rm opt}$ against the GRB peak energy from the prompt-emission integrated spectrum $E_{\rm peak}$. *Bottom panel:* Luminosity ratio of the SN $k_{\rm opt}$ against the GRB energy release $E_{\gamma,\rm iso}$.

The bulk of events lie at $E_{\rm peak} = 50$ keV and no trend is clear. I note however that there is a slightly significant lack of objects with low $E_{\rm peak}$ and high $k_{\rm opt}$ (grey shaded area). If a direct $E_{\rm peak}$-$k_{\rm opt}$ proportionality would exist, it should be present through the superposition of populations with different properties. This could be explained if the energy to expand the progenitor's envelope and produce the SN falls back to the collapsed core to power a GRB with higher energy. However, the data set still lacks precision to make stronger statements. To test further luminosity correlations, in the bottom panel of Fig. 6.10 shows the SN optical luminosity $k_{\rm opt}$ against the GRB isotropic energy release $E_{\gamma,\rm iso}$. As in the top-panel plot, there is also a lack of objects with low $E_{\gamma,\rm iso}$ and high $k_{\rm opt}$. However, there is no clear trend for this data set.

Given that both the GRB and the SN are powered by the core collapse, it can be argued that there must be a connection between the energies required to trigger the GRB and the SN. For CCSNe, the usual hypothesis is that the explosion is decoupled into the core collapse and the ejection of the envelope (e.g., Woosley and Weaver, 1994). Therefore, the total energy $E_{\rm tot}$ is divided into (1) the neutrino energy, which escapes barely without interaction, (2) the ejecta energy, and (3) the energy that goes to the core collapse. The second energy component is roughly equal to the kinetic energy of the SN, $E_{\rm k}$, which overpowers the thermal and radiative energy of the envelope (Bersten et al., 2011). The third component consists of the accretion energy and the jet energy (Woosley and Bloom, 2006). At the end, all the accretion-disk energy is transformed into jet energy, which is proportional the GRB energy release (Zhang et al.,

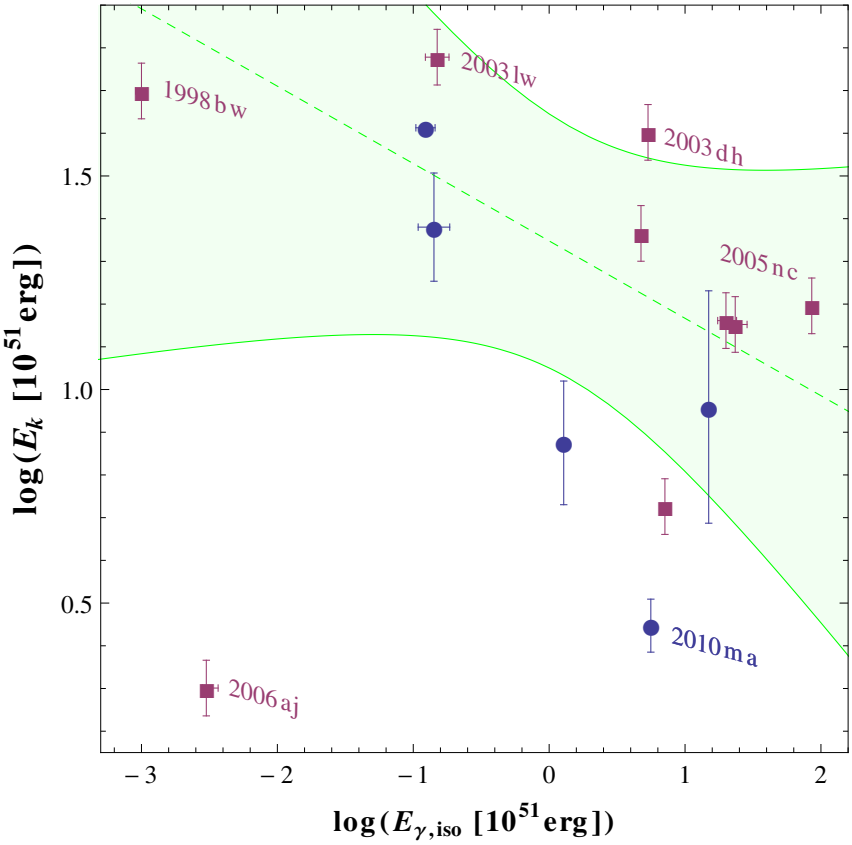

Figure 6.11. GRB energy release $E_{\gamma,\rm iso}$ against the kinetic energy of the SN explosion $E_{\rm k}$. Events observed by GROND are shown in blue circles. The anti-correlation and the corresponding 3-σ contours are shown with green dashed and solid lines, respectively.

2009). Although not corrected for collimation, $E_{\gamma,\mathrm{iso}}$ represents reliably the GRB energy release for the expected distribution of GRB opening angles. Figure 6.11 explores the $\log E_{\gamma,\mathrm{iso}}$-$\log E_{\mathrm{k}}$ plane. Here I found that, with the exception of XRF 060218/SN 2006aj and marginally GRB 101219B/SN 2010ma, a trend is clear. The higher the kinetic energy of the SN envelope, the lower the γ-ray energy release. This hints at a unique energy budget (E_{tot}). The data was fitted with a straight line of the form

$$\log E_{\mathrm{k},51} = (-0.18 \pm 0.06)\ \log E_{\gamma,\mathrm{iso},51} + (1.35 \pm 0.08), \tag{6.6}$$

where both E_{k} and $E_{\gamma,\mathrm{iso}}$ are in units of 10^{51} erg. The linear regression delivers $R^2 = 0.97$ after discarding SNe 2006aj and 2010ma as outliers. As explained in §6.2, SN 2006aj exhibited peculiar γ-ray, X-ray, and UV behaviour, which can also be explained through other mechanisms than SN (Shcherbakov et al., 2012). Therefore, it is unsurprising that SN 2006aj lies far from the empirical correlation also because soft events like XRF 060218 could have larger opening angles than normal. It is worth noticing that both E_{k} and $E_{\gamma,\mathrm{iso}}$ might be affected by the viewing angle with respect to the jet axis. This effect cancels out when comparing them together.

In the case of long GRBs in connection to SNe, the γ-ray emission and the ^{56}Ni are both produced in the core of a dying star. Therefore, it can be speculated that the nickel is synthesised by the GRB explosion itself. This is tested with E_{peak} and $E_{\gamma,\mathrm{iso}}$ from the GRB plus M_{Ni} from the SN emission. In the top panel of Fig. 6.12, a sub-sample of 10 bursts with E_{peak} and M_{Ni} data are plotted. After discarding the peculiar events XRF 060218/SN 2006aj and GRB 101219B/SN 2010ma discussed in the previous sections, an anti-correlation of the form

$$M_{\mathrm{Ni}} = (-2.1 \pm 0.8) \times 10^{-3}\, E_{\mathrm{peak}} + (0.65 \pm 0.09)\, \mathrm{M}_{\odot} \tag{6.7}$$

arises with $R^2 = 0.91$, where E_{peak} is in units of keV. This supports higher energetic γ-rays producing less ^{56}Ni, which hints at a fixed energy budget. If the total energy is mostly released as γ-rays, less will be available to synthesised nickel. This result is consistent with what was find for the SN kinetic energy and the isotropic GRB energy release shown in Fig. 6.11.

In the bottom panel of Fig. 6.12, the $E_{\gamma,\mathrm{iso}}$ values are plotted against M_{Ni}, however, no trend has been spotted. In conclusion, this data set suggests that the GRB energetics is partly coupled from the SN ^{56}Ni production, showing clear anti-correlations between optical and γ-ray observed properties ofof SNe and GRBs, respectively. However, more data is required to approach more comprehensive statistical studies.

6.4 Rate of GRB-SN Events

The combined event of a GRB followed by a SN explosion can be classified in different categories according to their GRB prompt and SN luminosity. Four categories are defined using data of 25 GRB-SNe from Table 6.1:

1. Luminous GRB ($E_{\gamma,\mathrm{iso}} > 2 \times 10^{51}$ erg), luminous SN ($k_{\mathrm{opt}} > 0.9$). The cornerstone event of this category is GRB 030329/SN 2003dh. Luminous GRBs are here the so-called "cosmological" GRBs ($z \gtrsim 0.4$), representative of the whole long-GRB sample. This category corresponds to the 40% of the whole sample.

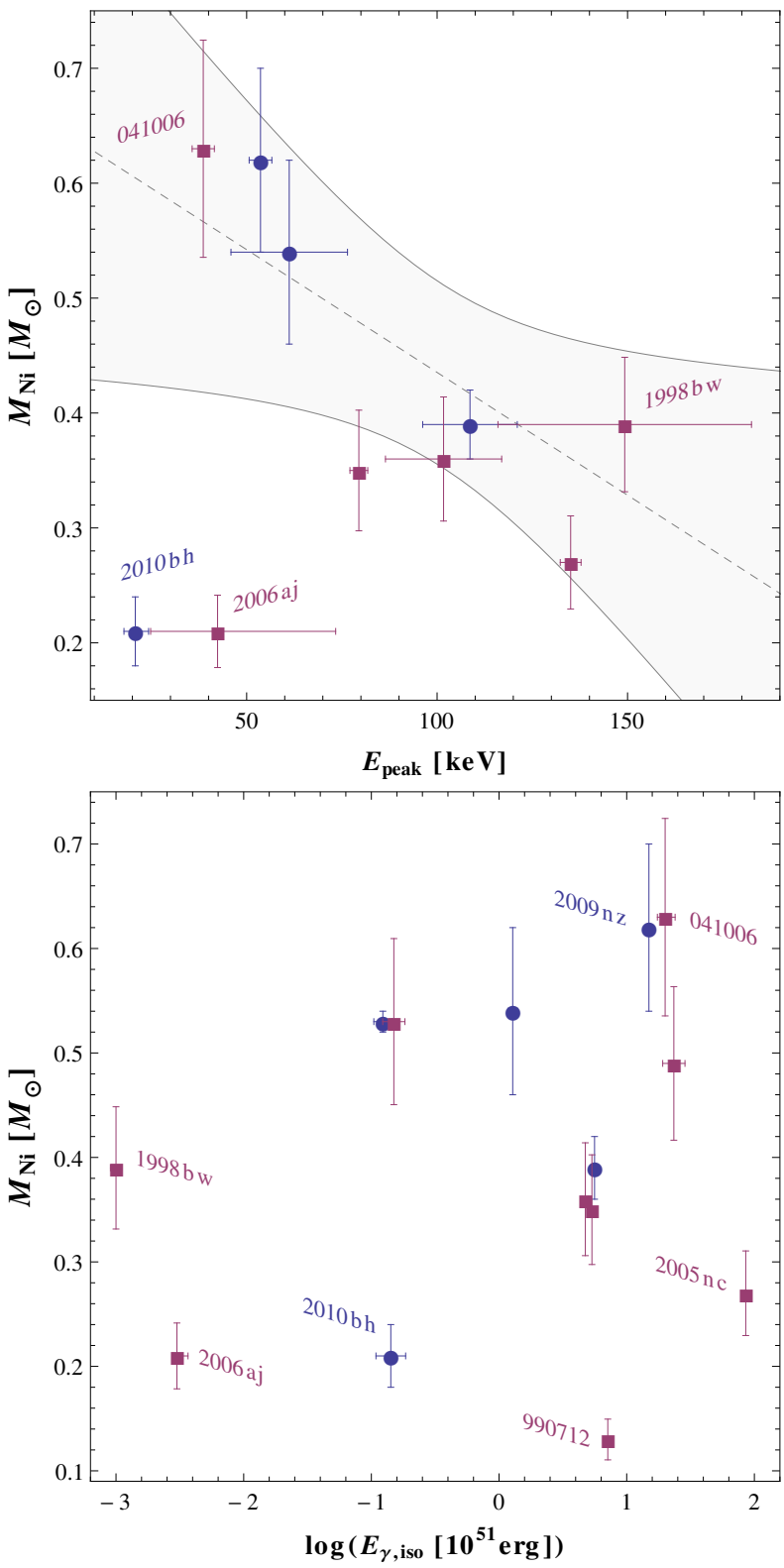

Figure 6.12. GRB and SN energetics. *Top panel:* Peak energy of the GRB $E_{\rm peak}$ against the ^{56}Ni mass synthesised by the SN $M_{\rm Ni}$. The linear fit and the corresponding 2-σ contours are shown with dashed and solid grey lines, respectively. *Bottom panel:* GRB energy release $E_{\gamma,\rm iso}$ against the ^{56}Ni mass synthesised by the SN explosion $M_{\rm Ni}$. For both panels, events observed by GROND are shown in blue circles.

2. Luminous GRB ($E_{\gamma,\mathrm{iso}} > 2 \times 10^{51}$ erg), under-luminous SN ($k_{\mathrm{opt}} < 0.9$). A representative case of this category is that of GRB 050525A/SN 2005nc. Even though these SN events are hard to detect due to their "cosmological" origin ($z \gtrsim 0.4$), the 32% of GRB-SNe belong to this category.

3. Under-luminous GRB ($E_{\gamma,\mathrm{iso}} < 2 \times 10^{51}$ erg), luminous SN ($k_{\mathrm{opt}} > 0.9$). The cornerstone events of this category are GRB 980425/SN 1998bw and GRB 031203/SN 2003lw. Only the 16% (4 events) fall in this category.

4. Under-luminous GRB ($E_{\gamma,\mathrm{iso}} < 2 \times 10^{51}$ erg), under-luminous SN ($k_{\mathrm{opt}} < 0.9$). The cornerstone of this category is GRB 060218/SN 2006aj. Only the 16% (4 events) fall in this category.

The limits on $E_{\gamma,\mathrm{iso}}$ and k_{opt} that define the different categories are arbitrarily defined by using approximate mean values and are plotted with dashed lines in the lower panel of Fig. 6.10.

In total, under-luminous GRBs associated with SNe account for the 32% of events. This could be due to the sensitivity limits both on luminosity and hardness of current γ-ray facilities. One example is that of SN 2008D, which was discovered thanks to its X-ray emission (Mazzali et al., 2008, and references therein). The other 68% of GRBs correspond to cosmological GRBs. Notice that off-axis beaming may also play a substantial role, e.g., GRB 980425 is considered as a GRB beamed perpendicularly to the line of sight (Kouveliotou et al., 2004, and references therein).

Chapter 7

GROND Statistics of Light-Curve Bumps

In recent years GROND has discovered mysterious rebrightenings in GRB AGs at late times through its excellent light-curve coverage. Their evolution brings fundamental information about the nature of the progenitor star and the explosion mechanism. Two kind of late-times bumps have been identified: (1) SN rebrightenings that show colour evolution and (2) AG rebrightenings that exhibit a power-law SED.

While four spectroscopically confirmed GRB-SNe have been observed by GROND since it became operational (SN 2008hw, SN 2009nz, and SN 2010ma in §5; SN 2010bh in §3 and Olivares E. et al., 2012), two late-time rebrightenings without a redshift determination were detected in the same period: GRBs 080120 (McBreen et al. in preparation) and 100902A (see §5 for the latter). The outstanding GROND capabilities of simultaneous multi-wavelength imaging have allowed to disentangle the nature of these rebrightenings, which are both unrelated to SNe.

Rebrightenings showing a synchrotron spectrum hint at late activity of the central engine and therefore offer a direct picture of what powers GRBs. The $g'r'i'z'JHK_{\rm s}$ rebrightening of GRB 100902A has been demonstrated in §5 to have a different origin from that of GRB-SNe. Its sharp early maximum luminosity and power-law SED differs greatly from the SN behaviour (see Fig. 5.3 and Fig. 5.6). Unfortunately no X-ray observations are available for this event at the rebrightening time. In addition, the case of GRB 080120 shows a late-time rebrightening in all optical GROND bands. This bump is interesting on its own, since it was also observed by the *Swift*/XRT. In theory, both the X-ray and the optical AG come from the same population of radiating electrons, however, the frequently observed inconsistency of the optical and X-ray decay argues against the interpretation of both being entirely due to the same emission mechanism. Nardini et al. (2010) proposed a scenario in which individual optical to X-ray behaviour can be modelled as a superposition of the standard forward-shock AG component and a purely phenomenological emission component (called "late prompt") that for example could be due to a prolonged activity of the central engine. Therefore, we identify the AG rebrightening of GRB 080120 and that of GRB 100902A as good candidates for the late-prompt scenario. Thanks to the presence of the XRT and to the much denser and faster optical/NIR follow-up performed by a wide net of ground-based instruments like GROND, we can now study the contemporaneous broad-band AG evolution from the NIR to X-ray energies. A broad wavelength coverage is needed to constrain the evolution of the spectral slope. Given that these rebrightenings are faint in the NIR, imaging of the AG at these wavelengths allows for better constraints on the spectral index, and therefore more accurate studies of the synchrotron

rebrightening and its evolution. Different values of the spectral slope before, during, and after the rebrightening will permit a description of the late-time activity of the central engine.

On the statistical side, while in the last 10 years about 400 AGs have been discovered in the optical bands (see `http://www.mpe.mpg.de/~jcg/grbgen.html`), 95% of them have no late-time AG detection at > 5 days after the corresponding burst (excluding here searches for the GRB host galaxies). For the GROND data set from August 2007 to February 2011 the statistics can be summarised as follows

- The fraction of AG detection at > 5 days is 41 AGs of a total of 273 observed (15%). The difference with the sample of 400 AGs is due to the systematic observing strategy of GROND. Our understanding of the GRB-SN connection and the AG phenomenology would be more clearly constrained if more such late-time observations were obtained accurately, for which telescopes with larger mirrors would be needed.

- Out of the 41 AGs detected by GROND at $t > 5$ days, 5 have no redshift determination ($\sim$ 10%). For both SN and synchrotron rebrightenings the redshift determination is required to yield the intrinsic luminosity. The obtained luminosity proves particularly useful at constraining the energy release from different models and at comparing with other similar events. In many cases the host galaxy lies below the detection limits of current facilities and it is not possible to obtain the redshift after the transient has faded.

- Out of the 41 AGs detected by GROND at $t > 5$ days, 10 show late-time rebrightenings ($\sim$ 24%) so far in the analysed data. These correspond GRBs 071112C ($z = 0.823$), 080120, 081007 (SN 2008hw), 090323 ($z = 3.57$), 091127 (SN 2009nz), 100316D (SN 2010bh), 100902A, 101219B (SN 2010ma), 111209A ($z = 0.677$), and 111211A ($z \simeq 0.478$); half of these were included in this thesis. Moreover, the late-time data of GRBs 080319D, 100316B ($z = 1.01$), 111129A, and 111228A ($z \simeq 0.716$) remain to be analysed in search of a photometric bump. If the rate of 10/41 is true, at least one out of the latter four events should exhibit a rebrightening.

In conclusion, about 25% of events show rebrightenings. This fraction suggest that GROND should detect light-curve bumps at a rate of approximately 3 per year, for which there are 55% chance of being a SN bump and 18% of belonging to the late-engine type.

Chapter 8

The Stripped-Envelope SN Sample

In this chapter I summarise the 3-year follow-up of SE SNe executed by the GROND team at La Silla Observatory, Chile. As secondary PhD project, I selected the candidates for follow-up and planned the observation campaign. The description of five projects that will analyse the SN data acquired by GROND follows.

8.1 The SN follow-up

The GROND SN project started in August 2009 with the purpose of gathering a significant number of early-sampled SE SNe light curves, which will allow us to perform a series of statistical studies (see below §8.2 for the scientific goals).

8.1.1 Logistics

There were two basic requirements for a SN to enter our follow-up program: (1) it had to be discovered before maximum light, since our scientific goals need this coverage, and (2) it had to belong to the SE class (type Ib/c and IIb SNe; see §1.2). To assess these requirements we used the Central Bureau Electronic Telegrams (CBET; `http://www.cbat.eps.harvard.edu/`) and the Astronomer's Telegram (ATel; `http://www.astronomerstelegram.org/`), which we receive in the form of e-mails as soon as a SN is discovered. For us to trigger observations, the telegrams should report either a rebrightening or a classification as SE SN before maximum. In both cases, we observed the SN field twice and check whether the SN was rising. If it was indeed still rising at least in our r'-band observations, the SN entered our sample unless a telegram was published with a different classification than SE SN. Else, we stopped the follow-up. As a result of this follow-up strategy we end up with 14 light curves of SE SN events, which are shown in Table 8.1.

8.1.2 Observations

For the presented SN sample, the follow-up observations were carried out using the $g'r'i'z'JHK_{\rm s}$ bands of GROND at the MPG/ESO 2.2-m telescope at La Silla Observatory. At the average seeing of $\sim 1''$ at La Silla Observatory and with a 2.2-m telescope mirror, most of the SNe in our sample were nicely detected with every filter until several months past the explosion. Data reduction has been performed as described in §2.2.2 for approximately 50% of the images. A sub-sample of the resulting light curves is shown in Fig. 8.1. Additionally, observations from the UVOT aboard the *Swift* satellite were obtained for SNe 2009jf (top right panel) and 2009mg.

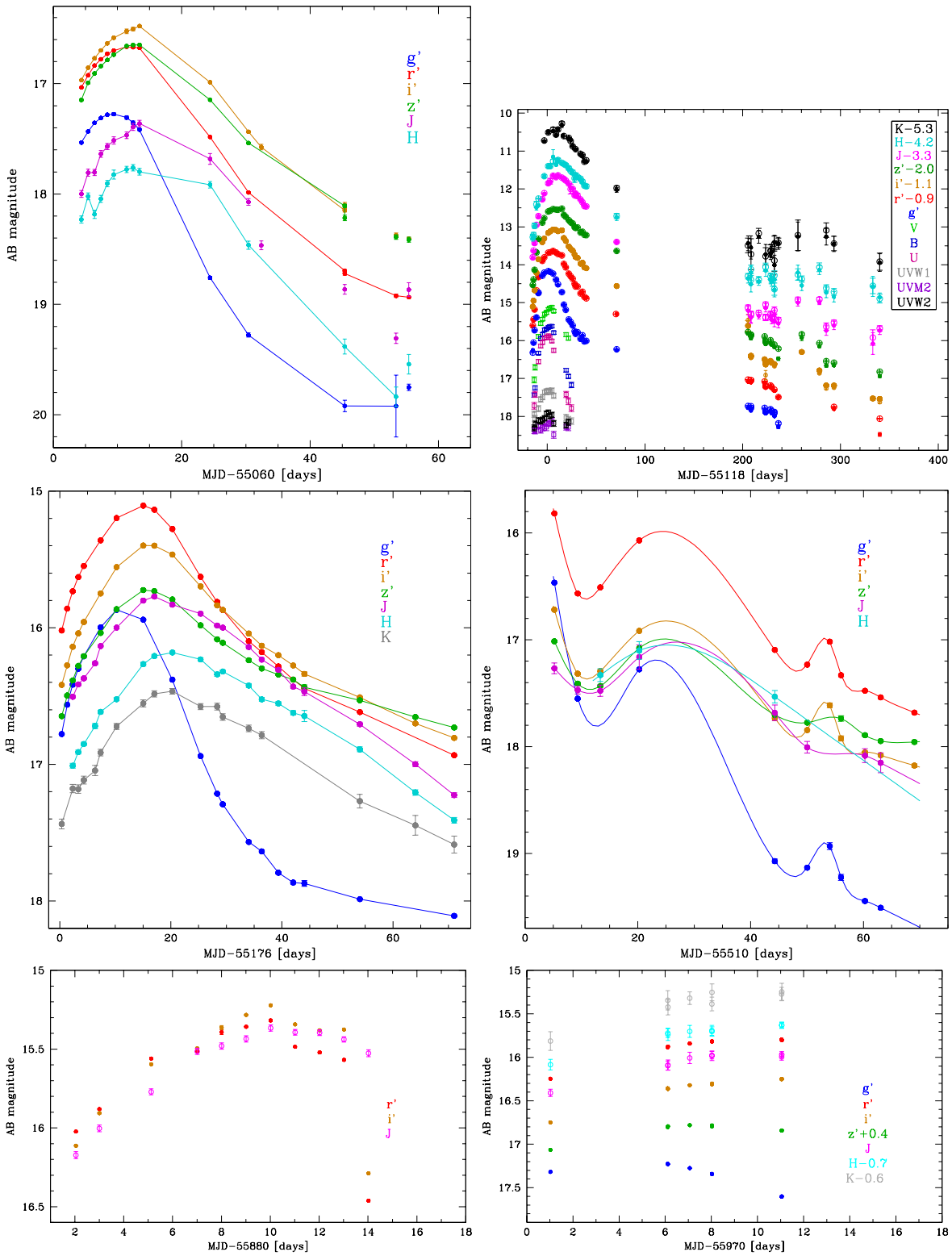

Figure 8.1. Multicolour light curves of six members representative of the SE SN sample. From left to right and top to bottom, panels show the light curves of SNe 2009if, 2009jf, 2009mg, 2010jr, 2011hs, and 2012ap.

Table 8.1. GROND sample of SE SNe.

SN	Type	RA(J2000) [h : m : s]	Dec.(J2000) [° : ′ : ″]	Host Galaxy	z [a]	$A_{V,\mathrm{Gal}}$ [b] [mag]
2012ap	Ibc	05:00:13.73	−03:20:51.4	NGC 1729	0.012115	0.139
2011hp	Ic	12:16:25.48	−43:19:50.4	NGC 4219	0.006635	0.362
2011hs	IIb	22:57:11.77	−43:23:04.8	IC 5267	0.005711	0.034
2011ei	IIb	20:34:22.63	−31:58:23.1	NGC 6925	0.009313	0.160
2011bm	Ic	12:56:53.95	+22:22:28.0	IC 3918	0.021778	0.092
2011D	IIb	03:02:14.57	+17:20:58.2	UGC 02498	0.023126	0.429
2010jw	Ic	08:47:06.91	+28:14:17.4	IC 2394	0.021218	0.145
2010jr	IIb	05:19:34.51	−32:39:14.4	ESO 362-G018	0.012445	0.046
2010as	Ibc	15:49:49.25	−29:23:09.8	NGC 6000	0.007315	0.467
2010cn	Ib	11:04:06.60	+04:49:58.1	SDSS J110406.43+044955.9	0.026	0.132
2009mg	IIb	06:21:44.93	−59:44:25.3	ESO 121-G026	0.007562	0.125
2009jf	Ib	23:04:53.01	+12:19:59.1	NGC 7479	0.007942	0.307
2009if	Ibc	04:24:36.89	−57:59:08.2	IC 2070	0.023443	0.048
2009dq	IIb	10:08:50.00	−67:01:57.4	IC 2554	0.004659	0.562

Note.— The coordinates are derived by comparing field stars in GROND images to USNO-B reference stars (Monet et al., 2003). The uncertainty of the astrometric solution is approximately 0.3 arcsec.

[a] The redshifts were obtained for the host galaxies from the NASA/IPAC Extragalactic Database web interface at http://nedwww.ipac.caltech.edu/.

[b] The values for Galactic foreground extinction are taken from the dust maps of Schlegel et al. (1998).

8.2 Science Prospects

Although SE SNe are relatively rare compared to type-Ia SNe[1], key questions can still be answered with state-of-the-art data of a small-sized sample. Below I summarise five major projects that will be assess for the data presented in the previous section.

8.2.1 Physical Parameters of the Explosion

With the advantage of having simultaneously the optical and NIR brightness of our SNe, the aim would be here to construct quasi-bolometric light curves. When available (e.g., for SN 2009jf), UV observations from the *Swift*/UVOT will constrain the UV contribution to the bolometric flux. For the rest, the UV share will be estimated from the published data for SE SNe. The physical parameters will be derived then by fitting the models of Arnett (1982, ApJ, 253, 785) à la Valenti et al. (2008, MNRAS, 383, 1485) to the quasi-bolometric light curves computed from UVOIR data.

As an example, the UVOIR bolometric light curve of SN 2007uy is illustrated in Fig. 8.2. Ground-based optical/NIR and *Swift*/UVOT photometry are the ingredients of this quasi-bolometric light curve. Using an photospheric expansion velocity of $\upsilon = 15201$ km s^{-1} from spectroscopy, the modelling (red and blue lines) was performed as described in §2.3.6 and following the same procedure used for SN 2010bh (§3.5). With total masses of $M_{\mathrm{Ni}} = 0.41 \pm 0.01\,\mathrm{M}_{\odot}$

[1]Type Ib, Ic, Ibc, and IIb SNe constitute only ∼5% of all spectroscopically confirmed SNe. Statistics taken from The Palomar Transient Factory website at http://www.astro.caltech.edu/ptf/.

and $M_{\rm ej} = 2.01 \pm 0.28\,{\rm M}_\odot$, the analysis will be published by Roy et al. (2013, in preparation). Moreover, the two component model delivers a mass fraction of $f_M = 0.259 \pm 0.004$ and a kinetic-energy fraction of $f_E = (1.9 \pm 0.3) \times 10^{-3}$ both for the inner component. These fractions are consistent with other SE SN events (Maeda et al., 2003; Olivares E. et al., 2012) and compatible with slow-expanding dense core plus a less dense outer component, which expansion carries out most of the kinetic energy.

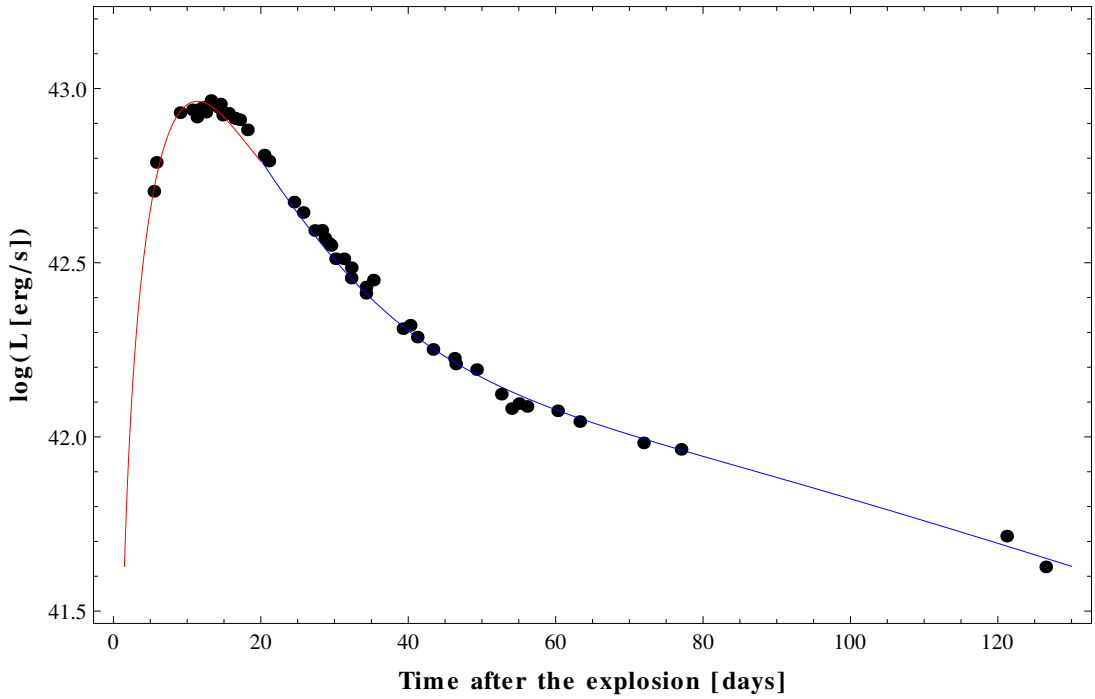

Figure 8.2. UVOIR bolometric light curve of the type-Ib SN 2007uy. The red line corresponds to the model by Arnett (1982) and the blue line is the nebular model described by Valenti et al. (2008) both discussed in §2.3.6 in detail.

8.2.2 A Standard NIR Light Curve

In this study, the NIR light curves of SE SNe in the GROND sample (Table 8.1) and in the literature (e.g., PAIRITEL[2]) will be compared similar to what Milne et al. (2010, ApJ, 721, 1627) has done for UV light curves of SNe Ia. In the ideal case of having enough events, NIR template light curves for each separate subclass (Ic, Ib, IIb) will be derived.

The NIR contribution to the bolometric flux is a long standing problem for distant SE SNe, for which a NIR detection is difficult to obtain (e.g., §5). It has been pointed out by Prabhu et al. (1995, A&A, 295, 403) that "infrared spectra of Swartz et al. (1993, Nature, 365, 232) show the important contributions due to Paschen-α, -β, Bracket-γ, He I 1.08, 2.16 μm, and Fe II 1.64 μm (...) in the NIR flux". Moreover, the NIR flux of core-collapse SNe has been compared by Valenti et al. (2008) showing intrinsic differences, however, a tight early evolution of the NIR flux fraction for four type-Ic SNe (see Fig. 8.3). Therefore, the next step would be to build a template of the NIR fraction over time for SE SNe using a larger sample. Data for SN prior

[2] `https://software.rc.fas.harvard.edu/pairitel/psn_Ibc.php`

2009 will be included from the literature in the analysis of the NIR contribution to the UVOIR bolometric light curves.

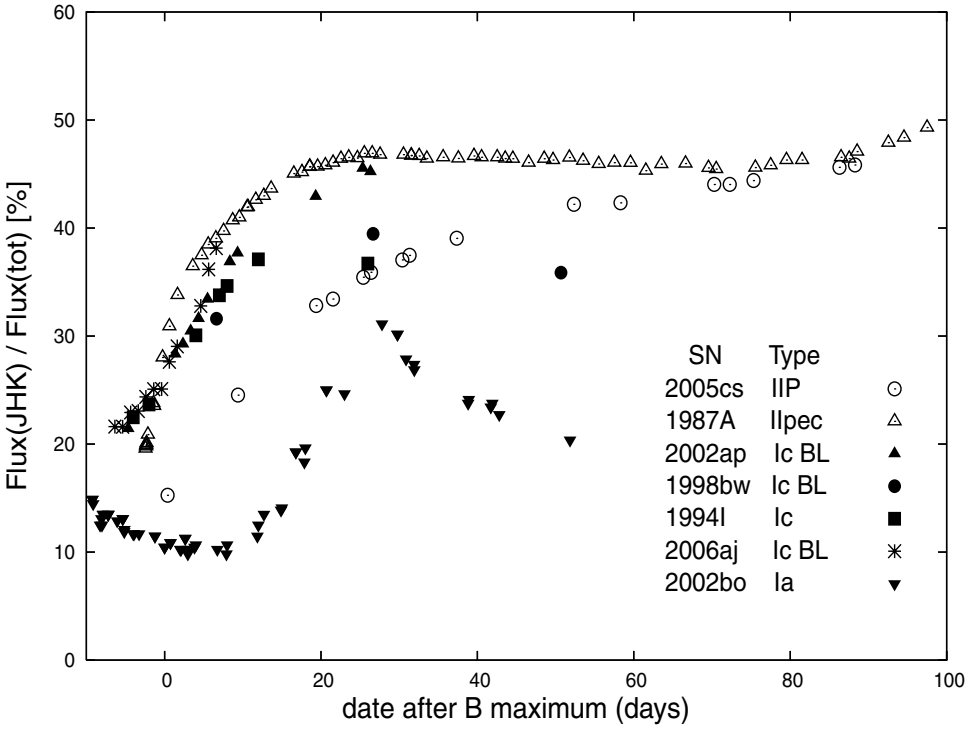

Figure 8.3. NIR contribution to the total UVOIR bolometric for different SN types. Although not statistically significant, the type-Ic SNe 2002ap, 1998bw, 1994I, and 2006aj show similar evolution between −5 and 15 days from blue maximum. Graphics was taken from Valenti et al. (2008).

8.2.3 Classification tool using NIR colours

The purpose here would be to distinguish SE SNe from other SNe using NIR colours. The motivation relies on the fact that intrinsic reddening in the host galaxies can strongly affect optical colours. The changes of NIR colours due to reddening are small and therefore, they probe better the intrinsic properties of SE SNe, which usually explode in dusty environments. Records of colour differences between SN types were established by Brown et al. (2009, AJ, 137, 4517) using UV/optical photometry from *Swift*/UVOT (see Fig. 8.4). This study will make use of NIR data from the literature.

8.2.4 Dereddening Techniques

It has been investigated that SNe might exhibit an intrinsic colour at some stages of their evolution. For SNe Ia, Phillips et al. (1999) proposed the used of the Lira relation, which exploits the similar $B - V$ evolution from 30 to 90 days after V-band maximum. For SNe IIP, Hamuy (2003) proposed the colour at the end of the optically thick phase, when the hydrogen envelope should reach the recombination temperature and thus reach a fixed photometric colour (see Olivares E. et al., 2010, for a current version of the method). Finally for SNe Ibc, the empirical method by Drout et al. (2011, ApJ, 741, 97) uses $UVBRI$ photometry to define an intrinsic colour at a fixed epoch to deredden SE SN photometry (see Fig. 8.5). We will then

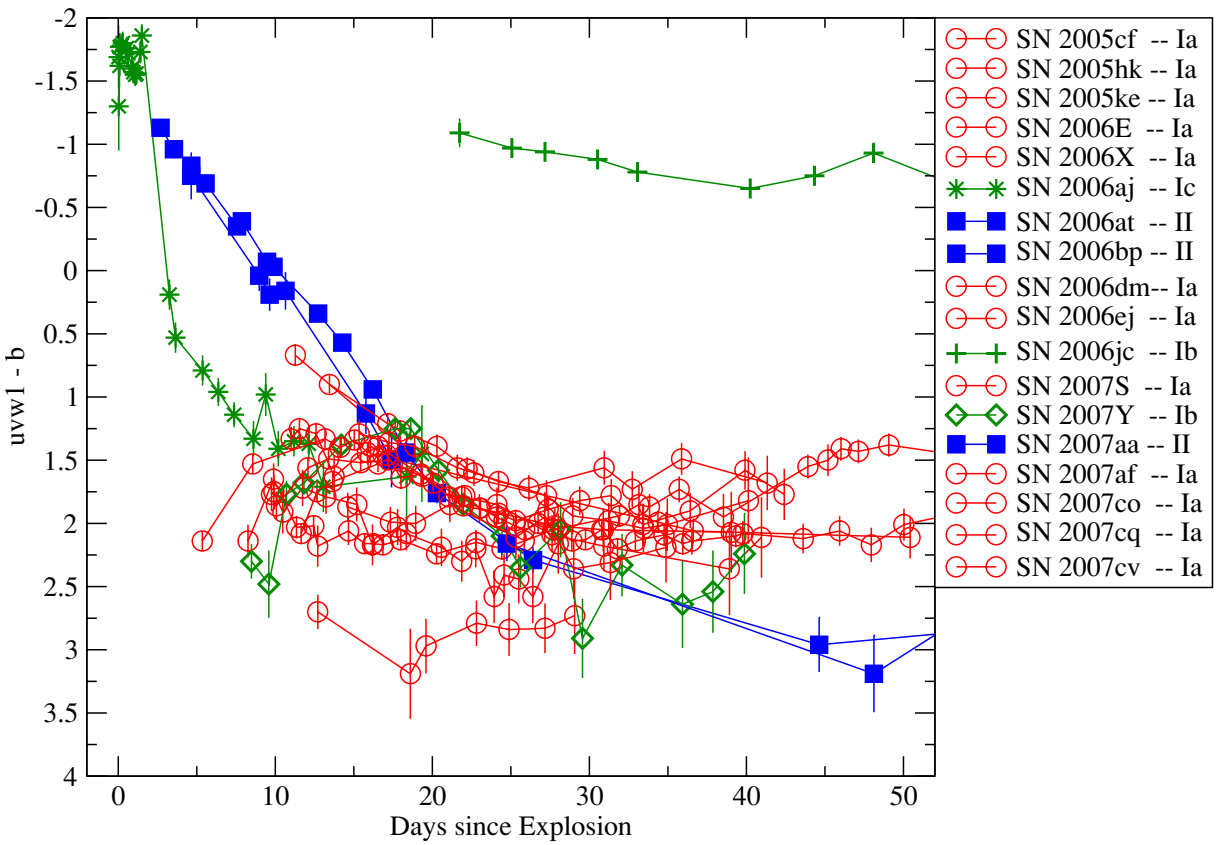

Figure 8.4. UV/optical colour evolution for diverse SN types observed by *Swift*/UVOT. The early-time colour differences vanish at about 15 days after the explosion. Graphics was taken from Brown et al. (2009).

explore this method for SNe Ibc using $g'r'i'z'JHK_{\rm s}$ photometry from GROND. A reddening study, which probes the circumstellar medium, might also deliver answers to questions like "are SE SNe stripped mostly by its own high-mass stellar winds or by a possible companion?"

8.2.5 Rise Times

Given that data before maximum is available for all SNe in Table 8.1, a statistical study of rise times can be developed. An important task will be to determine the explosion time, which serves as time origin for measuring reliably rise times. The difficulties I will encounter are that the explosion time is usually unconstrained by SN searches, which observation cadence of different fields is of the order of a few days. The quasi-bolometric light curve modelled as described in §2.3.6 can be modified by including an explosion-time parameter. For the particular case of SN 2007uy (Fig. 8.2), the fitted explosion time turned out to be $t_0 = 0.3 \pm 0.5$ d, which is consistent with the input time origin derived from a constraining pre-explosion imaging. Nevertheless, this is not usually the case and the pre-explosion images could have been taken several weeks apart. It is noted that results for t_0 derived from this method will be tied to the model assumptions (see §2.3.6). Another approach consists in building a light-curve template with a known explosion time. The template can then be fitted to our data including a time-stretch parameter and a brightness scale factor. With the resulting stretch factors, rise times can be precisely determined.

As it is known for SNe Ia, the width of their light curve correlates tightly with luminosity

(Phillips, 1993, ApJL, 413, L105). Therefore, the possible correlation between rise times and quasi-bolometric luminosity for SE SNe will be assessed. Moreover, the rise times are thought to be strongly correlated with the ^{56}Ni distribution in the SN envelope (Bersten et al., 2012, ApJ, 757, 31). Therefore, this study can assess whether the ^{56}Ni is centrally located or it is synthesised across the envelope.

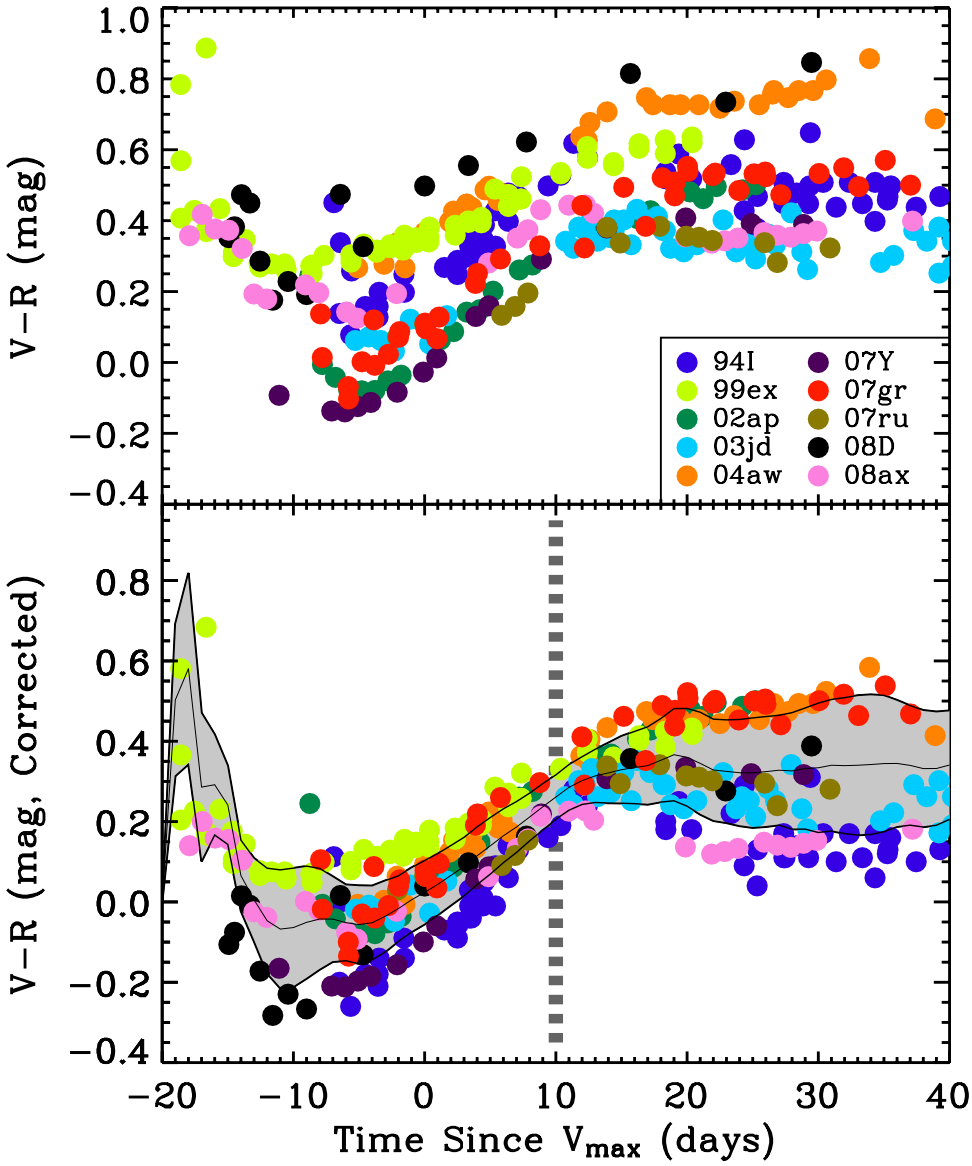

Figure 8.5. Colour evolution of 10 well-studied SNe Ibc from the literature. After correcting for the host-galaxy extinction determined by diverse methods (lower panel), the dispersion dramatically decreases. At 10 days after the V-band maximum, an intrinsic $V - R$ colour of 0.26 ± 0.06 mag is measured. Graphics was taken from Drout et al. (2011).

Chapter 9

Summary and prospects

In this thesis, I focused on the connection between GRBs and SNe. The aim is to understand better the connection by analysing individual events in deep and by performing statistics on the whole GRB-SN sample. To accomplish it, γ-ray, X-ray, UV, optical, and NIR data was employed covering approximately six orders of magnitude in the radiative energy domain.

The association between GRB 100316D and SN 2010bh was studied in Chapter 3. Using the early broad-band SED, I constrained the progenitor radius to a few times that of WR stars, which are the most likely GRB-SN progenitors, indicating the presence of a pre-explosion dense stellar wind. It is also shown that the optical emission and evolution of SN 2010bh are pretty similar to that of SN 2006aj using the multicolour GROND data. Chapter 4 shows the case of GRB 090424 at $z = 0.54$, for which no SN counterpart was found down to 49% of the peak luminosity of SN 1998bw.

In Chapter 5, four light-curve rebrightenings are analysed. As well as for GRB 100316D/SN 2010bh and GRB 090424, the host-galaxy extinction in the line of sight of each event is computed from the broad-band SED. The rest-frame optical brightness were obtained and the quasi-bolometric light curve was constructed. Using an analytical model for the quasi-bolometric light curve, the physical parameters of the SN explosion ($M_{\rm Ni}$, $M_{\rm ej}$, $E_{\rm k}$) were computed for each event analogously to the case of SN 2010bh in §3. The data for GRB 100902A turned out to be inconsistent with the SN nature and more compatible with the late-engine scenario (see §7). The other three rebrightenings are the sub-luminous ^{56}Ni-rich SN 2008hw, the luminous SN 2009nz, and the fast-evolving super-luminous SN 2010ma. The latter SN along with SN 2010bh has one of the earliest peaks ever recorded and thereafter fades more rapidly than any other GRB-SNe, HNe, or typical type-Ic SNe. This implies that a thin envelope is possibly expanding at very high velocities and is, therefore, unable to retain the γ-rays that would prolong the duration of the SN event.

The statistical analysis of 28 GRB-SN events is presented in Chapter 6. GROND data was used for the five events described above and data for the remaining 23 objects was acquired from the literature (Table 1.1). The main conclusions drawn here are that

- For most events there is a $M_{\rm Ni}$-$L_{\rm max}$ correlation. Peculiarities in XRF 060218/SN 2006aj, XRF 100316D/SN 2010bh, and GRB 101219B/SN 2010ma place them at the region of ^{56}Ni under-production (§6.2).

- Two populations are identified in the $M_{\rm Ni}$-$M_{\rm ej}$ plane, which hints at different pre-explosion mass-loss history (Fig. 6.8).

- No strong evidence for a correlation was found between GRB and SN luminosity (Fig. 6.10 and 6.12), which suggest that although they share their origin, GRB and SN are causally decoupled energetically.
- A weak indirect proportionality is discovered between $E_{\gamma,\mathrm{iso}}$ and E_{k}, which may indicate that the energy of the core collapse is partitioned between GRB and SN.

Additionally, rebrightenings in the full GROND sample are studied statistically in Chapter 7. It is found that rebrightenings in GROND light curves are expected at a rate of 3 per year, of which the majority (55%) would have a SN origin. A handful of these rebrightening events have not been analysed in this thesis. Future work consist in including all GROND SN bumps in the full sample of GRB-SNe. The estimate is that added to the five GRB-SNe of this thesis another three of four will join, expanding significantly the existing sample. This will allow better constraints on the findings above.

The last science chapter presents the sample of local SE SNe observed by GROND. These have not been discovered to have γ-ray emission and are less luminous than GRB-SNe. With a total of 14 objects, this sample is unique in terms of NIR coverage. So far only optical campaigns have been arranged to observe SE SNe and I have demonstrated that NIR is a very important addition to determine the reddening in the host galaxy and the physical parameters of the explosion through a thorough quasi-bolometric light curve among several other possible analyses detailed in Chapter 8. These SE SNe will also represent a comparison sample for that of GRB-SNe helping to understand more about the progenitor stars of this explosive events.

Bibliography

Abazajian, K. N., Adelman-McCarthy, J. K., Agüeros, M. A., et al., 2009, *ApJS* **182**, 543

Afonso, P., Elliott, J., and Greiner, J., 2011, *GCN Circular* **11954**, 1

Afonso, P., Updike, A., Nardini, M., et al., 2010, *GCN Circular* **10514**, 1

Allen, C. W., 1976, *Astrophysical Quantities*, Athlone Press, London

Amati, L., 2008, in C. L. Bianco & S. S. Xue (ed.), *Relativistic Astrophysics: 4th Italian-Sino Workshop*, Vol. 966 of *AIP Conference Series*, pp 3–6, AIP, Pescara, Italy

Amati, L., Della Valle, M., Frontera, F., et al., 2007, *A&A* **463**, 913

Amati, L., Frontera, F., Tavani, M., et al., 2002, *A&A* **390**, 81

Anderson, J. P. and James, P. A., 2008, *MNRAS* **390**, 1527

Andreev, M., Sergeev, A., and Pozanenko, A., 2010, *GCN Circular* **11192**, 1

Appenzeller, I., Fricke, K., Fürtig, W., et al., 1998, *The Messenger* **94**, 1

Arnett, D., 1996, *Supernovae and Nucleosynthesis*, Princeton University Press, New Yersey

Arnett, W. D., 1982, *ApJ* **253**, 785

Astier, P., Guy, J., Regnault, N., et al., 2006, *A&A* **447**, 31

Baade, W. and Zwicky, F., 1934, *Physical Review* **46**, 76

Balberg, S. and Loeb, A., 2011, *MNRAS* **414**, 1715

Band, D., Matteson, J., Ford, L., et al., 1993, *ApJ* **413**, 281

Barthelmy, S. D., Barbier, L. M., Cummings, J. R., et al., 2005, *Space Sci. Rev.* **120**, 143

Barthelmy, S. D., Baumgartner, W. H., Cummings, J. R., et al., 2012, *GCN Circular* **13246**, 1

Barthelmy, S. D., Cline, T. L., Butterworth, P., et al., 2000, in R. M. Kippen, R. S. Mallozzi, & G. J. Fishman (ed.), *Gamma-ray Bursts, 5th Huntsville Symposium*, Vol. 526 of *AIP Conference Series*, pp 731–735

Baumgartner, W. H., Barthelmy, S. D., Cummings, J. R., et al., 2009, *GCN Circular* **9530**, 1

Baumgartner, W. H., Cummings, J. R., Evans, P. A., et al., 2008, *GCN Circular* **8330**, 1

Beardmore, A. P., Evans, P. A., Goad, M. R., and Osborne, J. P., 2010, *GCN Circular* **11188**, 1

Benetti, S., Turatto, M., Valenti, S., et al., 2011, *MNRAS* **411**, 2726

Berger, E., Chornock, R., Holmes, T. R., et al., 2011, *ApJ* **743**, 204

Berger, E., Fox, D. B., Cucchiara, A., and Cenko, S. B., 2008, *GCN Circular* **8335**, 1

Berger, E., Price, P. A., Cenko, S. B., et al., 2005, *Nature* **438**, 988

Bersier, D., Fruchter, A. S., Strolger, L. G., et al., 2006, *ApJ* **643**, 284

Bersten, M. C., Benvenuto, O., and Hamuy, M., 2011, *ApJ* **729**, 61

Bersten, M. C., Benvenuto, O. G., Nomoto, K., et al., 2012, *ApJ* **757**, 31

Beuermann, K., Hessman, F. V., Reinsch, K., et al., 1999, *A&A* **352**, L26

Bissaldi, E., McBreen, S., and Connaughton, V., 2008, *GCN Circular* **8369**, 1

Blondin, S. and Tonry, J. L., 2007, *ApJ* **666**, 1024

Bloom, J. S., Kulkarni, S. R., and Djorgovski, S. G., 2002a, *AJ* **123**, 1111

Bloom, J. S., Kulkarni, S. R., Djorgovski, S. G., et al., 1999, *Nature* **401**, 453

Bloom, J. S., Kulkarni, S. R., Price, P. A., et al., 2002b, *ApJL* **572**, L45

Bloom, J. S., Perley, D. A., Li, W., et al., 2009, *ApJ* **691**, 723

Bloom, J. S., Prochaska, J. X., Pooley, D., et al., 2006, *ApJ* **638**, 354

Boella, G., Butler, R. C., Perola, G. C., et al., 1997, *A&AS* **122**, 299

Bolzonella, M., Miralles, J.-M., and Pelló, R., 2000, *A&A* **363**, 476

Bouchet, P., Lequeux, J., Maurice, E., Prevot, L., and Prevot-Burnichon, M. L., 1985, *A&A* **149**, 330

Bromberg, O., Nakar, E., Piran, T., and Sari, R., 2012, *ApJ* **749**, 110

Brown, P. J., Holland, S. T., Immler, S., et al., 2009, *AJ* **137**, 4517

Bufano, F., Benetti, S., Cappellaro, E., et al., 2010a, *GCN Circular* **10543**, 1

Bufano, F., Benetti, S., Cappellaro, E., et al., 2010b, *CBET* **2227**, 1

Bufano, F., Benetti, S., Sollerman, J., Pian, E., and Cupani, G., 2011, *Astronomische Nachrichten* **332**, 262

Bufano, F., Pian, E., Sollerman, J., et al., 2012, *ApJ* **753**, 67

Burrows, A., 2000, *Nature* **403**, 727

Burrows, D. N., Hill, J. E., Nousek, J. A., et al., 2005, *Space Sci. Rev.* **120**, 165

Butler, N. R., Kocevski, D., Bloom, J. S., and Curtis, J. L., 2007, *ApJ* **671**, 656

Campana, S., Mangano, V., Blustin, A. J., et al., 2006, *Nature* **442**, 1008

Campana, S., Starling, R. L. C., Evans, P. A., and Sakamoto, T., 2010, *GCN Circular* **11195**, 1

Cannizzo, J. K., Barthelmy, S. D., Beardmore, A. P., et al., 2009, *GCN Circular* **9223**, 1

Cano, Z., Bersier, D., Guidorzi, C., et al., 2011a, *ApJ* **740**, 41

Cano, Z., Bersier, D., Guidorzi, C., et al., 2011b, *MNRAS* **413**, 669

Cappa, C., Goss, W. M., and van der Hucht, K. A., 2004, *AJ* **127**, 2885

Cappellaro, E., Mazzali, P. A., Benetti, S., et al., 1997, *A&A* **328**, 203

Cardelli, J. A., Clayton, G. C., and Mathis, J. S., 1989, *ApJ* **345**, 245

Castro-Tirado, A. J. and Gorosabel, J., 1999, *A&AS* **138**, 449

Chavan, A. M., Silva, D. R., Boarotto, C., et al., 2000, in P. J. Quinn (ed.), *Observatory Operations to Optimize Scientific Return II*, Vol. 4010 of *Society of Photo-Optical Instrumentation Engineers (SPIE) Conference Series*, pp 81–89

Chevalier, R. A. and Soderberg, A. M., 2010, *ApJL* **711**, L40

Chornock, R., Berger, E., Levesque, E. M., et al., 2010a, *ApJL* submitted, arXiv:1004.2262

Chornock, R., Perley, D. A., Cenko, S. B., and Bloom, J. S., 2009, *GCN Circular* **9243**, 1

Chornock, R., Soderberg, A. M., Foley, R. J., et al., 2010b, *GCN Circular* **10541**, 1

Chornock, R., Soderberg, A. M., Foley, R. J., et al., 2010c, *CBET* **2228**, 1

Clocchiatti, A., Suntzeff, N. B., Covarrubias, R., and Candia, P., 2011, *AJ* **141**, 163

Clocchiatti, A. and Wheeler, J. C., 1997, *ApJ* **491**, 375

Cobb, B. E., Bailyn, C. D., van Dokkum, P. G., and Natarajan, P., 2006, *ApJL* **645**, L113

Cobb, B. E., Bloom, J. S., Cenko, S. B., and Perley, D. A., 2010a, *GCN Circ.* **10400**, 1

Cobb, B. E., Bloom, J. S., Morgan, A. N., Cenko, S. B., and Perley, D. A., 2010b, *CBET* **2288**, 1

Cobb, B. E., Bloom, J. S., Perley, D. A., et al., 2010c, *ApJL* **718**, L150

Colgate, S. A., 1968, *Canadian Journal of Physics* **46**, 476

Colgate, S. A., 1974, *ApJ* **187**, 333

Connaughton, V., 2009, *GCN Circular* **9230**, 1

Corsi, A., Ofek, E. O., Frail, D. A., et al., 2011, *ApJ* **741**, 76

Costa, E., Feroci, M., Frontera, F., et al., 1997a, *IAU Circular* **6572**, 1

Costa, E., Frontera, F., Heise, J., et al., 1997b, *Nature* **387**, 783

Cucchiara, A., Fox, D., Levan, A., and Tanvir, N., 2009, *GCN Circular* **10202**, 1

Cucchiara, A., Levan, A. J., Fox, D. B., et al., 2011, *ApJ* **736**, 7

Cummings, J. R., Barthelmy, S. D., Baumgartner, W. H., et al., 2010, *GCN Circular* **11475**, 1

D'Avanzo, P., Malesani, D., Covino, S., et al., 2009, *A&A* **498**, 711

D'Elia, V., Baumgartner, W. H., Beardmore, A. P., et al., 2011, *GCN Circular* **11699**, 1

Della Valle, M., Benetti, S., Mazzali, P., et al., 2008, *CBET* **1602**, 1

Della Valle, M., Chincarini, G., Panagia, N., et al., 2006a, *Nature* **444**, 1050

Della Valle, M., Malesani, D., Benetti, S., et al., 2003, *A&A* **406**, L33

Della Valle, M., Malesani, D., Bloom, J. S., et al., 2006b, *ApJL* **642**, L103

Deng, J., Tominaga, N., Mazzali, P. A., Maeda, K., and Nomoto, K., 2005, *ApJ* **624**, 898

Dessart, L. and Hillier, D. J., 2005, *A&A* **439**, 671

Dessart, L., Hillier, D. J., Livne, E., et al., 2011, *MNRAS* **414**, 2985

Drout, M. R., Soderberg, A. M., Gal-Yam, A., et al., 2011, *ApJ* **741**, 97

Eastman, R. G., Schmidt, B. P., and Kirshner, R., 1996, *ApJ* **466**, 911

Eichler, D., Livio, M., Piran, T., and Schramm, D. N., 1989, *Nature* **340**, 126

Ensman, L. and Woosley, S. E., 1987, in *AAS/CAS Joint Meeting*, Vol. 19 of *Bulletin of the American Astronomical Society*, p. 757, Vancouver, Canada

Evans, P. A., Beardmore, A. P., Page, K. L., et al., 2009, *MNRAS* **397**, 1177

Evans, P. A., Beardmore, A. P., Page, K. L., et al., 2007, *A&A* **469**, 379

Evans, P. A. and Holland, S. T., 2009, *GCN Circular* **9226**, 1

Falk, S. W., 1978, *ApJL* **225**, L133

Fan, Y.-Z., Zhang, B. B., Xu, D., Liang, E.-W., and Zhang, B., 2011, *ApJ* **726**, 32

Fenimore, E. E., Ricker, G., Atteia, J.-L., et al., 2004, *GCN Circular* **2735**, 1

Ferrero, P., Kann, D. A., Zeh, A., et al., 2006, *A&A* **457**, 857

Filgas, R., Greiner, J., Schady, P., et al., 2011, *A&A* **535**, A57

Filippenko, A. V., 1997, *ARA&A* **35**, 309

Filippenko, A. V., Matheson, T., and Barth, A. J., 1994, *AJ* **108**, 2220

Fitzpatrick, E. L., 1986, *AJ* **92**, 1068

Folatelli, G., Contreras, C., Phillips, M. M., et al., 2006, *ApJ* **641**, 1039

Foley, R. J., Papenkova, M. S., Swift, B. J., et al., 2003, *PASP* **115**, 1220

Fong, W., Berger, E., Chornock, R., et al., 2011, *ApJ* **730**, 26

Fox, D. B., Frail, D. A., Price, P. A., et al., 2005, *Nature* **437**, 845

Frontera, F., Amati, L., Vietri, M., et al., 2001, *ApJL* **550**, L47

Fryer, C. L., Hungerford, A. L., and Young, P. A., 2007, *ApJL* **662**, L55

Fryer, C. L., Woosley, S. E., and Hartmann, D. H., 1999, *ApJ* **526**, 152

Fukugita, M., Ichikawa, T., Gunn, J. E., et al., 1996, *AJ* **111**, 1748

Fynbo, J. P. U., Watson, D., Thöne, C. C., et al., 2006, *Nature* **444**, 1047

Gal-Yam, A., Fox, D. B., Price, P. A., et al., 2006, *Nature* **444**, 1053

Gal-Yam, A., Ofek, E. O., and Shemmer, O., 2002, *MNRAS* **332**, L73

Galama, T. J., Tanvir, N., Vreeswijk, P. M., et al., 2000, *ApJ* **536**, 185

Galama, T. J., Vreeswijk, P. M., Pian, E., et al., 1998a, *IAU Circular* **6895**, 1

Galama, T. J., Vreeswijk, P. M., van Paradijs, J., et al., 1998b, *Nature* **395**, 670

Galama, T. J., Wijers, R. A. M. J., Bremer, M., et al., 1998c, *ApJL* **500**, L101

Gehrels, N., Chincarini, G., Giommi, P., et al., 2004, *ApJ* **611**, 1005

Gelbord, J. M., Barthelmy, S. D., Burrows, D. N., et al., 2010, *GCN Circ.* **11473**, 1

Gezari, S., Rest, A., Huber, M. E., et al., 2010, *ApJL* **720**, L77

Goad, M. R., Osborne, J. P., Beardmore, A. P., and Evans, P. A., 2009, *GCN Circular* **9232**, 1

Golenetskii, S., Aptekar, R., Frederiks, D., et al., 2009, *GCN Circular* **10209**, 1

Golenetskii, S., Aptekar, R., Mazets, E., et al., 2004, *GCN Circular* **2754**, 1

Golenetskii, S., Aptekar, R., Mazets, E., et al., 2005, *GCN Circular* **3474**, 1

Golenetskii, S., Aptekar, R., Mazets, E., et al., 2008, *GCN Circular* **7482**, 1

Golenetskii, S., Aptekar, R., Mazets, E., et al., 2011a, *GCN Circular* **11951**, 1

Golenetskii, S., Aptekar, R., Mazets, E., et al., 2011b, *GCN Circular* **12663**, 1

Goodman, J., 1986, *ApJL* **308**, L47

Gorbovskoy, E., Lipunov, V., Kornilov, V., et al., 2010, *GCN Circular* **11185**, 1

Gorbovskoy, E. S., Lipunova, G. V., Lipunov, V. M., et al., 2012, *MNRAS* **421**, 1874

Gorosabel, J., Castro-Tirado, A. J., Guziy, S., et al., 2006, *A&A* **450**, 87

Granot, J., Piran, T., and Sari, R., 1999, *ApJ* **527**, 236

Greiner, J., Bornemann, W., Clemens, C., et al., 2008, *PASP* **120**, 405

Greiner, J., Bornemann, W., Clemens, C., et al., 2007, *The Messenger* **130**, 12

Greiner, J., Klose, S., Salvato, M., et al., 2003, *ApJ* **599**, 1223

Greiner, J., Krühler, T., Klose, S., et al., 2011, *A&A* **526**, A30

Greiner, J., Krühler, T., McBreen, S., et al., 2009, *ApJ* **693**, 1912

Grupe, D., Nousek, J. A., vanden Berk, D. E., et al., 2007, *AJ* **133**, 2216

Guidorzi, C., Melandri, A., and Tanvir, N., 2010, *GCN Circular* **11183**, 1

Hamuy, M., 2003, *ApJ* **582**, 905

Hamuy, M., Deng, J., Mazzali, P. A., et al., 2009, *ApJ* **703**, 1612

Hamuy, M., Phillips, M. M., Suntzeff, N. B., et al., 1996, *AJ* **112**, 2391

Hamuy, M. and Pinto, P. A., 2002, *ApJL* **566**, L63

Hansen, B. M. S., 1999, *ApJL* **512**, L117

Heger, A., Fryer, C. L., Woosley, S. E., Langer, N., and Hartmann, D. H., 2003, *ApJ* **591**, 288

Heise, J. and in 't Zand, J., 2001, in *From X-ray Binaries to Gamma Ray Bursts*, Vol. 308 of *Jan van Paradijs Memorial Symposium*, Amsterdam, Netherlands, arXiv:astro-ph/0112353

Heise, J., in't Zand, J., Kippen, R. M., and Woods, P. M., 2001, in E. Costa, F. Frontera, & J. Hjorth (ed.), *Gamma-ray Bursts in the Afterglow Era*, p. 16, ESO Astrophysics Symposia, Springer-Verlag, Rome, Italy

Hill, J., Garnavich, P., Kuhn, O., et al., 2007, *GCN Circular* **6486**, 1

Hillebrandt, W. and Niemeyer, J. C., 2000, *ARA&A* **38**, 191

Hjorth, J., Sollerman, J., Gorosabel, J., et al., 2005a, *ApJL* **630**, L117

Hjorth, J., Sollerman, J., Møller, P., et al., 2003, *Nature* **423**, 847

Hjorth, J., Watson, D., Fynbo, J. P. U., et al., 2005b, *Nature* **437**, 859

Horváth, I., 1998, *ApJ* **508**, 757

Horváth, I., Balázs, L. G., Bagoly, Z., Ryde, F., and Mészáros, A., 2006, *A&A* **447**, 23

Huang, K. Y., Urata, Y., Im, M., and Sakamoto, T., 2010, *GCN Circular* **11262**, 1

Hurley, K. and Cline, T., 1999, *GCN Circular* **450**, 1

Hurley, K., Cline, T., Frontera, F., et al., 2002, *GCN Circular* **1325**, 1

Hurley, K., Cline, T., Mazets, E., et al., 2000a, *ApJL* **534**, L23

Hurley, K., Cline, T., Mazets, E., and Golenetskii, S., 2000b, *GCN Circular* **791**, 1

Im, M., Choi, C., Jun, H., et al., 2010, *GCN Circular* **11210**, 1

Johnson, H. L. and Morgan, W. W., 1953, *ApJ* **117**, 313

Jones, M. I., Hamuy, M., Lira, P., et al., 2009, *ApJ* **696**, 1176

Kalberla, P. M. W., Burton, W. B., Hartmann, D., et al., 2005, *A&A* **440**, 775

Kaneko, Y., Preece, R. D., Briggs, M. S., et al., 2006, *ApJS* **166**, 298

Kaneko, Y., Ramirez-Ruiz, E., Granot, J., et al., 2007, *ApJ* **654**, 385

Kaufer, A., Stahl, O., Tubbesing, S., et al., 1999, *The Messenger* **95**, 8

Kawabata, K. S., Deng, J., Wang, L., et al., 2003, *ApJL* **593**, L19

Kippen, R. M., 1998, *GCN Circular* **67**, 1

Kippen, R. M., in't Zand, J. J. M., Woods, P. M., et al., 2004, in E. Fenimore & M. Galassi (ed.), *Gamma-Ray Bursts: 30 Years of Discovery*, Vol. 727 of *AIP Conference Series*, pp 119–122, AIP, Santa Fe, NM

Klebesadel, R. W., Strong, I. B., and Olson, R. A., 1973, *ApJL* **182**, L85

Klein, R. I. and Chevalier, R. A., 1978, *ApJL* **223**, L109

Kocevski, D., Modjaz, M., Bloom, J. S., et al., 2007, *ApJ* **663**, 1180

Kouveliotou, C., Meegan, C. A., Fishman, G. J., et al., 1993, *ApJL* **413**, L101

Kouveliotou, C., Woosley, S. E., Patel, S. K., et al., 2004, *ApJ* **608**, 872

Krimm, H. A., Yamaoka, K., Sugita, S., et al., 2009, *ApJ* **704**, 1405

Krühler, T., Küpcü-Yoldaş, A., Greiner, J., et al., 2008, *ApJ* **685**, 376

Krühler, T., Schady, P., Greiner, J., et al., 2011, *A&A* **526**, A153

Krushinski, V., Zalozhnich, I., Kopytova, T., et al., 2010, *GCN Circular* **11182**, 1

Kulkarni, S. R., Djorgovski, S. G., Ramaprakash, A. N., et al., 1998, *Nature* **393**, 35

Küpcü-Yoldaş, A., Krühler, T., Greiner, J., et al., 2008, in M. Galassi, D. Palmer, & E. Fenimore (ed.), *Gamma-Ray Bursts 2007*, Vol. 1000 of *AIP Conference Series*, pp 227–231, Santa Fe, NM

Kuroda, D., Hanayama, H., Miyaji, T., et al., 2010, *GCN Circular* **11206**, 1

Lamb, D. Q. and Reichart, D. E., 2000, *ApJ* **536**, 1

Landsman, W. and Sakamoto, T., 2010, *GCN Circular* **11193**, 1

Levesque, E. M., Berger, E., Soderberg, A. M., and Chornock, R., 2011, *ApJ* **739**, 23

Li, W., Filippenko, A. V., Gates, E., et al., 2001, *PASP* **113**, 1178

MacFadyen, A. I. and Woosley, S. E., 1999, *ApJ* **524**, 262

Maeda, K., Mazzali, P. A., Deng, J., et al., 2003, *ApJ* **593**, 931

Maiolino, R., Schneider, R., Oliva, E., et al., 2004, *Nature* **431**, 533

Malesani, D., Covino, S., D'Avanzo, P., et al., 2007, *A&A* **473**, 77

Malesani, D., Fynbo, J. P. U., Hjorth, J., et al., 2009, *ApJL* **692**, L84

Malesani, D., Tagliaferri, G., Chincarini, G., et al., 2004, *ApJL* **609**, L5

Mangano, V., Beardmore, A. P., Burrows, D. N., et al., 2011, *GCN Circular* **11941**, 1

Markwardt, C. M., Barthelmy, S. D., Baumgartner, W. H., et al., 2008, *GCN Circular* **8338**, 1

Masetti, N., Palazzi, E., Pian, E., et al., 2005, *A&A* **438**, 841

Masetti, N., Palazzi, E., Pian, E., et al., 2003, *A&A* **404**, 465

Matheson, T., Garnavich, P. M., Stanek, K. Z., et al., 2003, *ApJ* **599**, 394

Matzner, C. D. and McKee, C. F., 1999, *ApJ* **510**, 379

Maund, J. R. and Smartt, S. J., 2005, *MNRAS* **360**, 288

Maund, J. R., Smartt, S. J., and Schweizer, F., 2005, *ApJL* **630**, L33

Mazzali, P. A., Deng, J., Nomoto, K., et al., 2006a, *Nature* **442**, 1018

Mazzali, P. A., Deng, J., Pian, E., et al., 2006b, *ApJ* **645**, 1323

Mazzali, P. A., Deng, J., Tominaga, N., et al., 2003, *ApJL* **599**, L95

Mazzali, P. A., Iwamoto, K., and Nomoto, K., 2000, *ApJ* **545**, 407

Mazzali, P. A., Valenti, S., Della Valle, M., et al., 2008, *Science* **321**, 1185

McBreen, S., 2009, *GCN Circular* **9535**, 1

McBreen, S., Foley, S., Watson, D., et al., 2008, *ApJL* **677**, L85

Meegan, C., Lichti, G., Bhat, P. N., et al., 2009, *ApJ* **702**, 791

Meegan, C. A., Fishman, G. J., Wilson, R. B., et al., 1992, *Nature* **355**, 143

Mészáros, P., 2006, *Reports on Progress in Physics* **69**, 2259

Mészáros, P. and Rees, M. J., 1992, *ApJ* **397**, 570

Mészáros, P. and Rees, M. J., 1997, *ApJL* **482**, L29

Metzger, M. R., Djorgovski, S. G., Kulkarni, S. R., et al., 1997, *Nature* **387**, 878

Milne, P. A., Brown, P. J., Roming, P. W. A., et al., 2010, *ApJ* **721**, 1627

Minkowski, R., 1941, *PASP* **53**, 224

Mirabal, N., Halpern, J. P., An, D., Thorstensen, J. R., and Terndrup, D. M., 2006, *ApJL* **643**, L99

Modjaz, M., Li, W., Butler, N., et al., 2009, *ApJ* **702**, 226

Modjaz, M., Stanek, K. Z., Garnavich, P. M., et al., 2006, *ApJL* **645**, L21

Molinari, E., Vergani, S. D., Malesani, D., et al., 2007, *A&A* **469**, L13

Monet, D. G., Levine, S. E., Canzian, B., et al., 2003, *AJ* **125**, 984

Morganson, E., De Rosa, G., Decarli, R., et al., 2012, *AJ* **143**, 142

Mould, J. R., Huchra, J. P., Freedman, W. L., et al., 2000, *ApJ* **529**, 786

Mukherjee, S., Feigelson, E. D., Jogesh Babu, G., et al., 1998, *ApJ* **508**, 314

Nadyozhin, D. K., 2003, *MNRAS* **346**, 97

Nakamura, T., Mazzali, P. A., Nomoto, K., and Iwamoto, K., 2001, *ApJ* **550**, 991

Nakar, E. and Sari, R., 2010, *ApJ* **725**, 904

Nardini, M., Ghisellini, G., Ghirlanda, G., and Celotti, A., 2010, *MNRAS* **403**, 1131

Nikolov, N., Henning, T., Koppenhoefer, J., et al., 2012, *A&A* **539**, A159

Nomoto, K., Suzuki, T., Shigeyama, T., et al., 1993, *Nature* **364**, 507

Nomoto, K., Tanaka, M., Tominaga, N., and Maeda, K., 2010, *New A Rev.* **54**, 191

Oates, S. R., de Pasquale, M., and Stamatikos, M., 2010, *GCN Circular* **10520**, 1

Oates, S. R. and Mangano, V., 2011, *GCN Circular* **11948**, 1

Ofek, E. O., Cenko, S. B., Gal-Yam, A., et al., 2007, *ApJ* **662**, 1129

Olivares E., F., Afonso, P., Greiner, J., et al., 2009a, *GCN Circular* **9874**, 1

Olivares E., F., Greiner, J., Schady, P., et al., 2012, *A&A* **539**, A76

Olivares E., F. and Hamuy, M., 2011, *Core-Collapse Supernovae as Standard Candles*, Lambert Academic Publishing, Germany

Olivares E., F., Hamuy, M., Pignata, G., et al., 2010, *ApJ* **715**, 833

Olivares E., F., Küpcü-Yoldaş, A., Greiner, J., and Yoldaş, A., 2009b, *GCN Circular* **9245**, 1

Olivares E., F., Rossi, A., Greiner, J., Yoldaş, A., and Küpcü-Yoldaş, A., 2009c, *GCN Circular* **8812**, 1

Olivares E., F., Schady, P., Krühler, T., et al., 2011, *GCN Circular* **11578**, 1

Paciesas, W. S., Meegan, C. A., Pendleton, G. N., et al., 1999, *ApJS* **122**, 465

Paczyński, B., 1986, *ApJL* **308**, L43

Paczyński, B., 1998a, *ApJL* **494**, L45

Paczyński, B., 1998b, in C. A. Meegan, R. D. Preece, & T. M. Koshut (ed.), *Gamma-Ray Bursts: 4th Hunstville Symposium*, Vol. 428 of *AIP Conference Series*, pp 783–787, Huntsville, AL

Palmer, D. M., Barthelmy, S. D., Baumgartner, W. H., et al., 2011, *GCN Circular* **12640**, 1

Patat, F., Cappellaro, E., Danziger, J., et al., 2001, *ApJ* **555**, 900

Pei, Y. C., 1992, *ApJ* **395**, 130

Perlmutter, S., Aldering, G., Goldhaber, G., et al., 1999, *ApJ* **517**, 565

Perri, M., Barthelmy, S. D., Cummings, J. R., et al., 2007, *GCN Circular* **7058**, 1

Phillips, M. M., 1993, *ApJL* **413**, L105

Phillips, M. M., Lira, P., Suntzeff, N. B., et al., 1999, *AJ* **118**, 1766

Pian, E., Amati, L., Antonelli, L. A., et al., 2000, *ApJ* **536**, 778

Pian, E., Antonelli, L. A., Piro, L., and Feroci, M., 1998, *GCN Circular* **158**, 1

Pian, E., Mazzali, P. A., Masetti, N., et al., 2006, *Nature* **442**, 1011

Pignata, G., Stritzinger, M., Soderberg, A., et al., 2011, *ApJ* **728**, 14

Piran, T., 1999, *Phys. Rep.* **314**, 575

Poole, T. S., Breeveld, A. A., Page, M. J., et al., 2008, *MNRAS* **383**, 627

Prabhu, T. P., Mayya, Y. D., Singh, K. P., et al., 1995, *A&A* **295**, 403

Prevot, M. L., Lequeux, J., Prevot, L., Maurice, E., and Rocca-Volmerange, B., 1984, *A&A* **132**, 389

Price, P. A., Berger, E., Kulkarni, S. R., et al., 2002, *ApJ* **573**, 85

Price, P. A., Kulkarni, S. R., Berger, E., et al., 2003, *ApJ* **589**, 838

Qin, Y.-P., Xie, G.-Z., Xue, S.-J., et al., 2000, *PASJ* **52**, 759

Rau, A., Nardini, M., Updike, A., et al., 2010, *GCN Circular* **10547**, 1

Rau, A., Schady, P., Greiner, J., et al., 2012, *A&A* **538**, A26

Reichart, D. E., 1999, *ApJL* **521**, L111

Reichart, D. E., Lamb, D. Q., and Castander, F. J., 2000, in R. M. Kippen, R. S. Mallozzi, & G. J. Fishman (ed.), *Gamma-ray Bursts: 5th Huntsville Symposium*, Vol. 526 of *AIP Conference Series*, pp 414–418, AIP, Huntsville, AL

Rhoads, J. E., 2001, *ApJ* **557**, 943

Richardson, D., 2009, *AJ* **137**, 347

Richardson, D., Branch, D., and Baron, E., 2006, *AJ* **131**, 2233

Richmond, M. W., van Dyk, S. D., Ho, W., et al., 1996, *AJ* **111**, 327

Riess, A. G., Filippenko, A. V., Challis, P., et al., 1998, *AJ* **116**, 1009

Riess, A. G., Macri, L., Casertano, S., et al., 2009, *ApJ* **699**, 539

Roming, P. W. A., Kennedy, T. E., Mason, K. O., et al., 2005, *Space Sci. Rev.* **120**, 95

Roming, P. W. A., Pritchard, T. A., Brown, P. J., et al., 2009, *ApJL* **704**, L118

Rossi, A., Schulze, S., Klose, S., et al., 2011, *A&A* **529**, A142

Sadler, E. M., Stathakis, R. A., Boyle, B. J., and Ekers, R. D., 1998, *IAU Circular* **6901**, 1

Sahu, D. K., Tanaka, M., Anupama, G. C., Gurugubelli, U. K., and Nomoto, K., 2009, *ApJ* **697**, 676

Sahu, K. C., Livio, M., Petro, L., et al., 1997, *Nature* **387**, 476

Sakamoto, T., Barthelmy, S. D., Baumgartner, W. H., et al., 2009, *GCN Circular* **9231**, 1

Sakamoto, T., Barthelmy, S. D., Baumgartner, W. H., et al., 2010a, *GCN Circular* **10511**, 1

Sakamoto, T., Baumgartner, W. H., Beardmore, A. P., et al., 2010b, *GCN Circular* **11181**, 1

Sakamoto, T., Lamb, D. Q., Kawai, N., et al., 2005, *ApJ* **629**, 311

Sanders, N. E., Soderberg, A. M., Valenti, S., et al., 2012, *ApJ* **756**, 184

Sari, R., Piran, T., and Narayan, R., 1998, *ApJL* **497**, L17

Sato, G., Barbier, L., Barthelmy, S. D., et al., 2007, *GCN Circular* **7148**, 1

Savaglio, S., Glazebrook, K., and Le Borgne, D., 2009, *ApJ* **691**, 182

Sazonov, S. Y., Lutovinov, A. A., and Sunyaev, R. A., 2004, *Nature* **430**, 646

Schady, P., Dwelly, T., Page, M. J., et al., 2012, *A&A* **537**, A15

Schady, P., Page, M. J., Oates, S. R., et al., 2010, *MNRAS* **401**, 2773

Schawinski, K., Justham, S., Wolf, C., et al., 2008, *Science* **321**, 223

Schlegel, D. J., Finkbeiner, D. P., and Davis, M., 1998, *ApJ* **500**, 525

Shcherbakov, R. V., Pe'er, A., Reynolds, C. S., et al., 2012, in *Tidal Disruption Events and AGN Outbursts*, Vol. 39 of *European Physical Journal Web of Conferences*, p. 2007

Skrutskie, M. F., Cutri, R. M., Stiening, R., et al., 2006, *AJ* **131**, 1163

Smith, J. A., Tucker, D. L., Kent, S., et al., 2002, *AJ* **123**, 2121

Soderberg, A., Berger, E., and Fox, D., 2008a, *GCN Circular* **8662**, 1

Soderberg, A. M., Berger, E., Page, K. L., et al., 2008b, *Nature* **453**, 469

Soderberg, A. M., Kulkarni, S. R., Fox, D. B., et al., 2005, *ApJ* **627**, 877

Soderberg, A. M., Kulkarni, S. R., Price, P. A., et al., 2006, *ApJ* **636**, 391

Soderberg, A. M., Nakar, E., Cenko, S. B., et al., 2007, *ApJ* **661**, 982

Soffitta, P., Feroci, M., Piro, L., et al., 1998, *IAU Circular* **6884**, 1

Sollerman, J., Fynbo, J. P. U., Gorosabel, J., et al., 2007, *A&A* **466**, 839

Sollerman, J., Jaunsen, A. O., Fynbo, J. P. U., et al., 2006, *A&A* **454**, 503

Sparre, M., Fynbo, J., de Ugarte Postigo, A., Malesani, D., and Sollerman, J., 2011, *CBET* **2706**, 1

Sparre, M., Sollerman, J., Fynbo, J. P. U., et al., 2011b, *ApJL* **735**, L24

Stamatikos, M., Barthelmy, S. D., Baumgartner, W. H., et al., 2010a, *GCN Circular* **10496**, 1

Stamatikos, M., Barthelmy, S. D., Baumgartner, W. H., et al., 2009, *GCN Circular* **10197**, 1

Stamatikos, M., Barthelmy, S. D., Baumgartner, W. H., et al., 2010b, *GCN Circular* **11202**, 1

Stanek, K. Z., Garnavich, P. M., Nutzman, P. A., et al., 2005, *ApJL* **626**, L5

Stanek, K. Z., Matheson, T., Garnavich, P. M., et al., 2003, *ApJL* **591**, L17

Starling, R. L. C. and Sakamoto, T., 2010, *GCN Circular* **11194**, 1

Starling, R. L. C., Wiersema, K., Levan, A. J., et al., 2011, *MNRAS* **411**, 2792

Stratta, G., Maiolino, R., Fiore, F., and D'Elia, V., 2007, *ApJL* **661**, L9

Strobl, J., Nekola, M., Blazek, M., et al., 2010, *GCN Circular* **11339**, 1

Sutherland, P. G. and Wheeler, J. C., 1984, *ApJ* **280**, 282

Svoboda, R., McNaught, R. H., Jones, A., et al., 1987, *IAU Circular* **4340**, 1

Swartz, D. A., Clocchiatti, A., Benjamin, R., Lester, D. F., and Wheeler, J. C., 1993, *Nature* **365**, 232

Tanvir, N. R., Rol, E., Levan, A. J., et al., 2010, *ApJ* **725**, 625

Taubenberger, S., Pastorello, A., Mazzali, P. A., et al., 2006, *MNRAS* **371**, 1459

Taylor, G. B., Frail, D. A., Kulkarni, S. R., et al., 1998, *ApJL* **502**, L115

Tello, J. C., Sanchez-Ramirez, R., Sota, A., Gorosabel, J., and Castro-Tirado, A. J., 2010, *GCN Circular* **11196**, 1

Thöne, C. C., de Ugarte Postigo, A., Fryer, C. L., et al., 2011, *Nature* **480**, 72

Thöne, C. C., Goldoni, P., Covino, S., et al., 2009, *GCN Circular* **10233**, 1

Tinney, C., Stathakis, R., Cannon, R., and Galama, T., 1998, *IAU Circular* **6896**, 3

Todini, P. and Ferrara, A., 2001, *MNRAS* **325**, 726

Tody, D., 1993, in R. J. Hanisch, R. J. V. Brissenden, & J. Barnes (ed.), *Astronomical Data Analysis Software and Systems II*, Vol. 52 of *Astronomical Society of the Pacific Conference Series*, p. 173, ASP, San Francisco, CA

Troja, E., Barthelmy, S. D., Baumgartner, W. H., et al., 2009, *GCN Circular* **10191**, 1

Umeda, H. and Nomoto, K., 2008, *ApJ* **673**, 1014

Updike, A., Nicuesa Guelbenzu, A., Klose, S., and Greiner, J., 2010, *GCN Circular* **11209**, 1

Updike, A., Rossi, A., Rau, A., et al., 2009, *GCN Circular* **10195**, 1

Utrobin, V. P., 1996, *A&A* **306**, 219

Utrobin, V. P., 2007, *A&A* **461**, 233

Valenti, S., Benetti, S., Cappellaro, E., et al., 2008, *MNRAS* **383**, 1485

van der Horst, A. J., 2010, *GCN Circular* **11477**, 1

van Paradijs, J., Groot, P. J., Galama, T., et al., 1997, *Nature* **386**, 686

van Paradijs, J., Kouveliotou, C., and Wijers, R. A. M. J., 2000, *ARA&A* **38**, 379

Vergani, S. D., D'Avanzo, P., Levan, A. J., et al., 2010a, *GCN Circular* **10512**, 1

Vergani, S. D., Flores, H., Covino, S., et al., 2011, *A&A* **535**, A127

Vergani, S. D., Levan, A. J., D'Avanzo, P., et al., 2010b, *GCN Circular* **10513**, 1

Vietri, M. and Stella, L., 1999, *ApJL* **527**, L43

Vink, J. S. and de Koter, A., 2005, *A&A* **442**, 587

Vreeswijk, P. M., Smette, A., Malesani, D., et al., 2008, *GCN Circular* **7444**, 1

Wang, X.-Y., Li, Z., Waxman, E., and Mészáros, P., 2007, *ApJ* **664**, 1026

Watson, D., Hjorth, J., Levan, A., et al., 2004, *ApJL* **605**, L101

Waxman, E., Mészáros, P., and Campana, S., 2007, *ApJ* **667**, 351

Wiersema, K., D'Avanzo, P., Levan, A. J., et al., 2010, *GCN Circular* **10525**, 1

Wiersema, K., de Ugarte Postigo, A., and Levan, A., 2009, *GCN Circular* **9250**, 1

Wiersema, K., van der Horst, A. J., Kann, D. A., et al., 2008, *A&A* **481**, 319

Wilson-Hodge, C. A. and Preece, R. D., 2009, *GCN Circular* **10204**, 1

Wisotzki, L., Selman, F., and Gilliote, A., 2001, *The Messenger* **104**, 8

Wood-Vasey, W. M., Miknaitis, G., Stubbs, C. W., et al., 2007, *ApJ* **666**, 694

Woosley, S. E., 1993, *ApJ* **405**, 273

Woosley, S. E. and Bloom, J. S., 2006, *ARA&A* **44**, 507

Woosley, S. E., Heger, A., and Weaver, T. A., 2002, *Reviews of Modern Physics* **74**, 1015

Woosley, S. E. and MacFadyen, A. I., 1999, *A&AS* **138**, 499

Woosley, S. E. and Weaver, T. A., 1994, in S. A. Bludman, R. Mochkovitch, and J. Zinn-Justin (eds.), *Supernovae*, p. 63

Yoon, S.-C., Gräfener, G., Vink, J. S., Kozyreva, A., and Izzard, R. G., 2012, *A&A* **544**, L11

Yoshii, Y., Tomita, H., Kobayashi, Y., et al., 2003, *ApJ* **592**, 467

Yuan, F., 2009, *GCN Circular* **9224**, 1

Zeh, A., Klose, S., and Hartmann, D. H., 2004, *ApJ* **609**, 952

Zeh, A., Klose, S., and Kann, D. A., 2006, *ApJ* **637**, 889

Zhang, B. and Mészáros, P., 2004, *International Journal of Modern Physics A* **19**, 2385

Zhang, B., Zhang, B. B., Liang, E. W., et al., 2007, *ApJL* **655**, L25

Zhang, B., Zhang, B. B., Virgili, F. J., et al., 2009, *ApJ* **703**, 1696

Acknowledgments

I would like to thank all the people who helped me with the thesis research, namely, my supervisor and GROND PI Jochen Greiner and the whole GROND team. Thanks to Patricia Schady for preparing the UVOT data for my research and all the patience while teaching me how to use XSPEC. Thanks to Sandra Savaglio for her analysis of the host galaxies of GRBs 081007, 091127, and 101219B. I would like to thank Ferdinando Patat for stimulating discussion as well as for accurate comments and suggestions and also Pete Roming for stimulating discussion on the possible projects using the SE-SNe data. I am also very grateful to each member of the thesis committee for their invaluable advice: Nando Patat, Sandra Savaglio, most recently Arne Rau, and Patricia Schady. I would also like to thank all my colleagues and friends for their scientific and social support during those tough years. Andrea R. for having taught me how to operate GROND, Thomas K. for his very useful scripts, Robert F. for being my officemate, Jonny E. for sharing his Pisco bottles, Vlad S. for the always prompt software support. Also a special gratitude to Ana N., Marco N., Paulo A., Alex K., and Adria U. for being great colleagues and sharing the endless observing shifts. I am also grateful to Pablo Arias, Javier Alarcón, and all the TIOs at La Silla for helping me to survive the three-weeks observing shifts.

Most importantly, I would like to extend a special gratitude to my beloved wife Natalia Armijo S. for accompanying me to our German adventure, having so much patience, and being the happiness of my life. Without her, no PhD thesis would have been possible at all.

Part of the funding for GROND (both hardware and personnel) was generously granted from the Leibniz-Prize to Prof. G. Hasinger, *Deutsche Forschungsgemeinschaft* (DFG) grant HA 1850/28–1. This work made use of data supplied by the UK *Swift* Science Data Centre at the University of Leicester. The Ph. D. studies of F. O. E. are funded by the German *Deutscher Akademischer Austausch Dienst*, DAAD, and the Chilean *Comisión Nacional de Investigación Científica y Tecnológica*, CONICYT. T. K. acknowledges support by the DFG cluster of excellence "Origin and Structure of the Universe" and by the European Commission under the Marie Curie Intra-European Fellowship Programme. The Dark Cosmology Centre is funded by the Danish National Research Foundation. S. K., A. N. G., A. Rossi, and D. A. K. acknowledge support by DFG grant Kl 766/16–1. M. N. acknowledges support by DFG grant SA 2001/2–1. P. S. acknowledges support by DFG grant SA 2001/1–1. A. C. U., A. N. G., D. A. K., and A. Rossi are grateful for travel funding support through MPE. Figure 3.1 is partially based on observations made with the NASA/ESA Hubble Space Telescope, obtained from the data archive at the Space Telescope Science Institute. STScI is operated by the Association of Universities for Research in Astronomy, Inc. under NASA contract NAS 5–26555. This research has made use of NASA's Astrophysics Data System. This research has made use of data obtained from the HETE science team via the website `http://space.mit.edu/HETE/Bursts/Data`. HETE is an international mission of the NASA Explorer program, run by the Massachusetts Institute of Technology.